

UNIVERSITY OF CALIFORNIA

Los Angeles

Tectonic and Thermal Evolution of the  
Cordillera Blanca Detachment System, Peruvian Andes:  
Implications for Normal Faulting in a Contractional Orogen

A dissertation submitted in partial satisfaction of the  
requirements for the degree Doctor of Philosophy  
in Geology

by

Melissa Katherine Giovanni

2007

UMI Number: 3288230

### INFORMATION TO USERS

The quality of this reproduction is dependent upon the quality of the copy submitted. Broken or indistinct print, colored or poor quality illustrations and photographs, print bleed-through, substandard margins, and improper alignment can adversely affect reproduction.

In the unlikely event that the author did not send a complete manuscript and there are missing pages, these will be noted. Also, if unauthorized copyright material had to be removed, a note will indicate the deletion.

**UMI<sup>®</sup>**

---

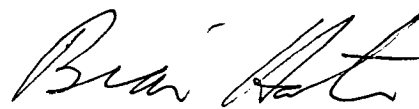
UMI Microform 3288230

Copyright 2008 by ProQuest Information and Learning Company.

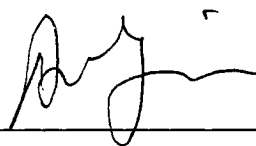
All rights reserved. This microform edition is protected against unauthorized copying under Title 17, United States Code.

ProQuest Information and Learning Company  
300 North Zeeb Road  
P.O. Box 1346  
Ann Arbor, MI 48106-1346

The dissertation of Melissa Katherine Giovanni is approved.



Brian K. Horton



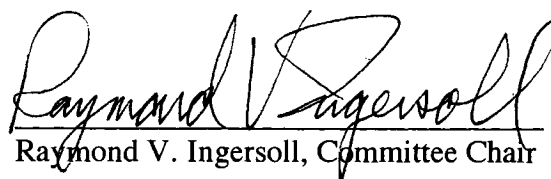
An Yin



Gilles F. Peltzer



Antony R. Orme



Raymond V. Ingersoll, Committee Chair

University of California, Los Angeles

2007

To my parents, Nick and Kathy  
and  
Frank



## TABLE OF CONTENTS

<b>Chapter 1: Introduction</b>	1
1.1 Introduction	2
1.2 Possible explanations for flat slab subduction	3
1.3 Models of the Peruvian flat slab segment	5
1.3.1 Reconstructions of the timing and location of initial Nazca Ridge subduction	5
1.3.2 The “Lost Inca Plateau”	8
1.4 Role of flat slab subduction in the evolution of the Cordillera Blanca normal fault	10
1.5 Observations from the Cordillera Blanca, Peru	13
1.6 References	19
 <b>Chapter 2: Asymmetrical growth of footwall topography in the Cordillera Blanca, Peru: Implications for normal fault control on landscape evolution</b>	 24
2.1 Abstract	25
2.2 Introduction	26
2.3 Regional setting of the Cordillera Blanca	29
2.3.1 Tectonic setting	29
2.3.2 Geologic setting	30
2.3.3 Geomorphic setting	34
2.4 Methods	35
2.5 Along-strike variations in the Cordillera Blanca footwall drainages	37
2.5.1 Elevation and relief	37
2.5.2 Drainage morphometry	40
2.5.3 Drainage hypsometry	41
2.5.4 Longitudinal profiles	42
2.6 Along-strike variations of the Cordillera Blanca normal fault	45
2.6.1 Normal fault evolution	45
2.6.2 Fault relief	45
2.6.3 Geomorphology as a proxy for displacement	46
2.7 Discussion	48
2.7.1 Morphometry of the Cordillera Blanca	48
2.7.2 Drainage network evolution in the Cordillera Blanca	52
2.7.3 Evolution of the Cordillera Blanca normal fault	53
2.8 Conclusions	55
2.9 References	96
 <b>Chapter 3: Supradetachment basin evolution along the Cordillera Blanca detachment fault, Peru: Implications for normal faulting and basin growth in a contractional orogen</b>	 103
3.1 Abstract	104
3.2 Introduction	105

3.3 Tectonic setting	108
3.3.1 Regional strain distribution	108
3.3.2 Cordillera Blanca extensional system	110
3.4 Basin analysis of the Callejon de Huaylas	111
3.4.1 Lithologic units	111
3.4.2 Methods and data	113
3.4.3 Stratigraphy of the Lloclla Formation	116
3.4.4 Stable isotopic studies of the Lloclla Formation	119
3.4.4.1 Carbonate oxygen isotope paleoaltimetry	119
3.4.4.2 Hydrogen isotopic composition of surface water	123
3.5 Discussion of basin evolution	123
3.6 Models of extensional basin evolution	126
3.6.1 Single-segment fault with one basin (Model 1)	127
3.6.2 Two-segment fault with two basins (Model 2)	129
3.7 Conclusions	130
3.8 References	155
<b>Chapter 4: U-Pb and <math>^{40}\text{Ar}/^{39}\text{Ar}</math> evidence for coeval Neogene pluton emplacement and fault-induced exhumation in the Cordillera Blanca, Peru</b>	162
4.1 Abstract	163
4.2 Introduction	164
4.3 Geologic setting	166
4.4 Emplacement ages of the Cordillera Blanca from U-Pb zircon dating	168
4.5 Spatial patterns of cooling ages	169
4.5.1 $^{40}\text{Ar}/^{39}\text{Ar}$ thermochronology	169
4.5.2 Mica $^{40}\text{Ar}/^{39}\text{Ar}$ results	170
4.5.3 K-feldspar $^{40}\text{Ar}/^{39}\text{Ar}$ results	172
4.6 Apatite (U-Th)/He results	173
4.7 Thermal models of batholith emplacement and exhumation	174
4.8 Structural model of fault evolution	177
4.8.1 Rolling-hinge model	178
4.8.2 Fault slip rates	180
4.9 Discussion	182
4.10 Conclusions	184
4.11 References	226
<b>Chapter 5: Conclusions</b>	233
5.1 Summary of Cordillera Blanca evolution	234
5.2 References	236

## LIST OF FIGURES

1.1 Shaded relief map of South America	15
1.2 Reconstruction of Nazca Ridge subduction	16
1.3 Location of subducted aseismic ridges	17
1.4 Reconstruction of subducted aseismic ridges	18
2.1 Hypsometric curves	58
2.2 Simplified regional tectonic map	59
2.3 Simplified regional geologic map	60
2.4 Geologic map of the Cordillera Blanca	61
2.5 DEM of northern fault tip	62
2.6 Possible fault terminations for northern fault tip	63
2.7 Rio Santa longitudinal profile	64
2.8 Drainage basins of the Cordillera Blanca	65
2.9 Schematic diagram of “bow-and-arrow” rule	66
2.10 Map of topographic profiles	67
2.11 Topographic profiles	68
2.12 Topographic profile of drainage divide	70
2.13 3D view of warped fault surface	71
2.14 Schematic footwall and drainage characteristics	74
2.15 Geomorphic parameters of Cordillera Blanca drainage basins	75
2.16 Hypsometric curves of Cordillera Blanca drainage basins	78
2.17 Longitudinal profiles of Cordillera Blanca drainages	80
2.18 3D view showing exposed fault scarps	87
2.19 Exposed fault relief	89
2.20 Cordillera Blanca footwall characteristics	90
2.21 Elongation ratios	91
3.1 Shaded relief map of South America	132
3.2 Simplified regional tectonic map	133
3.3 Simplified regional geologic map	134
3.4 Geologic map of the Cordillera Blanca	135
3.5 Field photos	136
3.6 Biotite $^{40}\text{Ar}/^{39}\text{Ar}$ age spectra from Yungay ignimbrites	138
3.7 Schematic cross section of sedimentary basin	139
3.8 Stratigraphic column for Lloclla Formation	140
3.9 Sandstone point count results	141
3.10 Field photo of Lloclla Formation	142
3.11 Paleocurrents and clast counts above and below 900 meter level	143
3.12 Field photo and biotite $^{40}\text{Ar}/^{39}\text{Ar}$ age spectrum from basal tuff	144
3.13 Dip changes and maximum clast sizes within Lloclla Formation	145
3.14 Oxygen isotopic data from Lloclla carbonates	146
3.15 Change in dip strata due to footwall flats and ramps	148

3.16 Schematic model of basin evolution – Model 1	149
3.17 Schematic model of basin evolution – Model 2	150
4.1 Simplified regional tectonic map	186
4.2 Geologic map of the Cordillera Blanca with sample locations	187
4.3 Zircon U-Pb ages from Llanganuco transect	188
4.4 Zircon U-Pb ages from Honda transect	189
4.5 Probability density distribution of zircon ages from Llanganuco and Honda transects	190
4.6 Geologic map with $^{40}\text{Ar}/^{39}\text{Ar}$ and (U-Th)/He cooling ages	191
4.7 Age-distance and age-elevation plots of biotite $^{40}\text{Ar}/^{39}\text{Ar}$ data	192
4.8 Mica $^{40}\text{Ar}/^{39}\text{Ar}$ age spectra	193
4.9 Age spectra and MDD model results from K-feldspar $^{40}\text{Ar}/^{39}\text{Ar}$ data	194
4.10 Schematic cross sections of Honda transect	195
4.11 Thermal histories from Honda transect	196
4.12 Age-distance and age-elevation plots of apatite (U-Th)/He data	197
4.13 Thermokinetic models of intrusion and exhumation	198
4.14 Combined thermal histories from Honda transect	199
4.15 3D view of fault facets to southeast	200
4.16 3D view of fault facets to northwest	202
4.17 Schematic cross-sections of rolling-hinge models	204
4.18 Definitions and calculations of vertical exhumation rate, horizontal extension rate, and fault slip rate	205

## LIST OF TABLES

2.1 Summary of geomorphic parameters	92
2.2 Morphometric characteristics for major drainage networks of the Cordillera Blanca	93
2.3 Elevation values for major drainage networks of Cordillera Blanca	94
2.4 Spacing and elongation ratios for drainages that reach the drainage divide	95
3.1 Petrographic parameters	151
3.2 Point-count raw data from Quebrada Lloclla	152
3.3 Recalculated detrital modes	153
3.4 Sedimentary facies of the Lloclla Formation	154
4.1 Summary of ages from Cordillera Blanca transects	206
4.2 Calculated average rates for Cordillera Blanca transects	207
4.3 Raw calculations of exhumation, extension, and slip rates	208

## LIST OF APPENDICES

Appendix 4.1 U-Pb zircon isotopic data	209
Appendix 4.2 $^{40}\text{Ar}/^{39}\text{Ar}$ isotopic data from muscovite and biotite step-heating analyses	214
Appendix 4.3 $^{40}\text{Ar}/^{39}\text{Ar}$ isotopic data from K-feldspar step-heating analyses	221
Appendix 4.4 (U-Th)/He apatite isotopic data	224

## Acknowledgements

The odyssey of the last five years began when my advisor, Dr. Brian Horton, offered me the opportunity to work in Peru. I wanted a field-work-intensive project and I got it: four months of field work that involved everything from learning that (a) burros can carry more rocks than I can, (b) guinea pig tastes like chicken, and (c) Cipro® can do nothing against viral gastroenteritis. I even accomplished some research along the way. I greatly appreciated Brian's advising style of letting me figure things out on my own, but always being available for discussion and guidance when I asked for it. Despite the fact that he was in Germany during my final year, he always answered questions as soon as possible. I must especially thank him for going over final revisions during his vacation in Scotland while I was here freaking out about missing the filing deadline. I look forward to our continued collaborations, especially a proposed field trip along the Calgary-Vancouver transect.

I would like to thank my committee members, Dr. An Yin, Dr. Gilles Peltzer, Dr. Antony Orme, and particularly Dr. Ray Ingersoll, for their teaching and advice. Their insistence on rigorous attention to fact has greatly improved my ability as a scientist. Even though Ray and I have differing opinions on the use of hyphens, I am indebted to him for improving my command of the English language. Dr. Marty Grove took a special interest in my project and helped me obtain my argon and zircon data. Dr. Oscar Lovera designed the thermal models of batholith intrusion.

Many people were instrumental to the success of my field work. Dr. Brendan McNulty led Brian and I through the Cordillera Blanca for the first time. His knowledge

of the local geology was invaluable. However, his transportation choice from Lima to Huaraz was the sketchiest bus ride I have ever been on in my life. I am still amazed that that bus could drive on a flat road, to say nothing of climbing 15,000 feet into the Andes. Still, Brendan introduced me to Alcides and Francisca Ames, who own the best hotel in Huaraz. Alcides provided me with a vehicle and drivers and Francisca gave me her special tea when the gastroenteritis struck. They took us in as family and made our time in Huaraz as easy as possible. My mighty field assistants, Joe Tarbill and Katy Miller, provided the moral and muscle support required for South American field work. In return, I dragged them up mountains and down ravines and yet they're still talking to me.

As I have said many times during the past five years, one must be quite insane to choose to go to grad school. Moral support from two of my undergraduate mentors, Dr. Pete DeCelles and Dr. Robert Butler, has been instrumental in helping me maintain the mental toughness required for the Ph.D. Fellow graduate students Mick McRivette, Carrie Menold, Rob Givler, and especially Bobby Gillis, have provided the commiseration necessary for soldiering on. Dr. Per Max Jögi and his Swedish perspective were always welcome during those all-nighters. Good times with Misa Cowee, Natanya Black, and Stephanie Briggs will go down in gingerbread-house-making history. Misa is the Seinfeld to my Kramer and gets special thanks for introducing me to Battlestar Galactica. Matt Bourke inspired me to explore New Zealand and still has to teach me how to telemark.

Apparently, I decided that a Ph.D was not enough work, so I designed and taught my own course during the same year that I wrote and (endlessly) revised my dissertation.



The Geology and Politics of the Grand Canyon included a field trip to the Grand Canyon for 21 students. I am very grateful to Dr. Patrick Wen and Kurt Rucker for agreeing to be drivers and act as my posse during our 4-day adventure. Sock puppets, Brokeback Canyon, and Colorado City will always generate fond memories.

Since the tenth grade, my perspective of the world has been broadened and challenged by Dean Tarbill. His passion for history and learning is contagious. I am honored to have had his friendship and support for the past twelve years. Our travels to Machu Picchu mirrored the journeys through ideas we have pursued. There will be many more.

The love and emotional support from my fiancé, Frank Miller, should earn him his own Ph.D. He has endured and survived my oral exams, mental breakdowns, and dissertation writing. He has been one of my biggest cheerleaders for which I can never thank him enough. Now that I am finally done, our biggest adventure can begin.

Most importantly, I want to thank my parents, Nick and Kathy Giovanni. Words cannot express the love and support they have given me over the past 27 years. This all started with Cosmos and a big blue canvas tent. No matter what goals I set, Mom and Dad are there to cheer me on. There is absolutely no way I could have achieved this without them. At long last, I can quote William Clark: "Ocian in view! O! the joy!"

## VITA

November 2, 1979	Born, Walnut Creek, California
2000, 2001, 2002	Dean's List with Distinction University of Arizona Tucson, Arizona
2001	Galileo Circle Dean's Scholarship College of Science University of Arizona
2001-2002	Student Researcher, 2001 Peru Earthquake University of Arizona Tucson, Arizona
2002	AGU Journal Highlight Giovanni et al. (2002)
2002	B.S. in Geology Department of Geosciences University of Arizona Tucson, Arizona
2002, 2003, 2005	Field Work, Cordillera Blanca, Peru
2002-2005	Teaching Assistant Department of Earth and Space Sciences University of California, Los Angeles
2003	Cross-Training Research Fellowship Department of Earth and Space Sciences University of California, Los Angeles
2003	Student Research Mini-Grant UC Pacific Rim Research Program
2004-2007	Graduate Research Fellowship National Science Foundation
2004	Student Research Grant Geological Society of America

2005	Outstanding Teaching Assistant Award Department of Earth and Space Sciences University of California, Los Angeles
2006	Lecturer Department of Geological Sciences California State University, Long Beach
2006-2007	Teaching Fellow Collegium of University Teaching Fellows University of California, Los Angeles

### **PUBLICATIONS AND PRESENTATIONS**

- Giovanni, M.K., Beck, S.L., Wagner, L., 2001, The June 23, 2001 Peru Earthquake and the Southern Peru Subduction Zone, AGU Fall Meeting.
- Rosenberg, E.J., Ross, G.M., Patchett, P.J., Hamilton, M., and Giovanni, M.K., 2002, Nd isotopic constraints on the provenance of synorogenic Canadian Cordilleran foreland basin sediment, Department of Geosciences Annual Symposium, University of Arizona
- Giovanni, M.K., Beck, S.L., Wagner, L., 2002, The June 23, 2001 Peru Earthquake and the Southern Peru Subduction Zone, *Geophysical Research Letters*, 30, doi: 10.1029/2002GL015774.
- Giovanni, M.K., Horton, B.K., McNulty, B., Grove, M., 2003, Evolution of the Cordillera Blanca normal fault, central Peruvian Andes: Evidence from basin analysis and  $^{40}\text{Ar}/^{39}\text{Ar}$  thermochronology, AGU Fall Meeting.
- Horton, B.K., Giovanni, M.K., McNulty, B., Grove, M., 2004, Thermochronologic and sedimentologic evidence for variations in exhumation of the Cordillera Blanca detachment fault system, Peru, AGU Fall Meeting.
- Ross G.M., Patchett, P.J., Hamilton, M., Heaman, L., DeCelles, P.G., Rosenberg, E., and Giovanni, M.K., 2005, Evolution of the Cordilleran orogen (southwestern Alberta, Canada) inferred from detrital mineral geochronology, geochemistry, and Nd isotopes in the foreland basin, *Geological Society of America Bulletin*, v. 117, no. 5-6, p. 747-763.

Giovanni, M.K., Horton, B.K., Peltzer, G., Grove, M., McNulty, B., 2005, Tectonic geomorphology,  $^{40}\text{Ar}/^{39}\text{Ar}$  thermochronology, and sedimentology of the Cordillera Blanca normal fault, central Peruvian Andes, 6<sup>th</sup> International Symposium on Andean Geodynamics, Barcelona, Spain.

Giovanni, M.K., Horton, B.K., Lovera, O.M., Grove, M., Farley, K.A., Kimbrough, D.L., McNulty, B., 2006, Emplacement and exhumation of the Cordillera Blanca batholith, Peru, Backbone of the Americas GSA Meeting, Mendoza, Argentina.

## ABSTRACT OF THE DISSERTATION

Tectonic and Thermal Evolution of the Cordillera Blanca  
Detachment System, Peruvian Andes:  
Implications for Normal Faulting in a Contractional Orogen

by

Melissa Katherine Giovanni

Doctor of Philosophy in Geology

University of California, Los Angeles, 2007

Professor Raymond V. Ingersoll, Chair

The Cordillera Blanca, Peru provides a unique opportunity to study a large active normal fault in the hinterland of a compressional orogen. Detailed geomorphology, sedimentology, and thermochronology allow comparison to large normal faults in classic extensional settings, such as the Basin and Range Province. The Cordillera Blanca normal fault measures 170 km in length and dips west-southwest at low to moderate angles (19-36°). The fault bounds the western side of the Cordillera Blanca, the highest single mountain range in the Peruvian Andes, where average elevations exceed 5000

meters. The footwall is composed of late Miocene granodiorite, which has been deeply incised by glacial activity. New U-Pb zircon crystallization ages indicate that the footwall batholith cooled ~5-8 Ma. Cooling ages from  $^{40}\text{Ar}/^{39}\text{Ar}$  studies of biotite and potassium feldspar reveal coeval exhumation ~4-6 Ma. The Cordillera Blanca lies directly above a shallowly-subducting segment of the Nazca Plate. Extension along the Cordillera Blanca normal fault may be a result of viscous coupling between the flat slab and overriding plate. Vertical exhumation rates have slowed since 3 Ma, likely caused by strengthening of the upper plate due to refrigeration.

The high relief, mappable fault trace, modern tectonic activity, and uniform footwall lithology make the Cordillera Blanca an ideal location to test models for the evolution of topography related to normal faulting. Classic normal fault models predict a tectonic and geomorphic symmetry in which maximum slip and surface uplift occur near the central fault segments and decrease toward the fault tips. Extraction of drainage network parameters from digital elevation models of the Cordillera Blanca reveal a pronounced asymmetry toward the northern fault tip. Initiation of faulting and basin subsidence is constrained at  $5.4 \pm 0.1$  Ma by  $^{40}\text{Ar}/^{39}\text{Ar}$  dating of a basal tuff. Oxygen isotopic compositions of modern waters and lacustrine carbonates are consistent with deposition at high altitude. Studies of fault propagation suggest that the geometry of sedimentary basin fill is related to fault growth. Distinct sedimentation patterns suggest that the Cordillera Blanca normal fault has behaved as a single segment and has propagated in a single, southward direction.

## **- Chapter 1 -**

### **Introduction**

## 1.1 INTRODUCTION

The Andes of northern and central South America are the product of compression and magmatism caused by subduction of the oceanic Nazca plate beneath the South American continental margin. The style of subduction is highly variable along the length of the Andes and the resulting orogenesis is not uniform along strike [*Gutscher et al.*, 2000]. It has long been recognized that two segments of the subducted plate beneath Peru and central Chile descend at very low dip [e.g., *Barazangi and Isacks*, 1976]. Early studies on the geometry of these flat slab segments reported an initial dip of  $\sim 30^\circ$  down to 100 km depth before flattening out for several hundred kilometers [*Hasegawa and Sacks*, 1981; *Isacks*, 1988]. Subsequent tomographic and earthquake hypocenter data have imaged a warped downgoing slab with significant topography [*Gutscher et al.*, 2000; *Gutscher*, 2002]. Spatial and temporal correlations have been proposed between flat slab segments and the subduction of aseismic ridges, which are areas of buoyant, thickened oceanic crust [e.g., *Pilger*, 1981; *Gutscher et al.*, 1999; *McNulty and Farber*, 2002].

The Cordillera Blanca is the highest mountain range in Peru and lies between  $8^\circ 30'S$  and  $10^\circ S$ , directly over the current Peruvian flat slab segment, which stretches from  $5$  to  $15^\circ S$  (Fig. 1.1). Despite its orientation parallel to active contractional structures that accommodate ongoing compression, the Cordillera Blanca is bounded by an active, 170 km-long normal fault. It has been suggested that this extension is a result of (1) gravitational collapse of overthickened crust [e.g., *Dalmayrac and Molnar*, 1981; *Suarez et al.*, 1983; *Deverchere et al.*, 1989]; (2) oblique slip and vertical-axis rotations in the Cordillera Blanca region [e.g., *McNulty et al.*, 1998; *Rousse et al.*, 2002, 2003]; (3)



thermally weakened crust resulting in reactivation of preexisting thrust faults [e.g., *Le Pourhiet et al.*, 2004]; or (4) the passage of the Nazca Ridge beneath the Cordillera Blanca, where the increased buoyancy of the subducted aseismic ridge caused coupling in the overriding plate, leading to extension by simple shear [e.g., *McNulty and Farber*, 2002].

This paper examines the fourth hypothesis by considering different reconstructions of the subduction of the Nazca Ridge and how the timing of ridge subduction compares to geomorphic, sedimentologic, thermochronologic, and geochronologic observations in the Cordillera Blanca. Not only does flat slab subduction play a role in the evolution of extension in the Cordillera Blanca, but the Cordillera Blanca may be considered a modern analogue to the flat slab subduction during the Laramide orogeny in North America [e.g., *Jordan et al.*, 1983; *Dickinson et al.*, 1988; *Saleeby*, 2003]. This dissertation focuses on obtaining better constraints on the relationship of flat slab subduction and extension in Peru in order to better understand the processes associated with these conditions.

## **1.2 POSSIBLE EXPLANATIONS FOR FLAT SLAB SUBDUCTION**

Several hypotheses have been proposed to explain the existence of flat subduction. A popular suggestion is the link between age and buoyancy, where very young (< 5 Ma) oceanic lithosphere is warm and buoyant [e.g., *Sacks*, 1983; *Cloos*, 1993], and thus, expected to occur at a shallow angle. However, the Peruvian and central Chilean flat slab segments are subducting oceanic lithosphere formed at 30-45 Ma

while young (5-10 Ma) lithospheric segments are observed subducting at “normal” angles in southern Chile [*Gutscher et al.*, 2000], western Mexico (3-10 Ma) [*Singh and Mortera*, 1991], and Oregon (5-8 Ma) [*Hyndman and Wang*, 1995]. Lithosphere age, therefore, does not seem to be the dominant factor for flat slab subduction [e.g., *Cruciani et al.*, 2005].

Another common model for flat slab subduction is the rapid “absolute” motion of the overriding plate. In other words, the upper plate is moving over the lower plate faster than the slab can sink [*Cross and Pilger*, 1982]. This scenario is observed in South America, which has an “absolute” velocity of 3-4 cm/yr [*Gutscher*, 2002] westward over the Nazca plate. Although this model suggests that the entire subduction zone would experience flat slab conditions, more than half of the South American margin subducts at “normal” slab dips with alternating flat slab segments.

The curvature of the subduction zone has also been suggested as a cause of flat slab subduction [*Bevis*, 1986; *Cahill and Isacks*, 1992; *Gephart*, 1994]. Numerous examples exist, however, of curved subduction zones where oceanic lithosphere similar in age to the Andean margin descends at steep angles (e.g. Sandwich arc, New Hebrides arc) [*Gutscher*, 2002]. Also contrary to this explanation is the fact that the central Chilean flat slab segment occurs along a straight section of the Andean margin.

An alternative explanation for flat slab subduction and the resulting geometry involves the subduction of buoyant aseismic ridges [*Pilger*, 1981; *Nur and Ben-Avraham*, 1981; *McGeary et al.*, 1985; *Gutscher et al.*, 1999, 2000; *Gutscher*, 2002; *Hampel*, 2002]. These aseismic ridges are relatively young (<30 Ma) and thicker (15-20 km) than average

oceanic crust, which can result in buoyant crust [Cloos, 1993]. Most of the known flat slab segments have spatial and temporal correlations to one or more of these regions of thickened crust [McGeary *et al.*, 1985; Gutscher *et al.*, 1999, 2000]. Therefore, the most likely explanation for flat slab subduction appears to be linked to buoyancy imparted by the presence of young, thick aseismic ridges.

### **1.3 MODELS OF THE PERUVIAN FLAT SLAB SEGMENT**

#### **1.3.1 Reconstructions of the timing and location of initial Nazca Ridge subduction**

The Nazca Ridge is a 1000-km-long, 200-km-wide aseismic ridge that formed at ~25-50 Ma at the Pacifica-Nazca/Farallon spreading center [Pilger, 1981; Pilger and Handschumacher, 1981; Schlanger *et al.*, 1984; von Huene *et al.*, 1996]. The crest of the ridge rises 1500 m above the sea floor, trending N42°E and has an average crustal thickness of  $18 \pm 3$  km [Woods and Okal, 1994]. Water depths in the trench are ~2500 m shallower at the intersection with the ridge, and the continental slope reveals surface erosion and faulting [Hagen and Moberly, 1994; Li and Clark, 1994]. On land, the collision zone is expressed by a narrowing of the continental shelf, a seaward shift of the coastline, and raised marine terraces [Machare and Ortlieb, 1992]. North of the ridge-trench collision zone, along the margin of north-central Peru, there is no large accretionary prism [von Huene *et al.*, 1996] because long-term tectonic erosion has occurred since the middle Miocene, leading to rapid subsidence in the forearc and an eastward shift of the trench and magmatic arc [von Huene and Lallemand, 1990].

Early models of the temporal evolution and spatial migration of the Nazca Ridge vary in predicted length of the original Nazca Ridge, lateral migration velocities, and timing of southward ridge passage [Hampel, 2002]. Pilger [1981] suggested that the Nazca Ridge first began to subduct at 5°S in the middle Miocene and passed 10°S latitude at ~9 Ma. Other studies use plate reconstructions and NUVEL-1A convergence rates to estimate that ridge subduction began at ~8 Ma at 8°S and reached 9°S at 6-7 Ma and 11.5°S at 4-5 Ma [DeMets *et al.*, 1994; Somoza, 1998]. McNulty and Farber [2002] used this reconstruction to suggest a model of detachment faulting in the Cordillera Blanca caused by lift related to passage of the buoyant Nazca Ridge.

Two recent studies attempted to refine the spatial and temporal subduction history of the Nazca Ridge, constraining the lateral migration velocity and original length of the ridge [Hampel, 2002; Rosenbaum *et al.*, 2005]. Hampel [2002] used updated South America-Nazca relative motions from the revised global geomagnetic time scale. In contrast, Rosenbaum *et al.* [2005] calculated the relative plate motions using a fixed-hotspot frame of reference, which can have maximum errors of 100-200 km between 0-15 Ma. The major difference between these two reconstructions is their assumption of the length of the original Nazca Ridge, a critical value that determines possible effects on the Cordillera Blanca.

Oceanic ridges and plateaus on the Nazca Plate have mirror images on the southeastern Pacific plate, as these features formed simultaneously at the Pacific-Nazca/Farallon spreading center, and are assumed to have similar lengths and shapes due to symmetrical spreading [Pilger, 1981; Cande and Haxby, 1991]. The Tuamotu Plateau

shares a common spreading-center origin with the Nazca Ridge and its current 4000 m contour is considered the mirror image of the consumed portion of the Nazca Ridge [Pilger, 1981; von Huene *et al.*, 1996] in both the Hampel [2002] and Rosenbaum *et al.* [2005] reconstructions. However, Hampel [2002] asserted that the northwesternmost tip of the Tuamotu Plateau does not have a corresponding mirror image on the Nazca plate because it may have formed on older crust located 600 km from the spreading center that created the Tuamotu Plateau and Nazca Ridge. Rosenbaum *et al.* [2005] cited new seismic-reflection surveys that suggest that older crust beneath the northwesternmost tip of the Tuamotu plateau formed at or near the spreading center, and thus, should be included in reconstruction of the Nazca Ridge.

Without that ~200 km long tip of the Tuamotu Plateau, Hampel [2002] calculated that the Nazca Ridge currently extends ~900 km beneath South America and entered the trench at 11°S at ~11.2 Ma. If the Tuamotu tip is considered, Hampel's [2002] reconstruction estimates ridge subduction beginning at ~12.5 Ma at 10°S. Rosenbaum *et al.* [2005] preferred to consider the Tuamotu tip and calculate that initial Nazca Ridge subduction began at ~15 Ma at 10°S (Fig. 1.2). Due to the oblique orientation of the ridge in relation to the Nazca plate convergence direction, the ridge has migrated laterally along the active margin. The Rosenbaum *et al.* [2005] model suggests that the leading tip of the subducting Nazca Ridge passed beneath the southern Cordillera Blanca region at ~10-12 Ma (Fig. 1.2). Hampel's [2002] model, without the Tuamotu tip, predicts that the Nazca Ridge was always south of the Cordillera Blanca and never passed directly beneath it.

*Hampel et al.* [2004] also pointed to variations in degree of tectonic erosion along the Peruvian margin as evidence for when and where the Nazca Ridge reached the trench. They suggested that subsidence and uplift caused by passage of the ridge are greater along the southern flat slab segment than along the north-central margin, implying that the ridge did not subduct north of 11°S. The geologic record at 9°S exhibits subsidence of >1000 m since 12-13 Ma, while the region at 11.5°S has been uplifted and eroded by ridge passage during 7-11 Ma, with subsequent subsidence (100s m) in the wake of the ridge since 6 Ma [*von Huene et al.*, 1988; *von Huene and Lallemand*, 1990; *Hampel*, 2002; *Clift et al.*, 2003].

### **1.3.2 The “Lost Inca Plateau”**

In addition to the Tuamotu Plateau being recognized as the mirror image of the Nazca Ridge, the Marquesas Plateau in the south Pacific is also assumed to have a corresponding feature on the subducted Nazca plate (“Inca Plateau”) [*Gutscher et al.*, 1999]. Common signatures of a subducted plateau are shallowly dipping downgoing slabs, volcanic gaps, and gaps in seismicity [*Dickinson and Snyder*, 1979]. The cessation of intermediate seismicity at 11-14°S delineates the subducted portion of the Nazca Ridge. The predicted location of the Inca Plateau is based on observed shallowing of the downgoing slab and reduced seismicity centered around 5°S (Fig. 1.3) [*Gutscher et al.*, 1999].

The Peru flat slab segment enters the trench at ~30°E dip and becomes subhorizontal at 100-150 km depth before steepening again several hundred kilometers

farther east [Cahill and Isacks, 1992; Norabuena *et al.*, 1994; Engdahl *et al.*, 1995].

There are several models suggesting that buoyancy of the Nazca Ridge alone is incapable of supporting a 1500-km-long flat slab segment beneath Peru [Gutscher *et al.*, 1999].

These models try to explain the large flat slab segment by proposing (1) hydrostatic suction between the South American and Nazca plates [Jischke, 1975]; (2) another subducted oceanic plateau that is a continuation of the Carnegie Ridge (0-2°S) [Pennington, 1981]; (3) a kink in the northern extent of the flat slab segment [Pilger, 1981]; (4) a delay in the basalt-to-eclogite transition due to young (<70 Ma) but cool (<600°C) oceanic lithosphere [Sacks, 1983]; and (5) curvature of the slab at a convex convergent margin [Bevis, 1986].

Detailed seismological imaging reveals that a completely horizontal, 1500-km-long segment is oversimplified [Hasegawa and Sacks, 1981; Norabuena *et al.*, 1994]. In actuality, the flat slab has a 20-40-km-long “sag” between two “highs” at 5°S and 13°S (Fig. 1.4), suggesting the existence of two buoyant plateaus, each supporting ~500 km of the slab [Gutscher *et al.*, 1999]. In this model of dual buoyant plateaus, Gutscher *et al.* [1999] asserted that, as the flattening slab shuts off volcanism in the overriding plate, volcanism in the “sag” region would persist the longest. The Cordillera Blanca extends from 8°30'S to 10°S and is centered over the proposed “sag” (5-13°S). Gutscher *et al.* [1999] cited an age of 2.7 Ma [K-Ar age from Stewart *et al.*, 1974] for the youngest volcanism over the “sag” – the Yungay ignimbrites located adjacent to the Cordillera Blanca normal fault. Gutscher *et al.* [1999] correctly pointed out that improved age data is needed on the youngest volcanic units located above the “sag” in the Nazca plate.

#### **1.4 ROLE OF FLAT SLAB SUBDUCTION IN THE EVOLUTION OF THE CORDILLERA BLANCA NORMAL FAULT**

Several hypotheses explain the relationships between flat slab subduction, southward migration of the subducted Nazca Ridge, and evolution of the Cordillera Blanca normal fault. The *McNulty and Farber* [2002] model of mechanical coupling between the Nazca slab and South American continental lithosphere is based on the NUVEL-1A plate reconstructions [*DeMets et al.*, 1994; *Somoza*, 1998] that place the Nazca Ridge directly beneath the Cordillera Blanca at ~5 Ma, thus initiating extension. Reconstructions by *Hampel* [2002] and *Rosenbaum et al.* [2005] argued that the Nazca Ridge did not enter the trench until 11.5°S and 10°S latitudes, respectively; the ridge would not have passed beneath most of the Cordillera Blanca region. *Rosenbaum et al.*'s [2005] model puts the ridge under the southern part of the Cordillera Blanca, but at 10-12 Ma, much earlier than the *McNulty and Farber* [2002] model.

The following hypotheses represent viable explanations for the link between flat-slab subduction and extension along the Cordillera Blanca normal fault. The main difference between the first two models is the role of the flattened slab as a cause for extension along the Cordillera Blanca normal fault. The first hypothesis suggests that mechanical coupling between the flat slab and overriding plate results in extension, whereas the *Gutscher et al.* [1999] model proposes that a sag (i.e., a lack of mechanical coupling between the two plates) in the subducting Nazca slab beneath the Cordillera Blanca caused the gravitational collapse of the overthickened crust. The third hypothesis



considers the possible link between migration of the Nazca Ridge and unidirectional propagation of the Cordillera Blanca normal fault. This scenario is compatible with both of the first two hypotheses. The fourth proposed hypothesis offers the idea that extension in the Cordillera Blanca may be independent of subduction of the Nazca Ridge and resulting flat-slab conditions, even though current observations from this dissertation and other studies do not support this idea.

(1) Even if the Nazca Ridge itself did not directly underlie the Cordillera Blanca, the slab would still have flattened around the ridge in all directions. Continued subduction caused the southward migration of the ridge, pulling the flattened slab behind it. Viscous interplate coupling can transmit stress from the subducting plate to the overriding plate [Spencer, 1994; Gutscher *et al.*, 2000; Gutscher, 2002]; this has been suggested as a mechanism for large-scale block uplifts in the Sierras Pampeanas [Jordan *et al.*, 1983; Smalley *et al.*, 1993] and during the Laramide orogeny [Jordan *et al.*, 1983; Bird, 1984, 1988; Dumitru *et al.*, 1991; Saleeby, 2003]. This mechanism is consistent with the sinistral-shear and vertical-axis rotations observed by Rouse *et al.* [2002, 2003], the Riedel shear model proposed by McNulty and Farber [2002], and the observed north-south asymmetry along the Cordillera Blanca normal fault [Chapters 2, 3], without requiring the Nazca Ridge to propagate directly beneath the Cordillera Blanca.

(2) In contrast, the model of Gutscher *et al.* [1999] accommodates extension by the lack of a support (i.e., the flat slab) beneath the thickened crust of the Cordillera Blanca. The “sag” between the Nazca Ridge and Inca Plateau proposed by Gutscher *et al.* [1999] lies directly beneath the Cordillera Blanca. Since flat-slab conditions result in

the cessation of volcanic activity, the youngest volcanic rocks above the Peruvian flat slab should lie above the “sag”. New  $^{40}\text{Ar}/^{39}\text{Ar}$  analyses of biotite from the basal tuff of the Lloclla Formation constrain the youngest volcanic activity at ~5.4 Ma [Chapter 3]. Crystallization ages from U-Pb analyses of zircon from the Cordillera Blanca batholith constrain emplacement at 5-8 Ma, with the majority of crystallization occurring at ~7 Ma [Chapter 4]. The lack of buoyant material beneath the Cordillera Blanca (i.e., the “sag”) may have initiated extension in the region [Gutscher *et al.*, 2000].

(3) Both the *Hampel* [2002] and *Rosenbaum et al.* [2005] reconstructions of Nazca Ridge subduction and southward propagation can be related to observed north-south along-strike variability in the Cordillera Blanca. One intriguing question is whether southward migration of the flat slab caused a southward migration in the onset of faulting along the Cordillera Blanca normal fault. Migration velocities of the Nazca Ridge parallel to the strike of the Cordillera Blanca range from 36 mm/yr [McNulty *et al.*, 1998] to 43-61 mm/yr [Hampel, 2002]. Given a fault length of 170 km, these arc-parallel migration rates would result in a 3-5 Myr difference between onset of faulting in the north and south along the Cordillera Blanca normal fault. Future  $^{40}\text{Ar}/^{39}\text{Ar}$  analyses from the entire batholith will test this model.

(4) It is possible that extension along the Cordillera Blanca normal fault is not related to the flat-slab conditions in Peru. For example, gravitational collapse of overthickened crust is one scenario that does not require the presence of a flat slab beneath the Cordillera Blanca [e.g., *Dalmayrac and Molnar*, 1981; *Suarez et al.*, 1983; *Deverchere et al.*, 1989]. Thermal weakening of the crust by the emplacement of the

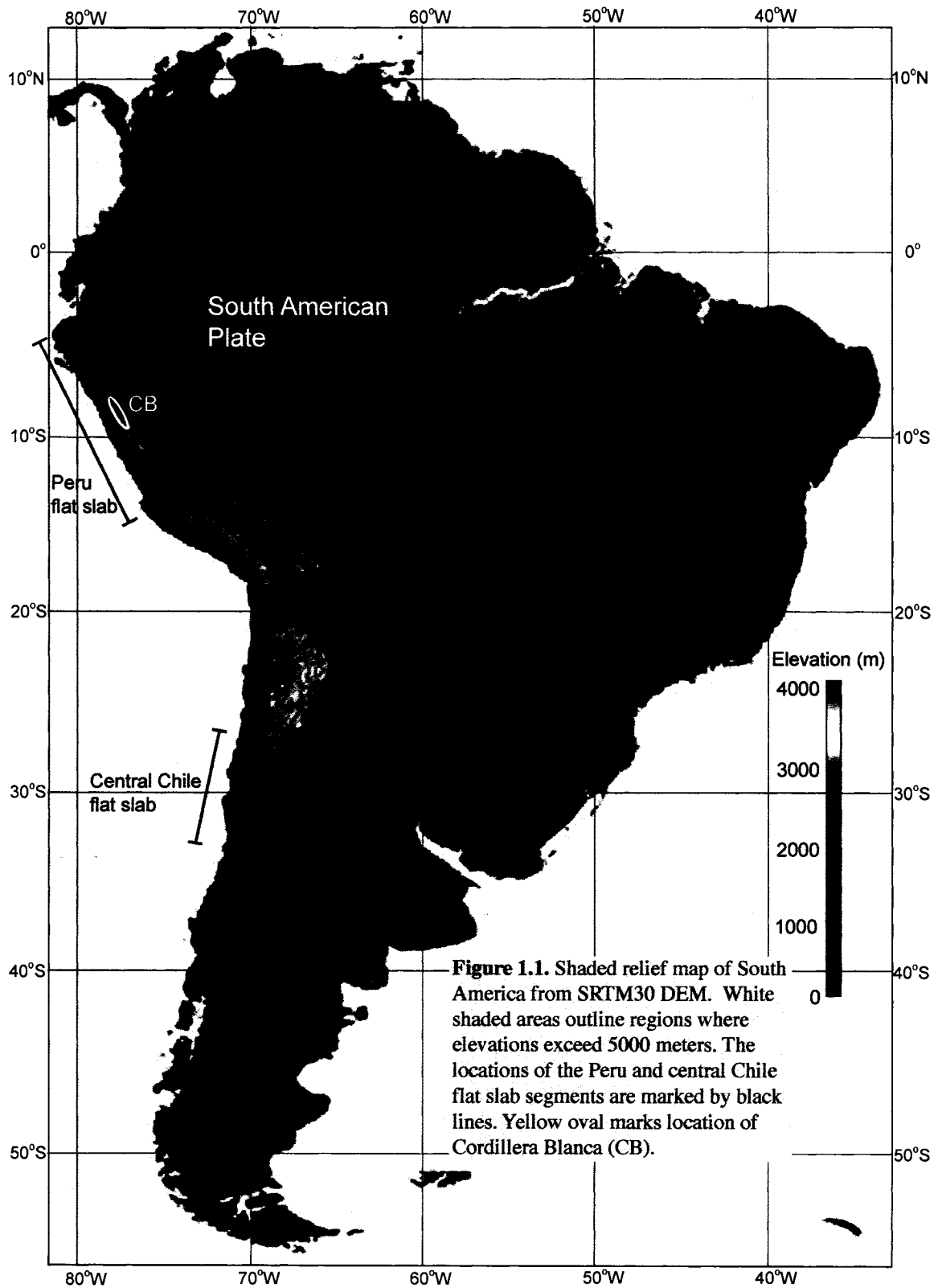
Cordillera Blanca batholith could also have triggered extension along a preexisting thrust fault [e.g., *Le Pourhiet et al.*, 2004]. On the other hand, flat slab subduction tends to refrigerate the upper plate and increase its strength [*Spencer*, 1994], which would require additional thermal effects from batholith emplacement to weaken the crust sufficiently to allow extension.

## **1.5 OBSERVATIONS FROM THE CORDILLERA BLANCA, PERU**

To test these various hypotheses, this dissertation focuses on obtaining improved isotopic age data and characterizing the evolution of the Cordillera Blanca normal fault. Studies of the geomorphology [*Chapter 2*], sedimentology [*Chapter 3*], and thermochronology and geochronology [*Chapter 4*] suggest a temporal and possibly mechanical link between flat-slab conditions and southward propagation of the subducted Nazca Ridge to the observed along-strike asymmetry of the Cordillera Blanca normal fault and the emplacement and exhumation of the Cordillera Blanca footwall batholith.

Geomorphic parameters extracted from a digital elevation model (DEM) of the Cordillera Blanca reveal a pronounced N-S asymmetry along the Cordillera Blanca normal fault in footwall topography and fault relief [*Chapter 2*]. Fault growth (by fault-tip propagation and segment linkage) is recorded by distinct sedimentation patterns in the associated basin. The Cordillera Blanca normal fault has likely evolved either as a single, long (>170 km) fault segment or as 2-3 segments that may have linked together over time. Regardless, sedimentary basin analysis suggests a southward propagation of displacement along strike [*Chapter 3*]. New  $^{40}\text{Ar}/^{39}\text{Ar}$  analyses of the Lloclla Formation

basal tuff define the youngest volcanism over the “sag” of *Gutscher et al.* [1999] at 5.4 Ma, which also constrains the onset age of faulting in the Cordillera Blanca [*Chapter 3*].  $^{40}\text{Ar}/^{39}\text{Ar}$  dating of mica and potassium feldspar from the footwall batholith constrain exhumation at 3-6 Ma [*Chapter 4*]. U-Pb analyses of zircon indicate batholith emplacement at 5-8 Ma, revealing that emplacement and exhumation clearly overlapped in time [*Chapter 4*].



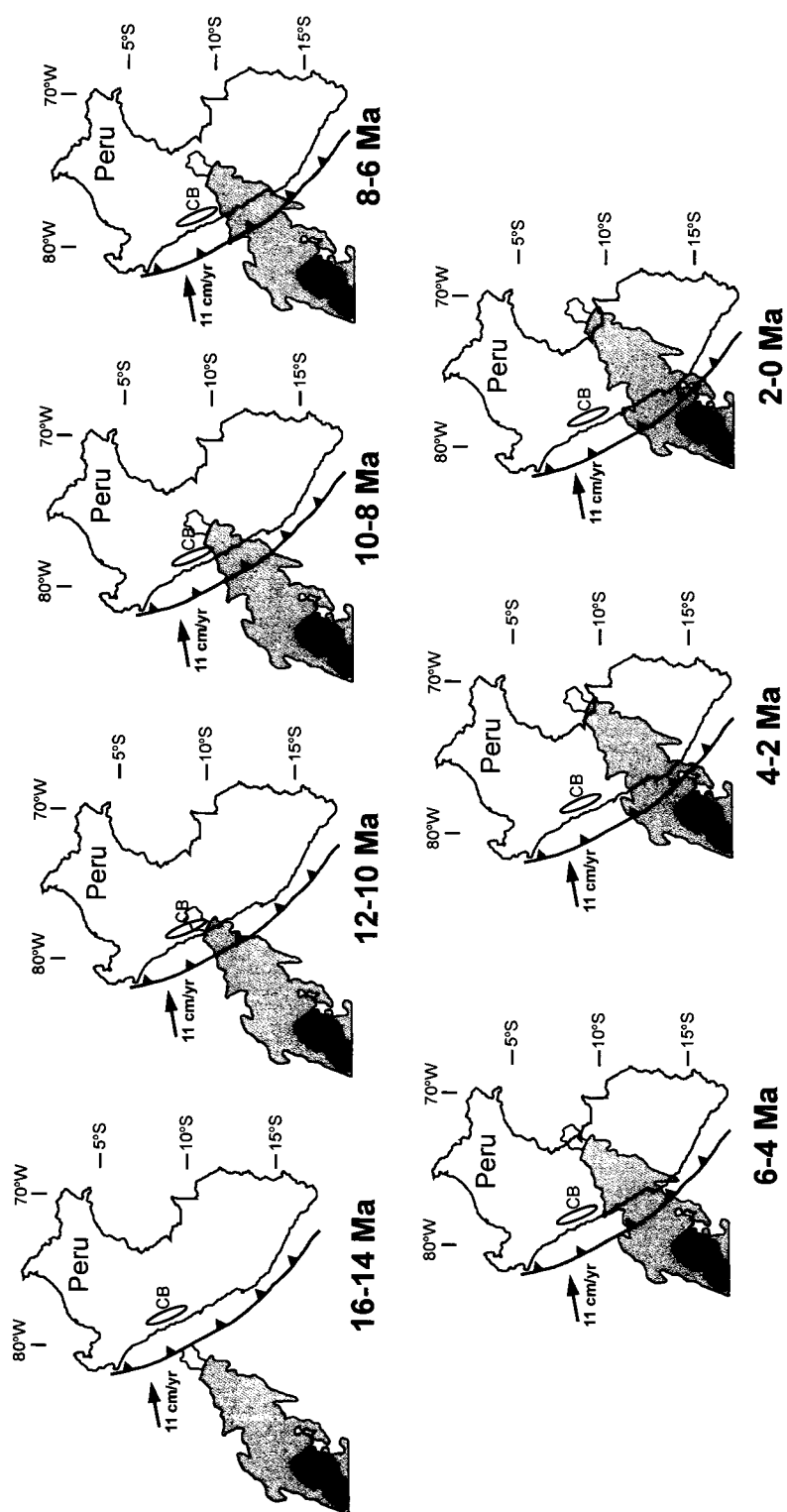


**Figure 1.2.** Reconstruction of Nazca Ridge subduction after [Rosenbaum *et al.*, 2005]. Shaded regions correspond to the Nazca Ridge (dark gray), the mirror image of the Tuamotu Plateau (medium gray), and the northwestern tip of the Tuamotu Plateau (light gray) that Hampel [2002] does not consider. CB = Cordillera Blanca.

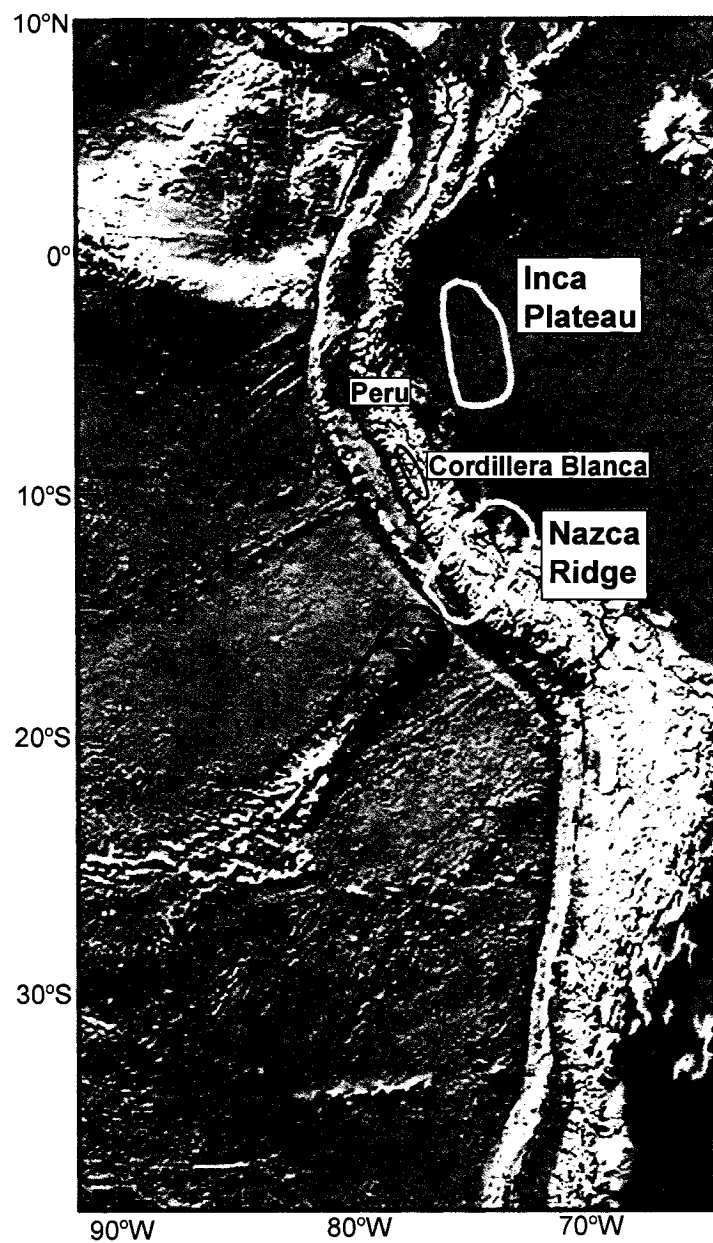


**Figure 1.3.** Topographic and bathymetric image of the Andes and eastern Pacific Ocean [after *Smith and Sandwell, 1997*]. Bold black line outlines Nazca Ridge (NR). Yellow lines outline subducted portion of the Nazca Ridge and the inferred Inca Plateau [after *Gutscher et al., 1999*]. Blue oval indicates location of Cordillera Blanca.

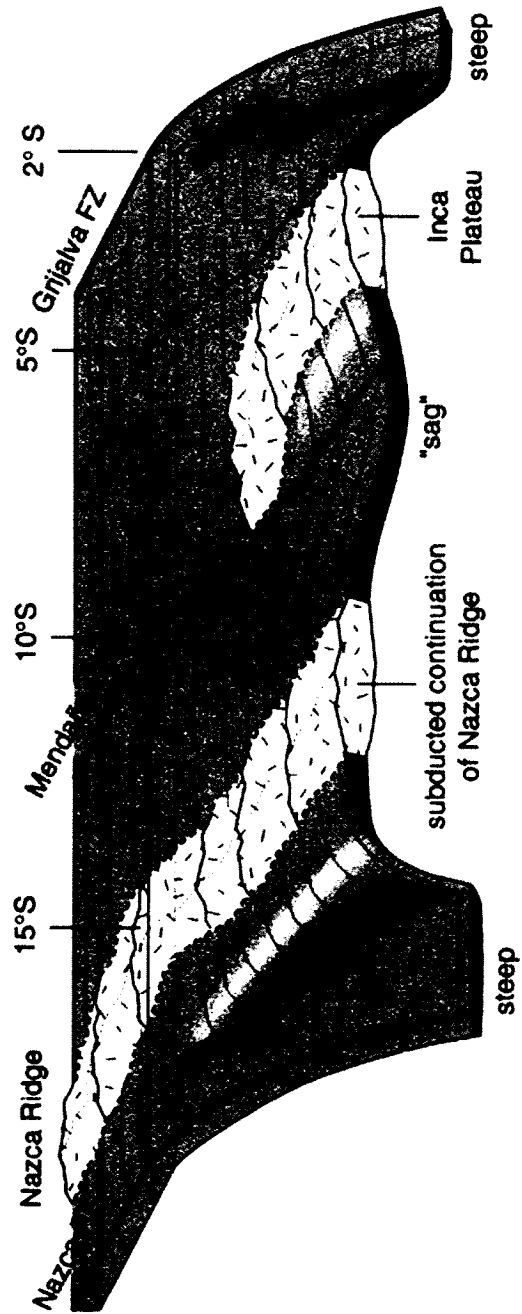


**Figure 1.4.** Reconstruction of the subducted Nazca Ridge and inferred Inca Plateau [from *Gutscher et al.*, 1999]. The two buoyant plateaus hold up the 1500 km length of the Peruvian flat slab segment. The seismically imaged "sag" lies directly beneath the Cordillera Blanca which stretches from 8°30'S to 10°S.



## 1.6 REFERENCES

- Barazangi, M., and Isacks, B.L., 1976, Spatial distribution of earthquakes and subduction of the Nazca plate beneath South America: *Geology*, v. 4, p. 686-692.
- Bevis, M., 1986, The curvature of the Wadati-Benioff zones and the torsional rigidity of subducting plates: *Nature*, v. 323, p. 52-53.
- Bird, P., 1984, Laramide crustal thickening event in the Rocky Mountain foreland and Great Plains: *Tectonics*, v. 3, p. 741-758.
- Bird, P., 1988, Formation of the Rocky Mountains, western United States: A continuum computer model: *Science*, v. 239, p. 1501-1507.
- Cahill, T., and Isacks, B.L., 1992, Seismicity and shape of the subducted Nazca plate: *Journal of Geophysical Research*, v. 97, p. 17,503-17,529.
- Cande, S. C., and Haxby, W.F., 1991, Eocene propagating rifts in the Southwest Pacific and their conjugate features on the Nazca Plate: *Journal of Geophysical Research*, v. 96, p. 19,609-19,622.
- Clift, P. D., Pecher, I., Kukowski, N., and Hampel, A., 2003, Tectonic erosion of the Peruvian forearc, Lima Basin, by subduction and Nazca Ridge collision: *Tectonics*, v. 22, doi:10.1029/2002TC001386.
- Cloos, M., 1993, Lithospheric buoyancy and collisional orogenesis: Subduction of oceanic plateaus, continental margins, island arcs, spreading ridges, and seamounts: *Geological Society of America Bulletin*, v. 105, p. 715-737.
- Cross, T. A., and Pilger, R.H., 1982, Controls of subduction geometry, location of magmatic arcs, and tectonics of arc and back-arc regions: *Geological Society of America Bulletin*, v. 93, p. 545-562.
- Cruciani, C., Carminati, E., and Doglioni, C., 2005, Slab dip vs. lithosphere age: No direct function: *Earth and Planetary Science Letters*, v. 238, p. 298-310.
- Dalmayrac, B., and Molnar, P., 1981, Parallel thrust and normal faulting in Peru and constraints on the state of stress: *Earth and Planetary Science Letters*, v. 55, p. 473-481.
- DeMets, C., Gordon, R.C., Argus, D.F., and Stein, S., 1994, Effect of recent revisions to the geomagnetic reversal time scale on estimates of current plate motions: *Geophysical Research Letters*, v. 21, p. 2191-2194.

- Deverchere, J., Dorbath, C., and Dorbath, L., 1989, Extension related to a high topography: results from a microearthquake survey in the Andes of Peru and tectonic implications: *Geophysical Journal International*, v. 98, p. 281-292.
- Dickinson, W. R., and Snyder, W.S., 1979, Geometry of subducted slabs related to San Andreas transform: *Journal of Geology*, v. 87, p. 609-627.
- Dickinson, W. R., Klute, M.A., Hayes, M.J., Janecke, S.U., Lundin, E.R., McKittrick, M.A. and Olivares, M.D., 1988, Paleogeographic and paleotectonic setting of Laramide sedimentary basins in the central Rocky Mountain region: *Geological Society of America Bulletin*, v. 100, p. 1023-1039.
- Dumitru, T. A., Gans, P.B., Foster, D.A., and Miller, E.L., 1991, Refrigeration of the western Cordilleran lithosphere during Laramide shallow-angle subduction: *Geology*, v. 19, p. 1145-1148.
- Engdahl, E. R., van der Hilst, R.D., and Berrocal, J., 1995, Imaging of subducted lithosphere beneath South America: *Geophysical Research Letters*, v. 22, p. 2317-2320.
- Gephart, J. W., 1994, Topography and subduction geometry in the central Andes: cues to the mechanics of a noncollisional orogen: *Journal of Geophysical Research*, v. 99, p. 279-288.
- Gutscher, M.-A., 2002, Andean subduction styles and their effect on thermal structure and interplate coupling: *Journal of South American Earth Sciences*, v. 15, p. 3-10.
- Gutscher, M.-A., Olivet, J.-L., Aslanian, D., Eissen, J.-P., and Maury, R., 1999, The "lost Inca Plateau": cause of flat subduction beneath Peru?: *Earth and Planetary Science Letters*, v. 171, p. 335-341.
- Gutscher, M.-A., Spakman, W., Bijwaard, H., and Engdahl, E.R., 2000, Geodynamics of flat subduction: Seismicity and tomographic constraints from the Andean margin: *Tectonics*, v. 19, p. 814-833.
- Hagen, R. A., and Moberly, R., 1994, Tectonic effects of a subducting aseismic ridge: The subduction of the Nazca Ridge at the Peru trench: *Marine Geophysical Research*, v. 16, p. 145-161.
- Hampel, A., 2002, The migration history of the Nazca Ridge along the Peruvian active margin: a re-evaluation: *Earth and Planetary Science Letters*, v. 203, p. 665-679.

- Hasegawa, A., and Sacks, I.S., 1981, Subduction of the Nazca Plate beneath Peru determined from seismic observations: *Journal of Geophysical Research*, v. 86, p. 4971-4980.
- Hyndman, R. D., and Wang, K., 1995, The rupture zone of the Cascadia great earthquakes from current deformation and the thermal regime: *Journal of Geophysical Research*, v. 100, p. 133-154.
- Isacks, B. L., 1988, Uplift of the central Andean plateau and bending of the Bolivian orocline: *Journal of Geophysical Research*, v. 93, p. 3211-3231.
- Jischke, M., 1975, On the dynamics of descending lithospheric plates and slip zones: *Journal of Geophysical Research*, v. 80, p. 4809-4813.
- Jordan, T. E., Isacks, B.L., Allmendinger, R.W., Brewer, J.A., Ramos, V.A., and Ando, C.J., 1983, Andean tectonics related to geometry of subducted Nazca plate: *Geological Society of America Bulletin*, v. 94, p. 341-361.
- Le Pourhiet, L., Burov, E., and Moretti, I., 2004, Rifting through a stack of inhomogeneous thrusts (the dipping pie concept): *Tectonics*, v. 23, TC4005, doi: 10.1029/2003TC001584.
- Li, C., and Clark, A.L., 1994, Tectonic effects of the subducting Nazca Ridge on the southern Peru continental margin: *Marine and Petroleum Geology*, v. 11, p. 575-586.
- Machare, J., and Ortlieb, L., 1992, Plio-Quaternary vertical motions and the subduction of the Nazca Ridge, central coast of Peru: *Tectonophysics*, v. 205, p. 97-108.
- McGeary, S., Nur, A., and Ben-Avraham, Z., 1985, Spatial gaps in arc volcanism: the effect of collision or subduction of oceanic plateaus: *Tectonophysics*, v. 119, p. 195-221.
- McNulty, B. A., and Farber, D.L., 2002, Active detachment faulting above the Peruvian flat slab: *Geology*, v. 30, p. 567-570.
- McNulty, B. A., Farber, D.L., Wallace, G.S., Lopez, R., and Palacios, O., 1998, Role of plate kinematics and plate-slip-vector partitioning in continental magmatic arcs: Evidence from the Cordillera Blanca, Peru: *Geology*, v. 26, p. 827-830.
- Norabuena, E. O., Snoke, J.A., and James, D.E., 1994, Structure of the subducting Nazca Plate beneath Peru: *Journal of Geophysical Research*, v. 99, p. 9215-9226.

- Nur, A., and Ben-Avraham, Z., 1981, Volcanic gaps and the consumption of aseismic ridges in South America, *in* Kulm, L., ed., *Nazca Plate: Crustal Formation and Andean Convergence: Geological Society of America Memoir 154*, Boulder, p. 729-740.
- Pennington, W. D., 1981, Subduction of the Eastern Panama Basin and seismotectonics of northwestern South America: *Journal of Geophysical Research*, v. 86, p. 10,753-10,770.
- Pilger, R. H., 1981, Plate reconstructions, aseismic ridges, and low-angle subduction beneath the Andes: *Geological Society of America Bulletin*, v. 92, p. 448-456.
- Pilger, R. H., and Handschumacher, D.W., 1981, The fixed hotspot hypothesis and origin of the Easter-Salas y Gomez-Nazca trace: *Geological Society of America Bulletin*, v. 92, p. 437-446.
- Rosenbaum, G., Giles, D., Saxon, M., Betts, P.G., Weinberg, R.F., and Duboz, C., 2005, Subduction of the Nazca Ridge and the Inca Plateau: Insights into the formation of ore deposits in Peru: *Earth and Planetary Science Letters*, v. 239, p. 18-32.
- Rousse, S., Gilder, S., Farber, D., McNulty, B., and Torres, V., 2002, Paleomagnetic evidence for rapid vertical-axis rotation in the Peruvian Cordillera ca. 8 Ma: *Geology*, v. 30, p. 75-78.
- Rousse, S., Gilder, S., Farber, D., McNulty, B., Patriat, P., Torres, V., and Sempere, T., 2003, Paleomagnetic tracking of mountain building in the Peruvian Andes since 10 Ma: *Tectonics*, v. 22, doi: 10.1029/2003TC001508.
- Sacks, I. S., 1983, The subduction of young lithosphere: *Journal of Geophysical Research*, v. 88, p. 3355-3366.
- Saleeby, J., 2003, Segmentation of the Laramide Slab - evidence from the southern Sierra Nevada region: *Geological Society of America Bulletin*, v. 115, p. 655-668.
- Schlanger, S. O., Garcia, M.O., Keating, B.H., Naughton, J.J., Sager, W.W., Hagerty, J.A., Philpotts, J.A., and Duncan, R.A., 1984, Geology and geochronology of the Line Islands: *Journal of Geophysical Research*, v. 89, p. 11,261-11,272.
- Singh, S. K., and Mortera, F., 1991, Source time functions of large Mexican subduction earthquakes, morphology of the Benioff Zone, age of the plate and their tectonic implications: *Journal of Geophysical Research*, v. 96, p. 21,487-21,502.
- Smalley, R., Pujol, J., Regnier, M., Chiu, J.-M., Chatelain, J.-L., Isacks, B.L., Araujo, M., and Puebla, N., 1993, Basement seismicity beneath the Andean Precordillera thin

- skinned thrust belt and implications for crustal and lithospheric behavior: *Tectonics*, v. 12, p. 63-76.
- Smith, W. H. F., and Sandwell, D.T., 1997, Global seafloor topography from satellite altimetry and ship depth soundings: *Science*, v. 277, p. 1957-1962.
- Somoza, R., 1998, Updated Nazca (Farallon) - South America relative motions during the last 40 My: implications for mountain building in the central Andean region: *Journal of South American Earth Sciences*, v. 11, p. 211-215.
- Spencer, J. E., 1994, A numerical assessment of slab strength during high- and low-angle subduction and implications for Laramide orogenesis: *Journal of Geophysical Research*, v. 99, p. 9227-9236.
- Stewart, J. W., Evernden, J.F., and Snelling, N.J., 1974, Age determinations from Andean Peru: a reconnaissance survey: *Geological Society of America Bulletin*, v. 85, p. 1107-1116.
- Suarez, G., Molnar, P., and Burchfiel, B.C., 1983, Seismicity, fault plane solutions, depth of faulting, and active tectonics of the Andes of Peru, Ecuador, and southern Colombia: *Journal of Geophysical Research*, v. 88, p. 10,403-10,428.
- von Huene, R., and Lallemand, S., 1990, Tectonic erosion along the Japan and Peru convergent margins: *Geological Society of America Bulletin*, v. 102, p. 704-720.
- von Huene, R., Pecher, I.A., and Gutscher, M.-A., 1996, Development of the accretionary prism along Peru and material flux after subduction of Nazca Ridge: *Tectonics*, v. 15, p. 19-33.
- von Huene, R., Suess, E., and Leg 112 Shipboard Scientific Party, 1988, Ocean Drilling Program Leg 112, Peru continental margin: Part 1: Tectonic history: *Geology*, v. 16, p. 934-938.
- Woods, T. M., and Okal, E.A., 1994, The structure of the Nazca Ridge and Sala y Gomez seamount chain from dispersion of Rayleigh waves: *Geophysical Journal International*, v. 117, p. 205-222.

**- Chapter 2 -**

**Asymmetric growth of footwall topography in the Cordillera Blanca, Peru:**

**Implications for normal fault control on landscape evolution**

## 2.1 ABSTRACT

Morphometric parameters and hypsometry of the >5-km-high Cordillera Blanca in Peru provide insights into the topographic evolution of the uplifted footwall of an active, high-magnitude-slip, low-angle normal fault within a contractional orogenic belt. The modern tectonic activity, mappable fault trace, high relief, and uniform footwall lithology make the Cordillera Blanca an ideal locality to test models for the evolution of topography related to normal faulting. Most models for normal fault growth suggest a tectonic and geomorphic symmetry in which maximum slip and maximum surface uplift occur along the central segments of the fault, with net slip, footwall uplift, and hanging-wall subsidence diminishing along strike toward the fault tips. A digital elevation model (DEM) of the Cordillera Blanca permits extraction of important geomorphic metrics for footwall transverse drainages and the hanging-wall axial river, including hypsometry, drainage area, drainage length, relief, channel gradient, surface slope, aspect ratio, and longitudinal profile. These data reveal a pronounced asymmetry in which footwall relief, exposed fault relief, channel gradient, and surface slope are greatest along the northern fault segment and become systematically lower southward along strike. In contrast to most models for normal fault growth, largely based on late Cenozoic systems in the Basin and Range province of the western United States, the Cordillera Blanca demonstrates that abrupt and significant along-strike variations in displacement and footwall uplift are possible in major normal fault systems. The causes of an asymmetric distribution of fault slip and footwall topography in the Cordillera Blanca may be related to: (a) mechanical coupling between the subducting flat Nazca slab and the overriding South American

plate; (b) gravitational collapse of overthickened crust along reactivated thrust faults; (c) climatic processes linked to the effect of glacial erosion in the footwall and/or fluvial incision in the hanging wall; or (d) a combination of rapid erosional processes and batholith intrusion that removed the strong upper crust and thermally weakened the remaining crust, allowing extension and exhumation along the Cordillera Blanca normal fault.

## 2.2 INTRODUCTION

The increasing availability of digital elevation models (DEMs) has made it easier to characterize and compare the geomorphology of mountainous regions in varied tectonic and climatic settings [e.g., *Bishop et al., 2002, 2003; Riquelme et al., 2003; Jamieson et al., 2004*]. Numerous variables pertaining to the area, slope, and relief of stream channels and drainage networks can be extracted from DEM data. Hypsometry (defined as the frequency distribution of elevation) remains a particularly useful tool in studying landscape morphology. Hypsometric curves and related parameters such as hypsometric integrals quantify the distribution of topography within a drainage area and are useful in understanding the tectonic, climatic, and lithologic influences on montane geomorphology [e.g., *Hurtrez et al., 1999; Dokka and Macaluso, 2001; Bishop et al., 2002*].

Despite these capabilities, few studies have utilized DEMs to quantitatively evaluate models of fault evolution, such as those based on studies of recently active faults in the Basin and Range province of the western United States [e.g., *Densmore et al.,*



2004, 2005 and references therein]. Investigations of normal faults have established a clear proportionality between net displacement and fault length [e.g., *Dawers et al.*, 1993], which allows consideration of the relationship between fault slip and topographic evolution [*Densmore et al.*, 2004]. Geologic studies have further led to the recognition that normal faults grow by accumulation of displacement, lateral tip propagation, and segment linkage [e.g., *Anders and Schlishe*, 1994; *Cowie et al.*, 2000; *McLeod et al.*, 2000]. Less well understood is the relationship between fault length and footwall topography. However, the models of *Densmore et al.* (2004) predict that fault growth and displacement accumulation should be accompanied by proportional variations in topographic development. The primary goal of this paper is to evaluate these predictions using DEM data from a major active normal fault in a contractional orogenic belt.

In addition to tectonics and lithologic variations, climate indicators such as glaciers may exert important control on mountain geomorphology. The long-term equilibrium line altitude or ELA (defined as the elevation where glacial ablation balances accumulation) may impose an upper limit on the development of topography, regardless of tectonic rates or processes [*Brozovic et al.*, 1997]. Therefore, the height obtained by an extensively glaciated mountain range may ultimately be a function of the ELA rather than rock uplift rates. Maximum and minimum elevations generally decrease with increasing latitude and decreasing ELA, signaling larger glacial coverage and higher rates of glacial erosion. *Brozovic et al.* [1997] asserted that in order to increase peak elevations in a tectonically active, glaciated mountain range, the long-term ELA would need to be raised, implying a shift to a warmer or drier climate. A similar idea, that

colder climatic conditions may lead to a reduction in relief in both glaciated and non-glaciated landscapes, was proposed by *Whipple et al.* [1999]. This is contrary to *Molnar and England's* [1990] hypothesis that climate cooling is required to increase peak elevations.

Hypsometry and glacial mass balance are strongly coupled. Hypsometric analyses [e.g., *Strahler*, 1952] are based on the area-altitude distribution within a drainage network. The hypsometric curve is governed by the volumetric relationship between preserved and eroded mass [*Bishop et al.*, 2002] and the shape of the curve gives a relative measure of the amount of glaciation within the drainage area (Fig. 2.1). One of the most important influences on the hypsometry of a region is the position of the ELA relative to the relief of a drainage area [*Brocklehurst and Whipple*, 2004]. When a large portion of a landscape lies near the same elevation, a small shift in the ELA due to climate change causes a significant area to be affected by glaciers. Moreover, intensified glacial erosion results in an increased proportion of the landscape at lower elevations [*Kirkbride and Matthews*, 1997]. *Brozovic et al.* [1997] studied the hypsometries of Himalayan drainage networks around Nanga Parbat and found that it is possible for glacial erosion rates to match uplift rates in actively deforming regions.

Recent hypsometric studies of mountain ranges have focused on areas with limited tectonic activity [e.g., *Brocklehurst and Whipple*, 2004; *Jamieson et al.*, 2004] or areas of strike-slip tectonics [e.g., *Dokka and Macaluso*, 2001; *Korup et al.*, 2005]. Similarly, most studies of the effect of normal faulting on topography have been conducted in the Basin and Range province [e.g., *Densmore et al.*, 2004]. The purpose of

this paper is to define morphometric parameters, including hypsometry, for the Cordillera Blanca of Peru in order to evaluate its topographic evolution in the context of current models of normal faulting, as modified by fluvial and glacial erosion. The most striking characteristic of the Cordillera Blanca normal fault is its location in the hinterland of an active fold-thrust belt and its orientation parallel to active contractional structures. Therefore, it is anticipated that significant departures from models of normal fault evolution [e.g., *Densmore et al.*, 2004] may be attributable to the distinctive position of the Cordillera Blanca extensional system within a broader zone of regional shortening rather than regional extension.

## **2.3 REGIONAL SETTING OF THE CORDILLERA BLANCA**

### **2.3.1 Tectonic setting**

The existence of extensional faulting in regionally compressional regimes has been observed in many of the world's highest mountain chains. For example, the South Tibet Detachment in the Himalayas [*Burchfiel et al.*, 1992; *Yin*, 2006] and the Brenner and Simplon extensional systems in the Alps [e.g., *Axen et al.*, 1995; *Wawrzyniec et al.*, 2001] are all low-angle detachment faults that accommodated compression-parallel extension, albeit in continental-collision settings rather than ocean-continent convergent settings. The South Tibetan Detachment has also been interpreted as a passive roof thrust fault rather than an extensional structure [e.g., *Yin and Kelty*, 1991; *Yin*, 2002]. Shortening in the Andes is linked to Cenozoic subduction of the Nazca plate beneath South America (Fig. 2.2). Along the active Andean margin, active extension is limited

and appears to be best expressed above the modern flat slab segment of the Nazca plate in the region of the Cordillera Blanca. There is clear evidence of recent normal faulting in the high Peruvian Andes along structures parallel to the strike of contractional structures farther east [*Dalmayrac and Molnar*, 1981; *Suarez et al.*, 1983]. The different stress distributions in the Cordillera Blanca have been explained by buoyancy forces arising from the gravitational body force acting on the high mountains and associated crustal root [*Dalmayrac and Molnar*, 1981; *Suarez et al.*, 1983; *Deverchere et al.*, 1989].

Alternatively, oblique slip and tectonic (vertical-axis) rotations in the Western Cordillera at the latitude of the Cordillera Blanca have been interpreted as the cause for sinistral slip and extension along the Cordillera Blanca normal fault [*McNulty et al.*, 1998; *Rousse et al.*, 2002, 2003]. A further possibility links extension in the Cordillera Blanca to subduction of the buoyant aseismic Nazca Ridge and the onset of flat-slab subduction conditions [*McNulty and Farber*, 2002; *Chapter 1*].

### **2.3.2 Geologic setting**

The 170-km-long Cordillera Blanca normal fault bounds the western side of the Cordillera Blanca, which represents the highest topography in Peru and one of the highest individual ranges in the Andean orogenic belt. The NNW-striking Cordillera Blanca normal fault is oriented parallel to the active contractional structures in the Eastern Cordillera and sub-Andean fold-thrust belt to the east (Fig. 2.3). In the footwall, the crest of the Cordillera Blanca defines the continental divide in the region, with elevations exceeding 5000 meters and more than 20 peaks above 6000 meters (Fig. 2.4). The

western boundary of the range is defined by the WSW-dipping Cordillera Blanca normal fault, with dips varying along strike from  $\sim 40^\circ$  in the north to  $\sim 19^\circ$  in the south. The fault strikes approximately N30°W and is bounded to the west by the narrow (10-15 km wide) Rio Santa valley and Callejon de Huaylas basin of the hanging wall. The Cordillera Blanca lies in the footwall and consists of a granodioritic batholith (Fig. 2.4) that intrudes the Upper Jurassic Chicama Formation. The Chicama Formation borders the eastern side of the range and makes up several high peaks in the Cordillera Blanca. The Cordillera Blanca batholith measures 200-km-long by 20-km-wide and is assumed to plunge to the south, based on the presence of smaller stocks with similar ages and mineralogy located  $\sim 50$ -75 km south [Cobbing *et al.*, 1981]. The overall shape of the batholith is a steep-sided flat-roofed body [Cobbing *et al.*, 1981] with the Jurassic Chicama Formation comprising the roof. The southward plunging orientation of the batholith is supported by the exposure of Jurassic roof rocks along the southern fault segment (Fig. 2.4). The batholith is composed of late Miocene granite that has a single reported U-Pb zircon crystallization age of  $8.2 \pm 0.2$  Ma [n=25, McNulty *et al.*, 1998]. However, new U-Pb analyses indicate crystallization ranging from  $5.3 \pm 0.3$  Ma to  $\sim 23 \pm 0.4$  Ma with a cluster of ages between 5 and 8 Ma and a peak  $\sim 7$  Ma [n=171, Chapter 4]. An  $\sim 1$ -km-thick mylonite zone extends from the fault into the footwall batholith [Petford and Atherton, 1992; McNulty and Farber, 2002].

Motion along the fault has been interpreted as extensional with a sinistral component [Bonnot *et al.*, 1988; Sebrier *et al.*, 1988; Petford and Atherton, 1992; McNulty *et al.*, 1998]. The Callejon de Huaylas basin has been interpreted both as a

supradetachment basin [McNulty and Farber, 2002] and as a “strike-slip rift basin” [Atherton and Petford, 1993]. Preserved in the southern part of the basin are upper Miocene-Pliocene sedimentary rocks that presumably record unroofing of the footwall [Bonnot, 1984]. At the southern tip of the Cordillera Blanca normal fault, south of Huaraz, the fault splays into several smaller segments that define a zone 10-15 m wide [Schwartz, 1988] (Fig. 2.4).

North of Huaraz, the Cordillera Blanca normal fault is well defined for over 100 km as a WSW-dipping fault scarp with up to 2500 m of vertical relief (Fig. 2.4). The northern fault tip is located approximately five kilometers north of the Cordillera Blanca batholith where it terminates abruptly (Fig. 2.5). East of this northern fault tip, the Cordillera Blanca is in intrusive contact with the Jurassic phyllites. There are four possibilities that explain this geometry (Fig. 2.6). The first option is that the fault tip dies out as shown and displacement goes to zero at that point (Fig. 2.6A). The second and third options are that slip has been transferred along an east-west-striking structure to other north-south-striking faults to either the east or west (Fig. 2.6B, C). The final option is that the fault disperses into a horsetail splay and slip gradually decreases north of the mapped fault tip (Fig. 2.6D).

Geologic mapping, field observations, and study of the DEM (digital elevation model) reveal no offset geologic markers or any geomorphic expression of the normal fault north of the fault tip (Fig. 2.5). To the west and north of the fault tip is a 50°-dipping, NNW-striking thrust fault placing Jurassic phyllites over Cretaceous sedimentary rocks. However, this thrust fault is of probable Eocene age, is not active

[*Cobbing et al.*, 1981], and clearly predated motion along the Cordillera Blanca normal fault. There is a linear east-west-oriented feature mapped by *Cossio and Blanco* [1964], but it does not cut or offset the Eocene thrust to the west or the Tertiary granodiorite exposed northwest of the Cordillera Blanca (Fig. 2.5). There is no evidence of any east-west-trending structures that follow the Rio Santa where the river course turns to the west. Thus, it is most reasonable to conclude the fault does indeed terminate at its northern point and displacement decays rapidly to zero (Fig 2.6A).

The only large earthquake recorded on a normal fault in the region was the 1946 Ancash earthquake ( $M_s = 7.2$ ) that occurred about 100 km east of the Cordillera Blanca [*Suarez et al.*, 1983; *Doser*, 1987]. However, in the Cordillera Blanca fault zone, the distribution of fault scarps that cut Pleistocene and Holocene glacial deposits demonstrate active faulting (Fig. 2.4). *Schwartz* [1988] conducted trenching and scarp profiling along the Cordillera Blanca normal fault and calculated Quaternary vertical exhumation rates of 0.86–1.36 mm/yr, with an average surface displacement per event of 2–3 m. Using those rates, *Schwartz* [1988] calculated rates of horizontal extension of 0.5 – 1.9 mm/yr along the Cordillera Blanca fault zone.  $^{40}\text{Ar}/^{39}\text{Ar}$  and (U-Th)/He thermochronologic analyses from the central batholith yield estimated long-term vertical exhumation rates ranging from 0.6 – 2.5 mm/yr and horizontal extension rates of 0.8 – 3.5 mm/yr [*Chapter 4*]. Further evidence for active faulting is provided by a microseismicity survey that recorded activity along the central fault segment (near Huascaran) that decayed both north and south along strike [*Deverchere et al.*, 1989].

### 2.3.3 Geomorphic setting

The Cordillera Blanca contains active glaciers above 5000 meters and is dissected by several distinct U-shaped valleys indicative of pronounced glacial erosion (Fig. 2.4). The range is dissected by numerous drainage networks of varying sizes. The western boundary of the Cordillera Blanca is defined by the NNW-striking Cordillera Blanca normal fault. In the hanging wall, the modern Rio Santa fluvial system flows from south-southeast to north-northwest, dropping ~3000 meters in elevation over a lateral distance of ~170 km (within the map area shown in Fig. 2.4). The longitudinal profile of the Rio Santa through this region (Fig. 2.7) reveals a relatively uniform gradient of 0.8°. Transverse drainages that cross the Cordillera Blanca normal fault and drain into the NNW-flowing Rio Santa (Fig. 2.8) have incised stream channels that vary between steeply-incising V-shaped valleys and broad U-shaped valleys. South of Huaraz, more braided, lower gradient streams cross the fault before joining the Rio Santa.

The modern equilibrium line altitude (ELA) for the Cordillera Blanca is 4985 meters above sea level on the western side of the divide [Rodbell, 1992]. Estimates of the ELA depression during the last glacial maximum (LGM) range from 400 to 900 meters lower than the modern ELA [Rodbell, 1991, 1992, 1993]. Rodbell [1992, 1993] and Rodbell and Seltzer [2000] estimated the minimum timing of the LGM to be ~13,200 ka by dating terminal moraines along the southern Cordillera Blanca. Farber *et al.* [2005] determined that the maximum extent of glaciation in the Cordillera Blanca during the LGM occurred between 34 – 21 ka. Current glaciation is dominated by cirque glaciers; valley glaciers last existed during the LGM.



Hypsometry is a powerful tool for determining the degree of glaciation in a drainage area, but could be misleading if used in isolation in quantifying a landscape [Brocklehurst and Whipple, 2004]. Quantifying the magnitude of glacial erosion is difficult but can be reasonably approximated if markers such as unconformities or cooling age isotherms can be located [Oskin and Burbank, 2005]. Recent landscape evolution models have demonstrated that the transition from glacial-dominated to fluvial-dominated conditions can lead to substantial changes in the landscape, underscoring the importance of understanding how climate change and tectonics interact in active mountain belts [Herman and Braun, 2006].

## 2.4 METHODS

The goal of this study is to characterize the morphology of the Cordillera Blanca normal fault in an attempt to distinguish the geomorphic expression of extensional deformation from other factors such as climate, lithology, and erosional processes. DEMs facilitate straightforward extraction of the morphology of individual drainage areas and their channel networks. Drainage area, drainage length, drainage slope and drainage relief, channel gradient, and longitudinal profiles are examples of data available from DEMs using Geographic Information Systems (GIS) and computer software programs such as River Tools [RIVIX, 2004]. In order to compare the drainage areas (Fig. 2.8), it is necessary to derive a set of morphometric parameters for each drainage. Table 2.1 defines the parameters used in this study, such as area, hypsometric integral, drainage length, drainage relief, drainage surface slope, channel gradient, and stream

profiles. The DEMs for Peru are derived from data from the Shuttle Radar Topography Mission (SRTM) of year 2000 and have a spatial resolution of 30 meters x 30 meters per pixel. Each pixel has an absolute vertical accuracy of 10 meters [Rodriguez *et al.*, 2005].

The River Tools software allows extraction of the parameters for each drainage network from corrected or “pitless” DEM data sets. Because the original DEM contains gaps or “pits” due to errors in the original data collection, those pits must be smoothed by an algorithm before data extraction. The pits are given values extrapolated from neighboring pixels that result in artificially flat areas of topography. Pit filling is necessary because River Tools requires a surface that water can flow over uninterrupted throughout the entire drainage area [Jamieson *et al.*, 2004]. In the Cordillera Blanca region, these filled pits create regions such as the artificially flat areas (dashed boxes) in the Rio Santa profile (Fig. 2.7) and three longitudinal profiles (Fig. 2.17C,D,F) which produce artificially steep gradients on their downstream margins. However, the overall extent of these problematic areas within the drainages themselves is limited and not a factor in the calculation of the morphometric parameters for each of the transverse drainage networks. The Rio Santa profile is the most affected region (Fig. 2.7).

Data from 28 transverse drainages were extracted from a DEM by defining the drainage outlets at their tributary points into the Rio Santa (Table 2.2). Hypsometric curves and integrals were calculated by River Tools algorithms similar to those described by Brocklehurst and Whipple [2004]. Topographic profiles were created from the DEM in order to define the geomorphic expression of the Cordillera Blanca normal fault.

## **2.5 ALONG-STRIKE VARIATIONS IN THE CORDILLERA BLANCA FOOTWALL DRAINAGES**

A fundamental way to measure landscape morphology is to compare the hypsometry of neighboring drainage networks. A working hypothesis for the Cordillera Blanca, based on general models of normal faults [e.g., *Elliott, 1976; Densmore et al., 2004, 2005*] is that the central fault segment will have the highest relief and largest displacement, both of which will decrease toward the fault tips (Fig. 2.9). This is based on studies of fault propagation that show that large faults grow by interaction and linkage of segments [e.g., *Cartwright et al., 1995; Dawers and Anders, 1995; Dawers and Underhill, 2000; McLeod et al., 2000*], such that fault tips experience less slip and lower slip rates than the central fault segment [e.g., *McLeod et al., 2000; Cowie and Roberts, 2001*]. Distance from the fault tip can thus be used as a proxy for increasing slip and slip rates [e.g., *McLeod et al., 2000; Densmore et al., 2004*]. A clear link has been established between fault length and displacement [e.g., *Cowie and Scholz, 1992; Dawers et al., 1993; Schlische et al., 1996*] which provides the framework to consider the relationship between topographic evolution of the footwall and fault displacement. *Densmore et al.* [2005] argue that footwall relief is simply a function of fault geometry though it may be modified by changes in base level, erosional processes, and lithology. This section presents the data for the drainage networks in the footwall of the Cordillera Blanca normal fault. Section 2.6 discusses along-strike variations in fault geometry.

### **2.5.1 Elevation and relief**

Elevations in the Cordillera Blanca range from ~1200 m to ~5500 m in the north, ~2500 m to ~6800 m in the center, and ~3750 m to 4750 m in the south. Eight across-strike topographic profiles were generated from the DEM (Fig. 2.10). These profiles were chosen to be roughly perpendicular to the Cordillera Blanca normal fault and encompass the axial Rio Santa in the WSW to the drainage divide in the ENE (Fig. 2.11). The main drainage divide is highly sinuous and its distance to the axial Rio Santa is minimal where elevations are highest (14 km and 19 km, respectively) in profiles 3 and 4 (Fig. 2.11). A topographic profile of the drainage divide shows a general southward increase in elevation along the divide (Fig. 2.12). This increase in elevation mirrors the southward-plunging orientation of the footwall batholith, marked by the position of the Jurassic roof rocks adjacent to the fault south of Huaraz (Fig. 2.4).

The fault surface is precisely defined by planar slopes expressed in the topographic profiles (dashed lines in Fig. 2.11). Previous studies have estimated the dip of the fault for the central region near Huascarán (profile 3, Fig. 2.11) only, giving values ranging from 20° to 45° [e.g. McNulty and Farber, 2002]. From the DEMs, the dips range from ~36° to ~19° and steadily decrease southward along strike. A planar fault surface is not defined for the southern region (profiles 7 and 8, Fig. 2.11). However, it is clear from the topographic profiles that the fault dip ranges from 36° to ~19°. Also visible in the northern topographic profiles (especially profiles 1 and 2, Fig. 2.11) is a decrease in dip in the up-dip direction. This warping of the fault surface into a convex-up geometry is visible in oblique 3D views of the fault northwest and southeast along strike (Fig. 2.13). Even though a rolling hinge model is interpreted for the Cordillera Blanca

footwall [*Chapter 4*], it is significant that these measured fault dips come from the steepest exposed portions of the fault and clearly delineate along-strike variations that may allow spatial differences to act as proxies for temporal evolution.

Average peak elevations cluster near 5000 m but relief varies drastically from north to south. Drainage basin relief is defined as the difference between the maximum and minimum elevations within each drainage network (Fig. 2.14). The maximum elevation is defined at the drainage divide and the minimum elevation represents the elevation of the drainage outlet. The elevation difference (i.e., relief) between the drainage divide and drainage outlets decreases from ~3000 meters in the north to <1500 meters in the south (Fig. 2.12). A plot of each drainage area versus distance from northern fault tip reveals that relief of the footwall decreases by ~3000 m from north to south along strike (Fig. 2.15A).

One of the most important influences on the formation of relief is the relative position of the equilibrium line altitude (ELA). During the last glacial maximum (~13,200 ka), the estimated ELA in the Cordillera Blanca ranged from 4085 to 4585 meters [Rodbell, 1991, 1992, 1993; Rodbell and Seltzer, 2000]. The modern ELA lies at 4985 meters above sea level on the western side of the Cordillera Blanca [Rodbell, 1992]. In order to consider the effect of the ELA on drainage relief, the relative ELA must be calculated for each drainage (Table 2.3). This is done by subtracting the minimum elevation in each drainage from the modern ELA.

The resulting relative ELA curve reveals that much of the drainage relief lies below the ELA, indicating that glaciation is dominated by cirque glaciers rather than

valley glaciers (Fig. 2.15A). The relative modern ELA shows a southward decrease analogous to that expressed in relief (Fig. 2.15A), which is to be expected in cases where the ELA determines the upper limit of topography, and hence, relief. If the relative ELA was lower in the past [e.g., *Rodbell*, 1991, 1992, 1993], then that implies a cooler climate and lower relief for the entire footwall. Estimates of paleoaltimetry from carbonate-oxygen isotopic concentrations suggest that the Cordillera Blanca region has been at the same altitude or higher since at ~5.4 Ma [*Chapter 3*]. Thus, a warming climatic trend is needed to raise the ELA and allow the evolution of higher relief along strike [e.g., *Brozovic et al.*, 1997; *Whipple et al.*, 1999].

### 2.5.2 Drainage morphometry

Measurements of the transverse drainage networks in Figure 2.8 include drainage relief, drainage area, drainage length (straight-line length from the outlet to the highest point in the drainage), surface slope (average downstream slope of all pixels within the drainage), channel gradient (average downstream slope of main trunk stream in each drainage) and hypsometric integral. The hypsometric curve and integral will be discussed in the next section. Many of these parameters exhibit sufficient scatter to complicate clear identification of along-strike trends. To minimize the effect of outliers, a running mean of three neighboring drainages was calculated. This value represents the average of a drainage and its adjacent neighbor to the north and south.

A plot of drainage area versus distance along strike shows no distinguishable pattern except that the larger drainages have a roughly 15 km spacing (Fig. 2.15B). The

running mean plot displays a general southward decrease in drainage area (Fig. 2.15B). Drainage length also shows a semi-regular 13-15 km spacing between the longer drainages while the running mean shows the same southward decrease along strike (Fig. 2.15C). The surface slope is higher in the northern drainages (30-35°) and decreases to the south where the lower slopes are ~10° (Fig. 2.15D). The steepness of the slopes in the northern drainages represents a higher degree of incision. Indeed, the northern drainages are characterized by very deep, steep-walled canyons whereas the southern drainages exhibit less topography. In general, the channel gradients of the main trunk streams within individual drainage networks average ~5° (Fig. 2.15E). However, for the drainages 60-100 kilometers south of the northern fault tip, channel gradients range from 7° to 10° (Fig. 2.15E), but are a result of steep, range-front drainages that do not reach the drainage divide to the east (Fig. 2.8).

### **2.5.3 Drainage hypsometry**

The hypsometric curve displays the frequency distribution of elevations and may indicate the relative degree of glacial modification when compared between several drainage networks [*Bishop et al.*, 2002]. Hypsometric curves of drainages can be used cautiously to assess geomorphic evolution caused by tectonic, climatic, lithologic, and/or erosional processes [*Strahler*, 1952; *Riquelme et al.*, 2003]. The hypsometric integral (the area under the hypsometric curve) is used to summarize the morphology of a drainage network as a single value [*Summerfield*, 1991]. Convex-up curves with higher integral values reflect drainage networks with a significant portion of their area at high

elevations (i.e. deeply incised drainages), while concave-up curves with lower integral values indicate drainages with most of their area at lower elevations.

For the footwall drainage networks of the Cordillera Blanca, their hypsometric curves and integrals can be divided into three groups based on the degree of convexity (Fig. 2.16A-D). Two groups easily identifiable as convex-up (black lines, Fig. 2.16B) and concave-up (light gray dotted lines, Fig. 2.16D) were separated. All other drainages were grouped as medium gray lines (Fig. 2.16C). The northern drainages (shaded black, Fig. 2.16B) have the highest integral values and the most convex curves. The central drainages (medium gray, Fig. 2.16C) are predominantly intermediate and the southern (light gray, Fig. 2.16D) drainages are the most concave. The shaded drainage map (Fig. 2.16) highlights the dominance of highly dissected drainages in the north. Five of the nine light gray drainages, which do not reach the drainage divide, correspond to the drainages with the steepest channel gradients (Fig. 2.15E). Those drainages are more affected by fluvial rather than glacial erosion. The general southward decrease along strike in hypsometric integral is similar to, but not as well as expressed as, the along-strike decrease in relief (Fig. 2.16E). Although the hypsometric integral is not strongly correlated with either drainage area or drainage relief (Fig. 2.16F-G), the lower integrals tend to occur in smaller drainages with less relief.

#### **2.5.4 Longitudinal profiles**

Geologic structures such as faults can strongly influence the longitudinal profiles of transverse drainages [Koons, 1995; Hallet and Molnar, 2001]. More generally, Bishop



*et al.* [2002] summarized four basic types of profiles that result from variations in surficial process over time: (1) a relatively smooth, concave-up profile that is considered characteristic of a stream in equilibrium with its sediment load and water discharge; (2) a linear profile, such as the Rio Santa (Fig. 2.7), where long linear gradients are the result of uniform erosion through homogeneous bedrock or sediment; (3) a convex-up profile caused by active tectonic uplift that exceeds the stream's ability to incise; (4) an irregular profile with knickpoints, characteristic of gradient disturbances caused by faults, lithologic shifts, or the upstream effects of base-level changes.

In order to investigate the effects of surface or tectonic processes on landscape evolution, I analyzed the longitudinal profiles for the trunk streams within the footwall drainage networks of the Cordillera Blanca. The longitudinal profiles of the 28 transverse drainage networks (Fig. 2.8) show a steady pattern of decreasing relief and increasing concavity from north to south along strike of the Cordillera Blanca normal fault (Fig. 2.17A-AB). The decrease in relief mirrors the aforementioned southward decrease of drainage relief. All of the streams pass through relatively homogeneous Cordillera Blanca granodiorite, while the streams south of Huaraz incise loosely-consolidated glacial sediments for much of their length (Fig. 2.4). The following descriptions proceed from the northernmost drainage (Urcon, Fig. 2.17A) to the southernmost drainage (Yana, Fig. 2.17AB).

Profile A (Fig. 2.17) has a relatively linear profile as it travels through predominately Jurassic metapelites and the Cordillera Blanca granodioritic batholith, with a small convex-up shape where it crosses the Cordillera Blanca normal fault (CBNF).

Profile B (Fig. 2.17) has a steep yet linear profile as it drops ~3000 meters in elevation over a distance of less than 20 kilometers with a small convexity at the CBNF. Profiles C-D (Fig. 2.17) reach the CBNF less than one kilometer from their junction with the Rio Santa. It is difficult to determine how much impact the fault has on the shape of these profiles, though profile D is convex-up, possibly due to thick glacial deposits in the drainage [e.g., *Bishop et al.*, 2002].

Profiles E-S (Fig. 2.17) show a clear convex-up shape where the streams cross the CBNF. Profile T (Fig. 2.17) has two convexities – one where it crosses the CBNF and one where it crosses a minor fault closer to the Rio Santa. This minor fault is mapped as inferred (Fig. 2.4) but the knickpoint occurs at the same distance along the profile as the fault. Profiles U-V (Fig. 2.17) are smooth, linear, and have very small convexities at the CBNF. Profile W does not cross the CBNF but does have a convexity as it crosses the inferred minor fault that profile T crosses. Profiles X-AA (Fig. 2.17) clearly have convexities as they cross the CBNF. Profile AB (Fig. 2.17) intersects the fault at the source of the stream; the profile itself is not affected by the CBNF.

In all of the longitudinal profiles (Fig. 2.17), the CBNF is plotted at its distance from the Rio Santa with the dip of the nearest topographic profile (Fig. 2.11). While the interpretation of longitudinal profiles can be debated, it should be noted that where each profile crosses the CBNF, there is a discernible knickpoint (except Fig. 2.17 V,W, AB). Profiles A-T (Fig. 2.17) all display knickpoints upstream of the Cordillera Blanca normal fault, which may be the result of knickpoint migration due to faulting, base level changes, lithologic differences, or a combination of these.

## **2.6 ALONG-STRIKE VARIATIONS OF THE CORDILLERA BLANCA NORMAL FAULT**

### **2.6.1 Normal fault evolution**

Many faults show predictable along-strike variations in slip and slip rate [Cowie and Scholz, 1992; Dawers *et al.*, 1993], with fault tip regions experiencing less net slip and lower slip rates than the central segments of faults [McLeod *et al.*, 2000; Cowie and Roberts, 2001]. These relationships should reveal a clear relationship between topography and fault displacement. In the Basin and Range province, Densmore *et al.* [2004] showed that several large normal faults have uniform drainage relief that decays to zero at the fault tips. Drainage relief discussed here is equivalent to the “footwall relief” of Densmore *et al.* [2004]. Evolution of the footwall can be examined by assuming that distance from the fault tip is a spatial approximation for increasing amounts of accrued slip through time [McLeod *et al.*, 2000]. Densmore *et al.* [2005] argued that drainage relief is simply a function of fault geometry and spacing, such that drainage relief will increase progressively until the range width reaches an upper limit, at which point drainage relief is no longer affected by continued fault slip.

### **2.6.2 Fault relief**

In order to characterize the drainage morphologies and fault evolution due to motion on the CBNF, the along-strike distance from the northern fault tip is taken as a proxy for the amount of cumulative fault slip [e.g., Densmore *et al.*, 2005]. Similar to drainage relief (Fig. 2.15A), the exposed relief of the Cordillera Blanca fault surface

decreases from north to south along strike (Fig. 2.18). Precise fault relief measurements from the DEM clearly show this southward decrease (Fig. 2.19). Due to a lack of offset markers, fault throw is considered to be approximated by the exposed vertical fault relief (defined in Fig. 2.11), though due to erosion, these values represent minimum estimates.

The largest amounts of fault relief (hence minimum throw) are skewed toward the northern fault tip with the highest values within 20-50 km of the tip. *Densmore et al.* [2005] noticed a similar skewed pattern in parts of the Basin and Range province and suggested this pattern may be caused by variations in crustal properties [e.g., *Burgmann et al.*, 1994], subsidence of the Snake River Plain [*McQuarrie and Rodgers*, 1998], or asymmetry in the long-term evolution of normal faults [e.g., *Manighetti et al.*, 2001].

### **2.6.3 Geomorphology as a proxy for displacement**

Drainage basin morphology can provide constraints on the rate and spatial distribution of uplift in regions of active faulting [*Talling et al.*, 1997]. Measurements of drainage network properties such as the drainage relief (measured between the fault trace and the drainage divide), the half width of the range (measured as the linear distance between the drainage outlet and the drainage divide), and drainage outlet spacing (Fig. 2.14) are useful in characterizing lateral variations in the geometry of the footwall when plotted as a function of distance along strike from the fault tip [e.g., *Densmore et al.*, 2005]. These parameters help reveal how drainage network evolution is linked to slip on a fault. In the Cordillera Blanca, all these properties were measured for each drainage between the Cordillera Blanca normal fault and the drainage divide. Only those drainages

that reach the divide are considered. In such basins, the range half-width is equal to the drainage length.

Drainage network relief decreases smoothly southward along strike (Fig. 2.20A). The range half-width matches this decrease (Fig. 2.20A) and correlates in a linear fashion (Fig. 2.20B). For normal fault systems in the Basin and Range province, the range half-width has a similar strong correlation with relief along strike [Densmore *et al.*, 2005] but, in contrast with the Cordillera Blanca, relief *increases* away from the fault tip, reaching a maximum relief near the central segment of the fault. The Cordillera Blanca fault has its highest relief and greatest range half-width near the northern fault tip with both parameters decreasing steadily southward along strike.

The spacing of drainage basin outlets has long been observed to be consistent along mountain fronts [e.g., Wallace, 1978; Mayer, 1986]. The spacing ratio (range half-width divided by outlet spacing) has been found to be quite uniform for linear mountain ranges [Hovius, 1996], varying between 1.91 and 2.23. The elongation ratio (drainage width divided by drainage length) is a measure of the drainage shape. When the elongation ratio approaches zero, it represents a very long and narrow drainage [Jamieson *et al.*, 2004]. Spacing ratios of the Cordillera Blanca drainages vary dramatically between 1.18 and 4.73, with a mean spacing ratio of 2.63 for the mountain range. This range falls outside of the spacing ratios measured by Hovius [1996], though the standard deviation is large due to three basins with exceptionally high spacing ratios (Table 2.4). Elongation ratios range from 0.13 to 0.95 with a mean of 0.44 (Table 2.4). The spatial distribution of elongation ratios along strike reflect the sinuosity of the drainage divide,

with the shortest drainages expressed along the central fault segment. The widest drainages occur along the northern segment (Fig. 2.21) and become longer and narrower southward along strike.

Drainage network outlet spacing is reduced where relief is low and increases as relief increases (Fig. 2.20C). However, in contrast to the Basin and Range faults studied by *Densmore et al.* [2005], the outlet spacing in the Cordillera Blanca is generally larger near the northern fault tip rather than near the fault center (Fig. 2.20C). One exception is the data point ~110 km from the northern tip. Outlet spacing is lowest (i.e. outlets are closer together) where relief is lowest, which corresponds to the southern end of the fault zone. *Densmore et al.* [2005] identified a relatively linear relationship between outlet spacing and relief in the Basin and Range. The Cordillera Blanca data is scattered but roughly linear (Fig. 2.20D).

## **2.7 DISCUSSION**

### **2.7.1 Morphometry of the Cordillera Blanca**

Drainage relief, drainage area, drainage length, surface slope, and hypsometric integrals all systematically decrease southward along strike with distance from the northern tip of the Cordillera Blanca normal fault. In the Basin and Range, *Densmore et al.* [2004] noted that for 50-100 km-long faults, the greatest amount of drainage relief, the largest drainage areas, and highest slopes occurred near the central segments of late Cenozoic normal faults. However, the most significant pattern observed in the drainage networks of the Cordillera Blanca is the southward decrease along strike of these same

parameters. The Cordillera Blanca normal fault, therefore, has a very asymmetrical profile compared to the Basin and Range normal faults.

In the western Himalayas, reduced relief and smaller values of hypsometric integrals are observed where extensive accumulations of alluvial sediments are found around the lower reaches of transverse drainages [*Jamieson et al.*, 2004]. In the Cordillera Blanca, these parameters yield lower values near the mapped extent of Quaternary sediments of principally glacial origin in the region south of Huaraz (Fig. 2.4). Similar to the western Himalayas, one possible explanation for the lower relief and hypsometric integrals in the southern part of the Cordillera Blanca might be that Quaternary sediment accumulation minimizes the relief produced by incision and/or subsidence. The much steeper longitudinal profiles for the northern drainages (Fig. 2.17) imply higher stream power and greater erosional capacity [*Korup et al.*, 2005], which has prevented significant sediment accumulation in the north. Instead, sediments in the north were transported into the Rio Santa axial fluvial system and rapidly evacuated to the north and west. This issue will be addressed in more detail in Chapter 3.

High values of the hypsometric integral imply deeply incised landscapes and a greater degree of glaciation, which *Brocklehurst and Whipple* [2004] considered to be controlled by the location of the ELA within the drainage network. A higher-elevation ELA (relative to the average drainage elevation) implies predominantly cirque glaciers whereas a lower-elevation ELA suggests the presence of valley glaciers. In the Cordillera Blanca, the northern drainages have the greatest amount of incision according to the hypsometric integral and the ELA is high relative to the drainage positions (Fig.

2.15A). Most of the modern (cirque) glaciers are situated to the south of these northern drainages. Furthermore, in cross section, many of the northern drainages are V-shaped rather than U-shaped, implying more fluvial dissection and diminished glacial influence.

If glaciers were not the cause of the higher degree of dissection in the north, then how did those drainage networks attain such a large area at high elevation? One possibility is that more pronounced slip along the northern segment of the Cordillera Blanca normal fault has raised the northern drainages to their current elevations. As a result of this footwall uplift, rivers have been forced to downcut rapidly, resulting in steeper longitudinal profiles (Fig. 2.17A-E). Experiments in alluvial drainage basin evolution suggest that the distribution of relief (i.e., the hypsometry) within a drainage influences denudation rates [Pelletier, 2003]. In particular, drainage systems with higher hypsometric integrals (i.e., most of their area is at high elevation) are most likely to have higher denudation rates leading to more rapid downcutting [Pelletier, 2003]. A combination of greater slip on the northern segment of the Cordillera Blanca normal fault and rapid incision in the uplifted footwall are likely the cause of the heavily dissected morphology of the northern drainages. Diminished slip on the southern reaches of the fault would explain the reduced relief, lower hypsometric integrals, and shallower longitudinal profiles observed in the south. These characteristics are in agreement with Pelletier's [2003] suggestion that drainages with less relief experience lower denudation rates. A possible way to test this hypothesis would involve thermochronologic ( $^{40}\text{Ar}/^{39}\text{Ar}$  and low-temperature (U-Th)/He) analyses of the cooling histories of footwall samples collected along strike [see Chapter 4].



Another explanation comes from the Nanga Parbat massif in the Himalaya where erosion rates and processes are the cause of rapid exhumation in the absence of extensional exhumation [Burbank *et al.*, 1996; Shroder *et al.*, 1999; Shroder and Bishop, 2000]. Zeitler *et al.* [2001] propose that feedback between erosional and tectonic processes can lead to deep and rapid river incision that removes the strong upper crust, exposing weaker, warmer crust that is already near mechanical failure. As a result, high elevations are gained and continued river incision creates high relief, leading to very rapid erosion rates. In the “tectonic aneurysm” model of Zeitler *et al.* [2001], mid- and deep-crustal material is exhumed rapidly and may experience decompression melting.

In the Cordillera Blanca, erosion along the axial Rio Santa river system is variable along strike. The river cuts through relatively soft sedimentary deposits for much of its course along the Cordillera Blanca normal fault until it is ~50 km from the northern fault tip. At that point, it begins to incise through Jurassic and Cretaceous metasedimentary and sedimentary rocks, as well as the Cordillera Blanca granodiorite (for only ~5-10 km) (Fig. 2.4). The increased erosional ability (higher stream power and larger sediment load) of the Rio Santa in the north may be the result of a significantly larger upstream drainage area for the northern segment of the river relative to the southern headwaters (Fig. 2.12). A combination of the increased erosional power of the Rio Santa in the north and the removal of footwall material by glacial erosion may have resulted in the denudation of the strong upper crust as described above by Zeitler *et al.* [2002]. One major difference between the Cordillera Blanca and Nanga Parbat is the intrusion of the Cordillera Blanca batholith, which is most likely the source of thermally-weakened crust

in the region that accommodated extension. However, that does not rule out the possibility that the crust was also weakened by high erosion rates that allowed warmer, weaker crust to rise to high elevations, accentuating the exhumation of the Cordillera Blanca batholith in the footwall of the Cordillera Blanca normal fault.

### **2.7.2 Drainage network evolution in the Cordillera Blanca**

Range half-width and outlet spacing are measures of across-strike and along-strike variability in drainage networks; their relationships can explain how drainage development is related to fault slip [Densmore *et al.*, 2005]. The strong correlations found in the Basin and Range province among drainage relief, range half-width, and outlet spacing led to the “two-stage model” of footwall topographic development of Densmore *et al.* [2005]. The drainage network begins to grow with an increase in across-strike direction (i.e., “elongation” in which the network lengthens by headward erosion and the distance increases between outlet and divide) followed by widening (i.e., “elaboration” in which the network expands laterally) in the along-strike direction [Hovius, 1996; Talling *et al.*, 1997; Densmore *et al.*, 2005; Frankel and Pazzaglia, 2005]. As a result, the range is widest and has the highest relief along the central fault segment. Range width and relief decrease along strike toward both fault tips.

The Cordillera Blanca exhibits a strong asymmetry along-strike in the relationship between drainage relief, range half-width, and outlet spacing. The range is widest and has the greatest relief near the northern tip of the Cordillera Blanca normal fault. The drainage divide is highly sinuous and the range is actually at its narrowest near the central

segment of the fault, ~80-100 km south of the northern fault tip. Overall, it appears that the range reached its maximum width in the north and elaboration has migrated to more southern drainage networks along strike.

The major difference between the Basin and Range faults studied by *Densmore et al.* [2005] and the Cordillera Blanca normal fault may be one of scale. They limited their study to 15 km-long segments of large normal faults, due to along-strike variability in pre-existing topography and lithologic contrasts in the footwalls. In contrast, this study considers the footwall of the Cordillera Blanca normal fault which has uniform lithology for almost its entire 170 km length (Fig. 2.4). Therefore, *Densmore et al.*'s [2005] observation of strong correlations among drainage relief, range half width, and outlet spacing may be scale dependent. However, the same correlations are indeed observed in the Cordillera Blanca (Fig. 2.20), suggesting that the two-stage model of footwall topographic development proposed by *Densmore et al.* [2005] is valid for long normal faults such as the Cordillera Blanca normal fault. Nevertheless, this two-stage model does not explain the pronounced asymmetry of the Cordillera Blanca expressed in footwall topography, drainage relief, hypsometry, and other morphometrics.

### **2.7.3 Evolution of the Cordillera Blanca normal fault**

This geomorphic analysis of the footwall drainage networks of the Cordillera Blanca provides a test of the prediction that the central fault segment will display morphometrics compatible with high relief and rapid surface uplift, whereas the fault tip regions will display lower relief and reduced uplift. The strong asymmetry of the

geomorphic indices suggests that the greatest rock uplift has occurred in the north, with reduced uplift southward along the fault. Fault scarps cutting Quaternary glacial deposits attest to the ongoing deformation in the southern region (Fig. 2.4) [Schwartz, 1988; McNulty and Farber, 2002]. The direct evidence for ongoing slip in the south suggest that footwall uplift along the Cordillera Blanca normal fault began in the north and has propagated southward.

The emplacement depth of the Cordillera Blanca is estimated to be >5 km and is likely 10-12 km, based on metamorphic mineral assemblages in the Chicama host rocks [Petford and Atherton, 1992; McNulty and Farber, 2002]. This pressure estimate comes from a single sample near Huascarán, along the central fault segment. Utilizing this depth constraint, and assuming a fault dip of  $27^\circ$  (from the nearest topographic profile, Fig. 2.11, profile 3), the magnitude of slip along the northern segment of the Cordillera Blanca normal fault is calculated to be 22-26 km. New U-Pb zircon crystallization ages from the central batholith range from 5 to 8 Ma, with an average  $\sim 7$  Ma [Chapter 4]. It is possible that the northern and southern batholith intruded and crystallized at different depths, and hence times, than the central part. The south-plunging orientation of the batholith, supported by the existence of the Jurassic roof rocks along the southernmost fault segment, suggest that differential intrusion is a likely possibility. This could explain the observed asymmetry of relief, displacement, and footwall morphometry.

However, such unidirectional propagation of one fault tip, but not the other, is at odds with most models of fault growth and displacement where lithology is uniform [e.g., Cowie and Scholz, 1992; Dawers et al., 1993; McLeod et al., 2000; Cowie and Roberts,

2001]. Unidirectional fault propagation has been proposed for the 1983 Borah Peak, Idaho earthquake [e.g., *Bruhn et al.*, 1991; *Janecke*, 1993] and the great Sumatra-Andaman earthquake of 2004 [e.g., *Piatanesi and Lorito*, 2007]. One possibility is that intensified erosion has led to a concentration of displacement along the northern part of the fault [e.g., *Zeitler et al.*, 2001]. Another explanation involves thermal weakening related to late Miocene intrusion of the Cordillera Blanca granite that was confined to the host rocks in close proximity to the batholith. In this case, normal faulting in weakened middle- to upper-crustal rocks may have been triggered earlier and accumulated greater displacement, if the northern end of the batholith was at shallower crustal levels in an original south-plunging configuration. A further possibility is the gravitational collapse of overthickened crust by the reactivation of a pre-existing compressional structure. A stronger alternative explanation may involve mechanical coupling between the flat subducting Nazca slab and the overriding South American plate. Sinistral shear transmitted to the Cordillera Blanca region by the southward-migrating slab may have caused southward-propagating extension. See *Chapter 1* for further discussion.

## 2.8 CONCLUSIONS

Morphometric parameters and hypsometry are useful tools in characterizing along- and across-strike variations of large faults. The fault activity, well exposed fault surface, high relief, and uniform footwall lithology make the Cordillera Blanca an excellent laboratory for testing models of normal fault control on landscape evolution. Most models of normal fault growth suggest a geomorphic and tectonic symmetry, where

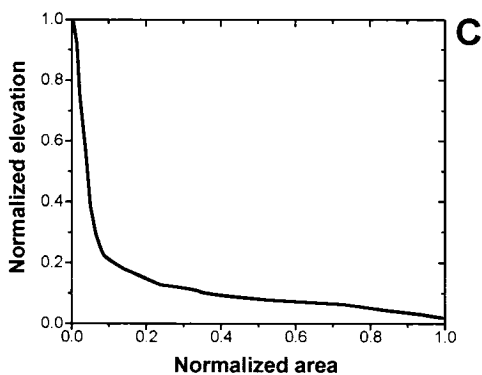
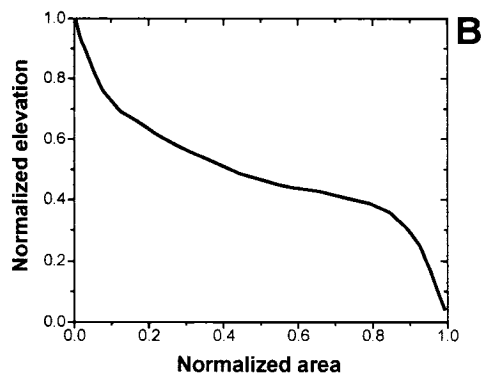
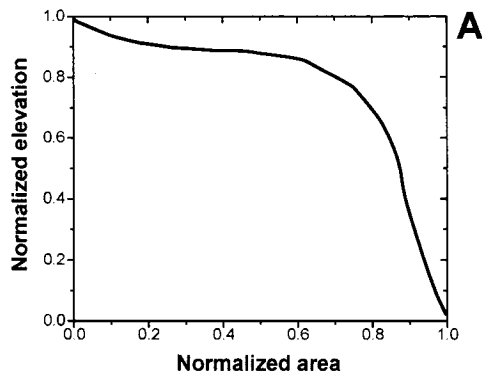
maximum slip and surface uplift occur along the central fault segments, with net slip and footwall uplift decreasing along strike toward the fault tips.

The transverse drainages in the footwall of the Cordillera Blanca normal fault have developed by a two-stage process of elongation (lengthening via headward erosion) followed by lateral elaboration (widening). Drainage network relief, drainage area, surface slope, range half-width, outlet spacing, and fault relief all exhibit well-defined reductions in magnitude from north to south along strike. This along-strike profile is highly asymmetric compared to otherwise similar normal faults in the Basin and Range. The geomorphic evidence presented here suggests that the Cordillera Blanca normal fault exhibits greatest displacement in the north and has undergone southward propagation of slip during its late Cenozoic history.

The reduced relief and hypsometric integrals in the south may be explained by Quaternary sediment accumulation that minimized the relief produced by incision and/or sedimentation. Pronounced slip along the northern segment of the Cordillera Blanca normal fault has uplifted the northern drainages to their current elevations. The resulting longitudinal profiles from the northern drainages are much steeper than those to the south. Furthermore, the higher stream power and greater erosional capacity of the northern streams prevented significant sediment accumulation. Instead, the sediments in the north were efficiently transported into the Rio Santa axial fluvial system and rapidly evacuated to the north and west.

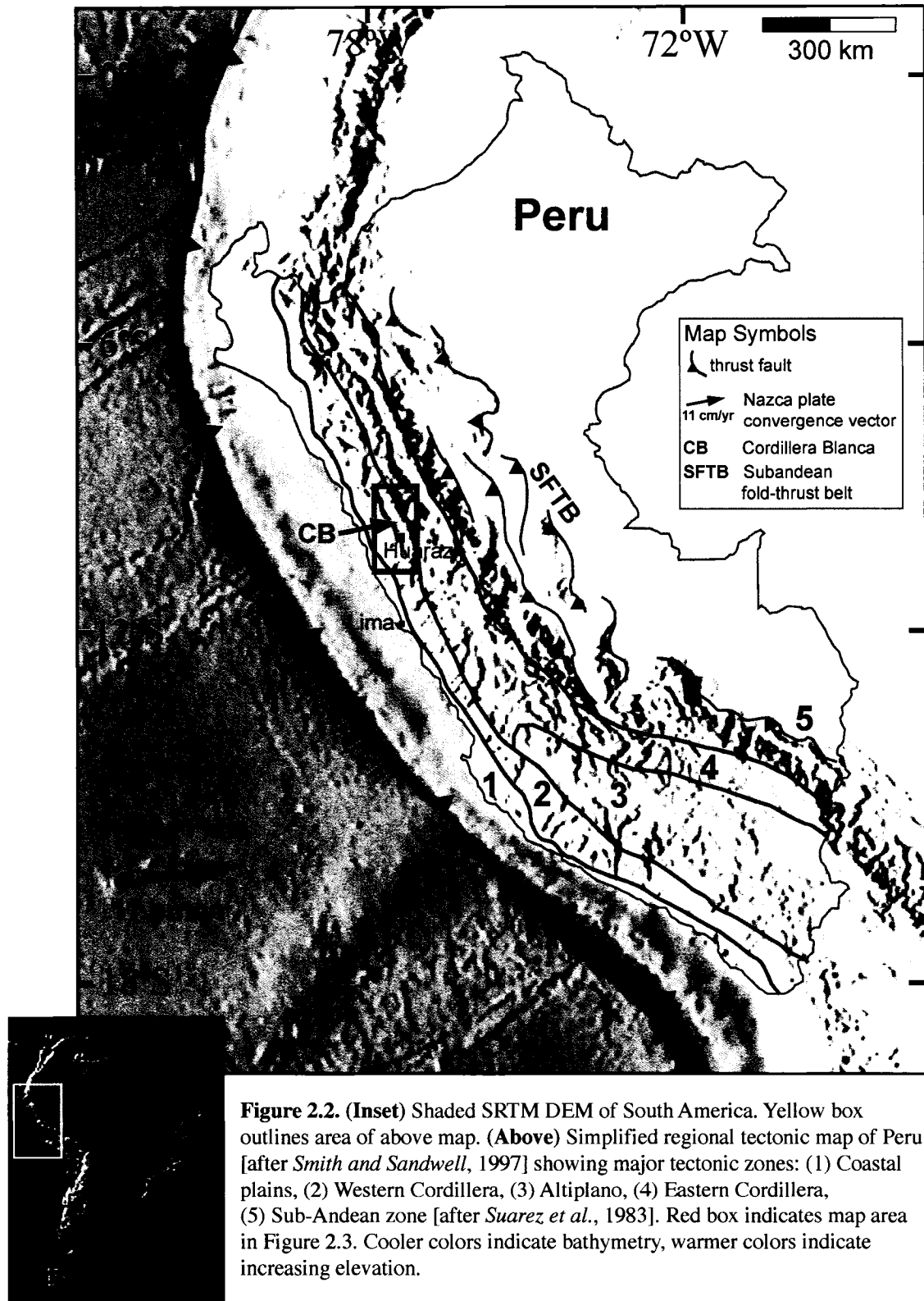
The 170-km-long Cordillera Blanca normal fault does not follow the classic normal fault model of greatest relief, displacement, and range width along the central

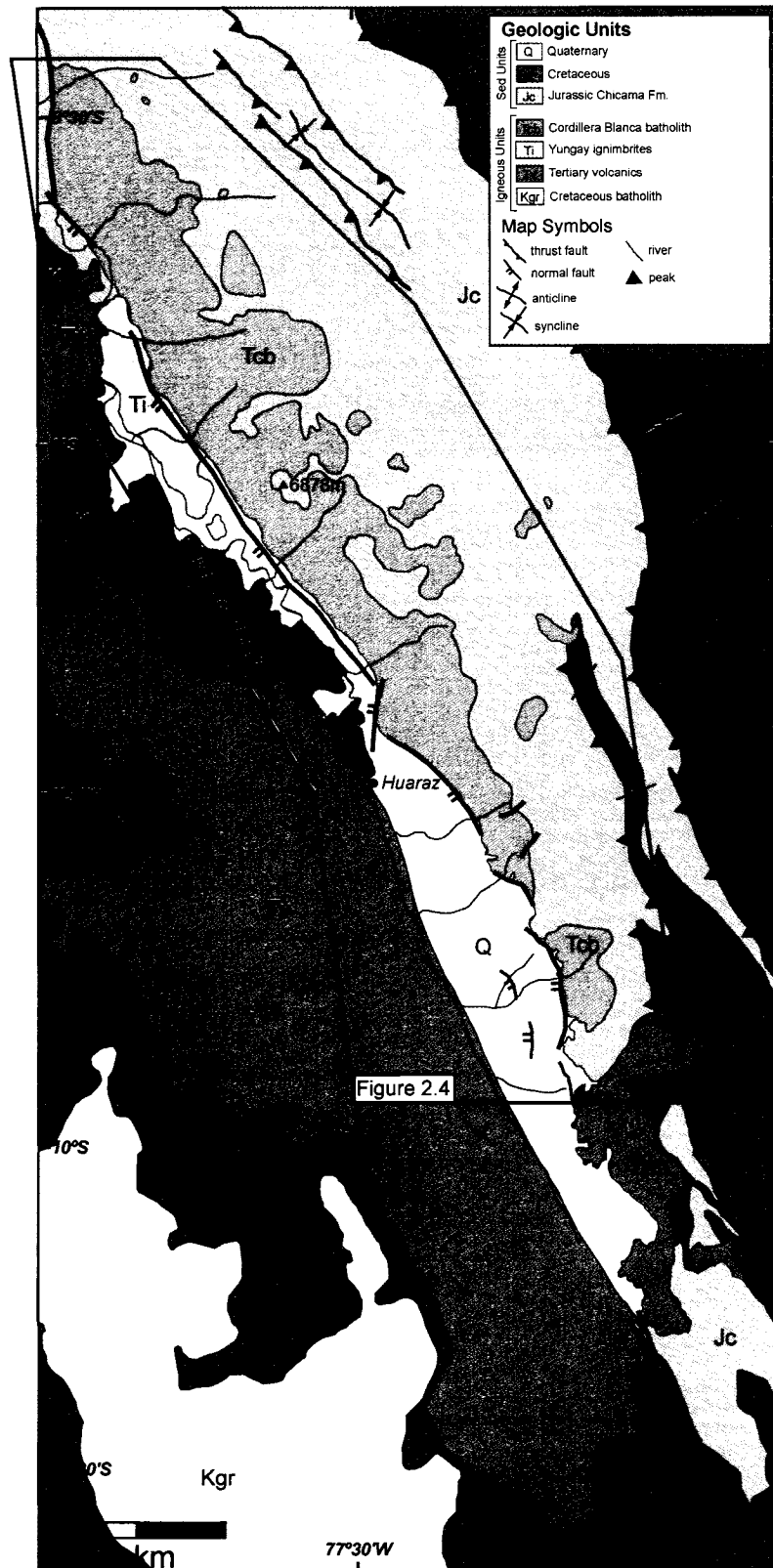
fault segment. The range is widest, relief of the drainages is highest, and fault relief is greatest within 20 km of the northern fault tip, where displacement decays to zero. This may be explained by (a) the south-plunging orientation of the batholith, resulting in the exposure of deeper structural levels of the Cordillera Blanca normal fault to the north; (b) southward propagation of the subducting flat-slab segment of the Nazca Plate beneath the Cordillera Blanca; (c) more intense erosion along the northern fault segment, resulting in preferential uplift caused by the removal of strong upper crust, which caused thermally weakened crust to be rapidly exhumed; or (d) reactivation of a pre-existing compressional structure that was weakened by overthickened crust and gravitationally collapsed.



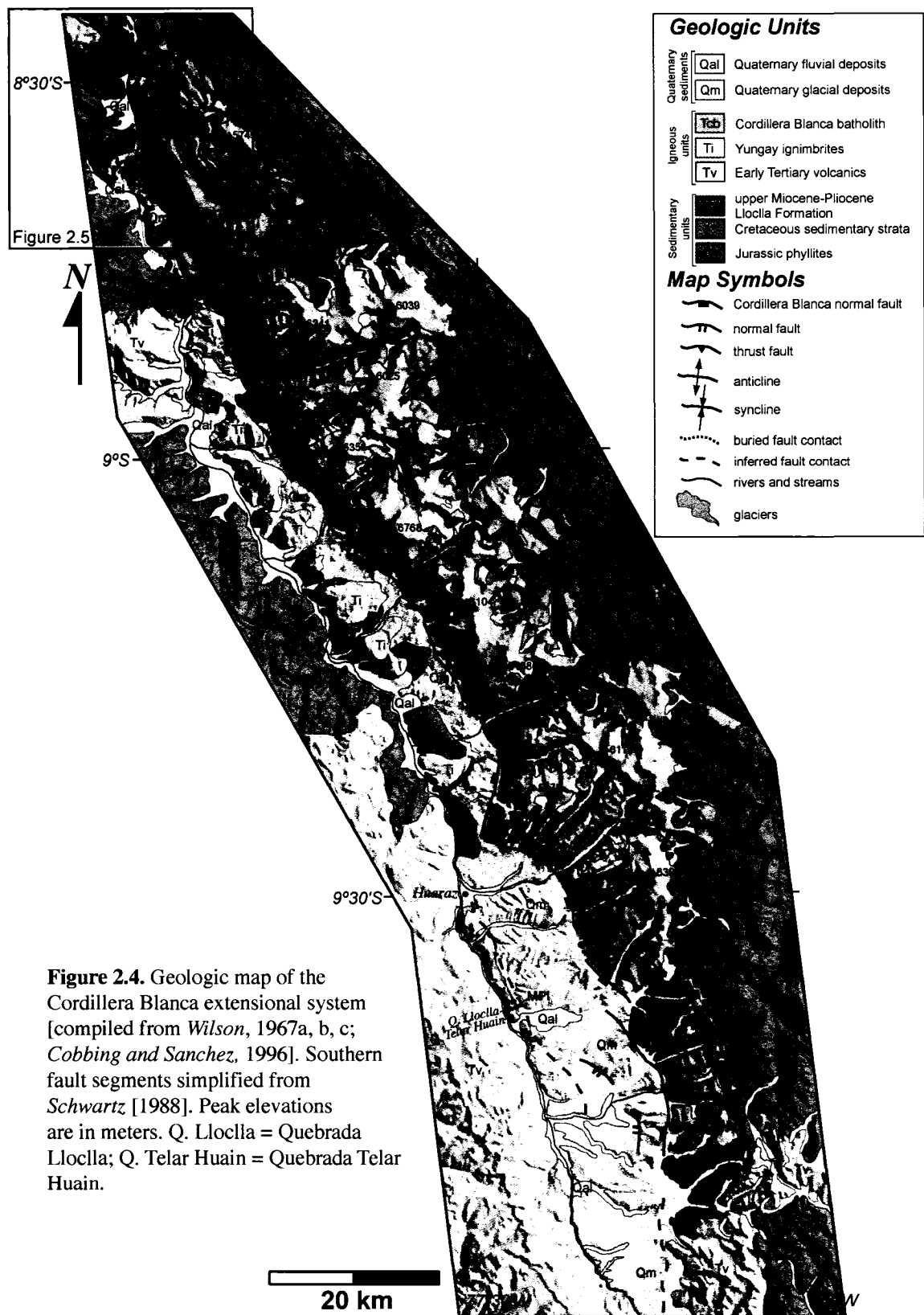
**Figure 2.1.** Hypsometric curves allow comparison of drainage basins of different size because area and elevation are normalized. Hypsometric curves are thus independent of drainage basin size and relief. High values of the hypsometric integral (area beneath the hypsometric curve) indicate that most of the topography in a drainage basin is high relative to the mean. Intermediate to low values of the hypsometric integral indicate more evenly distributed topography. **(A)** A convex-up curve with a high hypsometric integral is indicative of a highly-dissected drainage basin, commonly of fluvial origin. **(B)** An intermediate hypsometric integral is typical of a moderately-dissected drainage basin, often carved by glacial erosion. **(C)** A concave-up curve with a low hypsometric integral is associated with a small degree of dissection by either fluvial or glacial processes. The topography in such a drainage basin is subdued.

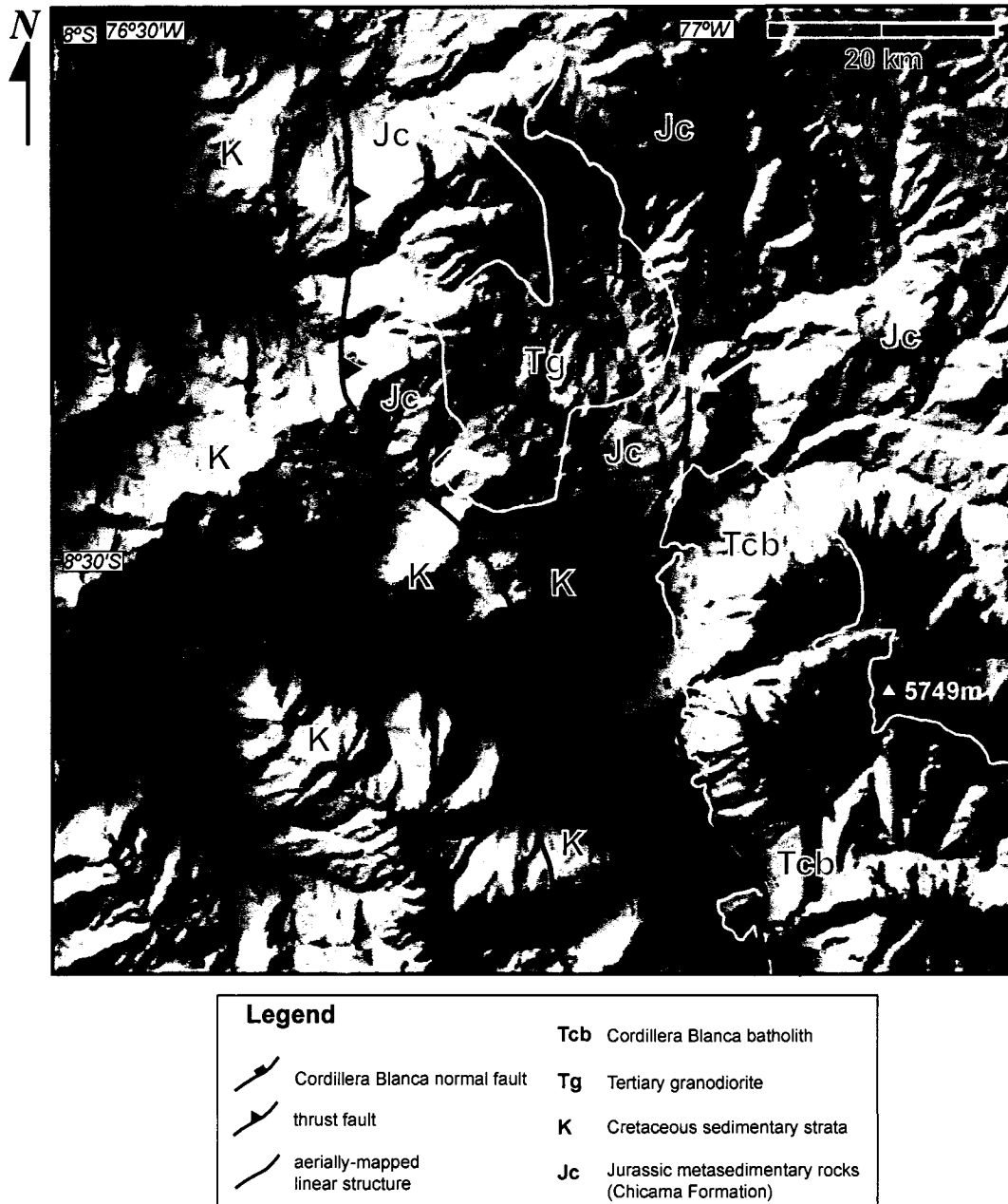




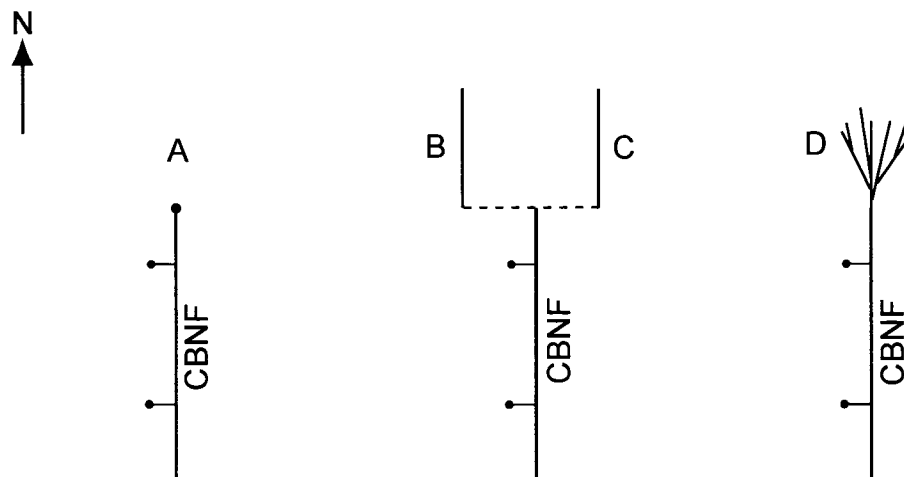


**Figure 2.3.** Simplified geologic map of the Cordillera Blanca region [after Cobbing *et al.*, 1981] showing major lithologic units and structures.

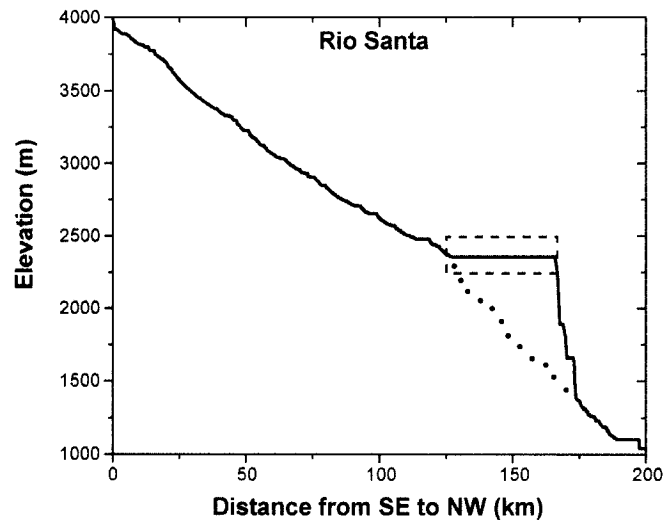




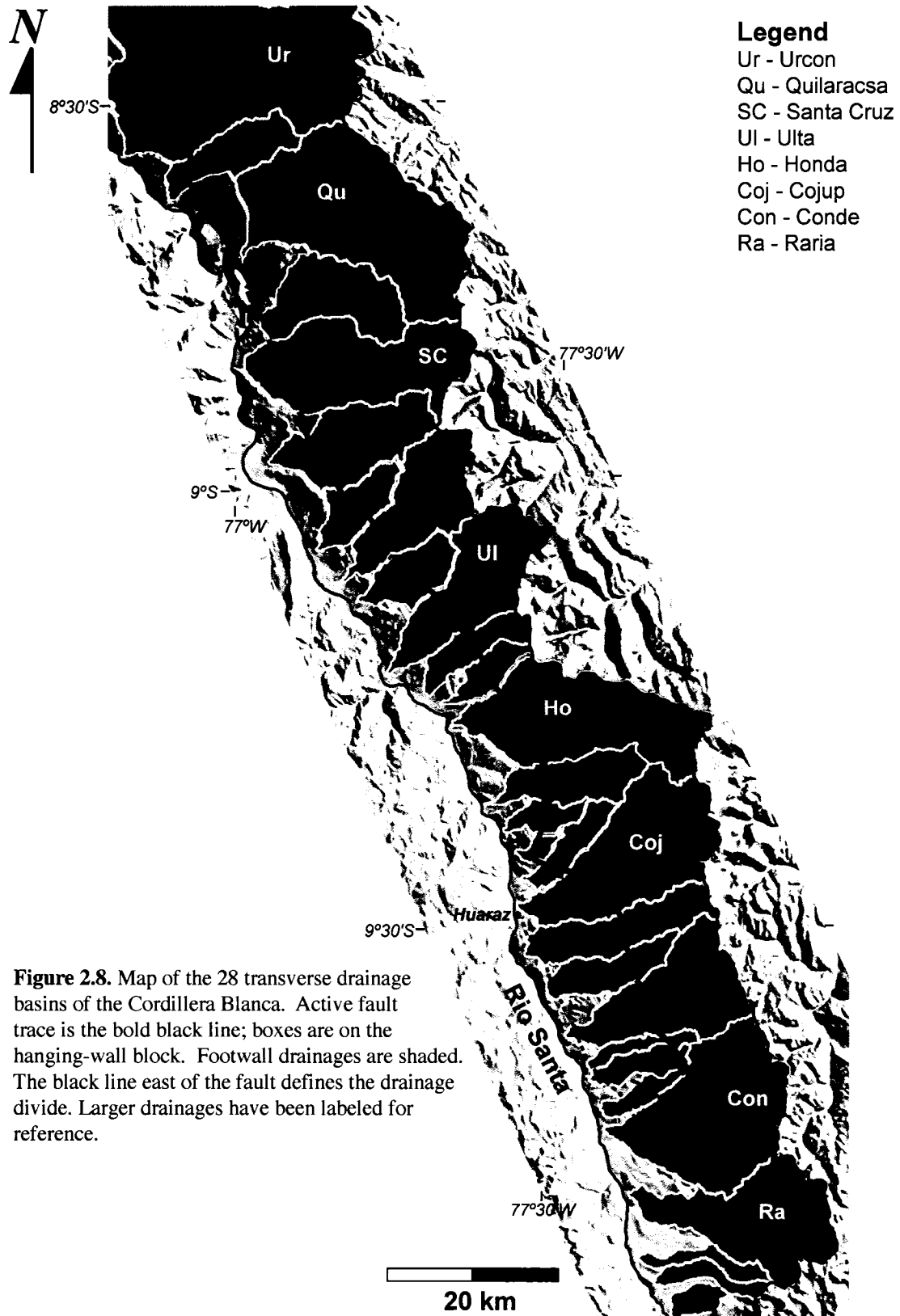
**Figure 2.5** Shaded DEM image of the northwestern corner of the Cordillera Blanca (see location in Fig. 2.4). Mapping modified from *Cossio and Blanco (1964)*, *Wilson (1967c)* and *Cobbing et al. (1981)*. Both the Cordillera Blanca batholith and Tertiary granodiorite (white lines) intrude the surrounding Jurassic Chicama Formation. Geologic mapping, field studies, and study of this DEM do not support continuation of the Cordillera Blanca normal fault past the northern tip marked by the white arrow.



**Figure 2.6.** Possible terminations for the northern fault tip of the Cordillera Blanca normal fault (CBNF). **A.** Fault tip dies out and displacement diminishes to zero. **B.** Slip is transferred to another fault to the west. **C.** Slip is transferred to another fault to the east. **D.** Slip is dispersed into a horsetail splay.



**Figure 2.7.** Longitudinal profile of Rio Santa for its length through Figure 2.4. Dashed black box outlines an area of filled "pits" in the DEM. This creates artificially steep gradients downstream. The black dotted line approximates the corrected profile.



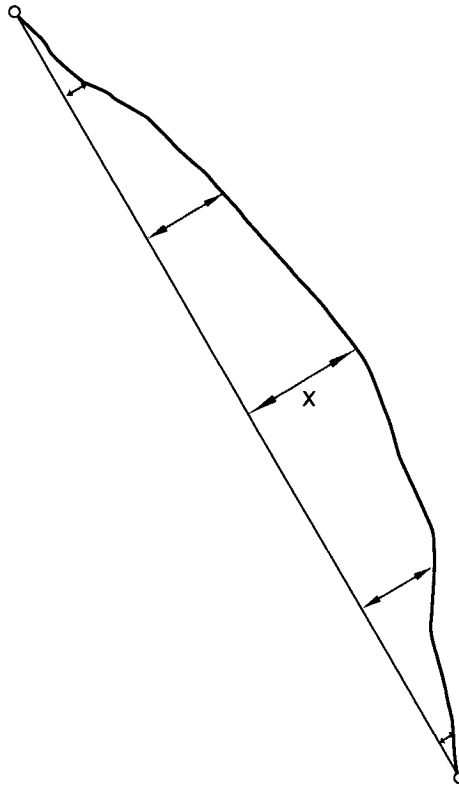


**Figure 2.9.** Schematic diagram of the "bow-and-arrow" rule [Elliott, 1976] which describes the distribution of displacement along a fault. Maximum displacement occurs where the fault trace is furthest from the straight line connecting the fault tips (x). Displacement goes to zero at the fault tips. This model is applicable to both normal and thrust faults [e.g., Elliott, 1976; Densmore *et al.* 2004; 2005].



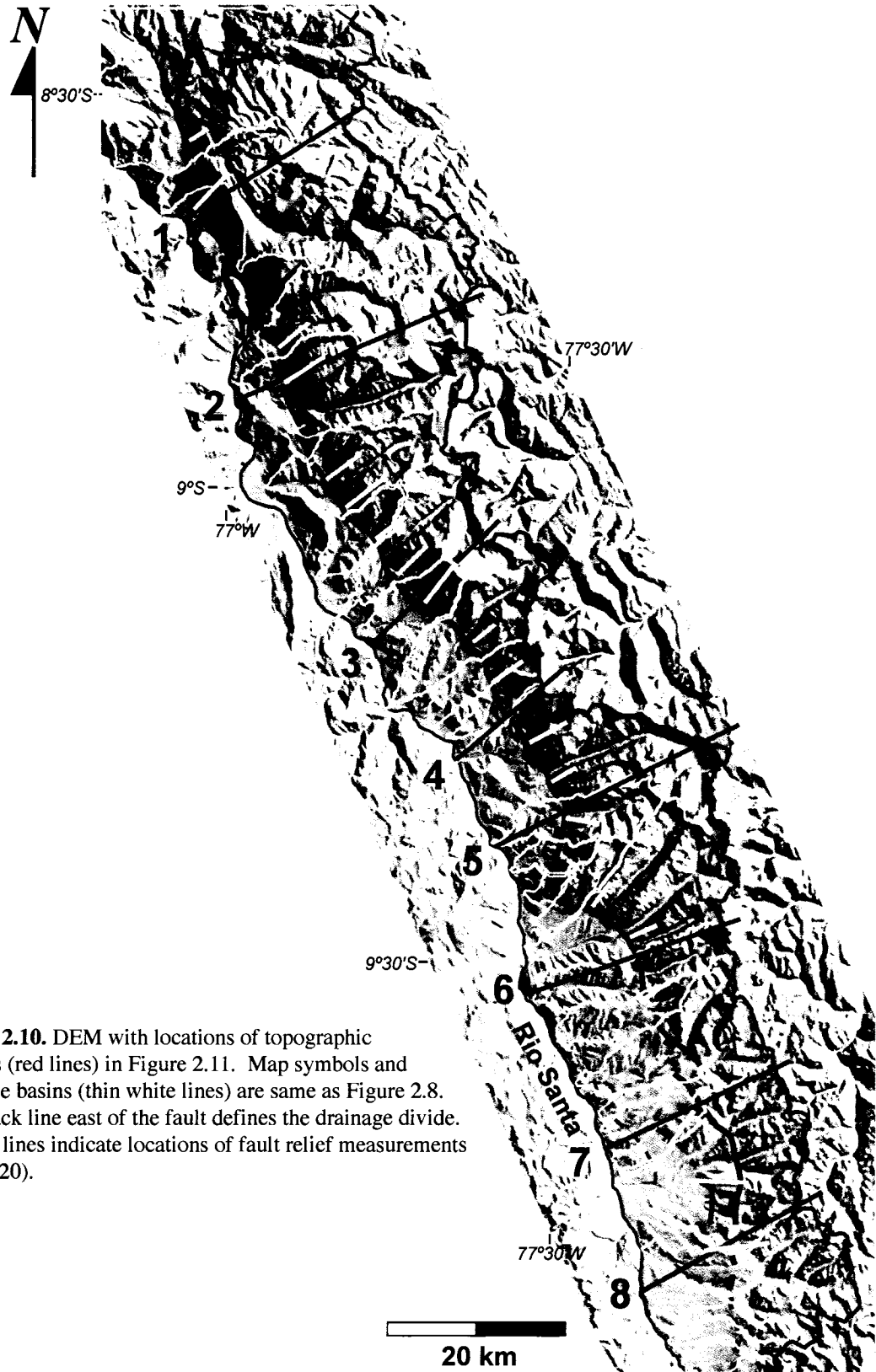


**Figure 2.10.** DEM with locations of topographic profiles (red lines) in Figure 2.11. Map symbols and drainage basins (thin white lines) are same as Figure 2.8. The black line east of the fault defines the drainage divide. Yellow lines indicate locations of fault relief measurements (Fig. 2.20).

**Figure 2.11.** Topographic profiles perpendicular to the Cordillera Blanca normal fault and generally trending E-W or WSW-ENE (see Fig. 2.10 for locations). Note that the range is narrowest in the central region (profiles 3 and 4). The vertical fault exposure is marked by arrows and CBNF (Cordillera Blanca normal fault). Black dashed lines approximate the fault surface, projected above and below the profile. Precise dip measurements were obtained from the DEM by calculating the slope of that line. Fault dips clearly decrease southward along strike, as does vertical fault exposure.

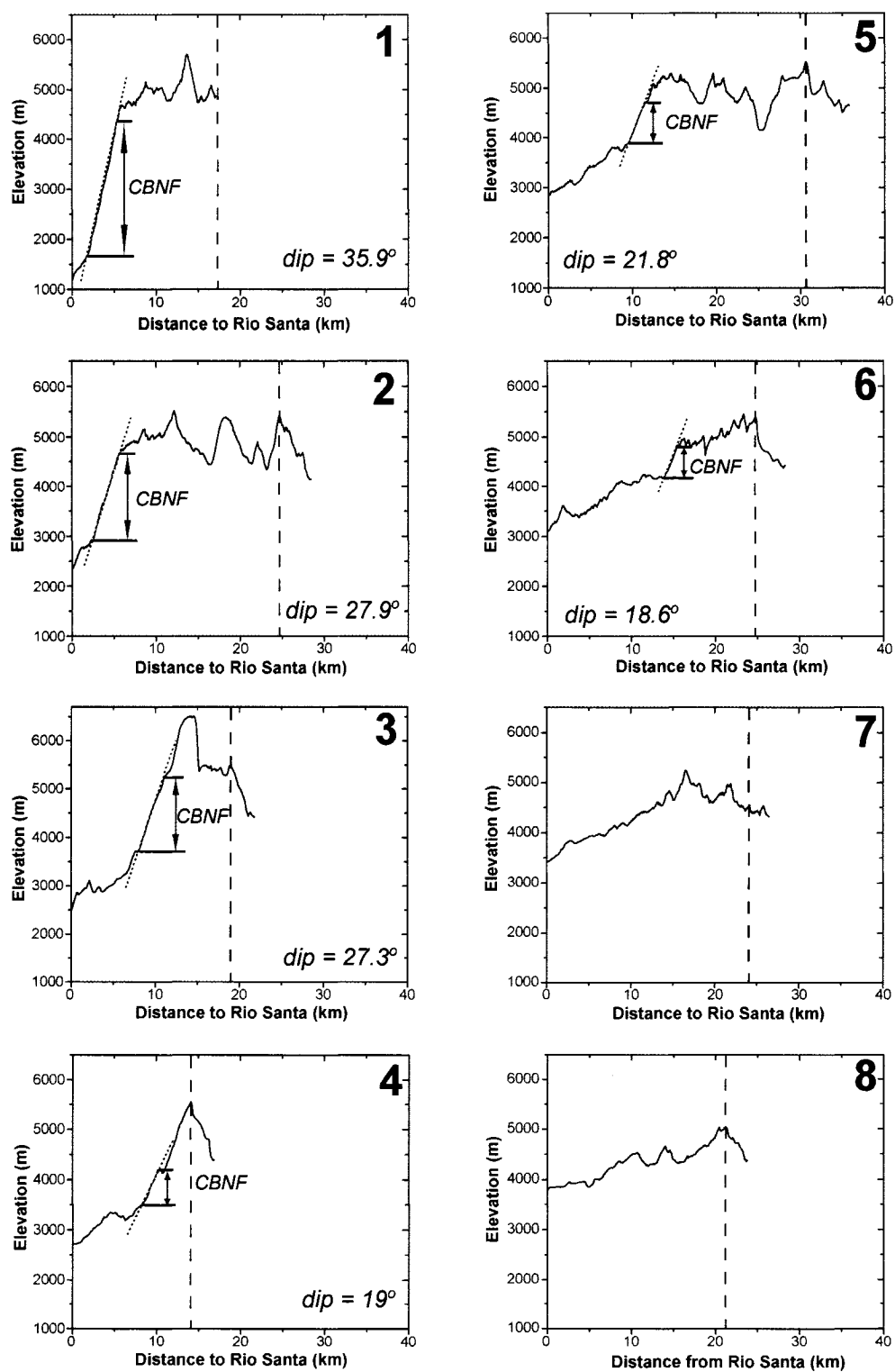
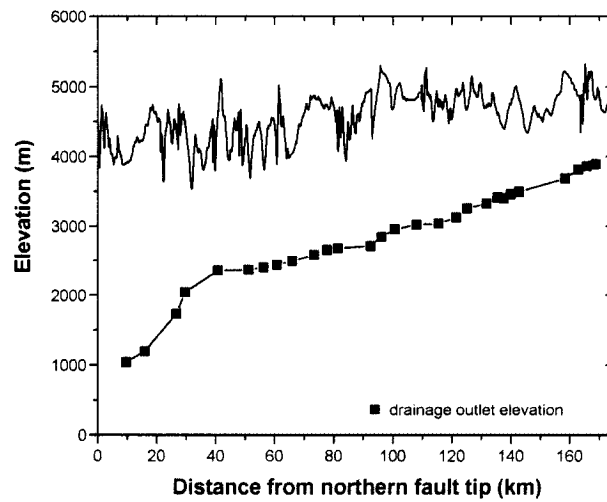


Figure 2.11



**Figure 2.12.** Topographic profile along drainage divide. Squares plot elevation of each drainage outlet. The elevation difference between the drainage divide and drainage outlets decreases from ~3000 meters in the north to <1500 meters in the south.

**Figure 2.13. (A)** 3D image from DEM of Cordillera Blanca looking northwest along strike. **(B)** 3D image from DEM looking southeast along strike. Cordillera Blanca normal fault (bold white line). Thin dashed white lines delineate exposed fault surface. Thin dotted white lines mark shallowing of dips in the updip direction. Greatest amount of fault surface exposure occurs along northern fault segment. Fault surface exposure and fault dips decrease drastically southward along strike, revealing the warped nature of the fault surface. Vertical exaggeration = 5x.

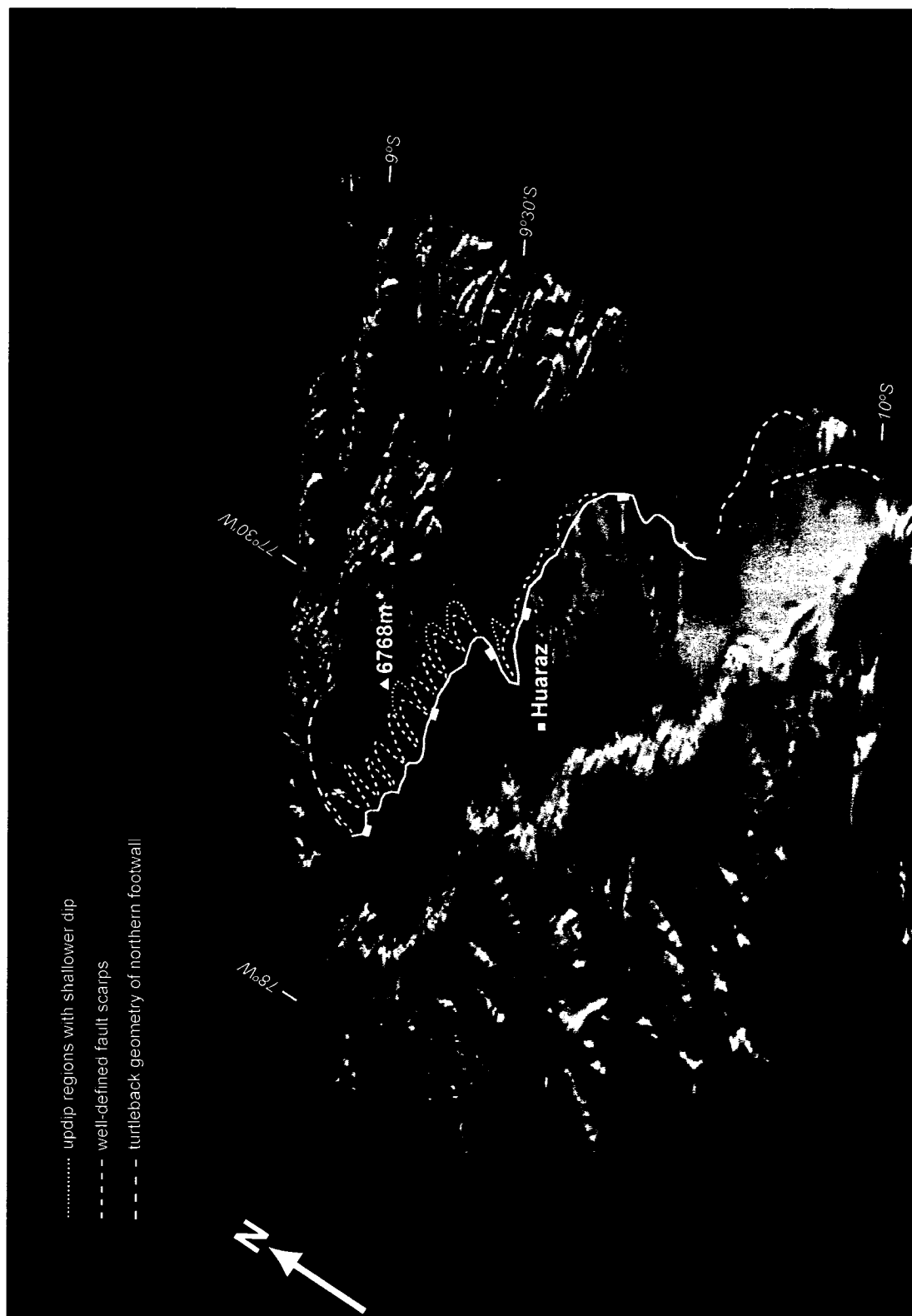
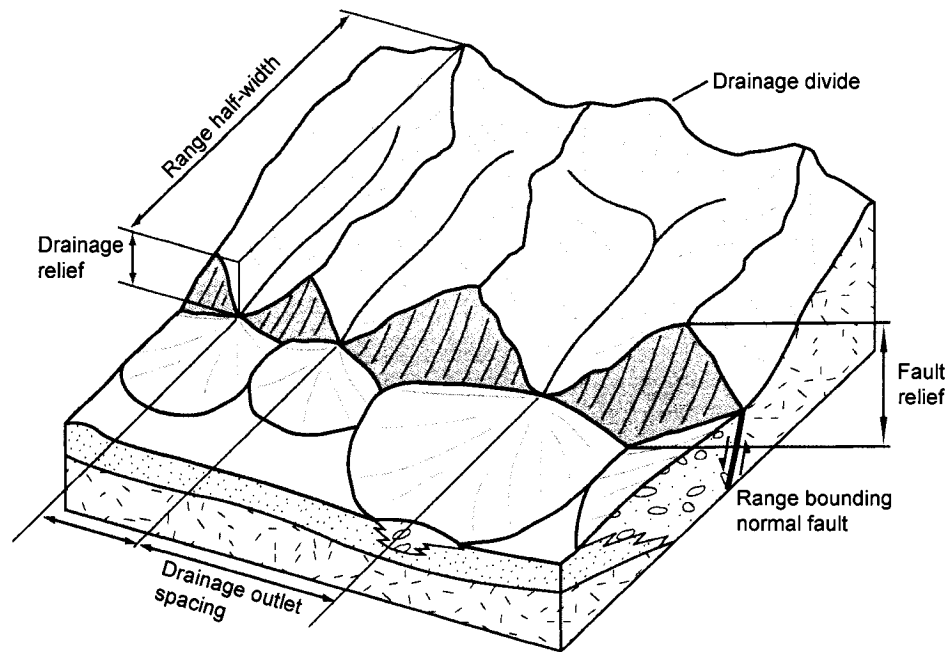


Figure 2.13A

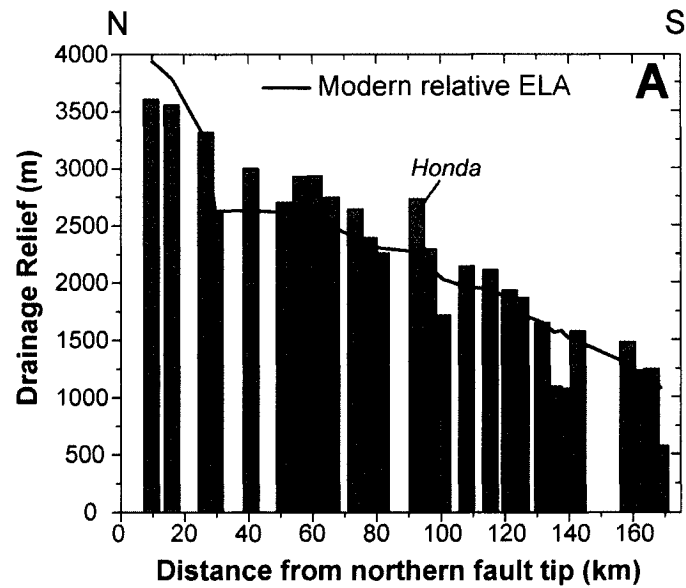


Figure 2.13B

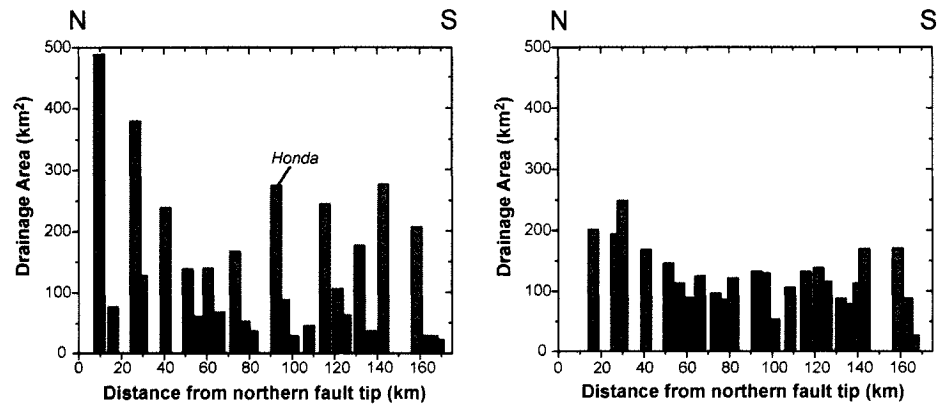


**Figure 2.14.** 3D block diagram illustrating geomorphic parameters used in this study [modified from *Densmore et al.*, 2005]. Drainage relief is equal to "footwall relief" of *Densmore et al.* [2005].

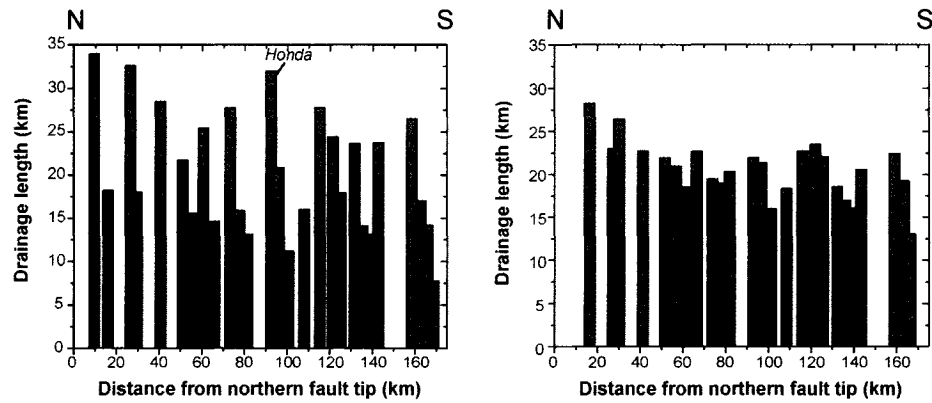




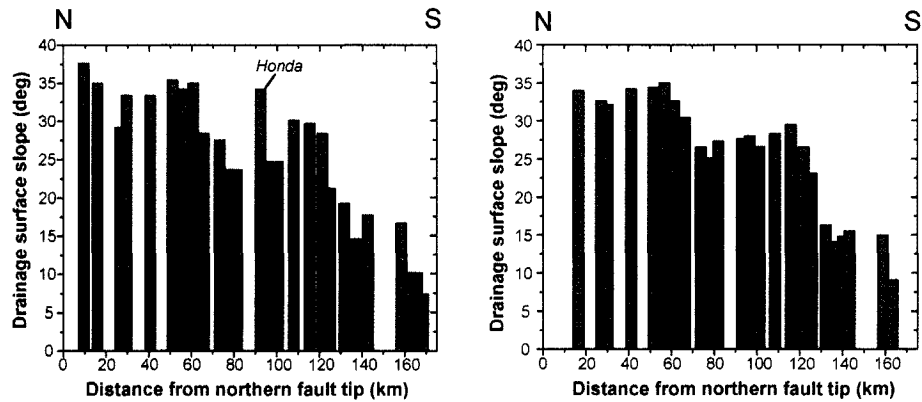
**Figure 2.15A.** Values for various geomorphic parameters of the drainage basins defined in Figure 2.8 plotted as a function of distance along strike from the northern fault tip. The Honda drainage is marked for reference. (A) Drainage basin relief steadily decreases southward along strike. The relative elevation of the modern ELA is plotted for reference. Most of the modern relief lies below the ELA, indicating that glaciation is dominated by cirque glaciers rather than valley glaciers.



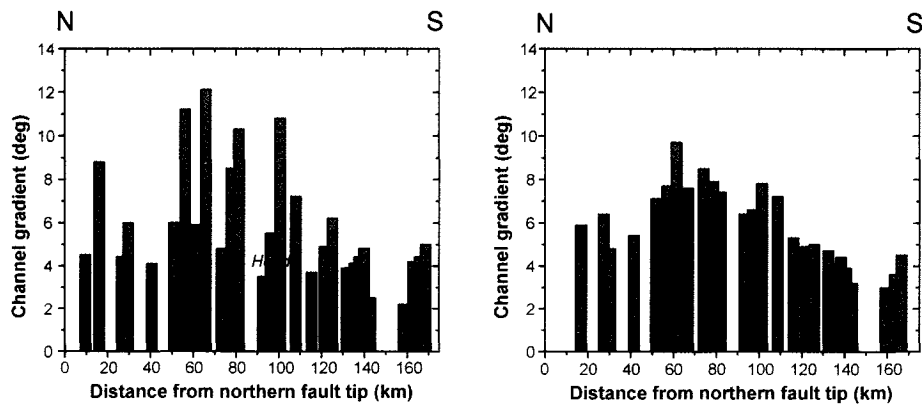
**Fig. 2.15B. (Left)** Drainage area generally decreases to the south, but there is a semi-regular spacing (15-20 km) between the larger drainages. **(Right)** Running mean reveals a general southward decrease in drainage area.



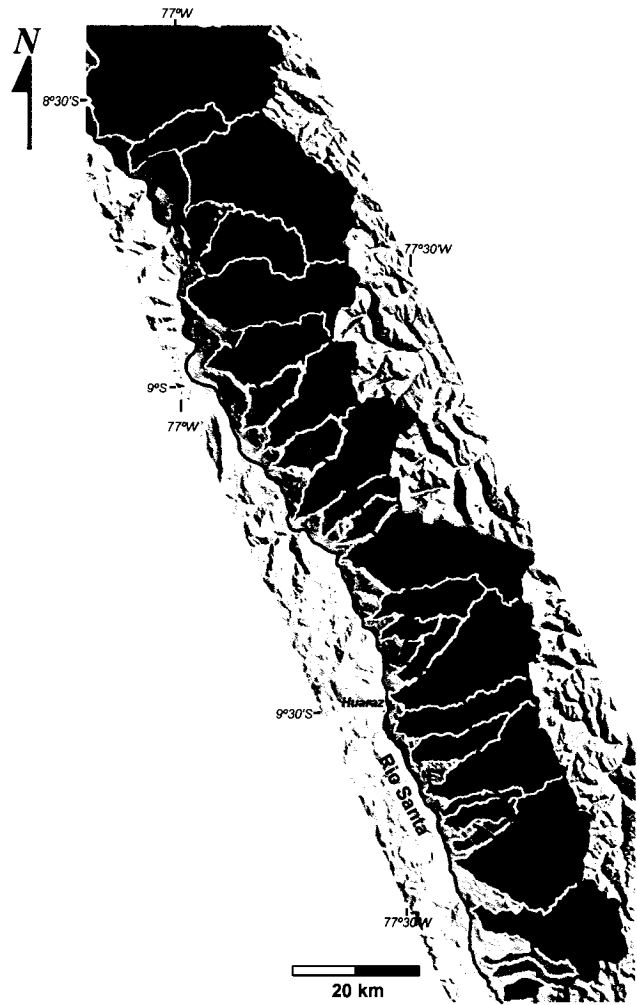
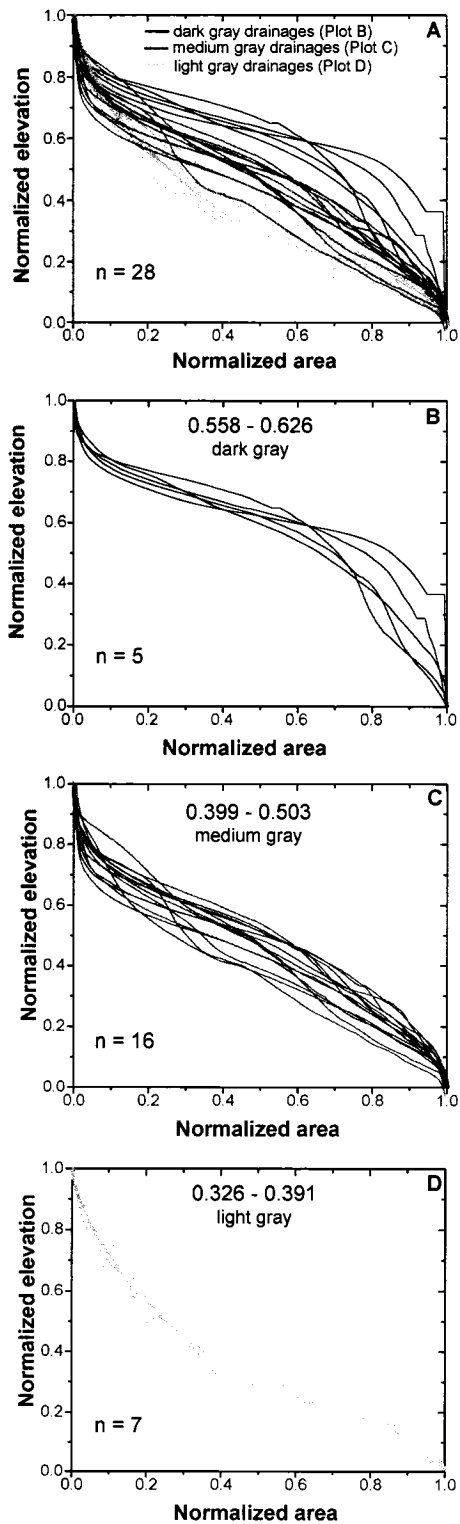
**Fig. 2.15C. (Left)** Drainage length also displays a regular spacing between larger drainages. **(Right)** Running mean reveals a general southward decrease in drainage length.



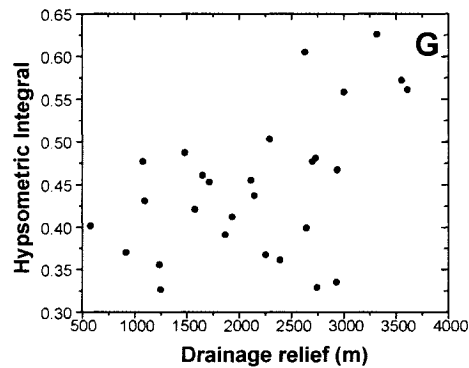
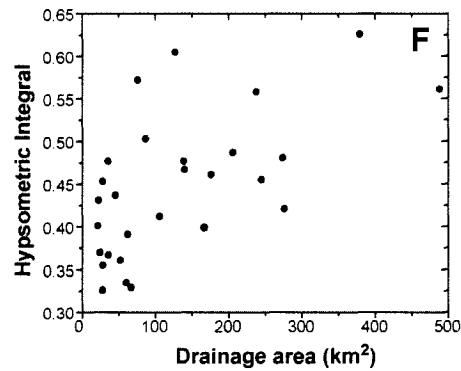
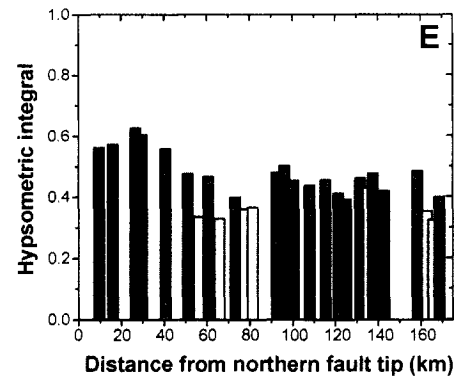
**Fig. 2.15D. (Left)** Drainage surface slopes generally decreases to the south, with the most dissected drainages located in the north. **(Right)** Running mean reveals the drainages >120 km from the northern fault tip have significantly lower surface slopes.



**Fig. 2.15E. (Left)** Channel gradients average 4-6° except for central drainages that do not reach the drainage divide (see longitudinal profiles in Fig. 2.16). **(Right)** Excepting those central drainages, channel gradients are relatively uniform along strike.



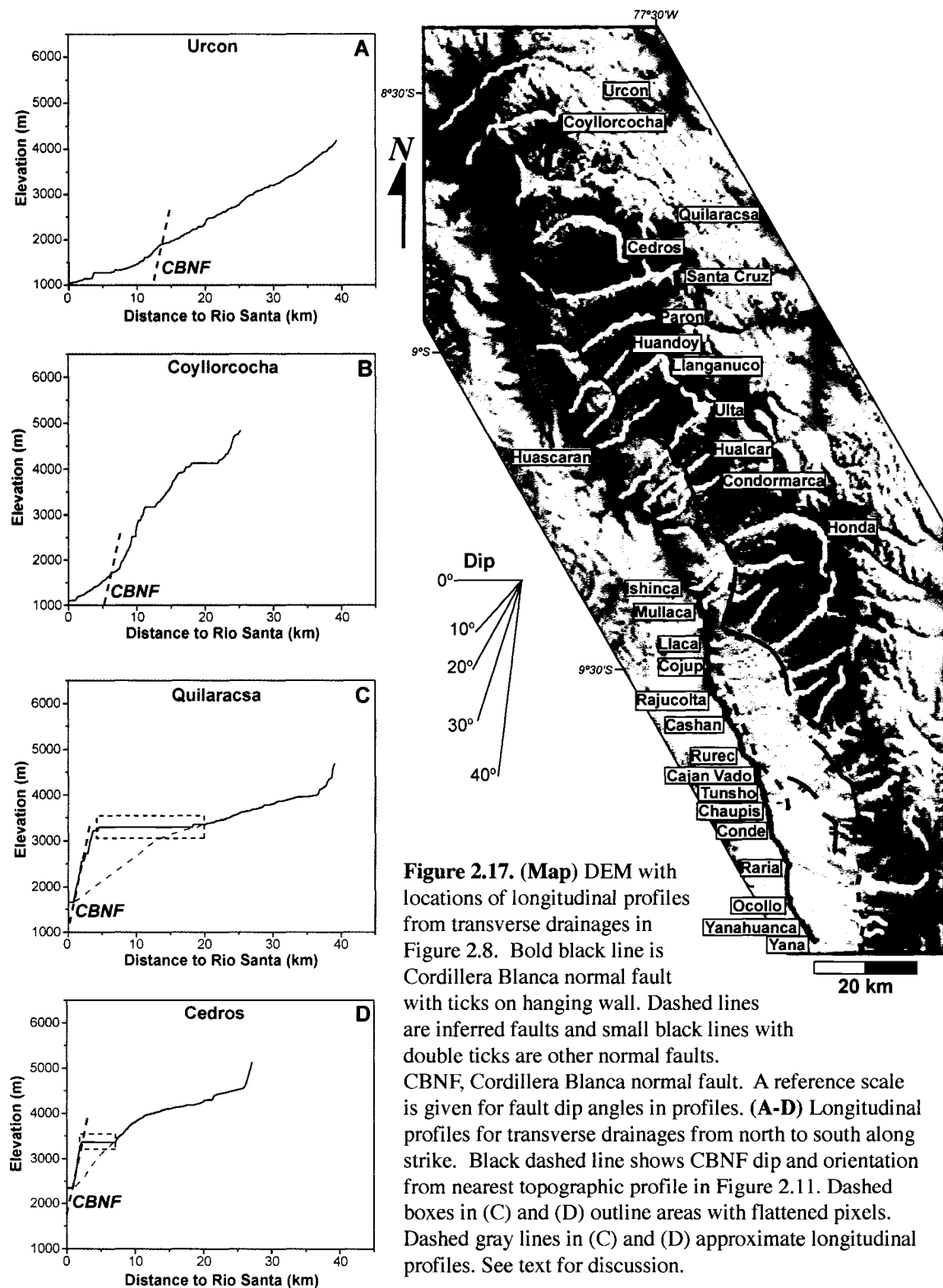
**Figure 2.16.** Hypsometric integrals for Cordillera Blanca drainage basins. (A) Hypsometric curves for all 28 drainages studied. (B-D) Hypsometric curves grouped by similar degree of convexity, corresponding to shaded drainages. Northern drainages have the highest integral values, indicating that the majority of their area is at high elevation and have undergone a high degree of dissection by either fluvial or glacial processes.



**Figure 2.16 (continued)**

(E) Plot of hypsometric integral values as a function of distance along strike. Shading corresponds to the shaded drainages on map in previous figure. Highest values occur in the north with an overall decrease southward along strike.

(F-G) The hypsometric integral is not strongly correlated to either drainage area or relief, though in general, the lower the integral value, the smaller the drainage and lower the relief.



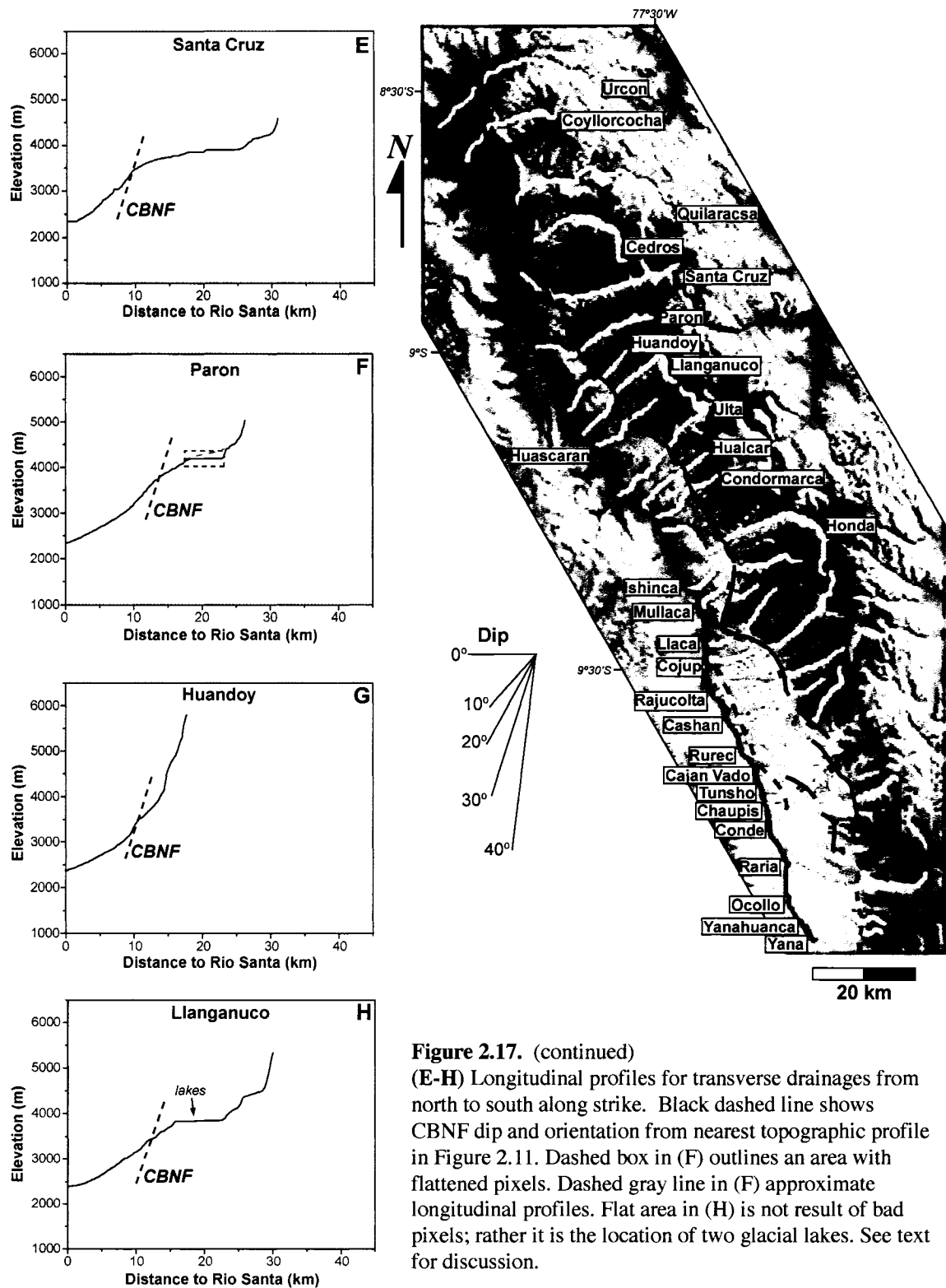


**Figure 2.17.** (continued)  
 (E-H) Longitudinal profiles for transverse drainages from north to south along strike. Black dashed line shows CBNF dip and orientation from nearest topographic profile in Figure 2.11. Dashed box in (F) outlines an area with flattened pixels. Dashed gray line in (F) approximate longitudinal profiles. Flat area in (H) is not result of bad pixels; rather it is the location of two glacial lakes. See text for discussion.

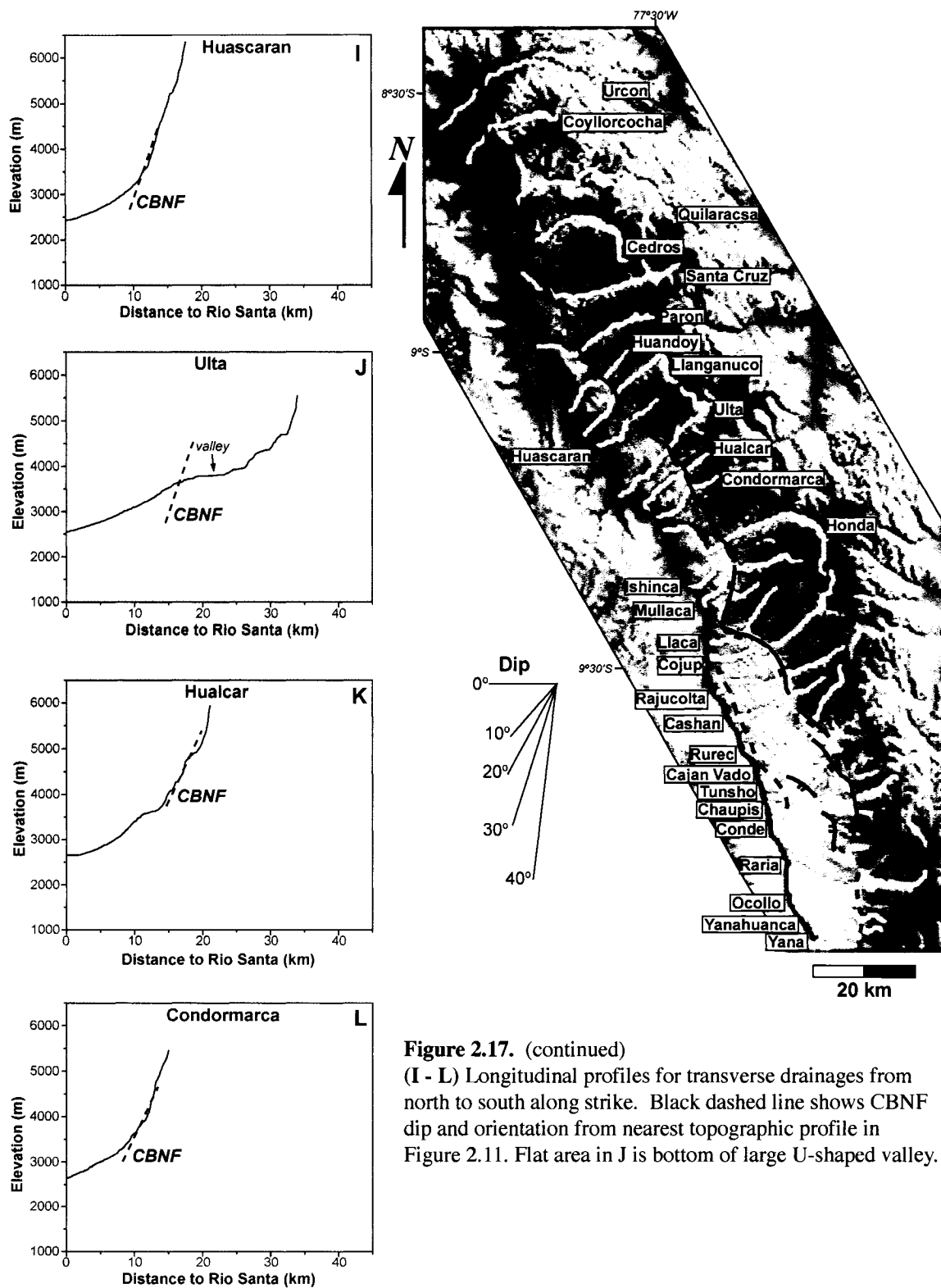


**Figure 2.17.** (continued)  
 (I - L) Longitudinal profiles for transverse drainages from north to south along strike. Black dashed line shows CBNF dip and orientation from nearest topographic profile in Figure 2.11. Flat area in J is bottom of large U-shaped valley.



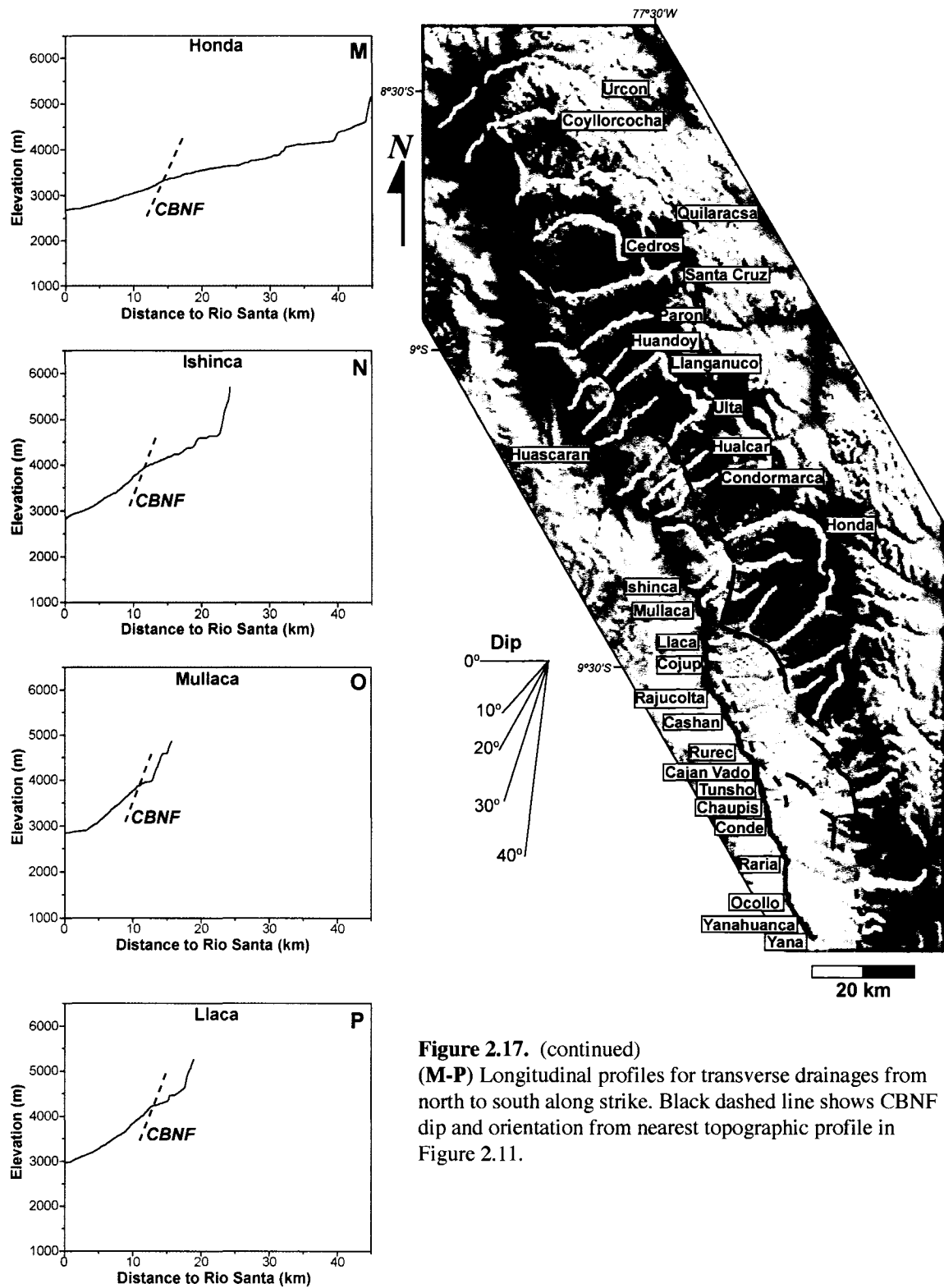


**Figure 2.17.** (continued)  
**(M-P)** Longitudinal profiles for transverse drainages from north to south along strike. Black dashed line shows CBNF dip and orientation from nearest topographic profile in Figure 2.11.

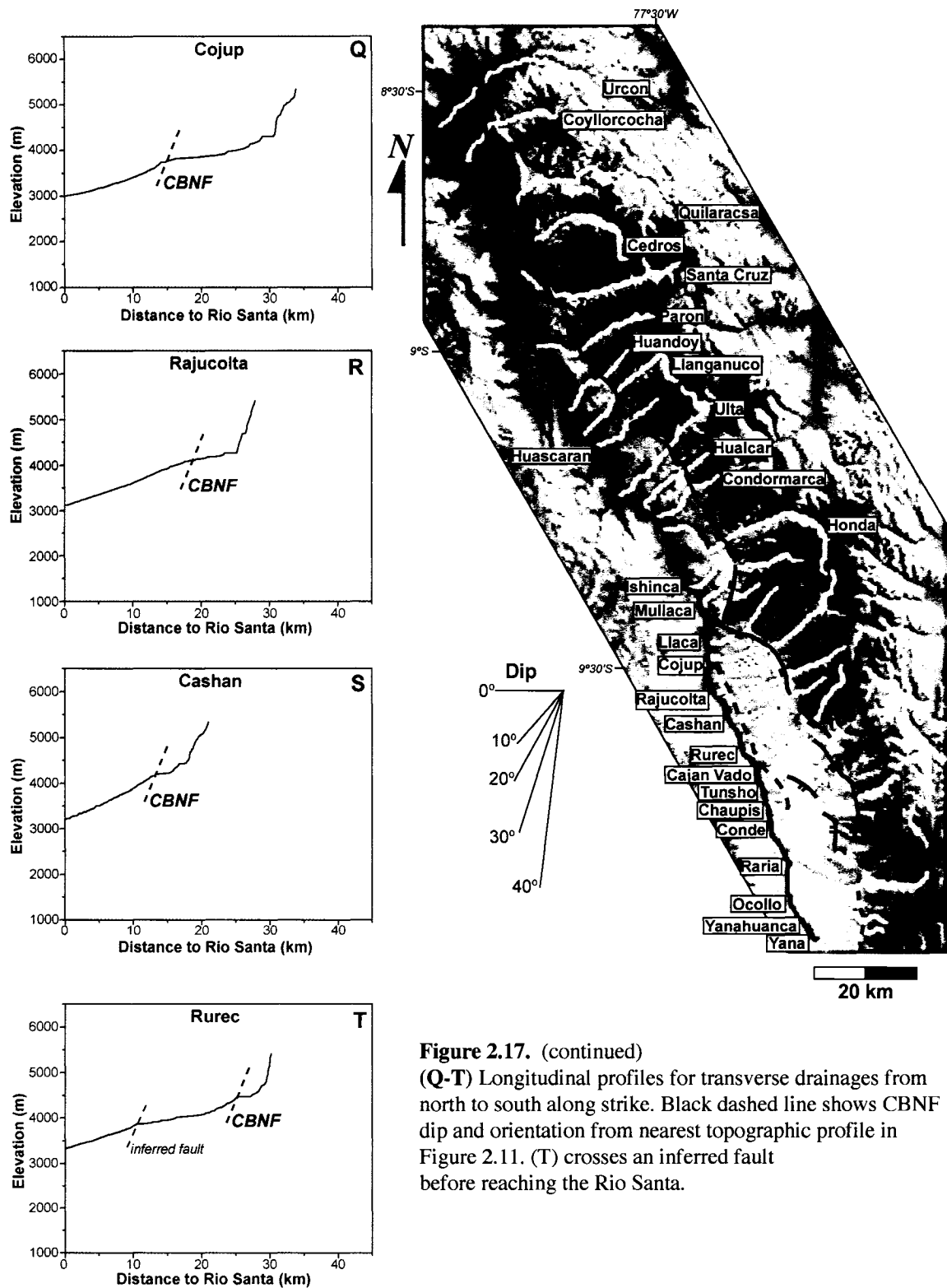


**Figure 2.17. (continued)**  
 (Q-T) Longitudinal profiles for transverse drainages from north to south along strike. Black dashed line shows CBNF dip and orientation from nearest topographic profile in Figure 2.11. (T) crosses an inferred fault before reaching the Rio Santa.

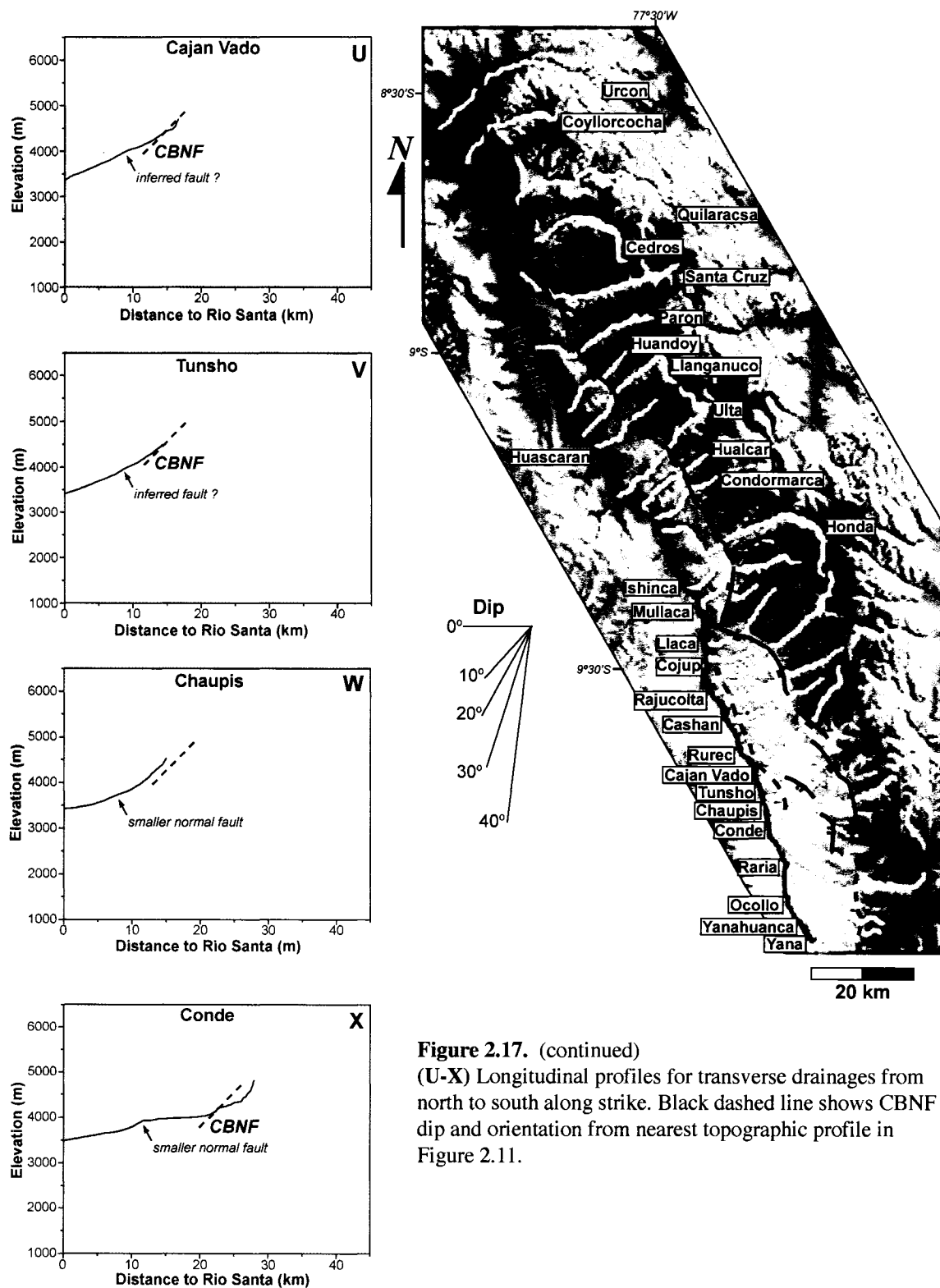


**Figure 2.17.** (continued)  
(U-X) Longitudinal profiles for transverse drainages from north to south along strike. Black dashed line shows CBNF dip and orientation from nearest topographic profile in Figure 2.11.

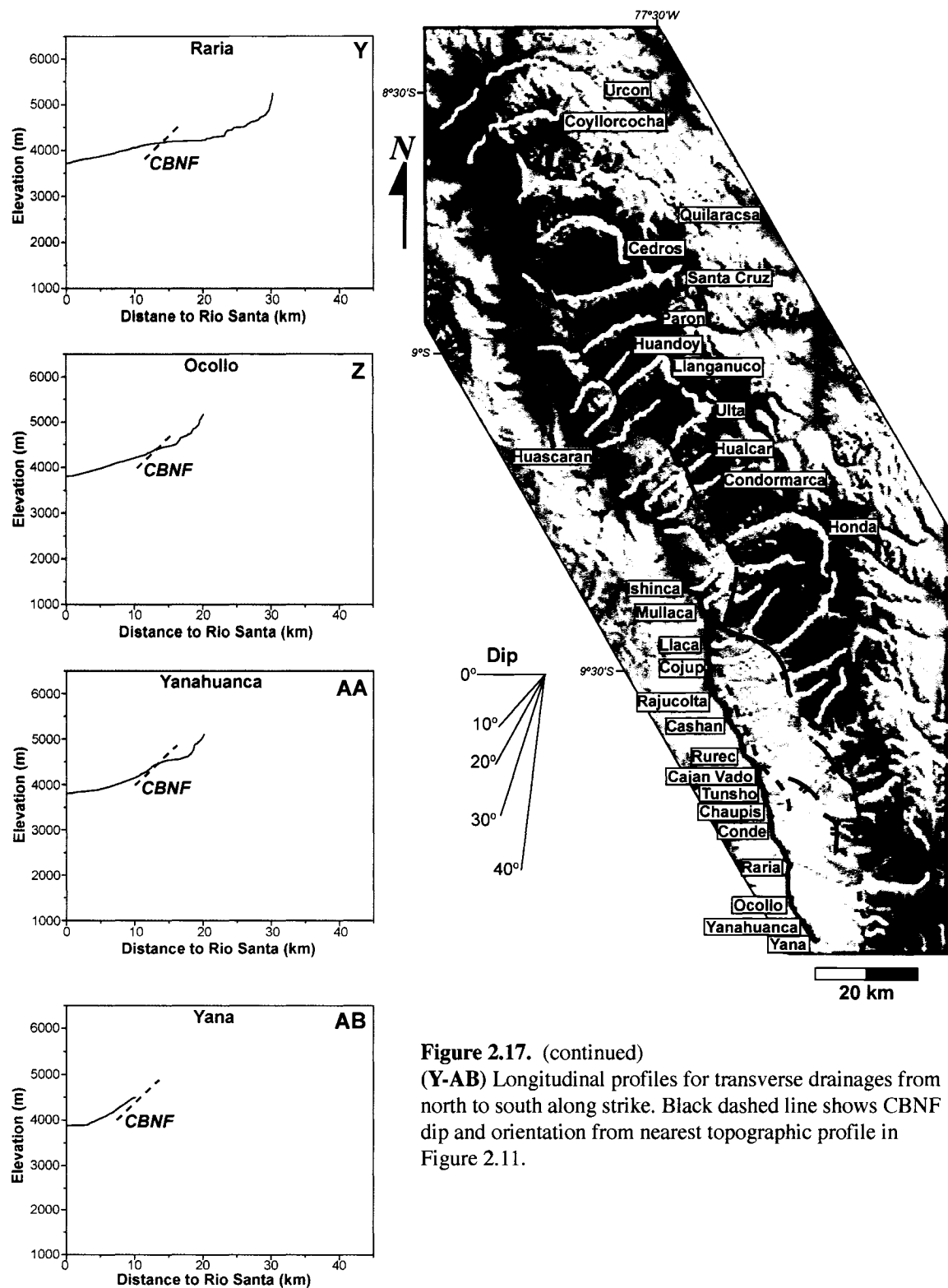
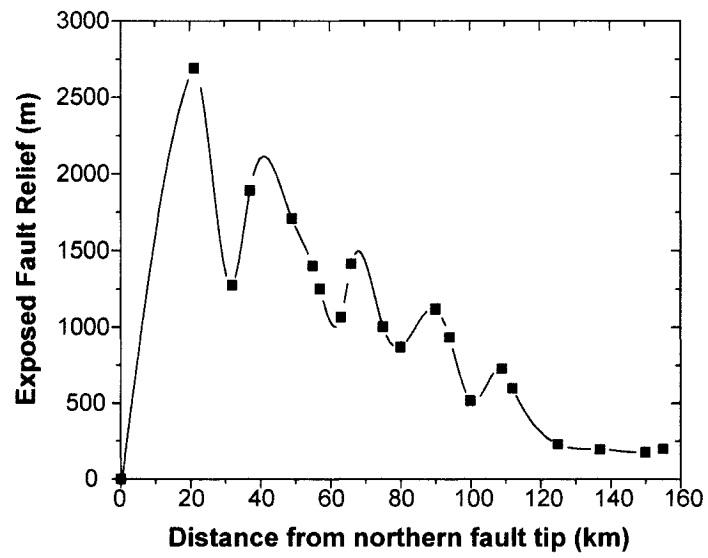


**Figure 2.17.** (continued)  
**(Y-AB)** Longitudinal profiles for transverse drainages from north to south along strike. Black dashed line shows CBNF dip and orientation from nearest topographic profile in Figure 2.11.

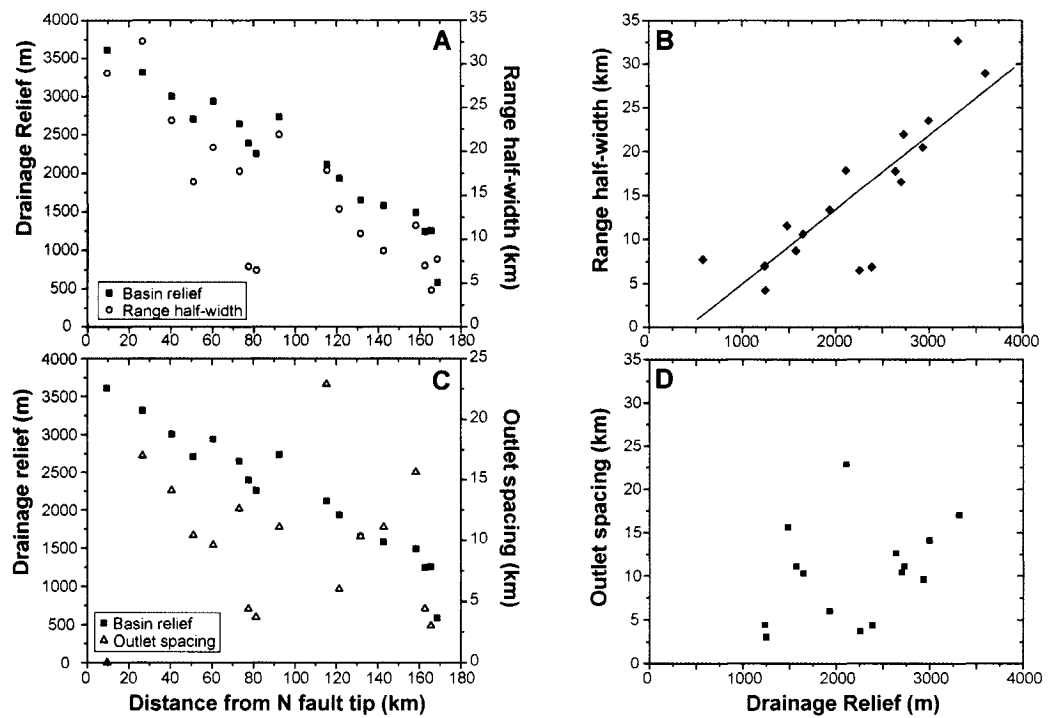
**Figure 2.18.** 3D image from DEM of Cordillera Blanca looking northeast perpendicular to strike. Cordillera Blanca normal fault (bold white line). Thin, dashed white lines delineate exposed fault surface. Greatest amount of fault surface exposure occurs along northern fault segment. Fault surface exposure decreases drastically southward along strike. Vertical exaggeration = 5x.



Figure 2.18



**Figure 2.19.** Fault relief as a function of distance along-strike from northern fault tip. Measurement locations marked by yellow lines in Figure 2.10.



**Figure 2.20.** Relationships between basin relief, range half-width, outlet spacing, and along-strike distance. Only drainages that reach the drainage divide are considered. **(A)** Basin relief and range half-width both decrease steadily away from the northern fault tip. **(B)** Linear relationship between range half-width and relief, suggesting that their development is linked to slip along the Cordillera Blanca normal fault. **(C)** Basin relief and outlet spacing decrease southward along-strike as well. **(D)** Outlet spacing and basin relief do not correlate as well, suggesting that the outlet spacing is less influenced by fault slip.



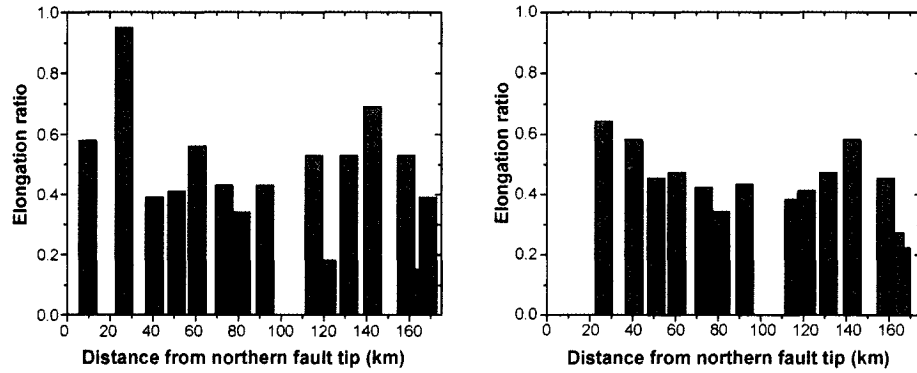


**Fig. 2.21. (Left)** Distribution of long and narrow drainages (ratio > 0.4) exhibit no discernible pattern. **(Right)** Running mean reveals the longest and narrowest drainages to be concentrated along the central and southernmost fault segments. This also reflects the sinuosity of the drainage divide (Fig. 2.8) in that the shorter basins occur where the divide approaches the fault along the central segment.

<b>Table 2.1 Summary of geomorphic parameters for individual drainages</b>	
Parameter	Description
Area	Total surface area of the drainage
Hypsometry	Area vs. elevation plot (hypsometric curve)
Hypsometric integral	Area under the hypsometric curve
Drainage length	Longest straight-line length across the drainage from the drainage outlet to the drainage divide
Elevation max.	Maximum elevation in the drainage
Elevation min.	Minimum elevation in the drainage (drainage outlet)
Drainage relief	Elevation difference within the drainage <i>Elevation max. – Elevation min.</i>
Drainage surface slope	Average downstream slope interpolated from all pixels within the drainage
Channel gradient	Slope of main trunk stream in the drainage
Stream profile	Longitudinal profile of main trunk stream in the drainage (elevation vs. distance plot)

**Table 2.2** Morphometric characteristics for major drainage networks of the Cordillera Blanca

Drainage	Distance from		Drainage Length (km)	Channel gradient (m/km)	Surface slope (deg)	Hypsometric	Relief (m a.s.l.)
	N fault tip (km)	Area (km <sup>2</sup> )				Integral	
Urcon	9.6	488.2	33.9	4.5	37.6	0.561	3608
Coyllorcocha	16	75.7	18.2	8.8	35	0.572	3556
Quilaracsá	26.6	379.5	32.6	4.4	29.2	0.626	3318
Cedros	29.6	127.5	18	6	33.4	0.605	2630
SantaCruz	40.7	238.1	28.5	4.1	33.4	0.558	3002
Paron	51.1	138.7	21.7	6	35.4	0.477	2703
Huandoy	56.2	60.4	15.6	11.2	34.2	0.335	2930
Llanganuco	60.7	139.9	25.4	5.9	35	0.467	2937
Huascarán	65.9	67.1	14.6	12.1	28.4	0.329	2746
Uta	73.3	167.1	27.7	4.8	27.5	0.399	2644
Hualcar	77.7	52.4	15.9	8.5	23.7	0.361	2392
Condormarca	81.4	35.7	13.1	10.3	23.7	0.367	2257
Honda	92.5	274.4	31.9	3.5	34.2	0.481	2734
Ishinca	96.2	87.1	20.8	5.5	24.7	0.503	2294
Mullaca	100.6	28.1	11.2	10.8	24.7	0.453	1716
Llaca	108	45.5	16	7.2	30.1	0.437	2146
Cojup	115.4	244.9	27.8	3.7	29.7	0.455	2114
Rajucolta	121.4	106.1	24.4	4.9	28.4	0.412	1935
Cashan	125.1	62.6	17.9	6.2	21.3	0.391	1869
Rurec	131.7	176.2	23.6	3.9	19.3	0.461	1650
CajanVado	135.4	22.6	14.1	4.1	8	0.431	1098
Tunsho	137.6	35.7	13.1	4.4	14.6	0.477	1083
Chaupis	139.9	24.5	11.3	4.8	11.9	0.37	921
Conde	142.8	276.4	23.7	2.5	17.7	0.421	1578
Raria	158.4	206.2	26.5	2.2	16.7	0.487	1484
Ocollo	162.8	28.4	17	4.2	10.2	0.355	1239
Yanahuanca	165.8	28.2	14.2	4.4	10.2	0.326	1251
Yana	168.7	21.7	7.7	5	7.4	0.401	581

<b>Table 2.3</b> Elevation values for major drainage networks of Cordillera Blanca				
<b>Drainage</b>	<b>Minimum elevation (m) (drainage outlet)</b>	<b>Maximum elevation (m) (drainage divide)</b>	<b>Relief * (m a.s.l.)</b>	<b>Relative ELA<sup>a</sup> (m a.s.l.)</b>
Urcon	1039	4647	3608	3946
Coyllorcocha	1194	4750	3556	3791
Quilaracsa	1730	5048	3318	3255
Cedros	2356	4986	2630	2629
SantaCruz	2356	5358	3002	2629
Paron	2368	5071	2703	2617
Huandoy	2405	5335	2930	2580
Llanganuco	2439	5376	2937	2546
Huascarán	2493	5239	2746	2492
Uta	2582	5226	2644	2403
Hualcar	2654	5046	2392	2331
Condormarca	2682	4939	2257	2303
Honda	2712	5446	2734	2273
Ishinca	2843	5137	2294	2142
Mullaca	2953	4669	1716	2032
Llaca	3022	5168	2146	1963
Cojup	3039	5153	2114	1946
Rajucolta	3128	5063	1935	1857
Cashan	3258	5127	1869	1727
Rurec	3330	4980	1650	1655
CajanVado	3415	4513	1098	1570
Tunsho	3401	4484	1083	1584
Chaupis	3464	4385	921	1521
Conde	3497	5075	1578	1488
Raria	3689	5173	1484	1296
Ocollo	3814	5053	1239	1171
Yanahuanca	3862	5113	1251	1123
Yana	3892	4473	581	1093

\* Relief = max elevation – min elevation

<sup>a</sup> Relative ELA = modern ELA (4985m) – min elevation

This allows comparison of how much of the relief of each drainage is high or low, relative to the ELA.

**Table 2.4** Spacing and elongation ratios for drainage networks that reach the drainage divide

<b>Drainage</b>	<b>Range half-width (km)</b>	<b>Outlet spacing (km)</b>	<b>Spacing Ratio</b>	<b>Drainage Length (km)</b>	<b>Drainage width (km)</b>	<b>Elongation Ratio</b>
Urcon	33.9			33.9	19.6	0.58
Quilaracsa	32.6	17.0	1.92	32.6	31.1	0.95
SantaCruz	28.5	14.1	2.02	28.5	11.1	0.39
Paron	21.7	10.4	2.09	21.7	8.9	0.41
Llanganuco	25.4	9.6	2.65	25.4	14.1	0.56
Uta	27.7	12.6	2.20	27.7	11.8	0.43
Hualcar	15.9	4.4	3.61	15.9	4.1	0.26
Condormarca	13.1	3.7	3.54	13.1	4.4	0.34
Honda	31.9	11.1	2.87	31.9	13.7	0.43
Cojup	27.8	22.9	1.21	27.8	14.8	0.53
Rajucolta	24.4	6.0	4.07	24.4	4.4	0.18
Rurec	23.6	10.3	2.29	23.6	12.6	0.53
Conde	23.7	11.1	2.14	23.7	16.3	0.69
Raria	26.5	15.6	1.70	26.5	14.1	0.53
Ocollo	17.0	4.4	3.86	17.0	2.2	0.13
Yanahuanca	14.2	3.0	4.73	14.2	2.2	0.15
Yana	7.7	6.5	1.18	7.7	3.0	0.39
Mean $\pm$ 1 $\sigma$ for all drainages			2.63 $\pm$ 1.05			0.44 $\pm$ 0.21

Spacing ratio = range half width / outlet spacing [Hovius, 1996; Talling *et al.*, 1997]Elongation ratio = drainage width / drainage length [Jamieson *et al.*, 2004]1 $\sigma$  = standard deviation

## 2.9 REFERENCES

- Anders, M. H., and Schlische, R.W., 1994, Overlapping faults, intrabasin highs, and the growth of normal faults: *Journal of Geology*, v. 102, p. 165-180.
- Atherton, M. P., and Petford, N., 1993, Generation of sodium-rich magmas from newly underplated basaltic crust: *Nature*, v. 362, p. 144-146.
- Axen, G. J., Bartley, J.M., and Selverstone, J., 1995, Structural expression of a rolling hinge in the footwall of the Brenner Line normal fault, eastern Alps: *Tectonics*, v. 14, p. 1380-1392.
- Bishop, M. P., Shroder Jr., J.F., Bonk, R., and Olsenholler, J., 2002, Geomorphic change in high mountains: a western Himalayan perspective: *Global and Planetary Change*, v. 32, p. 311-329.
- Bishop, M. P., Shroder Jr., J.F., and Colby, J.D., 2003, Remote sensing and geomorphometry for studying relief production in high mountains: *Geomorphology*, v. 55, p. 345-361.
- Bonnot, D., 1984, Neotectonique et tectonique active de la Cordillera Blanca et Callejon de Huaylas (Andes nord-peruviennes) [PhD thesis]: Universite de Paris-Sud, 115 p.
- Brocklehurst, S. H., and Whipple, K.X., 2004, Hypsometry of glaciated landscapes: *Earth Surface Processes and Landforms*, v. 29, p. 907-926.
- Brozovic, N., Burbank, D.W., and Meigs, A.J., 1997, Climatic limits on landscape development in the northwestern Himalaya: *Science*, v. 276, p. 571-574.
- Bruhn, R. L., Zhu-en, Y., Daning, W., and Yonkee, W.A., 1991, Structure of the Warm Spring and Northern Thousand Springs fault segments, Lost River fault zone, Idaho: possible effects on rupturing during the 1983 Borah Peak Earthquake: *Tectonophysics*, v. 200, p. 33-49.
- Burbank, D. W., Leland, J., Fielding, E., Anderson, R.S., Brozovic, N., Reid, M.R., and Duncan, C., 1996, Bedrock incision, rock uplift and threshold hillslopes in the northwestern Himalayas: *Nature*, v. 379, p. 505-510.
- Burchfiel, B. C., Chen, Z., Hodges, K.V., Liu, Y., Royden, L.H., Deng, C., and Xu, J., 1992, The South Tibetan detachment system, Himalayan orogen: Extension contemporaneous with and parallel to shortening in a collisional mountain belt, *Geological Society of America Special Paper* 269, 41 p.

- Burgmann, R., Pollard, D.D., and Martel, S.J., 1994, Slip distributions on faults: Effects of stress gradients, inelastic deformation, heterogeneous host-rock stiffness, and fault interaction: *Journal of Structural Geology*, v. 16, p. 1675-1690.
- Cartwright, J. A., Trudgill, B.D., and Mansfield, C.S., 1995, Fault growth by segment linkage: An explanation for scatter in maximum displacement and trace length data from the Canyonlands Graben of SE Utah: *Journal of Structural Geology*, v. 17, p. 1319-1326.
- Cobbing, E. J., and Sanchez, A.W., 1996, Mapa geologico del cuadrangulo de Recuay, 1:100 000, digitized 1996: Instituto Geologico Minero y Metalurgico.
- Cobbing, E. J., Pitcher, W.S., Wilson, J.J., Baldock, J.W., Taylor, W.P., McCourt, W., and Snelling, N.J., 1981, The geology of the Western Cordillera of northern Peru, *Overseas Memoir, Institute of Geological Sciences*, 143 pp.
- Cossio, A., and Blanco, E., 1964, Mapa geologico del cuadrangulo de Santa Rosa, 1:100 000: Instituto Geologico, Minero y Metalurgico.
- Cowie, P. A., and Roberts, G.P., 2001, Constraining slip rates and spacings for active normal faults: *Journal of Structural Geology*, v. 23, p. 1901-1915.
- Cowie, P. A., and Scholz, C.H., 1992, Displacement-length scaling relationship for faults: Data synthesis and discussion: *Journal of Structural Geology*, v. 14, p. 1149-1156.
- Cowie, P. A., Gupta, S., and Dawers, N.H., 2000, Implications of fault array evolution for synrift depocentre development: Insights from a numerical fault growth model: *Basin Research*, v. 12, p. 241-262.
- Dalmayrac, B., and Molnar, P., 1981, Parallel thrust and normal faulting in Peru and constraints on the state of stress: *Earth and Planetary Science Letters*, v. 55, p. 473-481.
- Dawers, N. H., and Anders, M.H., 1995, Displacement-length scaling and fault linkage: *Journal of Structural Geology*, v. 17, p. 607-614.
- Dawers, N. H., and Underhill, J.R., 2000, The role of fault interaction and linkage in controlling synrift stratigraphic sequences: Late Jurassic, Statfjord East area, northern North Sea: *American Association of Petroleum Geologists Bulletin*, v. 84, p. 45-64.
- Dawers, N. H., Anders, M.H., and Scholz, C.H., 1993, Growth of normal faults: Displacement-length scaling: *Geology*, v. 21, p. 1107-1110.

- Densmore, A. L., Dawers, N.H., Gupta, S., Guidon, R., and Goldin, T., 2004, Footwall topographic development during continental extension: *Journal of Geophysical Research*, v. 109, no. F03001, p. doi:10.1029/2003JF000115.
- Densmore, A. L., Dawers, N.H., Gupta, S., and Guidon, R., 2005, What sets topographic relief in extensional footwalls?: *Geology*, v. 33, p. 453-456
- Deverchere, J., Dorbath, C., and Dorbath, L., 1989, Extension related to a high topography: results from a microearthquake survey in the Andes of Peru and tectonic implications: *Geophysical Journal International*, v. 98, p. 281-292.
- Dokka, R. K., and Macaluso, K.Y., 2001, Topographic effects of the Eastern California Shear Zone in the Mojave Desert: *Journal of Geophysical Research*, v. 106, p. 30,625-30,644.
- Doser, D. I., 1987, The Ancash, Peru, earthquake of 1946 November 10: evidence for low-angle normal faulting in the high Andes of northern Peru: *Geophysical Journal of the Royal Astronomical Society*, v. 91, p. 57-71.
- Elliott, D., 1976, The energy balance and deformation mechanisms of thrust sheets: *Philosophical Transactions of the Royal Society of London. Series A, Mathematical and Physical Sciences*, v. 283, p. 289-312.
- Farber, D. L., Hancock, G.S., Finkel, R.C., and Rodbell, D.T., 2005, The age and extent of tropical alpine glaciation in the Cordillera Blanca, Peru: *Journal of Quaternary Science*, v. 20, p. 759-776.
- Frankel, K. L., and Pazzaglia, F.J., 2005, Tectonic geomorphology, drainage basin metrics, and active mountain fronts: *Geografica Fisica e Dinamica Quaternaria*, v. 28, p. 7-21.
- Hallet, B., and Molnar, P., 2001, Distorted drainage basins as markers of crustal strain east of the Himalaya: *Journal of Geophysical Research*, v. 106, p. 13,697-13,709.
- Herman, F., and Braun, J., 2006, Fluvial response to horizontal shortening and glaciations: A study in the Southern Alps of New Zealand: *Journal of Geophysical Research*, v. 111, F01008, doi:10.1029/2004JF000248.
- Hovius, N., 1996, Regular spacing of drainage outlets from linear mountain belts: *Basin Research*, v. 8, p. 29-44.
- Hurtrez, J. E., Sol, C., and Lucazeau, F., 1999, Effect of drainage area on hypsometry from an analysis of small-scale drainage basins in the Siwalik Hills, Central Nepal: *Earth Surface Processes and Landforms*, v. 24, p. 799-808.



- Jamieson, S. S. R., Sinclair, H.D., Kirstein, L.A., and Purves, R.S., 2004, Tectonic forcing of longitudinal valleys in the Himalaya: morphological analysis of the Ladakh Batholith, North India: *Geomorphology*, v. 58, p. 49-65.
- Janecke, S. U., 1993, Structures in segment boundary zones of the Lost River and Lemhi faults, east central Idaho: *Journal of Geophysical Research*, v. 98, p. 16,223-16,238.
- Kirkbride, M., and Matthews, D., 1997, The role of fluvial and glacial erosion in landscape evolution: the Ben Ohau Range, New Zealand: *Earth Surface Processes and Landforms*, v. 22, p. 317-327.
- Koons, P. O., 1995, Modeling the topographic evolution of collisional belts: *Annual Review of Earth and Planetary Sciences*, v. 23, p. 375-408.
- Korup, O., Schmidt, J., and McSaveney, M.J., 2005, Regional relief characteristics and denudation pattern of the western Southern Alps, New Zealand: *Geomorphology*, v. 71, p. 402-423.
- Manighetti, I., King, G.C.P., Gaudemer, Y., Scholz, C.H., and Doubre, C., 2001, Slip accumulation and lateral propagation of active normal faults in Afar: *Journal of Geophysical Research*, v. 106, p. 13,667-13,696.
- Mayer, L., 1986, Tectonic geomorphology of escarpment and mountain fronts, *in* Wallace, R. E., ed., *Active Tectonics*, National Academy of Science, USA, Washington D.C., p. 125-135.
- McLeod, A. E., Dawers, N.H., and Underhill, J.R., 2000, The propagation and linkage of normal faults: Insights from the Strathspey-Brent-Statfjord fault array, northern North Sea: *Basin Research*, v. 12, p. 263-284.
- McNulty, B. A., and Farber, D.L., 2002, Active detachment faulting above the Peruvian flat slab: *Geology*, v. 30, p. 567-570.
- McNulty, B. A., Farber, D.L., Wallace, G.S., Lopez, R., and Palacios, O., 1998, Role of plate kinematics and plate-slip-vector partitioning in continental magmatic arcs: Evidence from the Cordillera Blanca, Peru: *Geology*, v. 26, p. 827-830.
- McQuarrie, N., and Rodgers, D.W., 1998, Subsidence of a volcanic basin by flexure and lower crustal flow: The eastern Snake River Plain, Idaho: *Tectonics*, v. 17, p. 203-220.

- Molnar, P., and England, P., 1990, Late Cenozoic uplift of mountain ranges and global climate change: chicken or egg?: *Nature*, v. 346, p. 29-34.
- Oskin, M., and Burbank, D.W., 2005, Alpine landscape evolution dominated by cirque retreat: *Geology*, v. 33, p. 933-936.
- Pelletier, J. D., 2003, Drainage basin evolution in the Rainfall Erosion Facility: dependence on initial conditions: *Geomorphology*, v. 53, p. 183-196.
- Petford, N., and Atherton, M.P., 1992, Granitoid emplacement and deformation along a major crustal lineament: the Cordillera Blanca, Peru: *Tectonophysics*, v. 205, p. 171-185.
- Piatanesi, A., and Lorito, S., 2007, Rupture process of the 2004 Sumatra-Andaman earthquake from tsunami waveform inversion: *Bulletin of the Seismological Society of America*, v. 97, p. S223-S231 Part A Suppl. S.
- Riquelme, R., Martinod, J., Herail, G., Darrozes, J., and Charrier, R., 2003, A geomorphological approach to determining the Neogene to Recent tectonic deformation in the Coastal Cordillera of northern Chile (Atacama): *Tectonophysics*, v. 361, p. 255-275.
- RIVIX, 2004, RiverTools 3.0, Rivix LLC: Broomfield, CO.
- Rodbell, D. T., 1991, Late Quaternary glaciation and climatic change in the northern Peruvian Andes [Ph.D. thesis]: University of Colorado, Boulder, 216 p.
- Rodbell, D.T., 1992, Late Pleistocene equilibrium-line-altitude reconstructions in the northern Peruvian Andes: *Boreas*, v. 21, p. 43-52.
- Rodbell, D.T., 1993, Subdivision of Late Pleistocene moraines in the Cordillera Blanca, Peru, based on rock-weathering features, soils, and radiocarbon dates: *Quaternary Research*, v. 39, p. 133-143.
- Rodbell, D. T., and Seltzer, G.O., 2000, Rapid ice margin fluctuations during the Younger Dryas in the tropical Andes: *Quaternary Research*, v. 54, p. 328-338.
- Rodriguez, E., Morris, C.S., Belz, J.E., Chapin, E.C., Martin, J.M., Daffer, W., and Hensley, S., 2005, An assessment of the SRTM topographic products, Technical Report JPL D-31639: Jet Propulsion Laboratory, Pasadena, California, 143 p.
- Rousse, S., Gilder, S., Farber, D., McNulty, B., and Torres, V., 2002, Paleomagnetic evidence for rapid vertical-axis rotation in the Peruvian Cordillera ca. 8 Ma: *Geology*, v. 30, p. 75-78.

- Rousse, S., Gilder, S., Farber, D., McNulty, B., Patriat, P., Torres, V., and Sempere, T., 2003, Paleomagnetic tracking of mountain building in the Peruvian Andes since 10 Ma: *Tectonics*, v. 22, doi: 10.1029/2003TC001508.
- Schlische, R. W., Young, S.S., Ackermann, R.V., and Gupta, A., 1996, Geometry and scaling relations of a population of very small rift-related normal faults: *Geology*, v. 24, p. 683-686.
- Schwartz, D. P., 1988, Paleoseismicity and neotectonics of the Cordillera Blanca fault zone, northern Peruvian Andes: *Journal of Geophysical Research*, v. 93, p. 4712-4730.
- Sebrier, M., Mercier, J.L., Marchare, J., Bonnot, D., Cabarez, J., and Blanc, J.L., 1988, The state of stress in an overriding plate situated above a flat slab: the Andes of central Peru: *Tectonics*, v. 7, p. 895-928.
- Shroder, J. F., Jr., and Bishop, M.P., 2000, Unroofing of the Nanga Parbat Himalaya, *in* Khan, M. A., et al., , ed., *Tectonics of the Nanga Parbat Syntaxis and the western Himalaya*: London, Geological Society Special Publication, v. 170, p. 163-179.
- Shroder, J. F., Jr., Scheppy, R.A., and Bishop, M.P., 1999, Denudation of small alpine basins, Nanga Parbat Himalaya, Pakistan: *Arctic, Antarctic, and Alpine Research*, v. 31, p. 121-127.
- Smith, W. H. F., and Sandwell, D.T., 1997, Global seafloor topography from satellite altimetry and ship depth soundings: *Science*, v. 277, p. 1957-1962.
- Strahler, A. N., 1952, Hypsometric (area - altitude) analysis of erosional topography: *Geological Society of America Bulletin*, v. 63, p. 1117-1142.
- Suarez, G., Molnar, P., and Burchfiel, B.C., 1983, Seismicity, fault plane solutions, depth of faulting, and active tectonics of the Andes of Peru, Ecuador, and southern Colombia: *Journal of Geophysical Research*, v. 88, p. 10,403-10,428.
- Summerfield, M. A., 1991, *Global Geomorphology*: Singapore, Longman, 537 p.
- Talling, P. J., Stewart, M.D., Stark, C.P., Gupta, S., and Vincent, S.J., 1997, Regular spacing of drainage outlets from linear fault blocks: *Basin Research*, v. 9, p. 275-302.
- Wallace, R. E., 1978, Geometry and rates of changes of fault-generated range fronts, north-central Nevada: *U.S. Geological Survey Journal of Research*, v. 6, p. 637-650.

- Wawrzyniec, T. F., Selverstone, J., and Axen, G.J., 2001, Styles of footwall uplift along the Simplon and Brenner normal fault systems, central and Eastern Alps: *Tectonics*, v. 20, p. 748-770.
- Whipple, K. X., Kirby, E., and Brocklehurst, S.H., 1999, Geomorphic limits to climate-induced increases in topographic relief: *Nature*, v. 401, p. 39-43.
- Wilson, J. J., 1967a, Mapa geológico del cuadrangulo de Huari, 1:100 000: Instituto Geológico Minero y Metalúrgico.
- Wilson, J.J., 1967b, Mapa geológico del cuadrangulo de Carhuaz, 1:100 000: Instituto Geológico Minero y Metalúrgico.
- Wilson, J.J., 1967c, Mapa geológico del cuadrangulo de Corongo, 1:100 000: Instituto Geológico Minero y Metalúrgico.
- Yin, A., 2002, Passive-roof thrust model for the emplacement of the Pelona-Orocopia Schist in southern California, United States: *Geology*, v. 30, p. 183-186.
- Yin, A., 2006, Cenozoic tectonic evolution of the Himalayan orogen as constrained by along-strike variation of structural geometry, exhumation history, and foreland sedimentation: *Earth-Science Reviews*, v. 76, p. 1-131.
- Yin, A., and Kelty, T.K., 1991, Structural evolution of the Lewis plate in Glacier National Park, Montana - Implications for regional tectonic development: *Geological Society of America Bulletin*, v. 103, p. 1073-1089.
- Zeitler, P. K., Meltzer, A.S., Koons, P.O., Craw, D., Hallet, B., Chamberlain, C.P., Kidd, W.S.F., Park, S.K., Seeber, L., Bishop, M., and Shroder, J., 2001, Erosion, Himalayan geodynamics, and the geomorphology of metamorphism: *GSA Today*, v. 11, p. 4-9.

**- Chapter 3 -**

**Supradetachment basin evolution along the Cordillera Blanca detachment fault,  
Peru: Implications for normal faulting and basin growth in a contractional orogen**

### 3.1 ABSTRACT

Sedimentary basin analysis, carbonate oxygen isotopic data, and new models of extensional basin development provide insight into the evolution of the Callejon de Huaylas basin adjacent to the Cordillera Blanca, Peru. The Cordillera Blanca is the highest single mountain range in the Peruvian Andes, with average elevations > 5000 m. The range is bounded by a large, active, WSW-dipping normal fault striking parallel to active contractional structures located in the lower, eastern regions of the Andes. The 170-km-long normal fault is defined by moderate-to-low dips (19°-36° WSW), high footwall topography and moderate extension rates, and has likely accommodated > 10 km of dip slip since the late Miocene. The location of an active normal fault in the thickened hinterland of an active fold-thrust belt (the only example of its kind in the Andes) leads to questions regarding the evolution of the associated sedimentary basin.

Initial subsidence of the Callejon de Huaylas basin occurred at ~5.4 Ma as a result of normal slip along the Cordillera Blanca detachment fault. The basin is filled by ~1300 m of conglomerate, sandstone, siltstone, and lacustrine carbonate of the upper Miocene-Pliocene Lloclla Formation, which is overlain by Quaternary glacial sediments. Lithofacies associations of the Lloclla Formation are interpreted as recording deposition in a distal fan delta – lacustrine environment to a proximal alluvial fan environment. Sandstone provenance analysis reveals volcanic rocks, likely the Tertiary Calipuy Formation, as the primary sediment source for the lower member of the Lloclla Formation. Conglomerate clast counts and paleocurrent measurements for the upper 200-400m of the succession record the appearance of granite clasts derived from the

Cordillera Blanca batholith in the footwall and a change in sediment dispersal directions from northwest-directed to west-directed. These results suggest that initial unroofing and exposure of the Cordillera Blanca batholith due to fault slip was delayed until the latter period of basin development. Upsection dip changes within the basin strata and oxygen isotopic compositions of modern waters and lacustrine carbonates from the Lloclla Formation are consistent with syntectonic deposition at high altitude in a basin that experienced intermittent drainage closure. These data also suggest that the Cordillera Blanca normal fault is listric at depth.

Studies of fault propagation suggest that the geometry of sedimentary basin fill is related to fault growth (by fault tip propagation and segment linkage). An extensional basin adjacent to a fault behaving as a single segment will display distinctive sedimentation patterns discernible from those of basins located along segmented faults. Models of basin evolution suggest that the Callejon de Huaylas basin evolved along a large normal fault that behaved as a single segment and propagated in a single direction from north to south.

### **3.2 INTRODUCTION**

Sedimentary basins exposed in the hinterlands of active fold-thrust belts can provide records of denudation in the highest and most complex regions of mountain belts. Basin analysis may help resolve questions on the timing and magnitude of deformation, magmatism, and erosion in these hinterland and orogenic plateau settings [*Marocco et al.*, 1995; *Vandervoort et al.*, 1995; *Horton et al.*, 2002]. Synorogenic strata may record

sedimentary and structural indicators of tectonic activity. For example, compositional changes in sediment can record the erosion and uplift of particular sediment source areas. Progressive unroofing can help identify the timing and rates of deformation and erosion in the source area, basin growth, and relief evolution [Colombo, 1994 and references therein]. In addition, growth strata and progressive unconformities provide clear indicators of syndepositional deformation. Furthermore, understanding the elevation history of mountain belts is fundamental to evaluating models that describe the timing and mechanisms of surface uplift [Garzione *et al.*, 2004]. Oxygen isotope paleoaltimetry and hydrogen isotopic compositions of modern waters can be used to estimate paleoelevation, which, when coupled with detailed sedimentologic observations, can provide further insight into depositional environments and basin evolution.

The goal of this study is to characterize the extensional basin associated with the Cordillera Blanca normal fault by determining the timing of initial basin subsidence which constrains the onset of normal faulting. Analysis of carbonate oxygen isotopic compositions provides insight into the paleoaltitude during basin deposition, resolving the issue whether the basin formed at high elevation or was generated at lower elevation and later uplifted.

The active Cordillera Blanca normal fault and its associated sedimentary basin are distinctive because of their location in the hinterland of an active fold-thrust belt and their orientation perpendicular to the regional E-W to ENE-WSW compression direction. The Cordillera Blanca normal fault is similar in its structural geometry and displacement-length scaling to normal faults in regional extensional settings (e.g., Basin and Range,



Aegean, etc) but is distinguished by its position in a zone of regional shortening. The South Tibetan Detachment (STD) is also parallel to active shortening structures and, like the Cordillera Blanca, exhibits significant displacement (>10 km) and is situated in the hinterland of a major fold-thrust belt [Burchfiel *et al.*, 1992].

The current flat-slab subduction setting in Peru is often considered a modern analogue for the latest Cretaceous-early Tertiary Laramide orogeny in North America. Hallmarks of Laramide deformation (cessation of arc magmatism, westward migration of ignimbrites, and rapid metamorphic core-complex exhumation along low-angle normal faults) were the result of intensified coupling between the upper plate and the flattening subducting slab [Coney and Reynolds, 1977; Dickinson and Snyder, 1978; Coney and Harms, 1984; Bird, 1984, 1988; Miller *et al.*, 1992]. It was proposed that extension on low-angle normal faults only took place in regions where crust was sufficiently overthickened to collapse under its own weight [Coney and Harms, 1984; Coney, 1987; Sonder *et al.*, 1987]. Mechanical models developed by Yin [1989] determined that gravitational collapse alone is insufficient to initiate low-angle normal faults. An additional extensional stress field in the lithosphere is required, induced by asthenospheric flow likely caused by the collapse and/or steepening of the subducting slab [Yin, 1989].

More recent studies of the distribution of Laramide deformation suggest that the Laramide slab was segmented into areas of “normal” subduction and areas of flat subduction, much like the Nazca slab beneath Peru [Saleeby, 2003]. Though Saleeby [2003] asserts that flat-slab subduction was oblique during the Laramide and not in the

Andes, oblique subduction is certainly the case in Peru as the aseismic Nazca Ridge has swept southward along the Peru trench since at ~12 Ma [e.g., *Gutscher et al.*, 1999; *Hampel*, 2002; *Rosenbaum et al.*, 2005]. *Salisbury* [2003] likens the extension observed during late stages of Laramide flat-slab subduction to the deformation observed in the Cordillera Blanca over the flat-slab segment of the Nazca Plate, where the initiation of extension is linked in time to the passage of the flat-slab segment beneath the region [see *Chapter 1*; *Gutscher et al.*, 1999; *McNulty and Farber*, 2002].

### **3.3 TECTONIC SETTING**

#### **3.3.1 Regional strain distribution**

Evidence of extensional faulting in regionally compressional regimes has been documented in high mountain chains around the world (e.g., Himalayas, Alps, North American Cordillera), though in the Himalayas and Alps, extension is currently oriented orogen-perpendicular [e.g., *Burchfiel et al.*, 1992; *Axen et al.*, 1995; *Wawrzyniec et al.*, 2001; *Yin*, 2006]. In South America, most of the Andes are the result of Cenozoic compression due to subduction of the Nazca plate (Fig. 3.1). Although active large-scale extension is not generally observed along the active Andean margin, a zone of high-magnitude extension is concentrated in the Cordillera Blanca region above the modern flat-slab segment of the Nazca plate beneath Peru (Figs. 3.1 and 3.2).

Quaternary fault scarps in the Cordillera Blanca provide evidence of recent normal faulting oriented parallel to the strike of active compressional structures farther east in the fold-thrust belt of the Eastern Cordillera and Subandean zone [*Dalmayrac and*

*Molnar, 1981; Suarez et al., 1983*]. Normal-faulting earthquake focal mechanisms were recorded from the 1946 Ancash earthquake ( $M_s = 7.2$ ), located approximately 100 kilometers northeast of the Cordillera Blanca [*Suaraz et al., 1983; Doser, 1987*]. The conflicting strain distributions have been explained by buoyancy forces arising from the gravitational body force acting on the elevated Cordillera Blanca (on average, 5-6.8 km above sea level) and associated crustal root [*Dalmayrac and Molnar, 1981; Suarez et al., 1983; Deverchere et al., 1989*]. This configuration results in a delicate balance between the compressive forces applied to the eastern flank of the Andes and the gravitational force acting on the highest parts of the orogen.

Alternative models propose that oblique convergence between the Nazca and South American plates has caused oblique slip and tectonic (vertical-axis) rotations in the Western Cordillera as well as sinistral slip and extension along the Cordillera Blanca normal fault [*McNulty et al., 1998; Rousse et al., 2002, 2003*]. Oblique subduction of the aseismic Nazca Ridge has resulted in flat-slab subduction along the Peru margin for the past 10-12 Ma [e.g., *Hampel, 2002; Rosenbaum et al., 2005*], where viscous coupling between the overriding plate and flat-slab segment may have caused extension by a simple shear mechanism [e.g., *McNulty and Farber, 2002*]. Alternatively, a “sag” between two buoyant, subducted, aseismic ridges (the Nazca Ridge and the Inca Plateau) may lie directly beneath the overthickened Cordillera Blanca region [*Gutscher et al., 1999*]. They propose that the subducted ridges are responsible for holding up the overriding Peruvian crust and that the lack of buoyant crust beneath the Cordillera Blanca has accommodated extension [e.g., *Gutscher et al., 1999; Chapter 1*].

### 3.3.2 Cordillera Blanca extensional system

The Cordillera Blanca represents the highest topography and the greatest concentration of surface area above 5 km in Peru (Fig. 3.1). The range is bounded to the west by the 170-km-long Cordillera Blanca normal fault. The normal fault is oriented parallel to the active contractional structures in the fold-thrust belt to the east (Fig. 3.3). The crest of the Cordillera Blanca defines the continental divide in the region, with elevations exceeding 5000 meters and more than 20 peaks above 6000 meters. The WSW-dipping Cordillera Blanca normal fault strikes approximately N30°W, with dips varying along strike from ~40° in the north to ~20° in the south. To the west of the fault lies the narrow (10-15 km wide) Rio Santa valley and upper Miocene-Quaternary strata of the Callejon de Huaylas basin on the down-thrown hanging wall.

The Cordillera Blanca range lies in the footwall and consists of a granodioritic batholith (Fig. 3.4) that intrudes the Upper Jurassic Chicama Formation. The Chicama Formation forms the roof of the steep-sided, flat-roofed batholith. The Cordillera Blanca batholith is 200-km-long by 20-km-wide and plunges to the south [Cobbing *et al.*, 1981]. The batholith is composed of Miocene granite that has a reported U-Pb zircon crystallization age from a single sample of  $8.2 \pm 0.2$  Ma [McNulty *et al.*, 1998]. However, new zircon U-Pb analyses indicate crystallization ages ranging from  $5.3 \pm 0.3$  Ma to  $23.1 \pm 0.4$  Ma with ages clustering between 5 and 8 Ma [Chapter 4]. A mylonite zone with variable thickness (up to 1 km) continues downward from the fault into the footwall batholith [Petford and Atherton, 1992; McNulty and Farber, 2002].

North of Huaraz, the Cordillera Blanca normal fault is well defined for over 80 km with exposures exhibiting up to 2500 m of vertical relief (Figs. 3.4 and 3.5). At the southern tip of the Cordillera Blanca normal fault, ~ 15 km south of Huaraz, the fault breaks down into several smaller segments that define a disrupted zone of “step overs” tens of meters across [Schwartz, 1988]. The presence of fault scarps that cut Pleistocene and Holocene glacial deposits demonstrate continued active faulting along the southern Cordillera Blanca fault zone (Fig. 3.4).

The Callejon de Huaylas basin lies on the hanging wall of the Cordillera Blanca normal fault. Previous studies have suggested that accumulation was coeval with extension during the Pliocene [Bonnot, 1984; Bonnot *et al.*, 1988]. Motion along the fault has been interpreted as principally extensional with a left-lateral strike-slip component [Bonnot *et al.*, 1988; Sebrier *et al.*, 1988; Petford and Atherton, 1992; McNulty *et al.*, 1998]. The Callejon de Huaylas basin has been interpreted as both a supradetachment basin [McNulty and Farber, 2002] and a “strike slip rift valley” [Atherton and Petford, 1993]. Preserved in the southern part of the basin are upper Miocene-Pliocene sedimentary strata, referred to as the Lloclla Formation, that presumably record unroofing of the footwall [Bonnot, 1984; Bonnot *et al.*, 1988].

### **3.4 BASIN ANALYSIS OF THE CALLEJON DE HUAYLAS**

#### **3.4.1 Lithologic units**

South of Huaraz, the main units defining the Callejon de Huaylas basin include the upper Miocene-Pliocene Lloclla Formation and Quaternary glacial deposits (Fig. 3.4).

The Lloclla Formation is described in detail in the next section. The youngest Quaternary glacial deposits were deposited during the last glacial maximum, estimated to be ~13,200 years BP [Rodbell, 1992, 1993; Rodbell and Seltzer, 2000]. Cosmogenic radionuclide dating ( $^{10}\text{Be}$  and  $^{26}\text{Al}$ ) of glacial deposits suggest that regional glaciation initiated at ~1.4 Ma in Peru [Smith *et al.*, 2005]. Preserved in the northern part of the basin are the upper Miocene Yungay ignimbrites, which are probably the extrusive products related to emplacement of the Cordillera Blanca batholith (Fig. 3.4). The  $\leq 800\text{-m}$ -thick ignimbrites were draped over topography that included Jurassic and Cretaceous clastic sedimentary strata and the primarily volcanic rocks of the Tertiary Calipuy Formation ( $14.8 \pm 2.4$  Ma to  $52.5 \pm 2.3$  Ma) [Cobbing *et al.*, 1981; Petford and Atherton, 1992]. Cobbing *et al.* [1981] obtained K-Ar ages on biotite from the Yungay ignimbrites ranging from  $6.2 \pm 0.2$  Ma to  $7.6 \pm 0.2$  Ma. New  $^{40}\text{Ar}/^{39}\text{Ar}$  analyses of biotite yielded ages between  $7.5 \pm 0.2$  Ma and  $8.7 \pm 1.5$  Ma (Fig. 3.6).

A schematic cross section drawn through the southern region near Recuay illustrates the broad geometry of the Callejon de Huaylas basin (Fig. 3.7). Bonnot *et al.* [1988] interpreted an angular unconformity between the 14-53 Ma Calipuy Formation and the overlying basin strata. In terms of provenance, the expected sandstone and clast count compositions are dependent on the pre-faulting configuration of lithologic units. For example, if the Jurassic Chicama Formation or Tertiary Calipuy Formation was thin or nonexistent along the southern fault segment, then provenance data will reflect the dominance of the remaining units. One possible unroofing sequence due to faulting would begin with the erosion of the Tertiary Calipuy Formation and Yungay ignimbrites

(if exposed this far south). The Jurassic Chicama Formation would be next to erode, ultimately exposing the granite of the Cordillera Blanca batholith. On the basis of metamorphic mineral assemblages in the Chicama host rocks, the emplacement depth of the batholith is estimated to be >5 km and likely ~10-12 km [*Petford and Atherton, 1992; McNulty and Farber, 2002*]. Assuming a dip angle of 27°, the total amount of upper crustal exhumation is estimated to be ~22-26 km along the Cordillera Blanca normal fault [*Chapter 2*].

Based on this unroofing prediction, the expected upsection trend in sandstone and clast count compositions is as follows: (1) a decrease in Tertiary Calipuy Formation volcanic lithic grains and volcanic clasts; (2) an increase in Jurassic Chicama Formation metamorphic lithic grains and phyllite clasts; (3) an appearance of Cordillera Blanca granite clasts. The effect on sandstone composition from the Cordillera Blanca depends on the degree of granite breakdown into its constituent minerals (i.e., if the granite has not yet been eroded down to sand-sized particles, it will not be reflected in the sandstone compositions) (see Table 3.1 for sandstone compositions).

### **3.4.2 Methods and Data**

The provenance of the Lloclla Formation was determined using sandstone compositional data collected from petrographic analysis (point counts), conglomerate compositional data from clast counts, and sediment dispersal patterns from paleocurrent measurements. Most compositional data were collected from the measured section at Quebrada Lloclla (Fig. 3.8). Petrographic thin sections were cut from primarily medium-

grained sandstone. Each thin section was stained for plagioclase and potassium feldspar. Thirteen samples were counted using a modified Gazzi-Dickinson method of point counting [Ingersoll *et al.*, 1984]. Petrographic parameters (Table 3.1), raw point-count data (Table 3.2), and recalculated detrital modes (Table 3.3) are based on methods described by Ingersoll *et al.* [1984] and Dickinson [1985]. Recalculated detrital modes are plotted on Q-F-L, Qm-P-K, and Lm-Lv-Ls ternary diagrams (Fig. 3.9). The data are divided into four groups based on stratigraphic level where the most striking feature is the predominance of lithic grains as shown by the Q-F-L diagram (Fig. 3.9). The feldspar grains are dominantly plagioclase feldspar, from the Qm-P-K diagram (Fig. 3.9). The Lm-Lv-Ls diagram reveals a moderate upsection trend of increasing volcanic lithic grains (Fig. 3.9). Mean compositions, reported in percentages, are as follows: Q: F: L - 13: 13: 74. Qm: P: K - 51: 44: 5. Lm: Lv: Ls - 28: 66: 6.

Conglomerates are predominantly clast-supported, with some clast imbrication, and contain subangular to subrounded and rounded pebbles to boulders (Fig. 3.10). Clast counts were conducted every 40-50 meters of stratigraphic section. Each of the 13 clast counts identified the lithology of 100-125 individual clasts within a one-meter-square region. Clast types were grouped into the following categories: metapelites of the Jurassic Chicama Formation; volcanic rocks of the Tertiary Calipuy Formation; rhyolite, probably from the Tertiary Calipuy Formation, rather than the poorly consolidated Tertiary Yungay ignimbrites; and granite from the Cordillera Blanca batholith. The lower 900 meters of the stratigraphic section are dominated by clasts of the Tertiary



Calipuy Formation. The granite clasts first appear above the 900 meter level (Figs. 3.8 and 3.11).

Paleocurrent data were collected every ~50 meters of stratigraphic section as lithofacies allowed. Where clast imbrication was present in the conglomerate, an average of 20 clast orientations were measured. Rose diagrams for each site are plotted next to their stratigraphic level. A total of 317 clast measurements are plotted in a cumulative rose diagram that reveals two distinct paleoflow directions (Fig. 3.8). The lower 900 meters exhibit an average paleoflow direction to the northwest (314°). Above the 900 meter level, the average flow direction changes to the west (260°) (Fig. 3.11).

Biotites from the Yungay ignimbrites and basal Lloclla tuff were separated and analyzed using the  $^{40}\text{Ar}/^{39}\text{Ar}$  method. Standard magnetic separation techniques were employed, samples were handpicked for purity, and then packed into Cu foil packets. Five to eight milligrams of biotite from each sample were irradiated with sanidine flux monitors [Fish Canyon Tuff: nominal age 27.8 Ma, *Cebula et al.*, 1986] at the Ford reactor, University of Michigan for 45 hours. Step-heating analyses were carried out at the University of California, Los Angeles in a double-vacuum resistance furnace with a Ta crucible. Isotopic ratios were measured using a VG1200 gas-source automated mass spectrometer. An in-house data reduction program (AGECAL) was used to reduce the raw data. Reported ages are weighted mean ages with errors reported at the  $1\sigma$  level. Weighted mean ages do not include uncertainties in the J-factor or decay constants, but because all samples were analyzed in the same lab with the same flux monitors, it is

appropriate to report weighted mean ages with standard errors [McDougall and Harrison, 1999].

### 3.4.3 Stratigraphy of the Lloclla Formation

The Lloclla Formation was named by Bonnot *et al.* [1988] and encompasses the mainly clastic sedimentary rocks exposed ~15 km south of Huaraz that lie unconformably over the Eocene to middle Miocene Calipuy Formation (Fig. 3.4) and are overlain in angular unconformity by subhorizontal Quaternary glacial deposits tens to hundreds of meters thick [Bonnot *et al.*, 1988]. The formation is exposed in Quebrada Lloclla and Quebrada Telar Huain with a total thickness of ~1100 meters (Fig. 3.8). Exposure exists only in deeply-incised ravines making bed-to-bed correlation difficult within this coarse clastic unit. The basal tuff exposed at Quebrada Lloclla was not found in three other ravines (Quebrada Pariac, Quebrada Telar Huain, and Quebrada Pocra) mentioned by Bonnot [1984].

The Lloclla Formation can be divided into two members with only the lower member exposed in Quebrada Telar Huain (Fig. 3.8) [Bonnot, 1984]. The lower member is defined by the lower ~475 meters of section and is dominated by fine-grained sandstone and siltstone in thin-bedded intervals, with interbedded freshwater carbonates in 0.5-1 m thick beds (Fig. 3.8). There are a few clast-supported conglomerates present in 0.1-0.3 m thick beds within the lower member. Within the lower member are a few syn-depositional normal faults with small (< 1 m) displacement. Lithofacies of the lower member are dominated by medium to fine-grained sandstone with horizontal stratification

and normal grading (Sh, Sn) alternating with massive, thinly-bedded siltstone with occasional horizontal laminations (Fm, Fl) (Table 3.4). Horizontally stratified and normally graded sandstone (Sh, Sn) are interpreted to represent a fluvial channel in a mid-fan environment. Massive and horizontally stratified siltstone (Fm, Fl) reflect their deposition in a low-energy, lacustrine setting, which may have been a distal fan delta. The lower member displays lateral interfingering between sheet-flood facies and fluvial channel flow, interpreted as a mid-fan environment. The bottom 200 meters of the section are dominated by fine-grained sandstone and siltstone with horizontal laminations, interbedded with thin lacustrine carbonates. The lower member is interpreted as a distal fan delta – lacustrine environment.

At the base of the Quebrada Lloclla section is a ~7-8 m thick, dark gray volcanic tuff that dips ~25°E toward the Cordillera Blanca normal fault (Figs. 3.8 and 3.12). The basal tuff is identified as a separate lithofacies since it only appears once at the bottom of the section. It is comprised of an ashfall tuff with horizontal laminations (Fh) (Table 3.4). *Bonnot* [1984] reported a biotite K-Ar age of 4.6 Ma. New  $^{40}\text{Ar}/^{39}\text{Ar}$  analyses of biotite yield a weighted mean age of  $5.4 \pm 0.1$  Ma from a well-defined plateau age spectrum (Fig. 3.12). Flat age spectra indicate little or no thermal disturbance since crystallization [*McDougall and Harrison*, 1999]. This new data dates the initiation of basin subsidence at 5.4 Ma, which in turn constrains the timing of initiation of normal faulting.

The Upper Member is 625 m thick and is defined by very thick, clast-supported beds of imbricated conglomerate that are predominately massive with a few erosional

surfaces (Fig. 3.8). There is an observed coarsening-upward sequence within the Upper Member as well as over the entire ~1100 m of well-exposed section in Quebrada Lloclla. Mean clast size within the Upper Member ranges from 6 cm at the 500 m level to 14 cm at the top of the section (Fig. 3.13). Lithofacies of the Upper Member include (1) clast-supported, pebble-boulder conglomerates with clast imbrication (Gci) (Fig. 3.10); (2) massive, non-imbricated, poorly-sorted conglomerates with occasional erosional scours (Gcm); (3) sandy, well-sorted, pebble conglomerate with horizontal stratification (Gh); (4) sandy, pebble conglomerate with low-angle stratification, sandstone lenses, and basal scours (Glas); and (5) massive medium-coarse grained sandstone with occasional normal grading (Sm) (Table 3.4). The two uppermost lithofacies (Gcm, Gci) are interpreted as fluvial gravel bar deposits in a subaerial environment in a proximal alluvial fan setting. The smaller-grain-sized conglomerates (Gh, Glas) and medium to coarse-grained sandstone (Sm) represent fluvial channel flow deposits, also in a proximal alluvial fan setting. The Upper Member is composed of a boulder conglomerate deposited in a braided stream at the head of an alluvial fan while the sandy conglomerate and conglomeratic sandstone downsection represent sheet-flood facies further from their source [Blair and McPherson, 1994]. The Upper Member is interpreted as a mid-fan to proximal alluvial fan environment. The upsection trend is from a lacustrine/distal fan delta environment to a sheet-flood-dominated alluvial fan. The very top of the exposed Upper Member in Quebrada Lloclla is covered unconformably by sub-horizontal Quaternary glacial deposits.

The Lloclla Formation sits on the east-tilted hanging wall block of the Cordillera Blanca normal fault and strata in the section dip gently east. Dips plotted at their stratigraphic location reveal four distinct groups (Fig. 3.13). In the lower member, dips range between 25° and 15°NE from 0 to 250 m (Fig. 3.13). At 250 m, the dips shallow abruptly to 10° and range from 5° to 10° up to the 475 m level, which marks the base of the Upper Member (Fig. 3.13). Between 475 and 725 m, dips range from ~7° to 15°. Above 725 m, bedding is not well-defined in the thick, massive conglomerate of the Upper Member, but there does appear to be a steepening of dips from ~15° to 30° (Fig. 3.13).

#### **3.4.4 Stable isotopic studies of the Lloclla Formation**

##### **3.4.4.1 Carbonate oxygen isotope paleoaltimetry**

One question that needs consideration is whether the Lloclla Formation was deposited at elevations similar to its current altitude or if it was deposited at lower elevations and then uplifted. It is necessary to constrain the approximate paleoelevation when faulting initiated in order to evaluate different models of surface uplift in the Cordillera Blanca [e.g., *Chapter 2*]. Carbonate oxygen isotope paleoaltimetry is based on analysis of the  $\delta^{18}\text{O}$  value of carbonate precipitated from surface waters. The  $\delta^{18}\text{O}$  value of meteoric water varies systematically with elevation, providing a means to reconstruct paleoelevation if the  $\delta^{18}\text{O}$  values of paleowater are known [Garzione *et al.*, 2000b, 2004]. Previous studies [Drummond *et al.*, 1993; Garzione *et al.*, 2000a] demonstrated that oxygen isotopes of lacustrine and paleosol carbonates can be used as a gauge of

paleoelevation because they are largely determined by the  $\delta^{18}\text{O}$  value of meteoric water ( $\delta^{18}\text{O}_{\text{mw}}$ ), which is strongly dependent on altitude. As a vapor mass rises in elevation, it expands and cools, causing rainout of heavier isotopes, thus producing lower  $\delta^{18}\text{O}_{\text{mw}}$  values at progressively higher altitudes. Therefore, carbonates that precipitated from waters originating at higher altitudes will yield more negative  $\delta^{18}\text{O}$  values. It is possible to estimate paleoelevation from the oxygen isotope composition of carbonates by using a locally determined  $\delta^{18}\text{O}$  vs. altitude gradient and making reasonable assumptions about the past climate from available paleoclimate indicators [Garzione *et al.*, 2004].

The modern  $\delta^{18}\text{O}$  vs. altitude gradient can be used to reconstruct paleoelevation during carbonate precipitation but several factors can influence the  $\delta^{18}\text{O}$  values of carbonate:  $\delta^{18}\text{O}_{\text{mw}}$  values; evaporation; diagenetic effects; temperature of calcite precipitation, and average annual temperature [Garzione *et al.*, 2004]. It is also necessary to collect modern water samples from a large range of elevations in order to assess higher elevation rainfall upstream of the sampling location. In this study, water samples were collected in July, 2005 from the < 2-m-wide by <30 cm-deep stream in Quebrada Lloclla and analyzed for  $\delta^{18}\text{O}$  values (Fig. 3.14A). The samples were collected from the mouth of the stream (confluence with the Rio Santa) to the source of the stream, covering ~650 m in elevation. Although this data set provides a good constraint on modern surface water compositions at these elevations, it may be too limited in elevation to determine a local  $\delta^{18}\text{O}$  vs. altitude gradient. The data also fit the observation that  $\delta^{18}\text{O}$  values become more negative with increasing elevation [Garzione *et al.*, 2000a].

Lacustrine carbonate isotopic compositions commonly reveal a linear relationship between carbon and oxygen isotopes [Talbot, 1990]. Hence, isotopic covariance (i.e., the more linear the relationship, the higher the covariance) of carbon and oxygen can be a characteristic feature of particular lacustrine settings. However, several factors, including diagenesis, mixing, and temperature variations, can all skew values of oxygen and carbon isotopic compositions. If such caveats can be ruled out, the degree of covariance between carbon and oxygen isotopes can be informative.

Covariance in primary lacustrine carbonates has been attributed to closed basin conditions, though diagenetic alteration can skew  $\delta^{18}\text{O}$  and  $\delta^{13}\text{C}$  values. More positive values of  $\delta^{18}\text{O}$  in lacustrine carbonates are likely associated with basin closure and an increase in the degree of evaporation [Drummond *et al.*, 1995; Garzione *et al.*, 2004]. Generally, if the correlation coefficient ( $R^2$ ) for covariance between  $\delta^{13}\text{C}$  and  $\delta^{18}\text{O}$  is  $> 0.8$ , the carbonates were precipitated from a lake in a basin that experienced long periods of internal drainage. Moderately high covariance coefficients ( $R^2 \sim 0.6\text{--}0.7$ ) suggest periods of extended residence times in lakes that existed in basins that were closed periodically [Talbot, 1990]. It is necessary to use caution when interpreting covariance in terms of internally versus externally drained basins, but if used with other geologic evidence it can provide useful information.

Eight lacustrine carbonates were sampled from the measured section of the Lloclla Formation in Quebrada Lloclla (Fig. 3.8) and measured for  $\delta^{13}\text{C}$  and  $\delta^{18}\text{O}$  values (Fig. 3.14B). Sample numbers correspond to stratigraphic meter level. The sample (LL263) yielding the most negative  $\delta^{18}\text{O}$  value in the data set is considered an example of

diagenetic alteration, because two carbonates stratigraphically < 2 m below this sample (LL261 and LL262) yield the most positive  $\delta^{18}\text{O}$  values in the section. There is a relatively high degree of covariance ( $R^2 = 0.61$ ) between  $\delta^{13}\text{C}$  and  $\delta^{18}\text{O}$ , consistent with a lacustrine setting with intermittent basin closure, which suggests high rates of evaporation at higher elevations. There is a moderate upsection trend toward more negative values of  $\delta^{18}\text{O}$  consistent with, but not requiring, increased elevation in the source area. A shift in climate (i.e., temperature, aridity) could also produce this trend. However, the carbonates of the Lloclla Formation predate recent glaciation [ $\sim 1.4$  Ma, *Smith et al.*, 2005] by  $\sim 1$ -3 million years. Therefore, the presence of 3-5 Ma carbonates with  $\delta^{18}\text{O}$  values that are significantly more negative than modern waters (Fig. 3.14A,B) are a strong indicator of that the deposition of the Lloclla Formation occurred at elevations similar to, or higher, than its current elevation.

This is significant because different models of extension in the Cordillera Blanca require different starting elevations. For example, the *McNulty and Farber* [2002] model asserts that buoyant “lift” from the subducted Nazca Ridge pushed up on the crust beneath the Cordillera Blanca, resulting in extension. In contrast, the model by *Gutscher et al.* [1999] and reconstructions by *Hampel* [2002] and *Rosenbaum et al.* [2005] suggest that extension is the result of gravitational collapse of overthickened crust. These new carbonate data support the latter interpretations that the Cordillera Blanca was already at high elevation when normal faulting commenced.



#### 3.4.4.2 Hydrogen isotopic composition of surface water

Hydrogen and oxygen isotopes of water are widely used as tracers of hydrological processes involving precipitation and groundwater-surface water interactions [e.g., *Gibson et al.*, 2005 and references therein]. The  $\delta D$  (deuterium) and  $\delta^{18}O$  composition of global precipitation has been shown to vary in a systematic fashion called the global meteoric water line (GMWL) [*Gammons et al.*, 2006 and references therein]. It is recognized that the relationship between  $\delta D$  and  $\delta^{18}O$  values of precipitation can vary regionally, necessitating the measurement of a local meteoric water line (LMWL) for comparison. The slope of the LMWL can vary from that of the GMWL due to arid to semi-arid climates, seasonal temperature variations, and low humidity [*Gibson et al.*, 2005; *Gammons et al.*, 2006]. The slope of the LMWL for Quebrada Lloclla water is considerably lower than the GMWL (Fig. 3.14C), suggesting significant evaporation has affected these waters. This is consistent with the  $\delta^{18}O$  and  $\delta^{13}C$  values of late Miocene-Pliocene carbonates from Quebrada Lloclla.

### 3.5 DISCUSSION OF BASIN EVOLUTION

Paleocurrents can be interpreted in terms of paleogeography, sediment-dispersal systems, and deposition on alluvial fans [*Dorsey and Martin-Barajas*, 1999]. Clast counts and sandstone point counts provide detailed information about the sediment source. Changes in strata dip are related to fault motion.  $^{40}Ar/^{39}Ar$  cooling ages from the basal tuff can provide constraints on the initiation of footwall exhumation. Oxygen

isotopic compositions of modern waters and lacustrine carbonates can provide information on paleoaltitude and paleoclimatic conditions during basin deposition.

The Lloclla Formation displays a marked change around the 900 m level (Figs. 3.8 and 3.11). Below the 900 m level, clast counts are dominated by the metasedimentary Jurassic Chicama Formation and the volcanic Tertiary Calipuy Formation, which most likely includes the rhyolite clasts that were counted separately (Fig. 3.11). Paleocurrents from the lower ~900 m record a consistent transport direction toward the northwest. All sandstone compositions come from locations below the 900 m level (Fig. 3.8). The sandstone provenance is dominated by Lv, Lm, L, and Qm, which suggests that the Tertiary Calipuy and Jurassic Chicama Formations are the dominant source, similar to the clast counts. The upsection trend in Tertiary volcanics (Lv) (Fig. 3.9) is not predicted by the simple unroofing model proposed earlier. However, the individual clast counts also do not show the expected systematic upsection decrease in Tertiary Calipuy Formation and increase in Jurassic Chicama Formation (Fig. 3.8). One explanation is that the Tertiary Calipuy and Jurassic Chicama Formations were equally important sediment sources below the 900 m level. While normal faulting had already initiated by 5.4 Ma and unroofing of the Cordillera Blanca batholith was ongoing, paleocurrents from below the 900 m level reveal that the sediment source was to the southeast, a region dominated by the Tertiary Calipuy and Jurassic Chicama Formations (Fig. 3.3).

Above 900 m, several changes occur (Figs. 3.8 and 3.11). Clast count compositions now show the predicted unroofing pattern: a decrease in Tertiary Calipuy

clasts and an increase in Jurassic Chicama clasts. The appearance of Cordillera Blanca granite clasts is recorded for the first time above 900 m, indicating that the batholith is now exposed at the surface in this region (Fig. 3.11). This means that the Cordillera Blanca batholith was never a dominant sediment source during basin evolution which is in stark contrast to the present-day setting where modern drainages are dominated by clasts from the primarily granite footwall.

Geomorphic analysis of fault relief and footwall drainage networks reveal a strong N-S asymmetry along the Cordillera Blanca normal fault [*Chapter 2*]. The hypothesis that the Cordillera Blanca normal fault has propagated southward implies that the batholith was exposed in the footwall along the northern fault segment first and only later exhumed along the southern region. If this is the case, it is expected that paleocurrents would not record an eastern source direction until later in basin evolution. Above the 900 m level, paleocurrents record a dramatic change in paleoflow direction, implying that the dominant source region now lay due east of the basin, rather than southeast (Fig. 3.11). The coincidence of this direction shift and the appearance of granite clasts strongly argue for the N-S propagation of the Cordillera Blanca normal fault and asymmetrical exhumation of the footwall batholith.

Dip measurements record three locations where the dip changes during deposition of the Lloclla Formation (Fig. 3.13). Initial dips of 15°-25° are abruptly overlain by shallow dips (5°-10°) between 250-490 m, and then gradually transition to steeper dips (~15°-30°) above 725 m. The shallowing of dips at the 250 m level are consistent with syntectonic deposition (“growth strata”) along a listric normal fault and are expected

within the Lloclla Formation since faulting is known to have been ongoing since deposition of the basal tuff at 5.4 Ma. More puzzling is the observed *steepening* of dips above the 490 m level (Fig. 3.13).

While the Cordillera Blanca normal fault is listric in its overall shape, it is not required to be a smooth curve as it shallows at depth. Instead, the footwall may have a ramp-flat geometry with hanging wall strata that exhibit alternating steep and shallow dips [Gibbs, 1984]. This is a possible explanation for the steep-shallow-steep pattern of dips observed in the Lloclla Formation (Fig. 3.15). Although a growth stratal relationship (in which deposition was synchronous with normal fault slip and hanging-wall tilting) is favored for the lower transition from steep to shallow dip at 250 m (Fig. 3.13), the upper transition to steeper dip above 490 m (Fig. 3.13) may be better explained by hanging-wall rollover related to a ramp-flat relationship (Fig. 3.15).

### 3.6 MODELS OF EXTENSIONAL BASIN EVOLUTION

Extensional basins and their bounding fault systems tend to be segmented [e.g. *Gawthorpe and Hurst, 1993*] and basin evolution involves fault-tip propagation and linkage of smaller subbasins. It has been demonstrated that large normal faults display certain features as they grow over time: displacement is usually greatest at the center and decreases toward the fault tips; faults grow in length as displacement increases; and faults are segmented at a variety of scales [*Dawers et al., 1993; Dawers and Anders, 1995*]. Recent models of extensional basin evolution apply research on normal fault displacement geometry, fault segmentation, and fault growth to explore the stratigraphic

effects on the growth of basins in length, width, and depth through time [*Schlische and Anders, 1996*]. Their models are based entirely on the geometric evolution of faults and the associated basins and ignore isostatic effects of sediment loading, erosion of the footwall blocks, sediment compaction, and climatic influences. However, many workers conclude that the geometry of extensional basins are good indicators for the long-term evolution of a normal fault system.

### **3.6.1 Single-segment fault with one basin (Model 1)**

In this model, the normal fault is assumed to act as a single segment with one tip pinned and the other free to propagate. As fault length increases, the basin increases in length, width, and depth. Displacement is greatest near the pinned fault tip and decreases in the direction of propagation. This causes a broadly synclinal basin geometry in longitudinal section [*Schlische and Anders, 1996*]. As the fault grows, the thickness and geometry of synextensional strata are affected. Assuming that sedimentation keeps pace with subsidence, the model predicts that sediments will be thickest adjacent to the fault and near the fault center. The depocenter of the basin migrates in the same direction as the propagating fault tip, resulting in a characteristic signature in the stratigraphic record. The position of the depocenter through time will be offset from the region of original deposition in the basin [*Schlische and Anders, 1996*]. Younger sediments will be deposited over a larger surface area than older sediments. Due to the migration of the depocenter, younger strata onlap onto older strata on the “trailing end” of the migrating depocenter. Longitudinal cross-sections may show pinch-outs of units along-strike such

that the oldest units may be exposed at the surface near the origination of slip but will be buried by younger sediments as the depocenter migrates with the propagating fault tip.

The map pattern of the Callejon de Huaylas basin fill is elongate along strike and dominated by the Yungay ignimbrites north of Huaraz and by Quaternary glacial deposits to the south (Fig. 3.16). The Lloclla Formation is exposed only in a couple narrow ravines and is otherwise buried by the Quaternary glacial deposits. The basin is bounded to the east by the Cordillera Blanca normal fault, which is continuous for much of its 170 km length, except for the southernmost region. If we assume that the Cordillera Blanca normal fault acts as single segment and is pinned at its northwestern tip, the evolution of the Callejon de Huaylas may follow a pattern similar to the model of *Schlische and Anders* [1996]. Southeastward fault propagation would cause the depocenter to shift to the southeast, leaving the older Yungay ignimbrites exposed in the north and burying the Lloclla Formation beneath the Quaternary glacial deposits farther south. Longitudinal sections show the predicted onlap of younger sediments onto older strata at the “trailing edge” of the migrating depocenter (Fig. 3.17). Ages are constrained by  $^{40}\text{Ar}/^{39}\text{Ar}$  biotite ages from the Yungay ignimbrites and the basal tuff of the Lloclla Formation. The Lloclla Formation is shown as completely buried by the Quaternary glacial deposits; alternatively, it may have overlain the Yungay ignimbrites to the north of Huaraz but has since been eroded.

### 3.6.2 Two-segment fault with two basins (Model 2)

The single-segment fault model may be an oversimplification. Many normal fault systems in the Basin and Range consist of multiple fault segments [e.g. *Wu and Bruhn*, 1994; *Densmore et al.*, 2004]. In the case where the fault segments do not overlap in map view, each segment is associated with its own isolated sedimentary basin (each resembling a simple basin bounded by a single fault). In this model, the oldest units are restricted to each subbasin and thicken toward their own basin center. Each fault is assumed to propagate in both directions. As displacement on the fault segments increase, the fault tips propagate toward one another. Once the fault tips merge, new units are deposited basin-wide but thin toward the region of the fault tip merger (known as an intrabasin high). As displacement increases, the fault now propagates as a single segment and the strata begin to thicken in the center of the basin [*Schlische and Anders*, 1996].

If this were the case in the Cordillera Blanca, the fault would be divided into two segments at the salient just north of Huaraz where the Callejon de Huaylas is at its most narrow (Fig. 3.17). The two fault segments would be free to propagate in both directions. The model predicts that the two basins would fill independently until the fault segments join, allowing the youngest unit to fill both basins with a thin cover over the intrabasin high (Fig. 3.17). Alternatively, the two fault segments could have tips that migrate away from each other and not merge at the salient north of Huaraz. This would have the same sedimentation pattern as Model 2.

While both of models are viable for the Callejon de Huaylas, the single-segment fault model (Model 1) is considered more likely. As noted in Chapter 2, the Cordillera

Blanca normal fault exhibits morphometric features that suggest it currently moves as a single segment. Furthermore, it displays a pronounced asymmetry in its displacement profile, suggesting that its northwestern tip has been effectively pinned and displacement has propagated to the southeast, bringing the Cordillera Blanca batholith to the surface [see *Chapter 2*]. Neither model adequately explains why only the Yungay ignimbrites are preserved north of Huaraz. Was the Lloclla Formation deposited there and eroded away or was it not deposited at all? Chapter 2 noted that the much steeper longitudinal profiles from northern streams implied a higher stream power and greater erosional capacity, which prevented significant sediment accumulation in the north. Model 2 would require similar stream profiles for both segments instead of the steady decrease in gradient southward along strike [*Chapter 2*].

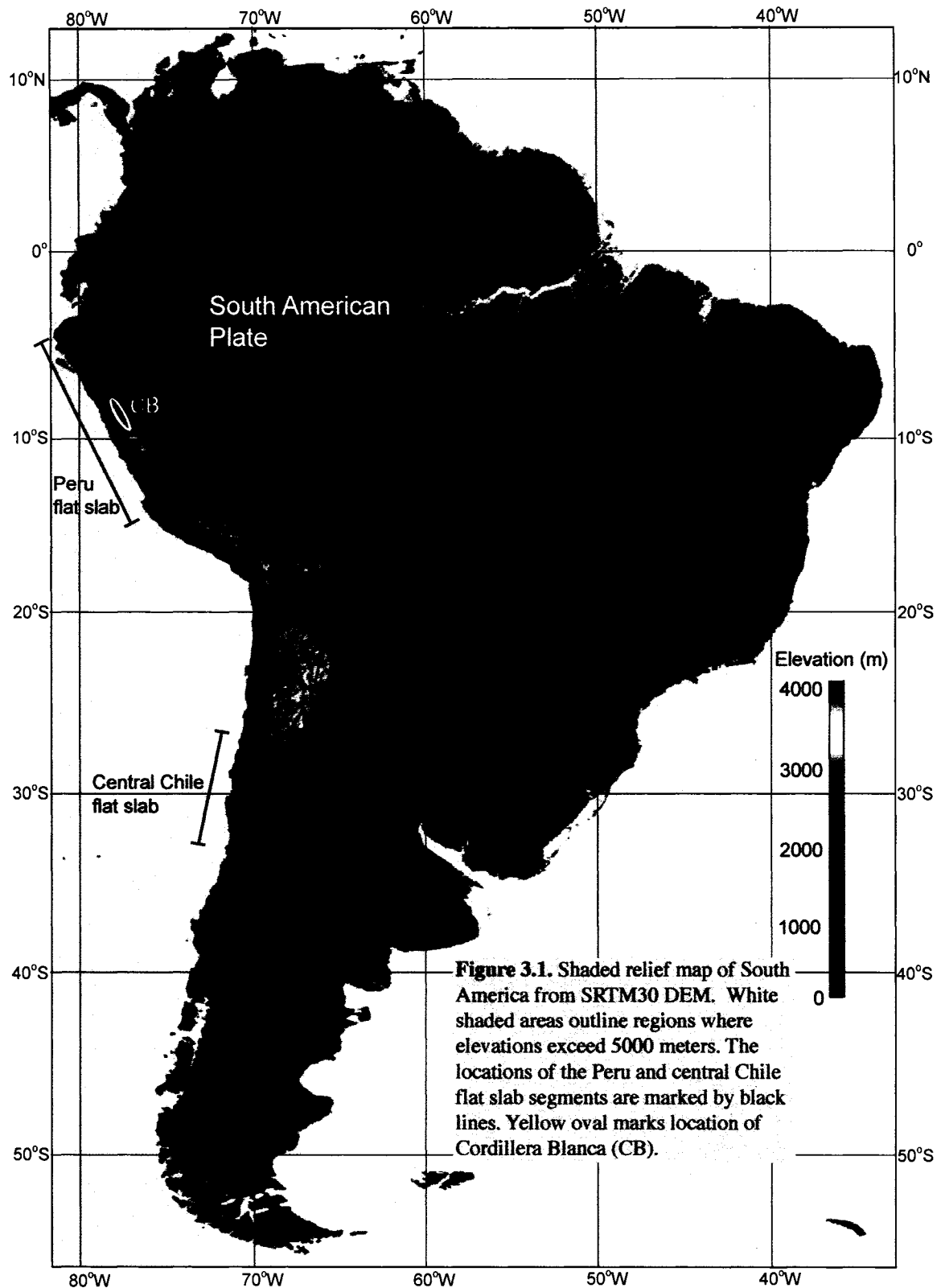
### 3.7 CONCLUSIONS

Basin analysis and  $^{40}\text{Ar}/^{39}\text{Ar}$  analyses of the upper Miocene-Pliocene Lloclla Formation have yielded new constraints on the timing of onset of supradetachment basin evolution along the Cordillera Blanca normal fault. Basin subsidence and thus, initial normal faulting began at  $5.4 \pm 0.1$  Ma. Provenance and paleocurrent data record the first appearance of the Cordillera Blanca batholith in the footwall along the southern fault region. Dip changes within the Lloclla Formation reveal syntectonic sedimentation along the listric Cordillera Blanca normal fault as well as a local (?) ramp-flat geometry of the fault. Carbonate oxygen isotope paleoaltimetry strongly suggests that the Lloclla Formation was deposited at equal or higher elevation than its current altitude, implying a



mechanism for extension along the Cordillera Blanca normal fault that does not involve regional surface uplift [i.e., *McNulty and Farber*, 2002].

The Callejon de Huaylas basin has evolved along a large normal fault that behaves as a single segment and propagates in one direction (Model 1), supporting the asymmetrical geomorphic observations from Chapter 2. The Yungay ignimbrites, though the oldest sediments in the basin, are still exposed in the north because the depocenter of the basin has moved in the direction of southward fault propagation. The younger Lloclla Formation has been deposited since 5.4 Ma and records the passing of the propagating fault tip. The Lloclla Formation was subsequently buried by Quaternary glacial deposits shed from the growing footwall topography.





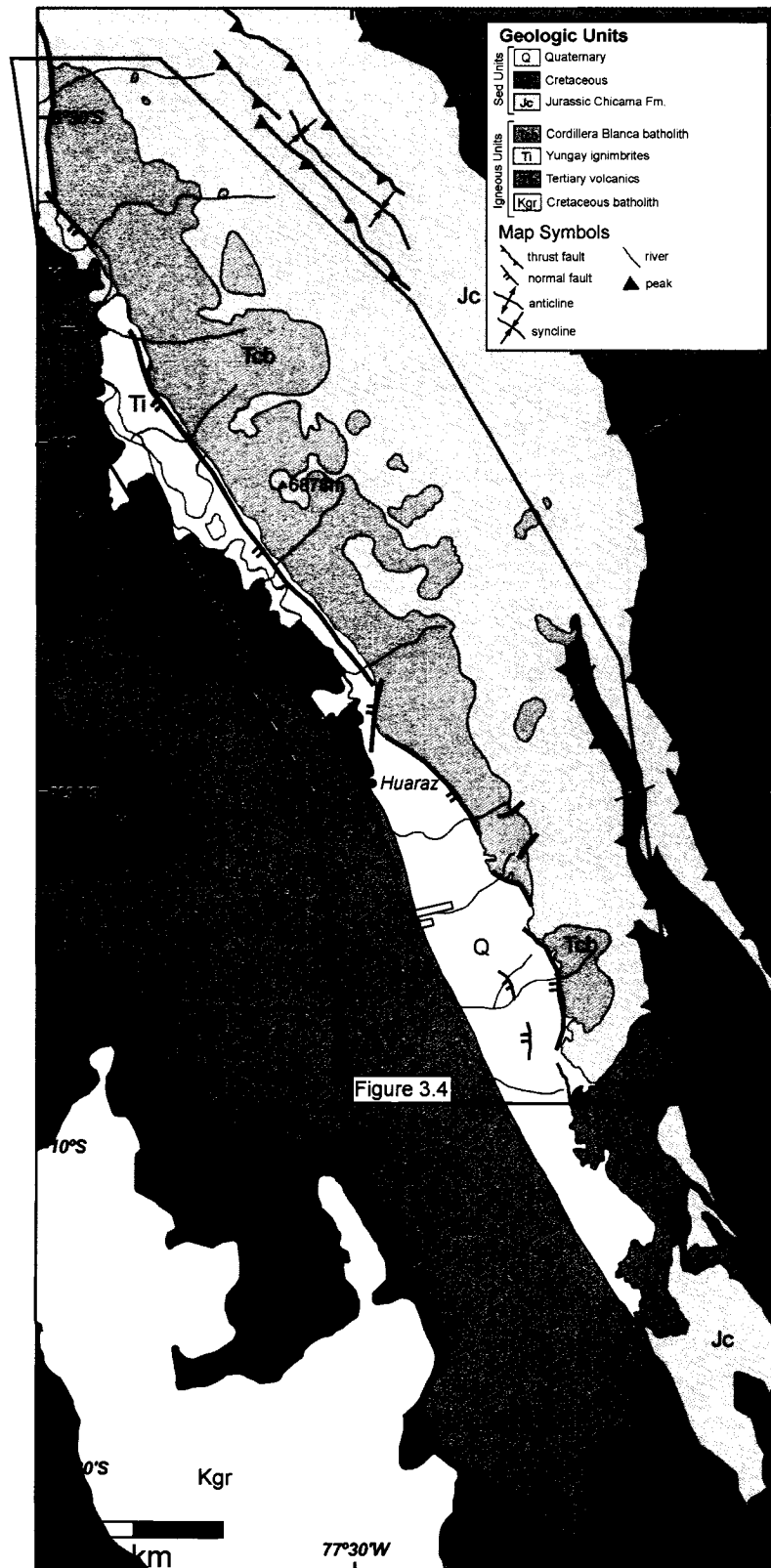


**Figure 3.3** Simplified geologic map of the Cordillera Blanca region (after Cobbing *et al.*, 1981) showing major lithologic units and structures. White rectangles south of Huaraz mark locations of measured sections.

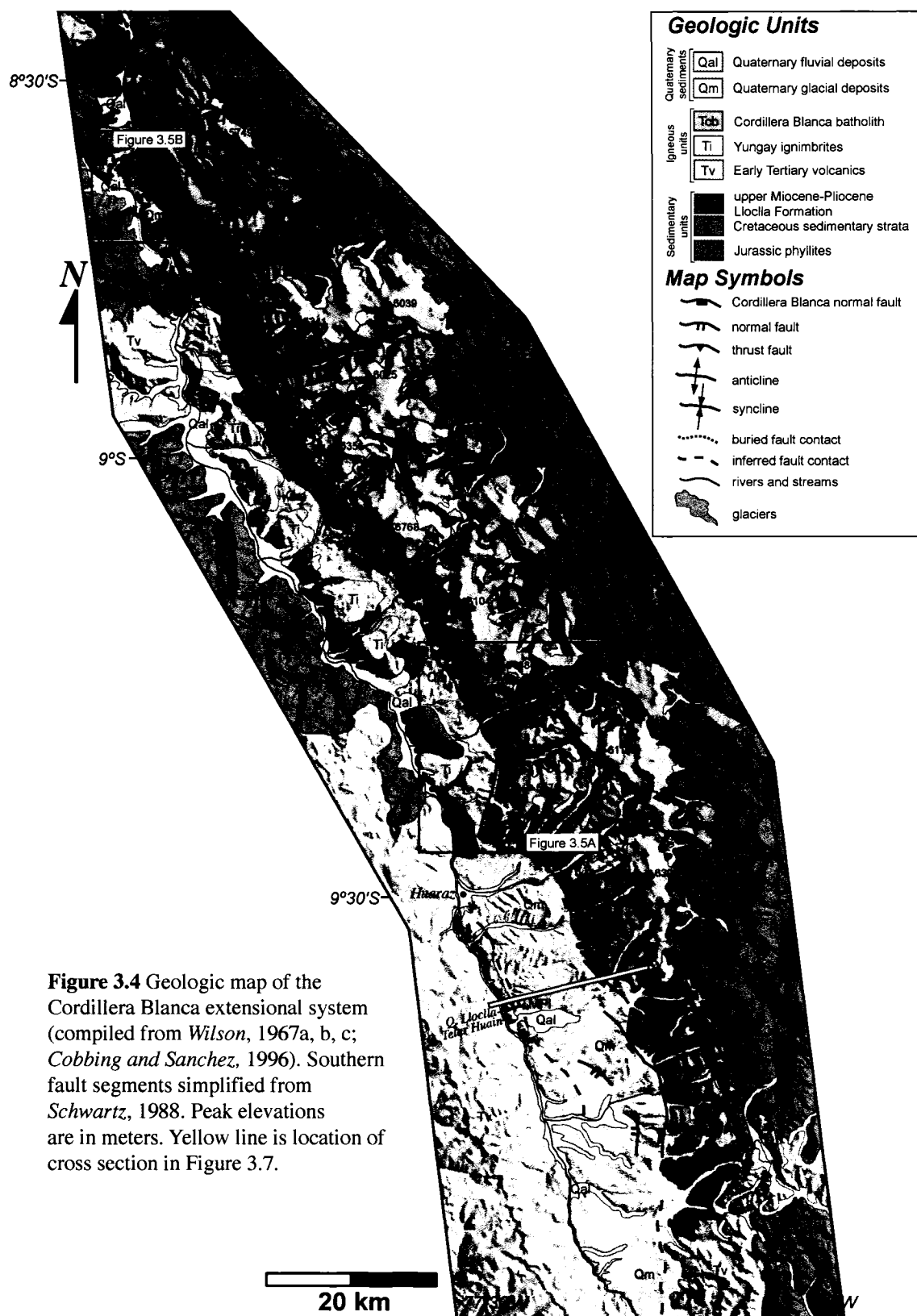




**Figure 3.5A (Above)** View south-southeast along fault scarp. Black dashed line marks the fault in the middle ground. White dashed line marks the fault in the background. Fault dip shallows in the updip (ENE) direction. **(Left)** Star marks location of photo and arrow shows direction of view.



**Figure 3.5B (Above)** View northwest along fault scarp. Houses at lower left for scale. In this region, fault scarp is exposed for > 2km. More than 1.5 km of relief is visible in this photo. **(Left)** Star marks location of photo and arrow shows direction of view.

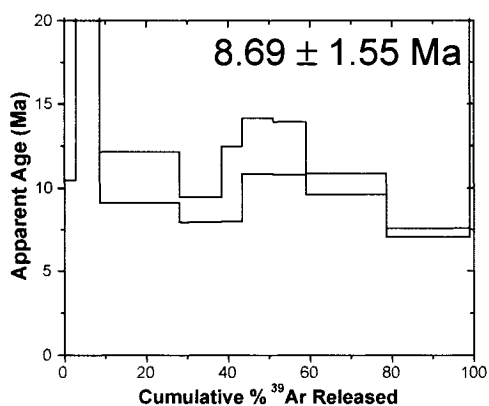
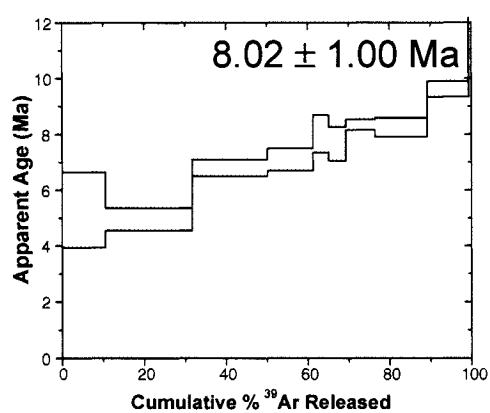
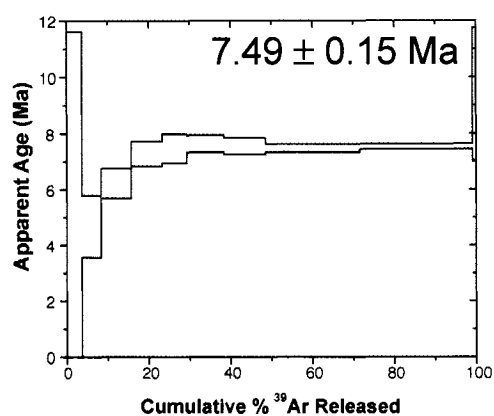


**Figure 3.6.** Biotite  $^{40}\text{Ar}/^{39}\text{Ar}$  age spectra and cooling ages for the Yungay ignimbrites. All ages are weighted mean ages with  $1\sigma$  standard errors. Note change of scale on y-axis.



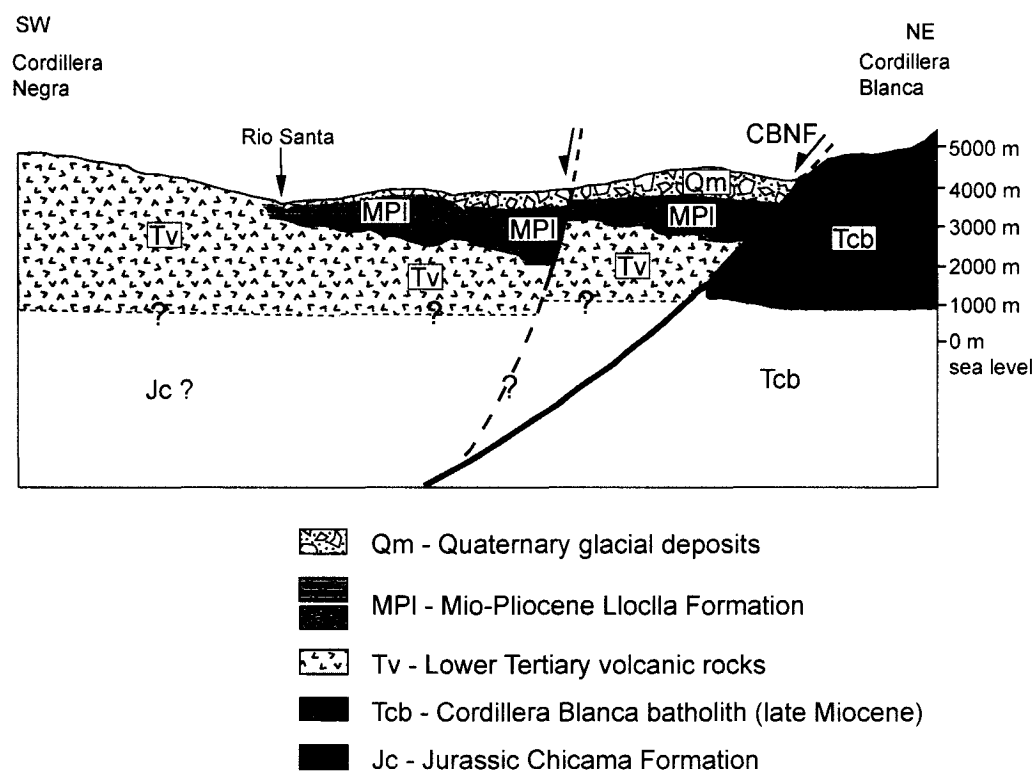


**Figure 3.7.** Schematic cross section through sedimentary basin adjacent to Cordillera Blanca normal fault (CBNF). Black line at base of Lloclla Formation indicates the basal tuff dated at  $5.4 \pm 0.1$  Ma.

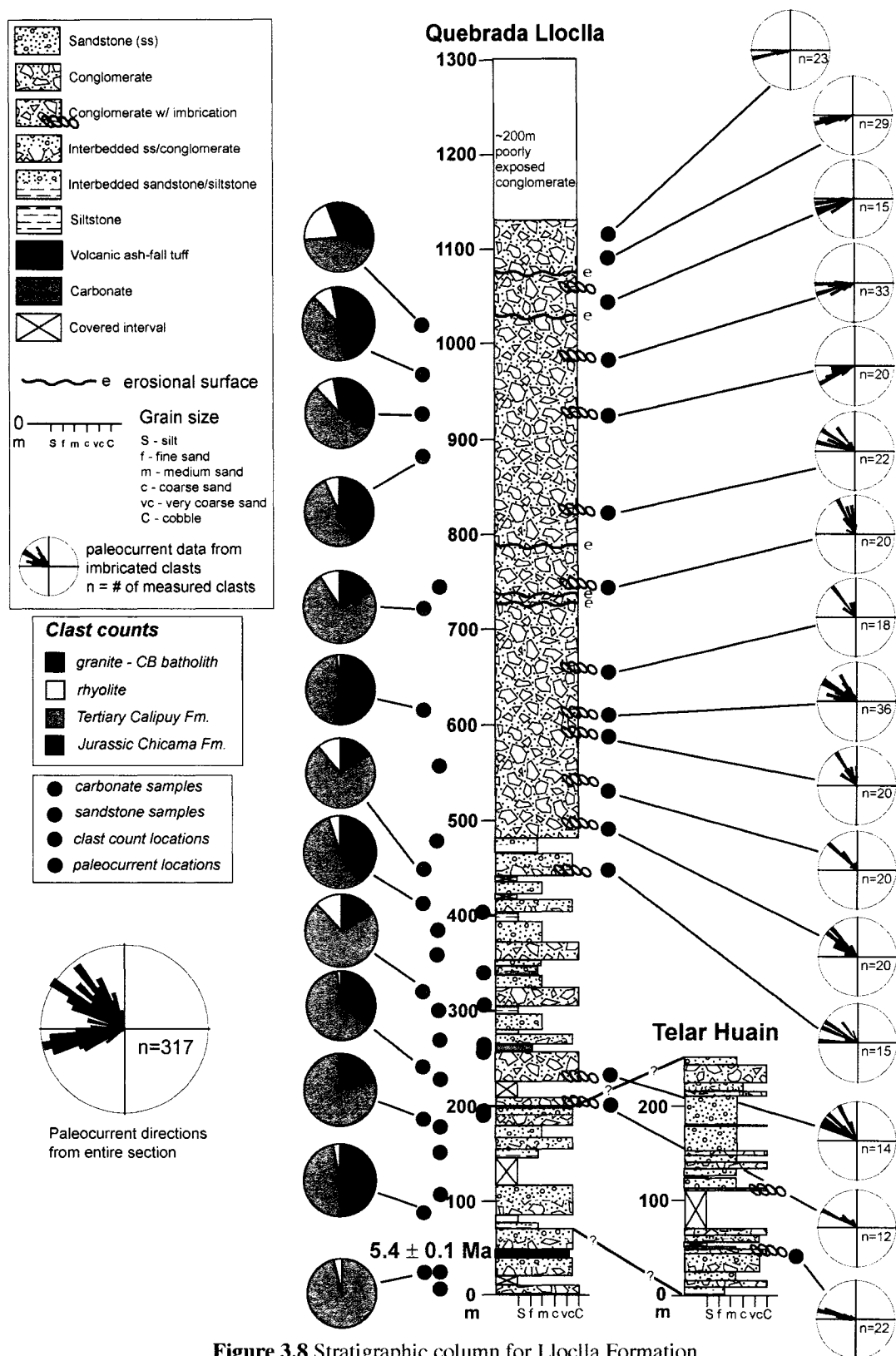


**Figure 3.8** Stratigraphic column for Lloclla Formation.

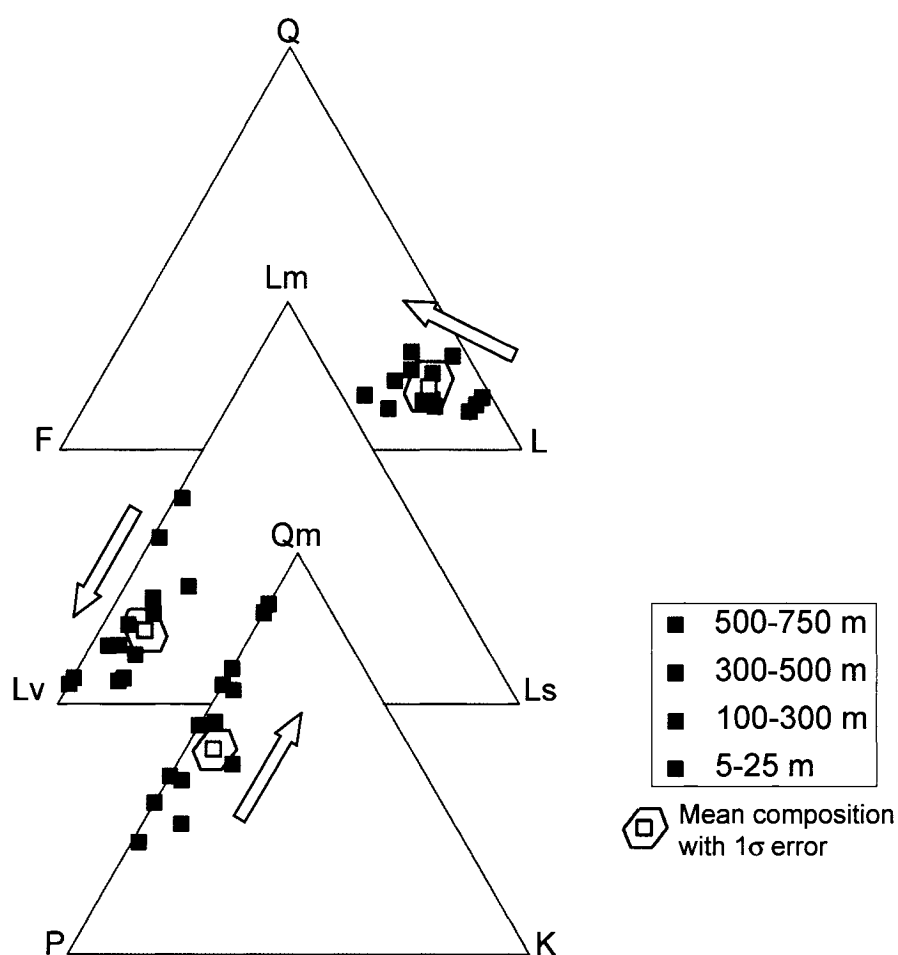


**Figure 3.9** Results from sandstone point counts. Sample groupings correspond to stratigraphic level (see Figure 3.8). Arrows indicate upsection trend of compositions. See text for discussion. Q - total quartz; Qm - monocrystalline quartz; F - total feldspar; P - plagioclase feldspar; K - potassium feldspar; Lm - total metamorphic lithic grains; Lv - total volcanic lithic grains; Ls - total sedimentary lithic grains.

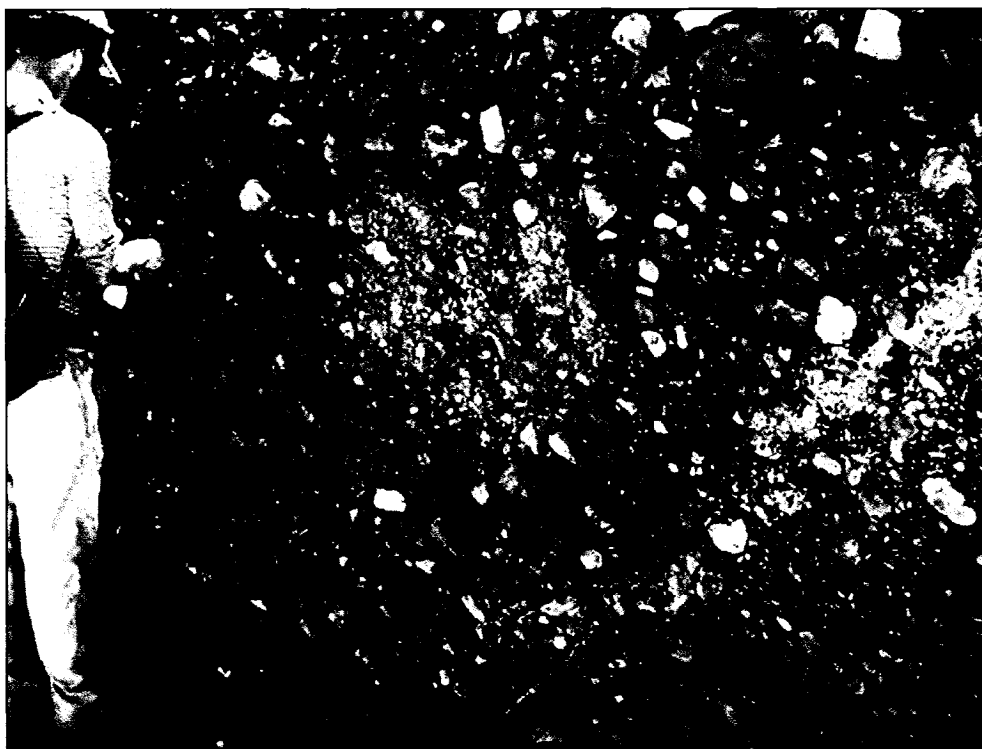
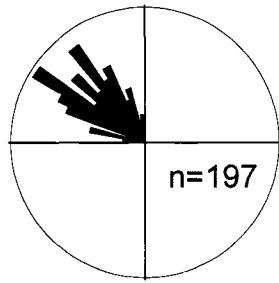
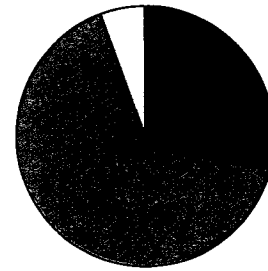


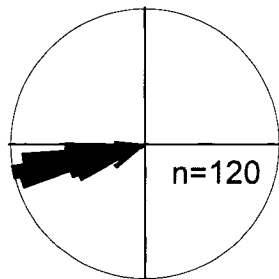
**Figure 3.10.** Upper Member, Lloclla Formation. Massive, clast-supported, cobble-boulder conglomerate with well-defined imbrication. Represents proximal alluvial fan facies that were deposited near sediment source.



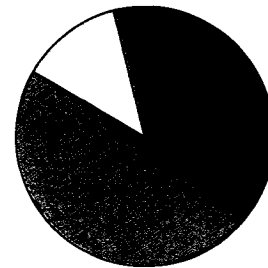
Paleocurrent directions  
below 900 meter level  
Avg =  $314^{\circ}$



Clast count compositions  
below 900 meter level



Paleocurrent directions  
above 900 meter level  
Avg =  $260^{\circ}$

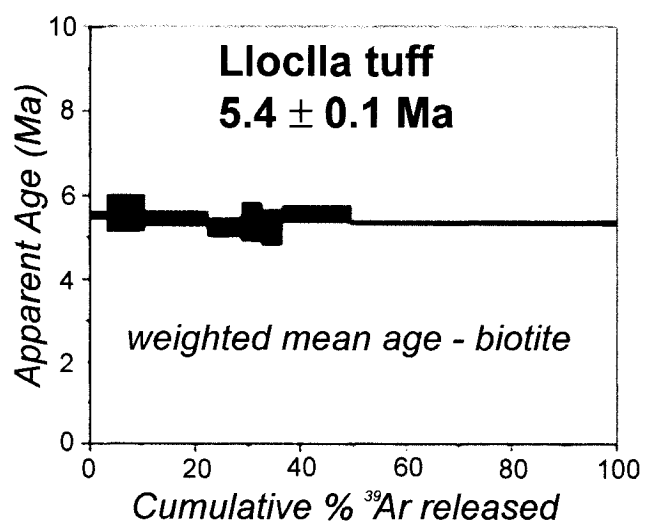


Clast count compositions  
above 900 meter level

**Figure 3.11.** Paleocurrent directions show abrupt change in paleoflow direction from NW to WSW above the 900 m stratigraphic level. Clast count compositions record the appearance of granite clasts from the Cordillera Blanca batholith above 900 m.



**Figure 3.12.** (Above) Basal ash fall tuff, Lloclla Formation. Total thickness ~7-8 m. Beds are dipping east toward the Cordillera Blanca normal fault. (Below) Age spectrum for basal tuff from  $^{40}\text{Ar}/^{39}\text{Ar}$  analysis of biotite.



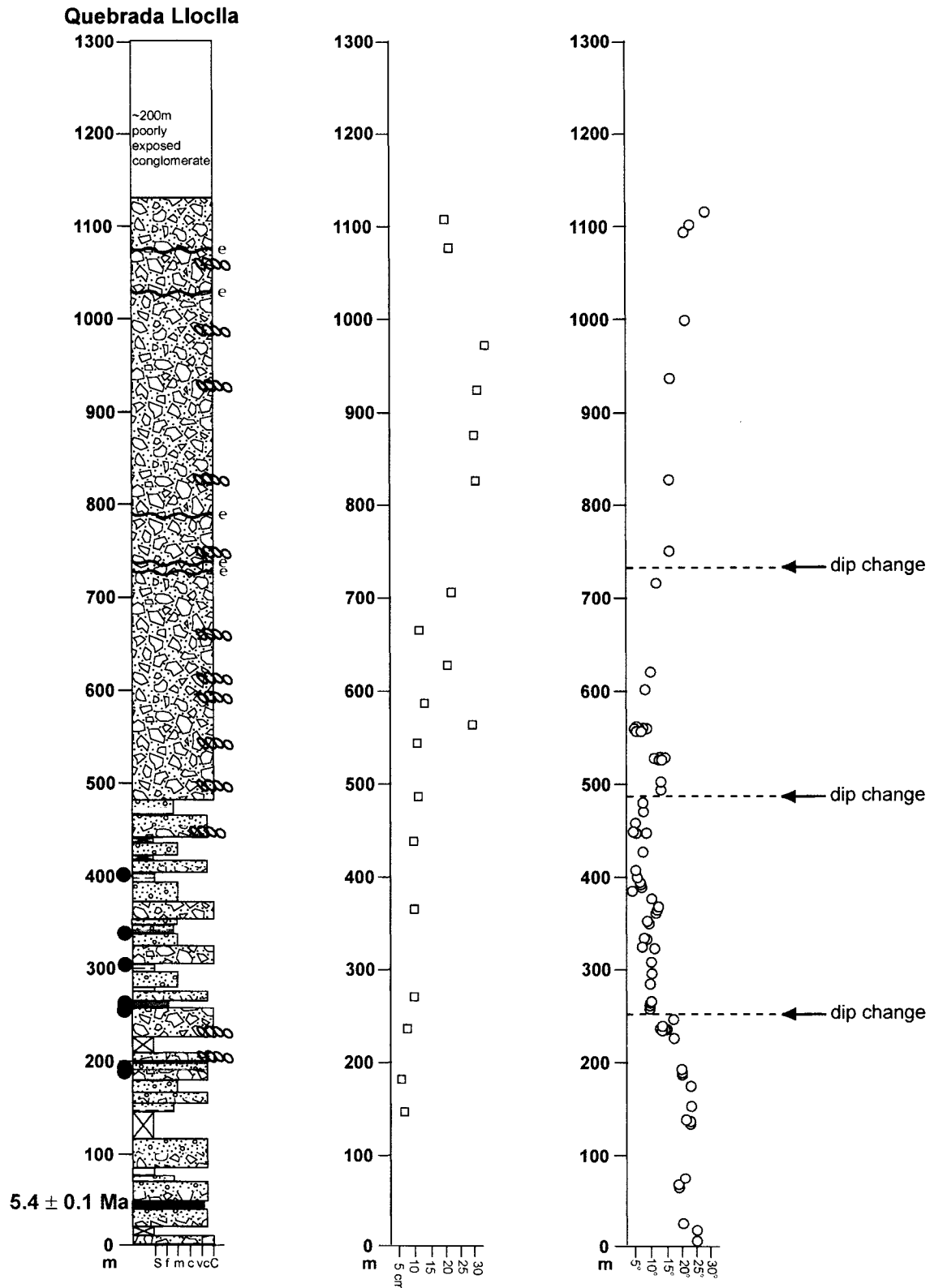


**Figure 3.13.** Dip changes (circles) and maximum clast sizes (squares) within the Lloclla Formation.

**Figure 3.14.** (A)  $\delta^{18}\text{O}$  vs. altitude plot for modern water from Quebrada Lloclla. Elevation range is too small to determine paleoelevation, but it does give a good constraint on surface water isotopic composition. (B) Covariant trend between  $\delta^{18}\text{O}$  and  $\delta^{13}\text{C}$  from Lloclla lacustrine carbonates. Sample names refer to stratigraphic meter level. There is a moderate upsection trend in more negative  $\delta^{18}\text{O}$  values, especially if sample LL263 is diagenetically altered, causing it to plot with extremely negative  $\delta^{13}\text{C}$  values. Covariance is consistent with evaporation at higher altitudes. (C) Hydrogen isotopic compositions from modern Lloclla waters. Local meteoric water line (LMWL) has a lesser slope than the global meteoric water line (GMWL) indicating significant evaporation has occurred.



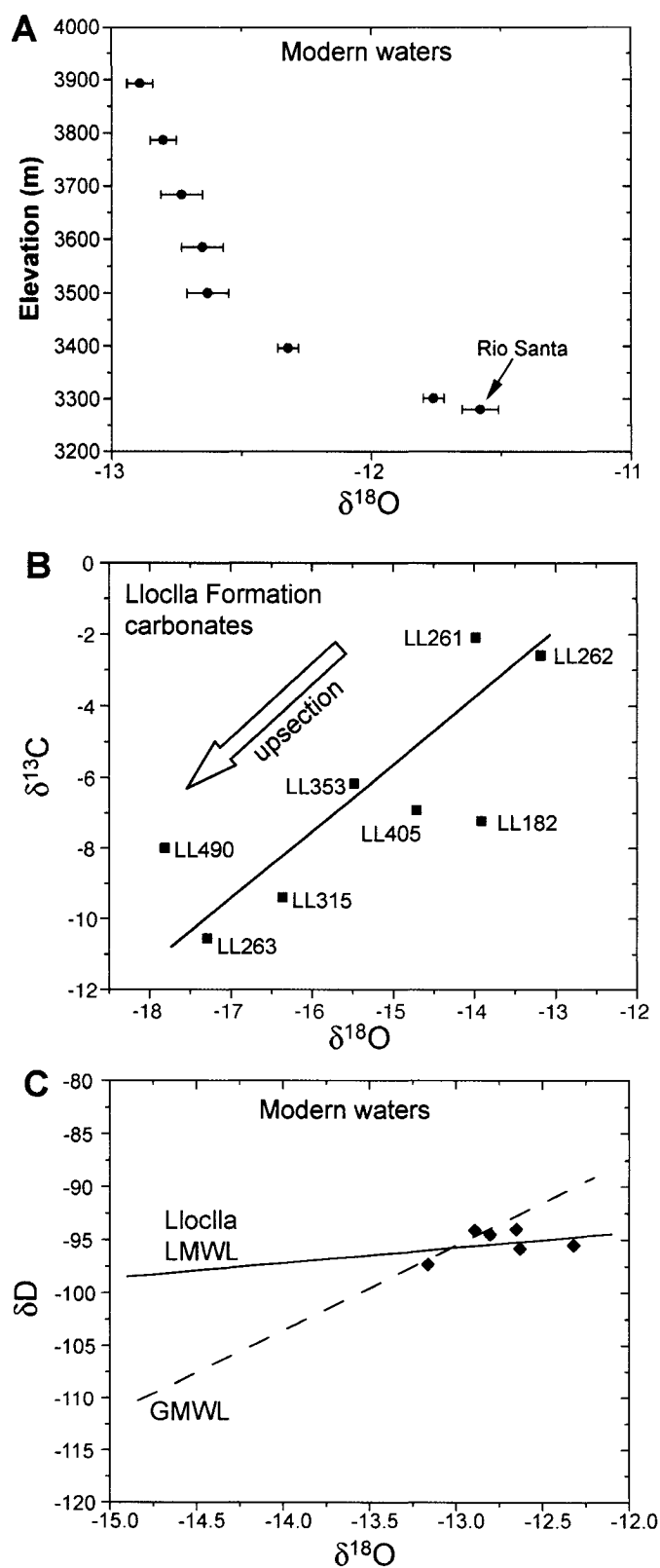
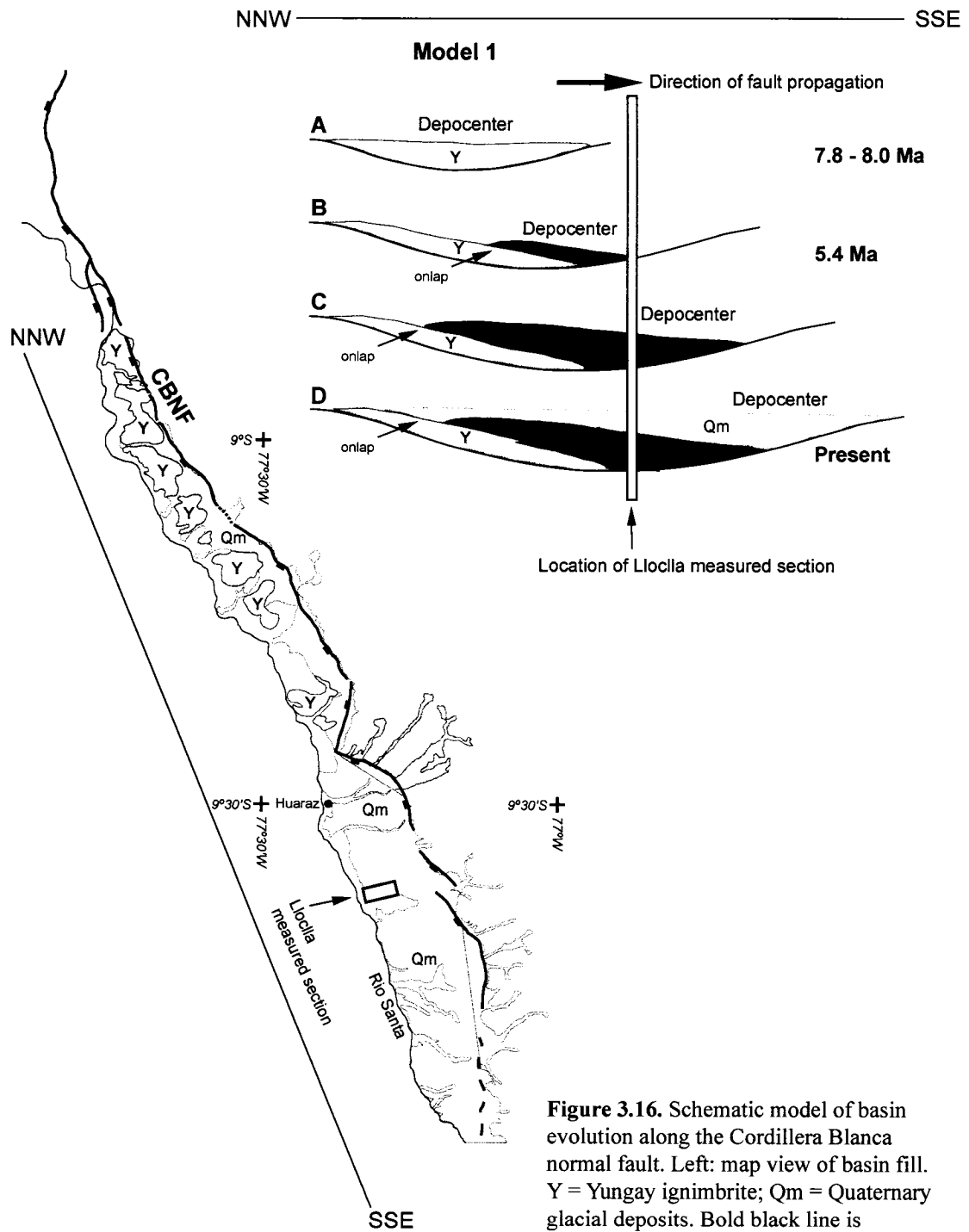
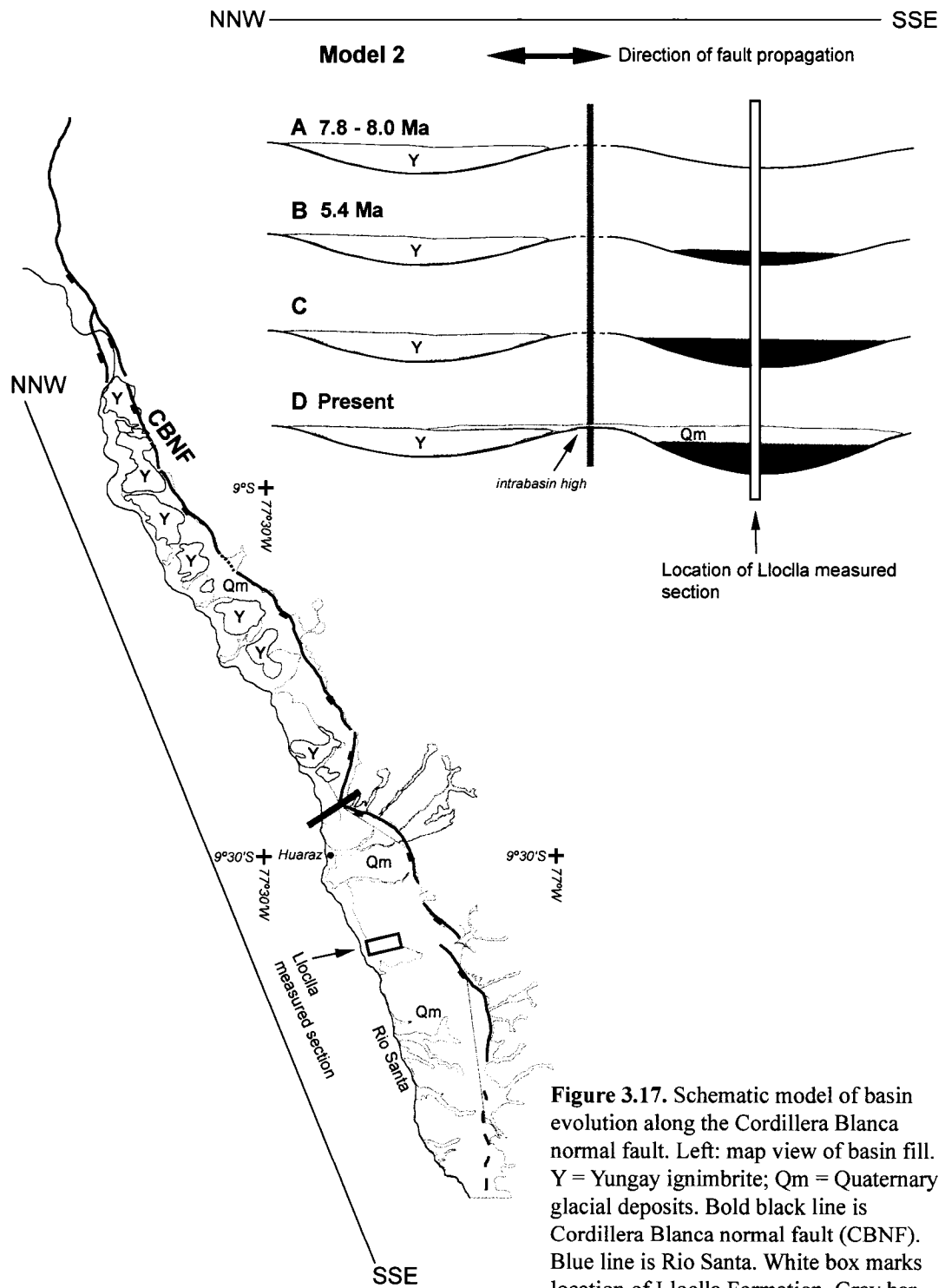


Figure 3.14





**Figure 3.16.** Schematic model of basin evolution along the Cordillera Blanca normal fault. Left: map view of basin fill. Y = Yungay ignimbrite; Qm = Quaternary glacial deposits. Bold black line is Cordillera Blanca normal fault (CBNF). Blue line is Rio Santa. White box marks location of Lloclla Formatino. See text for discussion.



**Figure 3.17.** Schematic model of basin evolution along the Cordillera Blanca normal fault. Left: map view of basin fill. Y = Yungay ignimbrite; Qm = Quaternary glacial deposits. Bold black line is Cordillera Blanca normal fault (CBNF). Blue line is Rio Santa. White box marks location of Lloclla Formation. Gray bar separates fault segments. See text for discussion.

**Table 3.1 Petrographic parameters**

---

Qm	Monocrystalline quartz
Qp	Polycrystalline quartz
Qt	Total quartzose grains (= Qm + Qp)
P	Plagioclase feldspar (includes Na and Ca varieties)
K	Potassium feldspar
F	Total feldspar grains (= P + K)
Lvm	Microlitic volcanic grains
Lvl	Lathwork volcanic grains
Lvf	Felsic volcanic grains
Lv	Total volcanic lithic grains (= Lvm + Lvl + Lvf)
Lm	Total metamorphic lithic grains (phyllite)
Lsh	Mudstone
Lc	Carbonate
Ls	Total sedimentary lithic grains (= Lsh + Lc)
L	(= Lv + Lm + Ls)

---

**Table 3.2** Point-count rawdata from Quebrada Lloclla

Sample	m level	Qm	Qp	Plag	Kspar	Lvm	Lvl	Lvf	Lm	Lsh	Lls	Bio	Musc	Other	Total Q	Total F	Total L	TOTAL
LL5	5	43	10	53	3	17	27	108	164	2	3	0	17	3	53	56	321	450
LL23	23	17	5	28	0	12	20	44	55	2	0	0	2	0	22	28	133	185
LL102	102	57	2	104	15	23	21	104	76	36	0	5	2	5	59	119	260	450
LL144	144	28	0	35	0	17	10	108	45	19	0	0	0	0	28	35	199	262
LL237	237	25	1	10	0	22	6	103	52	15	0	1	0	0	26	10	198	235
LL261	261	55	0	47	14	4	6	160	30	8	0	23	0	0	55	61	208	346
LL561	561	40	2	30	0	12	35	252	55	23	0	0	1	0	42	30	377	450
LL739	739	29	1	5	0	5	3	140	39	11	0	1	0	0	30	5	198	234

**Table 3.3** Recalculated detrital modes

<b>Sample</b>	<b>m level</b>	<b>Q</b>	<b>F</b>	<b>L</b>	<b>Qm</b>	<b>P</b>	<b>K</b>	<b>Lm</b>	<b>Lv</b>	<b>Ls</b>
LL5	5	53	56	321	43	53	3	164	152	5
LL23	23	22	28	133	17	28	0	55	76	2
LL102	102	59	119	260	57	104	15	76	148	36
LL144	144	28	35	199	28	35	0	45	135	19
LL237	237	26	10	198	25	10	0	52	131	15
LL261	261	55	61	208	55	47	14	30	170	8
LL561	561	42	30	377	40	30	0	55	299	23
LL739	739	30	5	198	29	5	0	39	148	11

**Table 3.4** Sedimentary facies of the Lloclla Formation

Facies	Lithofacies description	Sedimentary structures	Interpretation
Gcm	Conglomerate, boulder-cobble, clast-supported, poorly sorted	Massive, weak normal grading, no imbrication, occasional erosional scours	Fluvial gravel bar deposits, sub-aerial proximal fan
Gci	Conglomerate, boulder-cobble, clast-supported	Clast imbrication	Sub-aerial proximal fan
Gh	Conglomerate, pebble-coarse sand, medium- to well-sorted	Horizontal stratification	Fluvial channel flow deposits, proximal fan
Glas	Conglomerate, pebble	Low-angle stratification, scoured lower contacts, sand lenses	Fluvial channel flow deposits, proximal fan
Sm	Sandstone, medium- to coarse-grained	Massive, sand lenses, some normal grading	Fluvial channel flow deposits, proximal fan
Sh	Sandstone, medium- to coarse-grained	Horizontal stratification, contorted bedding	Fluvial, mid-fan
Sn	Sandstone, medium- to coarse-grained	Normally graded	Fluvial, mid-fan
Fm	Siltstone	Massive, thinly bedded	Lacustrine, distal fan delta
Fl	Siltstone	Horizontal laminations	Lacustrine, distal fan delta
Fh	Ash, quartz, sanidine, biotite	Horizontal laminations	Air-fall tuff deposit



### 3.8 REFERENCES

- Atherton, M. P., and Petford, N., 1993, Generation of sodium-rich magmas from newly underplated basaltic crust: *Nature*, v. 362, p. 144-146.
- Axen, G. J., Bartley, J.M., and Selverstone, J., 1995, Structural expression of a rolling hinge in the footwall of the Brenner Line normal fault, eastern Alps: *Tectonics*, v. 14, p. 1380-1392.
- Bird, P., 1984, Laramide crustal thickening event in the Rocky Mountain foreland and Great Plains: *Tectonics*, v. 3, p. 741-758.
- Bird, P., 1988, Formation of the Rocky Mountains, western United States: A continuum computer model: *Science*, v. 239, p. 1501-1507.
- Blair, T. C., and McPherson, J.G., 1994, Alluvial fans and their natural distinction from rivers based on morphology, hydraulic processes, sedimentary processes, and facies assemblages: *Journal of Sedimentary Research*, v. 64, p. 450-489.
- Bonnot, D., 1984, Neotectonique et tectonique active de la Cordillera Blanca et Callejon de Huaylas (Andes nord-peruviennes) [PhD thesis]: Universite de Paris-Sud, 115 p.
- Bonnot, D., Sebrier, M., and Mercier, J., 1988, Evolution geodynamique plio-quaternaire du bassin intra-cordillerain du Callejon de Huaylas et de la Cordillere Blanche, Perou: *Geodynamique*, v. 3, p. 57-83.
- Burchfiel, B. C., Chen, Z., Hodges, K.V., Liu, Y., Royden, L.H., Deng, C., and Xu, J., 1992, The South Tibetan detachment system, Himalayan orogen: Extension contemporaneous with and parallel to shortening in a collisional mountain belt, *Geological Society of America Special Paper* 269, 41 p.
- Cebula, G. T., Kunk, M.J., Mehnert, H.H., Naeser, C.W., Obradovich, J.D., and Sutter, J.F., 1986, The Fish Canyon Tuff, a potential standard for the  $^{40}\text{Ar}/^{39}\text{Ar}$  and fission-track dating methods: *Terra Cognita*, v. 6, p. 139-140.
- Cobbing, E. J., Pitcher, W.S., Wilson, J.J., Baldock, J.W., Taylor, W.P., McCourt, W., and Snelling, N.J., 1981, The geology of the Western Cordillera of northern Peru, *Overseas Memoir*, Institute of Geological Sciences, 143 p.
- Cobbing, E. J., and Sanchez, A.W., 1996, Mapa geologico del cuadrangulo de Recuay, 1:100 000, digitized 1996: Instituto Geologico Minero y Metalurgico.

- Colombo, F., 1994, Normal and reverse unroofing sequences in syntectonic conglomerates as evidence of progressive basinward deformation: *Geology*, v. 22, p. 235-238.
- Coney, P. J., 1987, The regional tectonic setting and possible causes of Cenozoic extension in the North American Cordillera, *in* Coward, M. P., Dewey, J.F., and Hancock, P.L., ed., *Continental Extensional Tectonics*, Geological Society Special Publication No. 28, p. 177-186.
- Coney, P. J., and Harms, T.A., 1984, Cordilleran metamorphic core complexes: Cenozoic extensional relics of Mesozoic compression: *Geology*, v. 12, p. 550-554.
- Coney, P. J., and Reynolds, S.J., 1977, Cordilleran Benioff zones: *Nature*, v. 270, p. 403-406.
- Cossio, A., and Blanco, E., 1964, Mapa geologico del cuadrangulo de Santa Rosa, 1:100 000: Instituto Geologico, Minero y Metalurgico.
- Dalmayrac, B., and Molnar, P., 1981, Parallel thrust and normal faulting in Peru and constraints on the state of stress: *Earth and Planetary Science Letters*, v. 55, p. 473-481.
- Dawers, N. H., Anders, M.H., and Scholz, C.H., 1993, Growth of normal faults: Displacement-length scaling: *Geology*, v. 21, p. 1107-1110.
- Dawers, N. H., and Anders, M.H., 1995, Displacement-length scaling and fault linkage: *Journal of Structural Geology*, v. 17, p. 607-614.
- DeCelles, P. G., and Horton, B.K., 2003, Early to middle Tertiary foreland basin development and the history of Andean crustal shortening in Bolivia: *Geological Society of America Bulletin*, v. 115, p. 58-77.
- Densmore, A. L., Dawers, N.H., Gupta, S., Guidon, R., and Goldin, T., 2004, Footwall topographic development during continental extension: *Journal of Geophysical Research*, v. 109, no. F03001, p. doi:10.1029/2003JF000115.
- Deverchere, J., Dorbath, C., and Dorbath, L., 1989, Extension related to a high topography: results from a microearthquake survey in the Andes of Peru and tectonic implications: *Geophys. J. Int.*, v. 98, p. 281-292.
- Dickinson, W. R., 1985, Interpreting provenance relations from detrital modes of sandstones, *in* Zuffa, G. G., ed., *Provenance of Arenites*: Dordrecht, The Netherlands, Reidel, p. 333-361.

- Dickinson, W. R., and Snyder, W.S., 1978, Plate tectonics of the Laramide orogeny: Geological Society of America Memoir 151, p. 335-366.
- Dorsey, R., and Martin-Barajas, A., 1999, Sedimentation and deformation in a Pliocene-Pleistocene transtensional supradetachment basin, Laguna Salada, north-west Mexico: *Basin Research*, v. 11, p. 205-221.
- Doser, D. I., 1987, The Ancash, Peru, earthquake of 1946 November 10: evidence for low-angle normal faulting in the high Andes of northern Peru: *Geophys. J. R. astr. Soc.*, v. 91, p. 57-71.
- Drummond, C. N., Patterson, W.P., and Walker, J.C.G., 1995, Climatic forcing of carbon-oxygen isotopic covariance in temperate-region marl lakes: *Geology*, v. 23, p. 1031-1034.
- Drummond, C. N., Wilkinson, B.H., Lohmann, K.C., and Smith, G.R., 1993, Effect of regional topography and hydrology on the lacustrine isotopic record of Miocene paleoclimate in the Rocky Mountains: *Palaeogeogr. Palaeoclimatol. Palaeoecol.*, v. 101, p. 67-79.
- Fillmore, R. P., Walker, J.D., Bartley, J.M., and Glazner, A.F., 1994, Development of three genetically related basins associated with detachment-style faulting: Predicted characteristics and an example from the central Mojave Desert, California: *Geology*, v. 22, p. 1087-1090.
- Friedmann, S. J., and Burbank, D.W., 1995, Rift basins and supradetachment basins: intracontinental extensional end-members: *Basin Research*, v. 7, p. 109-127.
- Gammons, C. H., Poulson, S.R., Pellicori, D.A., Reed, P.J., Roesler, A.J., and Petrescu, E.M., 2006, The hydrogen and oxygen isotopic composition of precipitation, evaporated mine water, and river water in Montana, USA: *Journal of Hydrology*, v. 328, p. 319-330.
- Garzzone, C. N., Dettman, D.L., and Horton, B.K., 2004, Carbonate oxygen isotope paleoaltimetry: evaluating the effect of diagenesis on paleoelevation estimates for the Tibetan plateau: *Palaeogeography, Palaeoclimatology, Palaeoecology*, v. 212, p. 119-140.
- Garzzone, C. N., Dettman, D.L., Quade, J., DeCelles, P.G., and Butler, R.F., 2000a, High times on the Tibetan Plateau: paleoelevation of the Thakkhola graben, Nepal: *Geology*, v. 28, p. 339-342.

- Garzione, C. N., Molnar, P., Libarkin, J.C., and MacFadden, B.J., 2006, Rapid late Miocene rise of the Bolivian Altiplano: Evidence for removal of mantle lithosphere: *Earth and Planetary Science Letters*, v. 241, p. 543-556.
- Garzione, C. N., Quade, J., DeCelles, P.G., and English, N.B., 2000b, Predicting paleoelevation of Tibet and the Himalaya from  $\delta^{18}\text{O}$  vs. altitude gradients in meteoric water across the Nepal Himalaya: *Earth and Planetary Science Letters*, v. 183, p. 215-229.
- Gawthorpe, R. L., and Hurst, J.M., 1993, Transfer zones in extensional basins: their structural style and influence on drainage development and stratigraphy: *Geological Society of London Journal*, v. 150, p. 1137-1152.
- Gibbs, A. D., 1984, Structural evolution of extensional basin margins: *Journal of the Geological Society of London*, v. 141, p. 609-620.
- Gibson, J. J., Edwards, T.W.D., Birks, S.J., St. Amour, N.W., Buhay, W.M., McEachern, P., Wolfe, B.B., and Peters, D.L., 2005, Progress in isotope tracer hydrology in Canada: *Hydrological Processes*, v. 19, p. 303-327.
- Gutscher, M.-A., Olivet, J.-L., Aslanian, D., Eissen, J.-P., and Maury, R., 1999, The "lost Inca Plateau": cause of flat subduction beneath Peru?: *Earth and Planetary Science Letters*, v. 171, p. 335-341.
- Hampel, A., 2002, The migration history of the Nazca Ridge along the Peruvian active margin: a re-evaluation: *Earth and Planetary Science Letters*, v. 203, p. 665-679.
- Horton, B. K., and DeCelles, P.G., 1997, The modern foreland basin system adjacent to the central Andes: *Geology*, v. 25, p. 895-898.
- Horton, B. K., Hampton, B.A., LaReau, B.N., and Baldellon, E., 2002, Tertiary provenance history of the northern and central Altiplano (Central Andes, Bolivia): A detrital record of plateau-margin tectonics: *Journal of Sedimentary Research*, v. 72, p. 711-726.
- Ingersoll, R. V., Bullard, T.F., Ford, R.L., Grimm, J.P., Pickle, J.D., and Sres, S.W., 1984, The effect of grain size on detrital modes: A test of the Gazzi-Dickinson point-counting: *Journal of Sedimentary Petrology*, v. 54, p. 103-116.
- Leeder, M. R., and Gawthorpe, R.L., 1987, Sedimentary models for extensional tilt-block/half graben basins, *in* Coward, M., Dewey, J.F., and Hancock, P.L., ed., *Continental extensional tectonics*: London, Geological Society Special Publication, p. 139-152.

- Marocco, R., Lavenu, A., and Baudino, R., 1995, Intermontane late Paleogene-Neogene basins of the Andes of Ecuador and Peru: sedimentologic and tectonic characteristics, *in* Tankard, A. J., Suarez, R., and Welsink, H.J., ed., *Petroleum Basins of South America*, AAPG Memoir 62, p. 597-613.
- McClaghry, J. D., and Gaylord, D.R., 2005, Middle Eocene sedimentary and volcanic infilling of an evolving supradetachment basin: White Lake Basin, south-central British Columbia: *Canadian Journal of Earth Sciences*, v. 42, p. 49-66.
- McDougall, I., and Harrison, T.M., 1999, *Geochronology and thermochronology by the  $^{40}\text{Ar}/^{39}\text{Ar}$  method*: New York, Oxford University Press, 269 p.
- McNulty, B. A., and Farber, D.L., 2002, Active detachment faulting above the Peruvian flat slab: *Geology*, v. 30, p. 567-570.
- McNulty, B. A., Farber, D.L., Wallace, G.S., Lopez, R., and Palacios, O., 1998, Role of plate kinematics and plate-slip-vector partitioning in continental magmatic arcs: Evidence from the Cordillera Blanca, Peru: *Geology*, v. 26, p. 827-830.
- Megard, F., 1984, The Andean orogenic period and its major structures in central and northern Peru: *J. geol. Soc. London*, v. 141, p. 893-900.
- Miller, D. M., Nilsen, T.H., and Bilodeau, W.L., 1992, Late Cretaceous to early Eocene geologic evolution of the U.S. Cordillera, *in* Burchfiel, B. C., Lipman, P.W., and Zoback, M.L., ed., *Geology of North America, Cordilleran orogen: Conterminous U.S.*: v. G-3, p. 205-260.
- Miller, J. M. G., and John, B.E., 1988, Detached strata in a Tertiary low-angle normal fault terrane, southeastern California: A sedimentary record of unroofing, breaching, and continued slip: *Geology*, v. 16, p. 645-648.
- Noblet, C., Lavenu, A., and Marocco, R., 1996, Concept of continuum as opposed to periodic tectonism in the Andes: *Tectonophysics*, v. 255, p. 65-78.
- Petford, N., and Atherton, M.P., 1992, Granitoid emplacement and deformation along a major crustal lineament: the Cordillera Blanca, Peru: *Tectonophysics*, v. 205, p. 171-185.
- Rodbell, D.T., 1993, Subdivision of Late Pleistocene moraines in the Cordillera Blanca, Peru, based on rock-weathering features, soils, and radiocarbon dates: *Quaternary Research*, v. 39, p. 133-143.
- Rodbell, D. T., 1992, Late Pleistocene equilibrium-line-altitude reconstructions in the northern Peruvian Andes: *Boreas*, v. 21, p. 43-52.

- Rodbell, D. T., and Seltzer, G.O., 2000, Rapid ice margin fluctuations during the Younger Dryas in the tropical Andes: *Quaternary Research*, v. 54, p. 328-338.
- Rosenbaum, G., Giles, D., Saxon, M., Betts, P.G., Weinberg, R.F., and Duboz, C., 2005, Subduction of the Nazca Ridge and the Inca Plateau: Insights into the formation of ore deposits in Peru: *Earth and Planetary Science Letters*, v. 239, p. 18-32.
- Rousse, S., Gilder, S., Farber, D., McNulty, B., and Torres, V., 2002, Paleomagnetic evidence for rapid vertical-axis rotation in the Peruvian Cordillera ca. 8 Ma: *Geology*, v. 30, p. 75-78.
- Rousse, S., Gilder, S., Farber, D., McNulty, B., Patriat, P., Torres, V., and Sempere, T., 2003, Paleomagnetic tracking of mountain building in the Peruvian Andes since 10 Ma: *Tectonics*, v. 22, doi: 10.1029/2003TC001508.
- Saleeby, J., 2003, Segmentation of the Laramide Slab - evidence from the southern Nevada region: *Geological Society of America Bulletin*, v. 115, p. 655-668.
- Schlische, R. W., and Anders, M.H., 1996, Stratigraphic effects and tectonic implications of the growth of normal faults and extensional basins, *in* Beratan, K. K., ed., *Reconstructing the History of Basin and Range Extension Using Sedimentology and Stratigraphy*: Boulder, CO, Geological Society of America Special Paper 303.
- Schwartz, D. P., 1988, Paleoseismicity and neotectonics of the Cordillera Blanca fault zone, northern Peruvian Andes: *Journal of Geophysical Research*, v. 93, p. 4712-4730.
- Sebrier, M., Mercier, J.L., Marchare, J., Bonnot, D., Cabarez, J., and Blanc, J.L., 1988, The state of stress in an overriding plate situated above a flat slab: the Andes of central Peru: *Tectonics*, v. 7, p. 895-928.
- Smith, J. A., Finkel, R.C., Farber, D.L., Rodbell, D.T., and Seltzer, G.O., 2005, Moraine preservation and boulder erosion in the tropical Andes: interpreting old surface exposure ages in glaciated valleys: *Journal of Quaternary Science*, v. 20, p. 735-758.
- Smith, W. H. F., and Sandwell, D.T., 1997, Global seafloor topography from satellite altimetry and ship depth soundings: *Science*, v. 277, p. 1957-1962.
- Sonder, L. J., England, P.C., Wernicke, B.P., and Christiansen, R.L., 1987, A physical model for Cenozoic extension of western North America, *in* Coward, M., Dewey, J.F., and Hancock, P.L., ed., *Continental Extensional Tectonics*, Special Publication 28: London, Geological Society of London, p. 187-201.

- Suarez, G., Molnar, P., and Burchfiel, B.C., 1983, Seismicity, fault plane solutions, depth of faulting, and active tectonics of the Andes of Peru, Ecuador, and southern Colombia: *Journal of Geophysical Research*, v. 88, p. 10,403-10,428.
- Talbot, M. R., 1990, A review of the palaeohydrological interpretation of carbon and oxygen isotopic ratios in primary lacustrine carbonates: *Chemical Geology*, v. 80, p. 261-279.
- Vandervoort, D. S., Jordan, T.E., Zeitler, P.K., and Alonso, R.N., 1995, Chronology of internal drainage development and uplift, southern Puna plateau, Argentine central Andes: *Geology*, v. 23, p. 145-148.
- Wawrzyniec, T. F., Selverstone, J., and Axen, G.J., 2001, Styles of footwall uplift along the Simplon and Brenner normal fault systems, central and Eastern Alps: *Tectonics*, v. 20, p. 748-770.
- Wilson, J. J., 1967a, Mapa geológico del cuadrangulo de Huari, 1:100 000: Instituto Geológico Minero y Metalúrgico.
- Wilson, J. J., 1967b, Mapa geológico del cuadrangulo de Carhuaz, 1:100 000: Instituto Geológico Minero y Metalúrgico.
- Wilson, J. J., 1967c, Mapa geológico del cuadrangulo de Corongo, 1:100 000: Instituto Geológico Minero y Metalúrgico.
- Wu, D., and Bruhn, R.L., 1994, Geometry and kinematics of active normal faults, South Oquirrh Mountains, Utah: implication for fault growth: *Journal of Structural Geology*, v. 16, p. 1061-1075.
- Yin, A., 2006, Cenozoic tectonic evolution of the Himalayan orogen as constrained by along-strike variation of structural geometry, exhumation history, and foreland sedimentation: *Earth-Science Reviews*, v. 76, p. 1-131.
- Yin, A., 1989, Origin of regional, rooted low-angle normal faults: A mechanical model and its tectonic implications: *Tectonics*, v. 8, p. 469-482.

**- Chapter 4 -**

**U-Pb and  $^{40}\text{Ar}/^{39}\text{Ar}$  evidence for coeval Neogene pluton emplacement and fault-induced exhumation in the Cordillera Blanca, Peru**



#### 4.1 ABSTRACT

Thermochronology has been used to decipher the history of fault slip and footwall uplift along major normal faults. The Cordillera Blanca is the highest single range in the Peruvian Andes, with average elevations exceeding 5000 m. The western boundary of the range is well-defined by the active, 170-km-long Cordillera Blanca normal fault, which exhibits a range of dips along strike, from 36°WSW in the north to 19°WSW in the south. The footwall is defined by high topography, variable relief along strike from north to south (from >2500 m to 500 m), and has likely accommodated > 10 km of dip slip since the late Miocene. The footwall of the Cordillera Blanca normal fault is a granodioritic batholith with U-Pb zircon crystallization ages that suggest emplacement between 5 and 8 Ma. Based on a basal tuff in the associated hanging-wall supradetachment basin, normal faulting had initiated by 5.4 Ma. The goal of this study is to constrain the timing of fault initiation, age of intrusive activity, fault slip rates, and history of unroofing events along the Cordillera Blanca normal fault.

In this study, multiple thermochronometers are applied to the footwall of the Cordillera Blanca normal fault. Spatial patterns from mica and feldspar  $^{40}\text{Ar}/^{39}\text{Ar}$  ages and apatite (U-Th)/He ages indicate that the Cordillera Blanca detachment fault can be described as a flexural rolling hinge that has exhumed the footwall since 3-6 Ma. Deeply incised glacial valleys indicate that erosion has played a significant role during footwall exhumation. Provided that simplified assumptions are made about the geothermal gradient, fault dip, and mineral closure temperatures, calculations of fault slip rates, vertical exhumation rates, and horizontal extension rates are derived from  $^{40}\text{Ar}/^{39}\text{Ar}$ ,

apatite (U-Th)/He, and apatite fission-track data. When combined with published Quaternary slip rates, it is apparent that these rates have been decreasing since the late Miocene. From this study, it is clear that pluton emplacement and footwall exhumation along the Cordillera Blanca normal fault overlapped temporally. Therefore, cooling ages record elevated temperatures due to both magmatic cooling and fault slip. New analyses of zircon (U-Pb) and potassium feldspar ( $^{40}\text{Ar}/^{39}\text{Ar}$ ) constrain the initiation of exhumation between 5.5 and 7.5 Ma.

## 4.2 INTRODUCTION

Low-angle detachment fault systems that develop in regional extensional provinces are commonly explained by gravitational collapse of over-thickened crust and/or referred to as “late orogenic extension” [e.g., *Coney and Harms*, 1984; *Wernicke and Axen*, 1988; *Yin*, 1989; *Malavieille*, 1993; *Brunel et al.*, 1994]. Similar large normal faults, such as the South Tibetan detachment system, indicate low-angle extension sub-parallel to the coeval compression direction [e.g., *Burchfiel et al.*, 1992; *Yin*, 2006]. Such faults need not involve a decrease in average crustal thickness because they add to mountain elevation and are the manifestation of synorogenic extension rather than late crustal collapse [*Brunel et al.*, 1994]. The South Tibetan detachment is interpreted as the surface trace of a long-lived crustal-scale decoupling horizon between the upper and middle lower crust of the Tibetan Plateau [*Burchfiel et al.*, 1992; *Yin*, 2006].

Large normal faults in the hinterland of fold-thrust belts, such as the Cordillera Blanca detachment fault in Peru, have been explained as the result of gravitational

collapse of overthickened crust [*Dalmayrac and Molnar*, 1981; *Suarez et al.*, 1983; *Deverchere et al.*, 1989; *Ruppel*, 1995]. The simplest explanation for extension in a zone of net regional compression considers only the local stress state within thickened continental lithosphere. Slab rollback is also a possible explanation, driving backarc extension in the overriding plate [*Ruppel*, 1995]. However, in the region of the Cordillera Blanca, the dip of the subducting Nazca Plate is nearly horizontal, inconsistent with rollback [e.g., *Yin and Kelty*, 1991]. Alternative models link subduction of the aseismic Nazca Ridge and oblique convergence between the South American and Nazca plates to vertical-axis rotations observed in the Western Cordillera and combined sinistral slip and extension along the Cordillera Blanca normal fault [e.g., *McNulty et al.*, 1998; *Rousse et al.*, 2002, 2003]. Viscous coupling between the obliquely subducting flat Nazca slab and the overriding plate may have transferred stress to the Cordillera Blanca region, helping to accommodate extension [e.g., *Spencer*, 1994; *Gutscher et al.*, 1999; *Gutscher*, 2002; *McNulty and Farber*, 2002]. Alternatively, a “sag” in the Nazca plate between two subducted aseismic ridges lies directly beneath the Cordillera Blanca, implying that the lack of buoyant material beneath overthickened crust promoted extension [*Gutscher et al.*, 1999; *Chapter 1*].

Evaluation of extension mechanisms requires an accurate chronological record of intrusive heating and exhumation-related cooling. In extensional tectonic regimes (e.g., Basin and Range province), most exhumation occurs in the footwalls of normal fault-bounded ranges. Use of multiple low-temperature thermochronometers provides constraints on the cooling and exhumation history of footwall rocks [e.g., *Armstrong et*

*al.*, 2003; *Ehlers et al.*, 2003]. By analyzing and modeling different thermochronometers with different closure temperatures, this study seeks to answer the following questions about the Cordillera Blanca detachment fault: How long has exhumation been active? How fast was the footwall exhumed? Are there spatial and temporal variations in exhumation rate? How did emplacement of the batholith affect faulting and exhumation? What structural mechanism best accounts for the distribution of the thermochronologic data? This paper presents new  $^{40}\text{Ar}/^{39}\text{Ar}$ , (U-Th)/He, and U-Pb data that address the above questions in an attempt to determine the thermal evolution of the Cordillera Blanca detachment fault system.

#### 4.3 GEOLOGIC SETTING

In northern and central South America, the Andes are the result of Cenozoic compression due to subduction of the Nazca plate (Fig. 4.1). In Peru, active extension is only observed in the Cordillera Blanca region, located above the modern flat slab segment of the Nazca plate. Quaternary fault scarps and tensile earthquake focal mechanisms provide evidence of recent normal faulting oriented parallel to the strike of active compressional structures in the Eastern Cordillera and Sub-Andean zone to the east [Dalmayrac and Molnar, 1981; Suarez *et al.*, 1983; Doser, 1987]. The Cordillera Blanca detachment fault is a seismogenic low-angle extensional fault zone on which motion began immediately after the final phase of continental arc magmatism in the region, nearly coincident with initial subduction of the Nazca Ridge and flattening of the Nazca

slab [Deverchere *et al.*, 1989; Gutscher *et al.*, 1999; Hampel, 2002; McNulty and Farber, 2002; Rosenbaum *et al.*, 2005; Chapter 1].

The Cordillera Blanca represents the highest topography in Peru and is bounded to the west by the 170-km-long, WSW-dipping Cordillera Blanca normal fault that is well defined by a fault scarp with up to 2500 m of vertical relief (Fig. 4.2). The Cordillera Blanca lies in the footwall and consists of a granodioritic batholith that intrudes the Upper Jurassic Chicama Formation. The Cordillera Blanca batholith measures 200-km-long by 20-km-wide and plunges to the south [Cobbing *et al.*, 1981]. The detachment fault overlies a mylonite zone of variable thickness (up to ~1 km) [McNulty and Farber, 2002] and foliation extends another 1.5 km into the batholith [Petford and Atherton, 1992]. Kinematic indicators in the mylonite zone (S-C fabric, oblique quartz fabrics, mica fish, asymmetric tails on feldspar porphyroclasts) show sinistral, down-to-the-west ductile shear. Mineral assemblages in the mylonite are quartz + biotite + muscovite  $\pm$  actinolite  $\pm$  epidote  $\pm$  titanite, representing shear under upper- to lower-greenschist facies. Retrograde mineral reactions include hornblende  $\rightarrow$  actinolite  $\pm$  biotite, amphibole  $\pm$  biotite  $\rightarrow$  chlorite, feldspar  $\rightarrow$  white mica [Petford and Atherton, 1992]. Toward the fault, the mylonite is progressively overprinted by cataclasite and chlorite breccia, recording motion through the brittle-ductile transition. This has been interpreted by Petford and Atherton [1992] as faulting that occurred during and after emplacement of the batholith, although they presented no evidence to indicate active faulting during intrusion.

The batholith is composed of late Miocene granite that has a single U-Pb zircon crystallization age of  $8.2 \pm 0.2$  Ma [McNulty *et al.*, 1998]. Previous K-Ar ages obtained from the central batholith near Llanganuco were interpreted as rapid cooling facilitated by uplift and exhumation along the detachment fault prior to 3.6 Ma [Cobbing *et al.*, 1981; Petford and Atherton, 1992]. A long-term vertical exhumation rate of 2.4 mm/yr (estimated from K-Ar ages) is proposed for the central batholith [Petford, 1990]. Dating of offset glacial moraines with  $^{10}\text{Be}$  and  $^{26}\text{Al}$  cosmogenic radionuclide model ages yielded Quaternary vertical exhumation rates of 1.7 – 2.3 mm/yr [DeSmedt *et al.*, 1999].

#### **4.4 EMPLACEMENT AGES OF THE CORDILLERA BLANCA FROM U-PB ZIRCON DATING**

Zircons were separated from the Llanganuco and Honda transects and analyzed for U-Pb crystallization ages [Giovanni *et al.*, 2006]. Cumulative probability plots (Figs. 4.3 and 4.4) display the full range of ages obtained. All samples have a well defined peak between 5.5-7.5 Ma, except for HON4 (Fig. 4.4). Most of the samples have older zircon populations ranging from 10-30 Ma up to 60-70 Ma. Three samples have extremely old zircon populations ranging in age from 150 to 795 Ma. Appendix 4.1 lists the age ranges for each sample. It was assumed that the zircons that record the crystallization of the Cordillera Blanca batholith would have a similar standard error to the homogeneous Durango standard. Only those zircons that fell in the  $1\sigma$  (0.3 Ma) range were considered to represent the crystallization age (Appendix 4.1). The older zircons (italicized in

Appendix 4.1) were excluded from the probability density distribution (Fig. 4.5) that defines the Cordillera Blanca crystallization ages.

The most recent zircon crystallization age reported for the Cordillera Blanca batholith was based on a single sample from Llanganuco with an age of  $8.2 \pm 0.2$  Ma [n=25, *McNulty et al.*, 1998]. An older study yielded a U-Pb zircon age of  $6.3 \pm 0.3$  Ma from the same locale [*Mukasa*, 1984]. Another study found biotite K-Ar ages ranging from 2 to 13 Ma and assumed that emplacement occurred between 9 and 10 Ma [*Stewart et al.*, 1974].

The new results from this study (n=171) place the age of batholith intrusion between 5 and 8 Ma, with a range from  $5.3 \pm 0.3$  Ma to  $23.1 \pm 0.4$  Ma (Fig. 4.5). The youngest age is very similar to the age of the basal tuff of the Lloclla Formation ( $5.36 \pm 0.10$  Ma) [*Chapter 3*], which is considered to represent the final magmatism associated with emplacement of the batholith and constrain the beginning of fault-induced subsidence of the hanging wall basin [*Chapter 3*].

## **4.5 SPATIAL PATTERNS OF COOLING AGES**

### **4.5.1 $^{40}\text{Ar}/^{39}\text{Ar}$ thermochronology**

In order to examine the spatial and temporal patterns of exhumation along the Cordillera Blanca normal fault, samples from fault-perpendicular transects were collected during the 2002, 2003, and 2005 field seasons (Fig. 4.2). Muscovite, biotite, and potassium feldspar separates from 18 samples (those labeled in blue in Fig. 4.2) were analyzed using the  $^{40}\text{Ar}/^{39}\text{Ar}$  method. Mineral separates were collected from each sample

by standard mineral separation techniques (heavy liquid and magnetic separation), handpicked to purify the sample further, and packed into Cu foil packets. Five to eight milligrams of each mica separate and ten to fifteen milligrams of each potassium feldspar separate from each sample were irradiated with sanidine flux monitors [Fish Canyon Tuff: nominal age 27.8 Ma, *Cebula et al.*, 1986] at the Ford reactor, University of Michigan for 45 hours. All samples were step-heated in a Ta crucible in a double-vacuum resistance furnace at the University of California, Los Angeles. Isotopic ratios were measured with a VG1200 gas-source automated mass spectrometer. Raw data were reduced using an in-house data reduction program AGEAL. Analytical results from the step-heating analyses are given in Appendices 4.2 and 4.3. All age uncertainties are reported at the  $1\sigma$  level. Reported ages are weighted mean ages that do not include uncertainties in the J-factor or decay constants. However, since all samples were analyzed in the same lab with the same technique and flux monitors, it is appropriate to report weighted mean ages with standard errors [*McDougall and Harrison*, 1999].

#### **4.5.2 Mica $^{40}\text{Ar}/^{39}\text{Ar}$ results**

The Yanac (YAN), Llanganuco (LLAN), and Honda (HON) transects are along deeply incised valleys through the footwall. The Pachma Alta (PA) samples were collected directly adjacent to the fault over a vertical relief of ~2000 m. Only two preliminary samples were analyzed from Pachma Alta. Samples are labeled by transect and sample number (i.e. YAN1 is the Yanac sample closest to the fault, HON6 is the Honda sample farthest from the fault). A total of 21 mica samples were analyzed: four



biotite and one muscovite from YAN; two biotite and two muscovite from PA; five biotite and one muscovite from LLAN; and four biotite and two muscovite from HON.

Biotite ages from the Yanac transect range from  $4.30 \pm 0.05$  Ma (YAN1) to  $6.77 \pm 0.06$  Ma (YAN4). One muscovite sample from this transect yields an age of  $5.07 \pm 0.09$  Ma (YAN1). Llanganuco biotite ages range between  $4.14 \pm 0.09$  Ma (LLAN1) to  $6.22 \pm 0.21$  Ma (LLAN6). A muscovite sample from the middle of this transect has an age of  $4.82 \pm 0.06$  Ma (LLAN3). The Honda biotite samples have ages from  $4.62 \pm 0.07$  Ma (HON1) to  $6.68 \pm 0.07$  Ma (HON6). Two muscovite samples have ages of  $4.92 \pm 0.12$  (HON1) and  $7.25 \pm 0.16$  (HON5). All ages are listed in Table 4.1. Spatial patterns of the cooling ages become apparent when plotted on the geologic map (Fig. 4.6). The three valley transects (YAN, LLAN, HON) show an increase in age with increased distance from the Cordillera Blanca detachment fault (Fig. 4.7A,C,E). Data plotted on age versus elevation plots (Fig. 4.7B,D,F) also reveal a trend of increasing age with increasing elevation.

Micas from analyzed samples yield plateau age spectra (Fig. 4.8), which indicate little or no thermal disturbance since crystallization. Flat age spectra can also be interpreted as a result of rapid cooling [McDougall and Harrison, 1999]. The plateau age corresponds to the temperature at which the sample retains all  $^{40}\text{Ar}$  (closure temperature). Closure temperatures for biotite range between 300 and 350°C and in rapidly cooled rocks will closely approximate the age of emplacement and cooling, assuming no reheating [McDougall and Harrison, 1999]. The closure temperature for muscovite is ~350°C and the cooling age reflects time since a sample cooled from that temperature.

A major limitation on young samples, such as those from the Cordillera Blanca, is the difficulty in detecting a small amount of radiogenic argon from a much larger background of atmospheric argon [McDougall and Harrison, 1999]. If there is insufficient radiogenic argon released from the sample, the detector may not be able to measure the gas quantities accurately. The initial samples reported in this study, from the Yanac, Pachma Alta, and Llanganuco transects, all suffered from small sample sizes (~5 mg per sample; need 10-15 mg per sample due to young age). As a result, the reported cooling ages are reasonable, but potentially inaccurate. Reanalysis of these samples with larger sample size will yield more robust cooling ages.

#### 4.5.3 K-feldspar $^{40}\text{Ar}/^{39}\text{Ar}$ results

Potassium feldspars display a range of closure temperatures for argon, and therefore, have the ability to record temperature-time information. For example, substantial age gradients in  $^{40}\text{Ar}/^{39}\text{Ar}$  age spectra can be interpreted as slow cooling through the partial retention zone. Multidomain diffusion (MDD) modeling of age spectra can yield unique cooling histories that can be interpreted in terms of the fault slip history [Lovera *et al.*, 1989, 1997, 2002; McDougall and Harrison, 1999]. Potassium feldspars from the Honda transect were analyzed and modeled using the MDD technique (Table 4.1 and Fig. 4.9).

The three Honda samples have weighted mean ages of  $3.96 \pm 0.14$  Ma (HON1),  $4.36 \pm 0.15$  Ma (HON3), and  $5.21 \pm 0.11$  Ma (HON6). Similar to the mica samples, the feldspar samples increase in age with increasing distance from the fault (Fig. 4.10). The

results of MDD modeling show that rapid cooling began ~5-6 Ma farthest from fault (HON6). The sample nearest the fault (HON1) experienced rapid cooling ~3 Ma (Fig. 4.11). To illustrate the almost contemporaneous nature of batholith emplacement and fault-related exhumation, the zircon crystallization ages from the Honda transect are overlain on the cooling histories from the potassium feldspars (Fig. 4.11).

#### **4.6 APATITE (U-TH)/HE RESULTS**

The low-temperature (U-Th)/He thermochronometer allows recent cooling histories to be measured due to the low retention temperature of helium in apatite (40-85°C) [House *et al.*, 1997; Farley, 2000]. This closure temperature is low enough that topographic variations (on the order of a few kilometers) can affect isotherms differently for different parts of the footwall (i.e., the isotherms will not be simple horizontal surfaces that rise uniformly as the footwall is uplifted). Samples collected from transects through the footwall (i.e., from very-near to very-far from the fault) will have passed through variably advected isotherms, which may lead to variations in helium age [House *et al.*, 1998; Braun, 2002]. Deep, glacially-incised valleys, such as those in the Cordillera Blanca, can affect the cooling histories of a low-temperature thermochronometer such as (U-Th)/He. The low closure temperature for helium in apatite means that the uppermost 1-2 km of crust are likely to be influenced by deep incision by erosion.

Four to eight grains of apatite were analyzed from each of ten samples. Analyses were conducted at the California Institute of Technology. Euhedral grains were hand-selected and loaded into platinum tubes. <sup>4</sup>He was extracted from each sample and

measured with isotope dilution quadrupole mass spectrometry. U and Th ratios were measured from the dissolved apatite with inductively coupled plasma mass spectrometry. Ages were corrected for alpha particle emission during radioactive decay [e.g., *Farley et al.*, 1996; *Farley*, 2000].

Two transects were analyzed for (U-Th)/He ages (Table 4.1). The Honda transect yielded ages ranging from  $1.87 \pm 0.85$  Ma (HON1) to  $2.59 \pm 1.36$  Ma (HON6). Llanganuco sample ages range between  $4.18 \pm 0.92$  Ma (LLAN1) to  $3.13 \pm 0.46$  (LLAN6). Results from (U-Th)/He analyses of apatite from the Llanganuco and Honda transects reveal an overall trend of increasing age with increasing distance from the fault (Fig. 4.12A,C). Age versus elevation plots (Fig. 4.12B,D) display an increase in age with elevation. These reported ages are averages; raw data is listed in Appendix 4.4.

#### **4.7 THERMAL MODELS OF BATHOLITH EMPLACEMENT AND EXHUMATION**

Slip on a normal fault can result in rapid cooling of the footwall and associated heating of the hanging wall. The thermal history of the footwall can potentially constrain the displacement history of the fault [*McDougall and Harrison*, 1999; *Armstrong et al.*, 2003; *Kapp et al.*, 2005]. Previous models of normal fault exhumation have not considered the effect from nearby intrusions on the cooling histories. Plutons emplaced at shallow crustal levels can have relatively rapid cooling rates ( $>100^{\circ}\text{C}/\text{Ma}$ ) [*McDougall and Harrison*, 1999]. This is an important consideration in the Cordillera Blanca,

because the zircon data imply that intrusion occurred immediately before, and possibly during, footwall exhumation along the Cordillera Blanca detachment fault (Fig. 4.11).

A thermokinetic model that combines the effects of both intrusion and normal faulting is used to recreate the thermal histories obtained from the Honda potassium feldspar samples (Fig. 4.13A). In this model, the thermal structure of the upper 30 km of crust is reconstructed, using boundary conditions of a constant surface temperature (25°C), constant flux at the base, and zero lateral flux at the boundaries. Spherical intrusions were randomly intruded between 6.5 and 8 Ma (a range based on zircon U-Pb ages, Fig. 4.5) to simulate the thermal effects of batholith emplacement. Slip along a normal fault (30° dip) was initiated at 5.5 Ma (a value based on the age of the basal tuff within the supradetachment basin), with a constant slip rate of 2 mm/yr. The resulting cooling histories (Fig. 4.13B) represent three synthetic samples assumed to be equivalent to the three Honda samples with MDD modeled thermal histories.

Compared to the thermal histories from the three Honda samples that yielded mica and potassium feldspar  $^{40}\text{Ar}/^{39}\text{Ar}$  and apatite (U-Th)/He cooling ages, the modeled thermal history has a relatively high degree of correlation (Fig. 4.14). This demonstrates that intrusive cooling, in addition to exhumation, is required to explain the thermochronologic data. This underscores the importance of a detailed intrusion history when interpreting thermochronologic data in terms of exhumation, particularly in the Cordillera Blanca, where structural and thermochronologic observations require a combination of batholith intrusion and emplacement, as well as coeval exhumation along the Cordillera Blanca normal fault [*Petford and Atherton, 1992*].

An important question to consider is the relationship between batholith emplacement and the initiation of faulting. Detachment faults are regional low angle normal faults rooted in the ductile middle crust that facilitate large amounts of crustal extension [*Davis and Lister, 1988*]. Metamorphic core complexes typically exhibit a hanging wall of less deformed, brittle rocks juxtaposed across a detachment fault from older footwall rocks of higher metamorphic grade or greater structural depth [*Coney and Harms, 1984; Miller and John, 1988*]. A metamorphic core complex is the result of isostatic rebound of the footwall of a detachment fault and is characterized by brecciation, cataclasis, retrograde alteration, and mylonitization, as observed from the fault down into the footwall. Tilted high-angle normal faults above the detachment and doming of the footwall are also characteristic features [*Spencer, 1984; Wernicke and Axen, 1988; Lister and Davis, 1989*]. The Cordillera Blanca is considered to be in the early stages of metamorphic core complex development [*Chery, 2001; McNulty and Farber, 2002*].

Numerical models show that high heat flow is favorable to initiate low-angle normal faulting [*Buck, 1991*]. However, the present-day heat flow in the Cordillera Blanca region is low, indicating a low regional geothermal gradient since the latest Miocene [*Henry and Pollack, 1988*]. Local thermal anomalies, such as those associated with pluton intrusion, may potentially trigger low-angle extension [*Lister and Baldwin, 1993*]. The lithospheric heat necessary for detachment faulting may have originated from, and been restricted to, the Cordillera Blanca batholith; the thermal effects associated with batholith emplacement played a key role in initiation of detachment

[McNulty and Farber, 2002]. The regional compressional stress distribution across Peru also supports the interpretation that the Cordillera Blanca may not be a full-fledged metamorphic core complex. Alternatively, detachment faulting may have been triggered in warm crust by mechanical coupling and oblique shear associated with the flattening of the Nazca slab due to ridge subduction [McNulty and Farber, 2002; Chapter 1].

#### **4.8 STRUCTURAL MODEL OF FAULT EVOLUTION**

The turtlebacks of Death Valley are detachment surfaces that separate brittlely deformed hanging wall rocks from mylonitic, ductilely deformed footwall rocks [Miller, 1991, 1992]. Cemen *et al.* [2005] recognized a turtleback detachment surface in western Turkey, asserting that turtlebacks are characteristic of detachment fault footwalls. Identification of a turtleback surface lends support to the interpretation of footwall isostatic rebound and a rolling hinge. Despite the Cordillera Blanca's location in an active compressional orogen, digital elevation models (DEMs) reveal an updip shallowing of the fault surface, especially along the northern facets (Figs. 4.15 and 4.16). There is an overall convex-up shape to the Cordillera Blanca normal fault surface and it separates brittlely-deformed hanging wall rocks from the mylonites observed beneath the fault surface. It is likely that the Cordillera Blanca normal fault is a partially-formed turtleback surface, consistent with other low angle normal faults, isostatic rebound, and rolling hinges.

Spatial age gradients result from variations of the thermal history with structural position in relation to the fault [Ketcham, 1996]. Cooling ages can provide information

on the timing of initiation of faulting and progressive exhumation [e.g., *Wells et al.*, 2000]. The onset of rapid cooling is often equated with the beginning of faulting and footwall denudation [*Davis and Lister*, 1988]. However, rapid cooling events defined by thermochronology only provide minimum estimates of the absolute age of tectonic denudation [*House and Hodges*, 1994]. Cooling age patterns in the footwalls of detachment faults can be predicted by thermal models [*Robinson*, 2005] that account for large magnitudes of erosion during exhumation.

#### **4.8.1 Rolling-hinge model**

The rolling-hinge model [*Buck*, 1988; *Wernicke and Axen*, 1988; *Axen and Bartley*, 1997] has been used to explain the thermal and structural evolution of the Kongur Shan extensional system in the Pamir [*Robinson*, 2005]. Active normal faulting is accommodated at all times by a normal fault that is listric at depth. Isostatic rebound of the footwall during faulting results in variable tilting of footwall rocks away from the fault. The net result of the rolling hinge model is that the cross section exposed at the surface represents an oblique slice through the footwall with the deepest structural levels exposed directly adjacent to the active normal fault [*Harrison et al.*, 1995].

In such cases, samples from transects like those in the Cordillera Blanca are collected in oblique cross sections rather than from positions directly beneath the detachment surface. Thermal models can predict the pattern of cooling ages expected for different versions footwall uplift, including the rolling hinge model [e.g., *Robinson*, 2005]. 1. If the footwall exhumes as a rigid block (the opposite of a rolling hinge), age-



distance plots show a constant age with distance from the fault, which differs from observations in all detachment footwalls, including the Cordillera Blanca (Fig. 4.17A). 2. For a flexural rolling hinge [Buck, 1988], cooling age patterns show a roughly linear increase in age with distance from fault. All transect samples now exposed in the footwall were originally located directly adjacent to the fault surface at various depths prior to exhumation (Fig. 4.17B). 3. A simple shear rolling hinge [Wernicke and Axen, 1988; Axen and Bartley, 1997] will have identical thermal histories as the flexural rolling hinge (for same fault dips and slip rates) but exhumed samples will be farther apart at the surface than they were at depth (Fig. 4.17C). 4. When erosion is added to the flexural rolling hinge model, part of the footwall is eroded when it reaches the surface, causing the hinge axis to migrate away from the fault (Fig. 4.17D). Erosion of the footwall during exhumation can significantly affect the observed pattern of cooling ages and must be taken into account with deeply incised footwalls [Robinson, 2005].

Thermochronologic studies from the Nyainqentanglha [Harrison *et al.*, 1995] put constraints on fault dips that match predictions of the rolling hinge model. Thermal histories predicted for samples at the tops and bottoms of valleys (in Cordillera Blanca, HON1 versus HON6) vary considerably with slip rate. In general, structurally higher samples cool mainly due to surface erosion whereas fault-adjacent samples cool due to both erosional and tectonic denudation. For slip rates of a few mm/yr, the initial temperature difference between these two vertically separated samples is maintained during exhumation. Thus, the thermal history from the top of the valley (structurally highest sample) exhibits the most direct record of the timing of fault initiation.

Meanwhile, the sample nearest the fault provides the best measure of slip rate. A model of variable fault dip angles shows that if the dip angle is low ( $\sim 27^\circ$ ), regardless of slip rate, samples closest to the fault will cool before those structurally higher [Harrison *et al.*, 1995]. Fault dips of  $\sim 40^\circ$  are required to obtain cooling age patterns that show increasing age with increasing distance from fault. Normal faults that exhume as a rolling hinge probably had initial fault dips  $\sim 40^\circ$  which were then tilted to lower angles.

#### 4.8.2 Fault slip rates

Many exhumation studies use the slope of a best-fit line through the age-elevation plots to estimate an apparent vertical exhumation rate but this method does not consider important parameters such as the fault dip angle, footwall tilt, duration of exhumation, or true vertical exhumation rate. Thermochronologically-determined slip rates rely on the assumption that isotherms are stationary with respect to the surface during footwall exhumation [Ketcham, 1996; Brady, 2002]. Sources of error with that assumption include: isotherms do move significantly during extension, advecting toward the surface; the active fault plane may be tilted during extension; and uncertainties in age determinations [Brady, 2002; Carter *et al.*, 2004]. Higher temperature thermochronometers such as  $^{40}\text{Ar}/^{39}\text{Ar}$  are more affected by isotherm advection than lower-temperature systems, like apatite (U-Th)/He and apatite fission-track. Slip rates calculated from  $^{40}\text{Ar}/^{39}\text{Ar}$  ages thus most likely underestimate the true slip rate. The  $^{40}\text{Ar}/^{39}\text{Ar}$  system is also susceptible to perturbations from intrusive cooling which would result in an overestimate of slip rate. However, for all these systems, if there is any

significant erosion-related contribution to exhumation, the slip rates will be overestimates [Carter *et al.*, 2004].

Estimates of slip rates using the slope of age-elevation plots range from 1.75 mm/yr (Yanac) to 5.35 mm/yr (Llanganuco) (Fig. 4.7). The anomalously high Llanganuco slip rate is an excellent example of how intrusive heat can result in an overestimate of slip rate (Fig. 4.7). In comparison, the vertical exhumation rate was calculated and used to constrain the fault slip rate (Fig. 4.18). Calculating the vertical exhumation rate requires assumptions about the geothermal gradient, fault dip, and closure temperatures of the various thermochronometers. A geothermal gradient of 25°C/km and a fault dip of 35° were assumed by Montario [2001] to calculate vertical exhumation rates from apatite fission-track ages. The same values are assumed here to allow comparison to those data. Closure temperatures of 300°C and 150°C are assumed for biotite and potassium feldspar [McDougall and Harrison, 1999]. Closure temperatures for apatite (U-Th)/He range from 40-85°C with a best estimate of 65°C [Farley, 2000]. The closure temperature isotherm is assumed to be stationary which can be problematic [Brady, 2002].

Table 4.2 lists the calculated average vertical exhumation rates, horizontal extension rates, and fault slip rates from each of the transects analyzed in this study. Rates from apatite fission-track cooling ages from Llanganuco [Montario, 2001; Garver *et al.*, 2003] were calculated using the same method and are comparable to the 1.1 mm/yr vertical exhumation rate reported by Montario [2001]. The apatite (U-Th)/He fault slip rates (Table 4.2) are similar to the Quaternary slip rates of 0.86-1.36 mm/yr measured

near Pachma Alta and south of the Honda transect [Schwartz, 1988]. Individual rates calculated for each sample are listed in Table 4.3.

Multiple thermochronometers can allow comparison of slip rates. For example, in the Wasatch Mountains, vertical exhumation rates seem to decrease over time [Ehlers *et al.*, 2003]. In the Cordillera Blanca, vertical exhumation rates and slip rates also appear to decrease over time, from >2 mm/yr to 0.9 mm/yr in the Llanganuco region (Table 4.2). A Quaternary vertical exhumation rate of 0.86 mm/yr was estimated for the southern region of the Cordillera Blanca fault [Schwartz, 1988]. With the limited spatial coverage of the transects in this study, it is not yet possible to determine if there is an along-strike variability of slip rates.

#### 4.9 DISCUSSION

This study contributes a new thermochronologic and geochronologic data set that reveals that emplacement and then exhumation of the Cordillera Blanca batholith occurred in rapid succession or possibly overlapped in time.  $^{40}\text{Ar}/^{39}\text{Ar}$  cooling ages of mica and potassium feldspar were affected by magmatic cooling, causing the  $^{40}\text{Ar}/^{39}\text{Ar}$  system to record cooling, starting between 5.5 to 7.5 Ma. The batholith itself has an average crystallization age ~7 Ma. The similar ages of zircon crystallization and feldspar cooling histories strongly suggest a temporal link between batholith emplacement and exhumation. Thermal modeling of the Honda transect reveals a strong correlation between emplacement ages and  $^{40}\text{Ar}/^{39}\text{Ar}$  cooling histories. Assumptions about slip rate, fault dip, and surface temperature are preliminary in this study.

The  $^{40}\text{Ar}/^{39}\text{Ar}$  cooling ages from the Llanganuco and Honda footwall transects exhibit a consistent increase in age with distance from the fault. This pattern implies that cooling is a continuous process, whether by tectonic unroofing, erosion or magmatic cooling [Armstrong *et al.*, 2003]. The best explanation is a rolling-hinge model of exhumation, either a flexural, simple-shear, or simple-shear plus erosion rolling hinge. The heavy glaciation experienced by the Cordillera Blanca during the last ~1-2 Ma [Smith *et al.*, 2005; Chapter 2] requires erosion to be considered in all models of exhumation. Thus, the simple-shear plus erosion rolling hinge (Fig. 4.17D) best explains the cooling age patterns in the Cordillera Blanca.

Footwall samples farthest from the fault provide the best estimates of the timing of fault initiation. Samples located adjacent to the fault provide the best fault slip rate estimates. Due to the similar ages of zircon crystallization and mica cooling ages, the  $^{40}\text{Ar}/^{39}\text{Ar}$  cooling ages from potassium feldspar offer the most reasonable estimates for initiation of faulting and vertical exhumation and fault slip rates. Similar to the Wasatch fault [Armstrong *et al.*, 2003], vertical exhumation rates, horizontal extension rates, and fault slip rates along the Cordillera Blanca normal fault have been decreasing since faulting initiated ~5-6 Ma (Tables 4.2 and 4.3) in the Honda transect.  $^{40}\text{Ar}/^{39}\text{Ar}$  potassium feldspar and apatite (U-Th)/He data from Honda reveal that slip rates have slowed from 2.35 mm/yr to 1.89 mm/yr since ~3 Ma.

Why would extension be slowing down? One option is that the crustal weakening caused by the heat from batholith intrusion has now diminished or disappeared (as the batholith is now at the surface), resulting in colder, stronger crust that is more resistant to

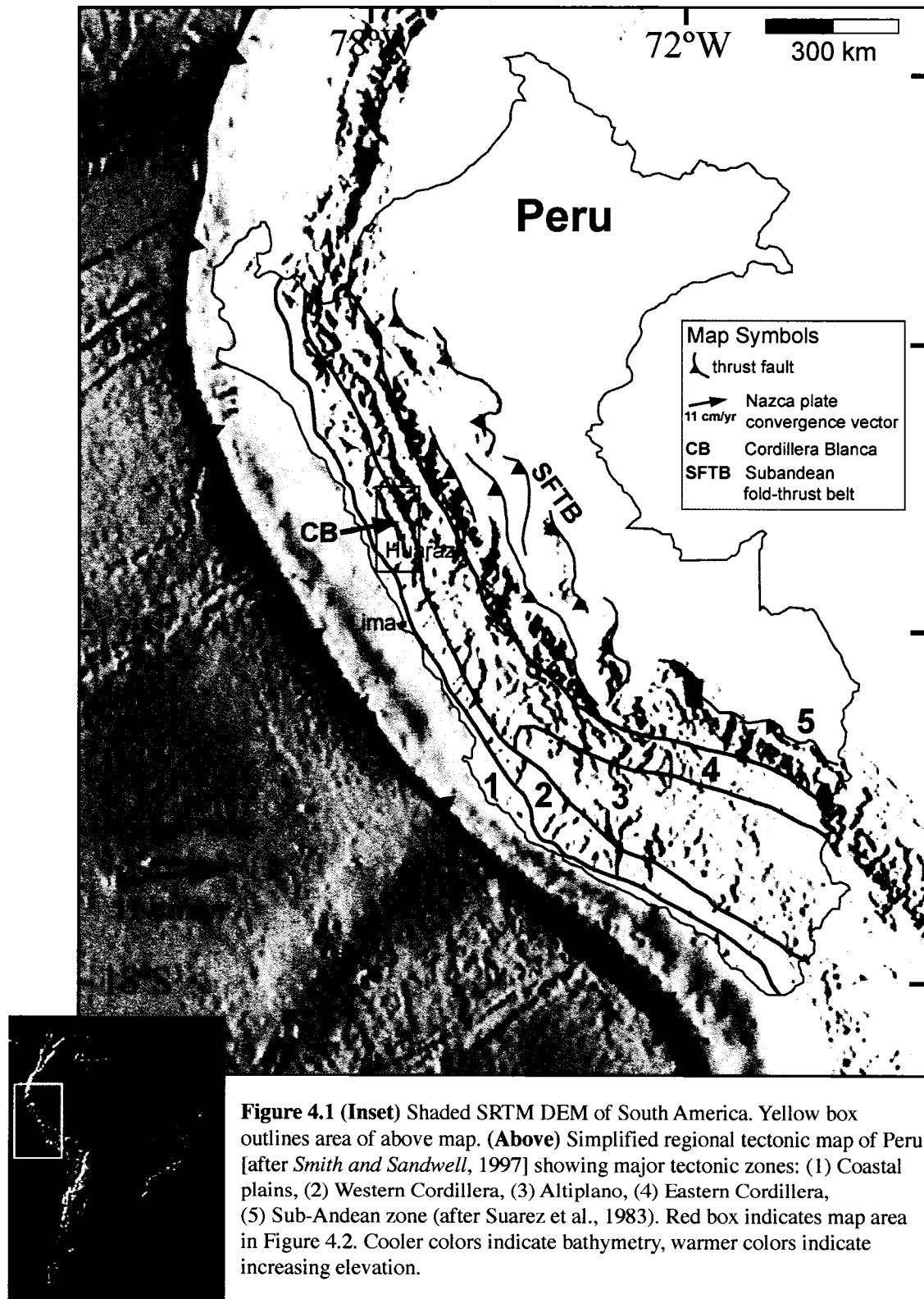
extension. Another possibility is that continued refrigeration of the upper plate from the cold flat slab has strengthened the crust, removing the main driving force behind extension.

The spread in zircon ages is intriguing. There is a well-defined group of ages between 5-8 Ma that peak ~7 Ma that clearly reflect the emplacement and crystallization of the Cordillera Blanca batholith (Figs. 4.3 and 4.4). What are the possible sources for the older ages that range from 25 to 800 Ma? The Cordillera Blanca batholith intruded the Jurassic Chicama Formation which is predominantly composed of phyllite. Studies of detrital zircons may reveal the Jurassic wallrocks to be the source of the older zircon ages in the Cordillera Blanca [e.g. *Jacobson et al.*, 2000]. If that is the case, it is reasonable to expect a spread of ages from Jurassic to Proterozoic. Another possible source of the older ages may be an older pluton at depth that the Cordillera Blanca intruded and assimilated during emplacement. One highly speculative hypothesis suggests that those older zircons come from material that was subducted, underplated to the South American plate, and then assimilated by the Cordillera Blanca source melt as it rose into the upper crust. Of the three suggested sources for the older zircon ages, the most likely source are the Jurassic wall rocks. Further study of the zircon source region is needed.

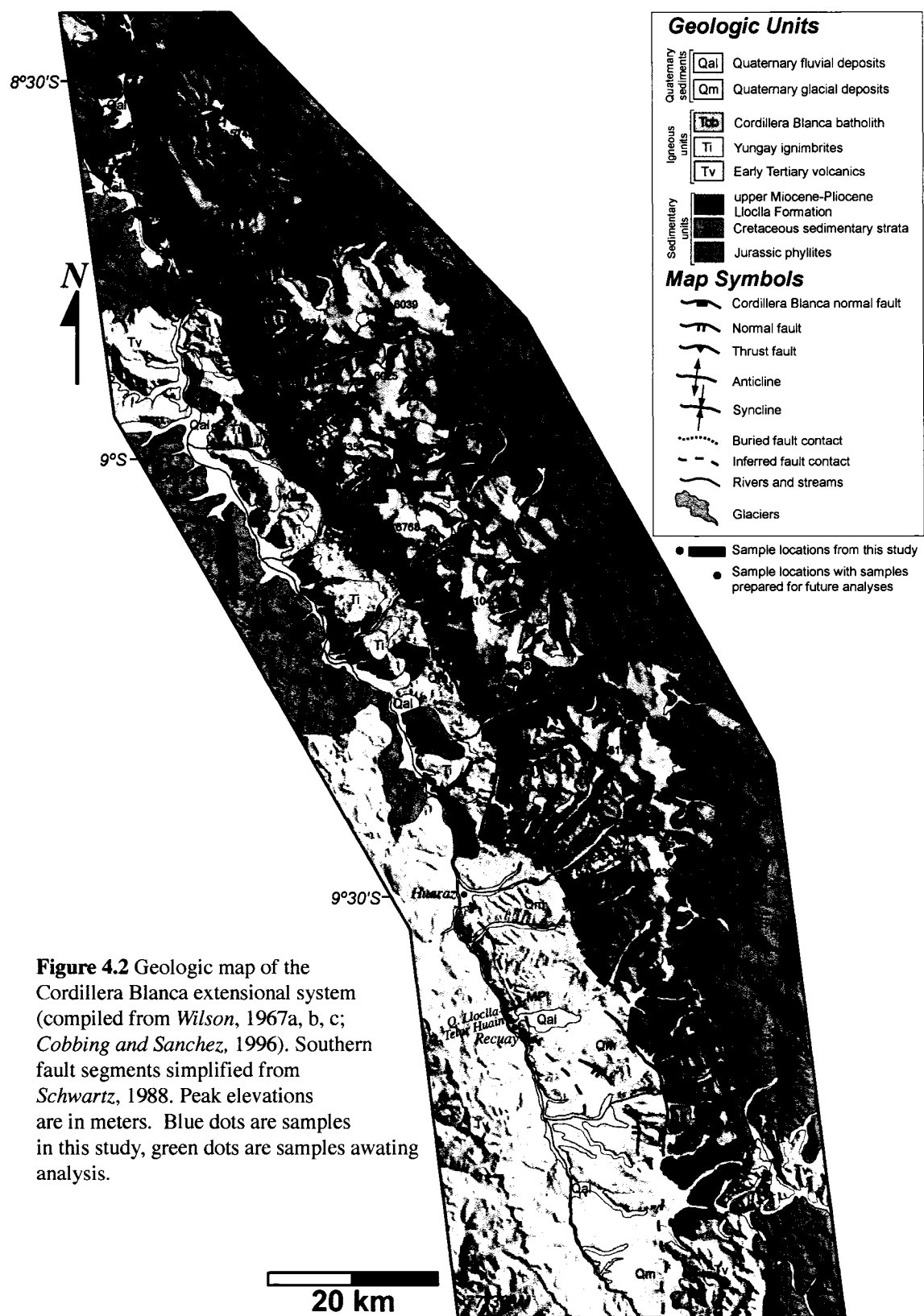
#### **4.10 CONCLUSIONS**

New  $^{40}\text{Ar}/^{39}\text{Ar}$  cooling ages from mica and potassium feldspar from the Cordillera Blanca batholith record exhumation-related cooling beginning between 5.5 and 7.5 Ma.

These data suggest that motion along the Cordillera Blanca normal fault initiated at ~5-6 Ma. Spatial patterns of  $^{40}\text{Ar}/^{39}\text{Ar}$  cooling ages reveal a constant increase in age with increased distance from the fault, which is best explained by a rolling-hinge model for exhumation that includes erosion. New U-Pb zircon crystallization ages from the batholith range between 5 and 8 Ma, with an average age ~7 Ma. The overlapping ages of zircon crystallization and modeled thermal histories from potassium feldspar reveal a temporal link between batholith emplacement and exhumation. Calculations of vertical exhumation rates, horizontal extension rates, and fault slip rates along the Cordillera Blanca normal fault show that extension has been slowing since faulting initiated at ~5-6 Ma. This slowing may be due to the lack of intrusive heating (now that the batholith has been brought to the surface) and/or refrigeration of the upper plate by continued flat slab subduction, resulting in stronger, colder crust that can no longer accommodate extension.







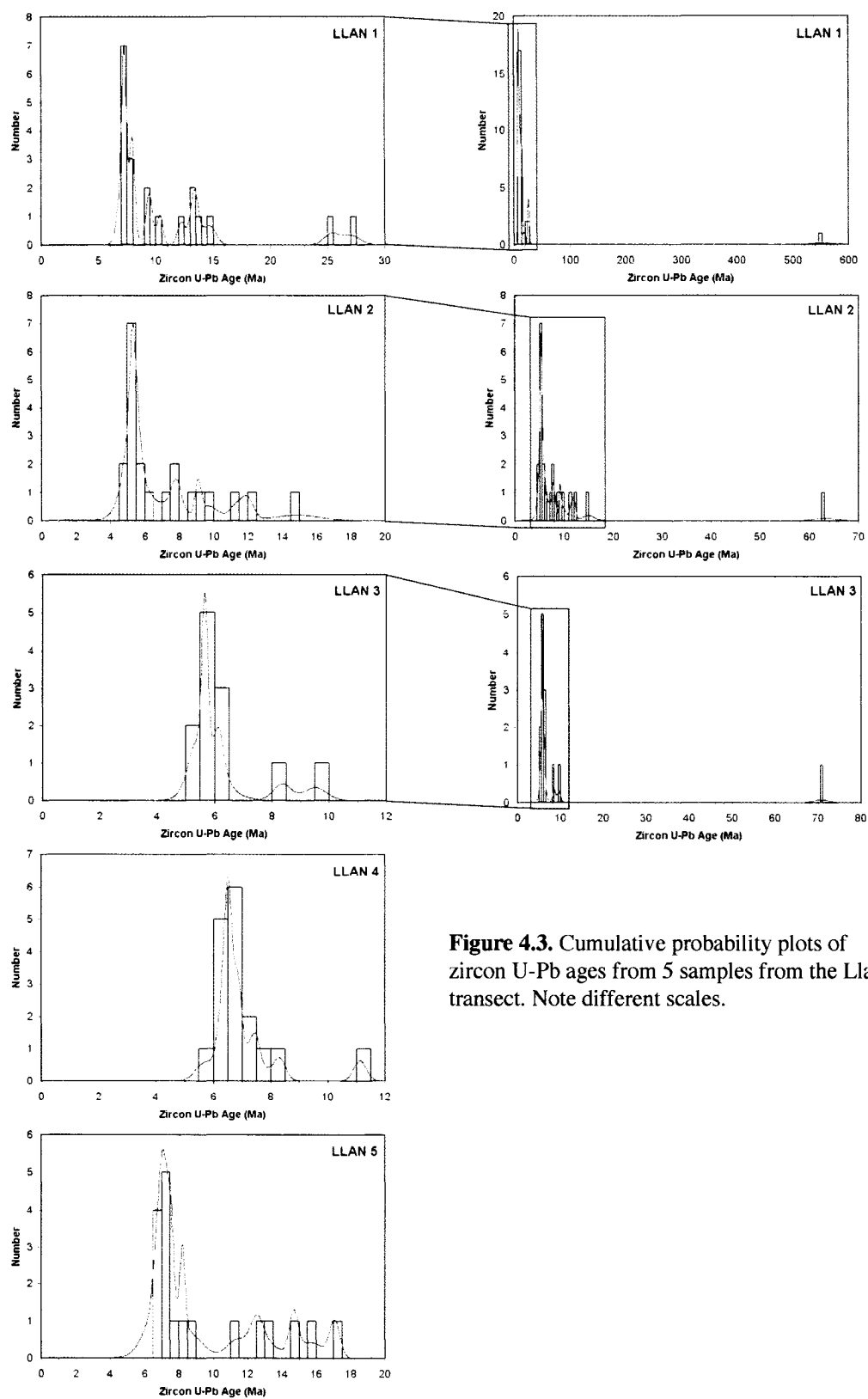


**Figure 4.3.** Cumulative probability plots of zircon U-Pb ages from 5 samples from the Llanganuco transect. Note different scales.

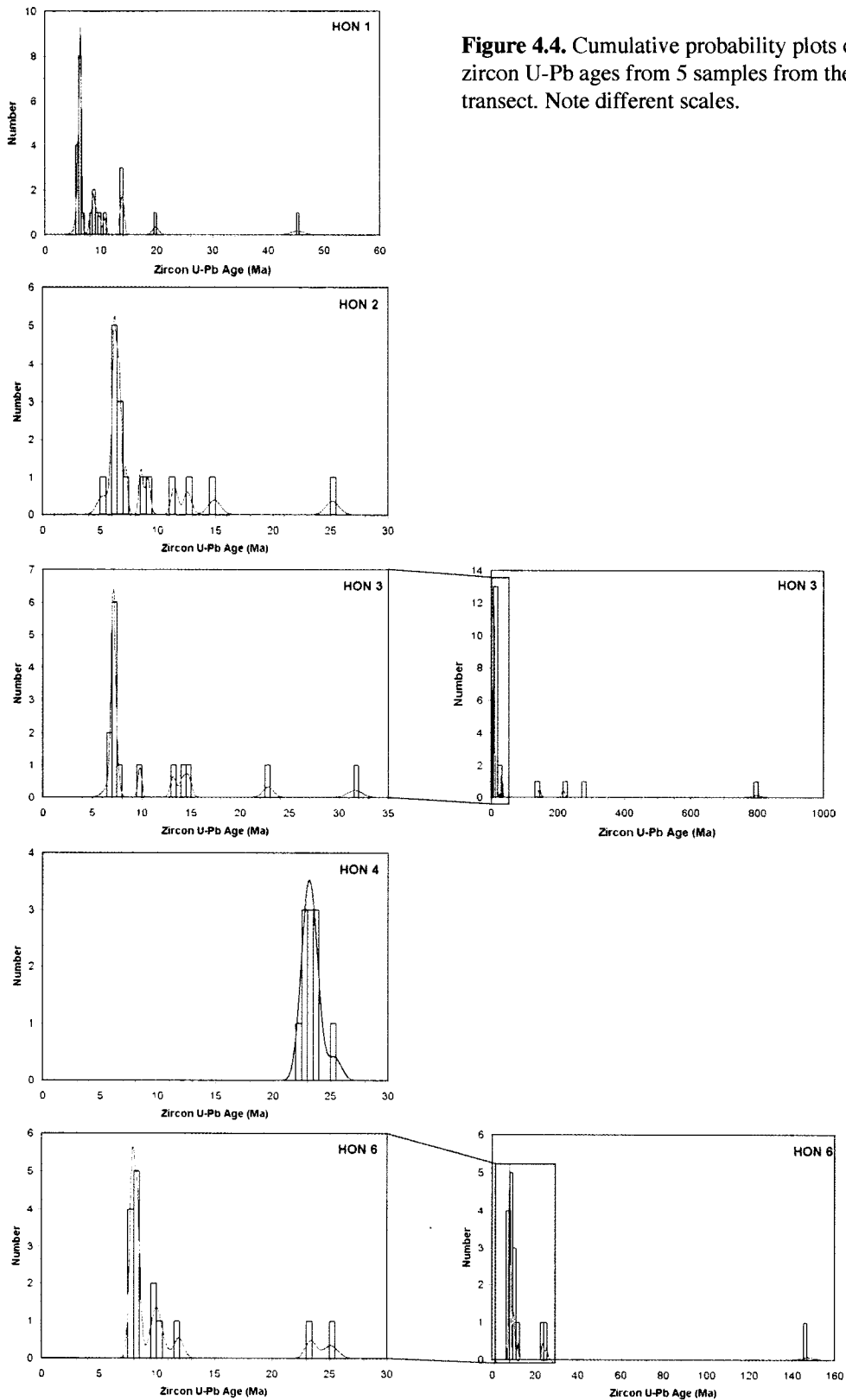


**Figure 4.4.** Cumulative probability plots of zircon U-Pb ages from 5 samples from the Honda transect. Note different scales.

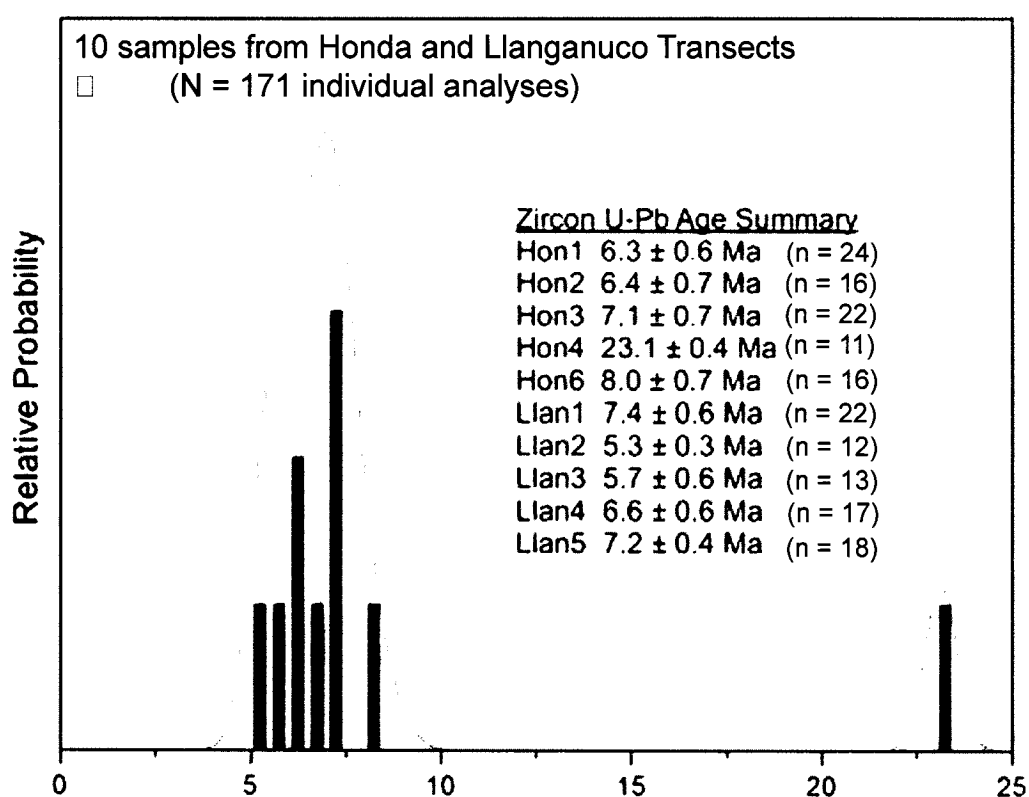


**Figure 4.5.** Probability density distribution for all U-Pb zircon analyses from Honda and Llanganuco transects. Previously, the emplacement of the batholith had been estimated at  $8.2 \pm 0.1$  Ma [McNulty *et al.*, 1998]. These results demonstrate that local granite crystallization took place as recently as 5.3 Ma, similar in age to the basal tuff within the fault-adjacent Lloclla Formation [Chapter 3]. These results also overlap with some  $^{40}\text{Ar}/^{39}\text{Ar}$  cooling ages from these transects.

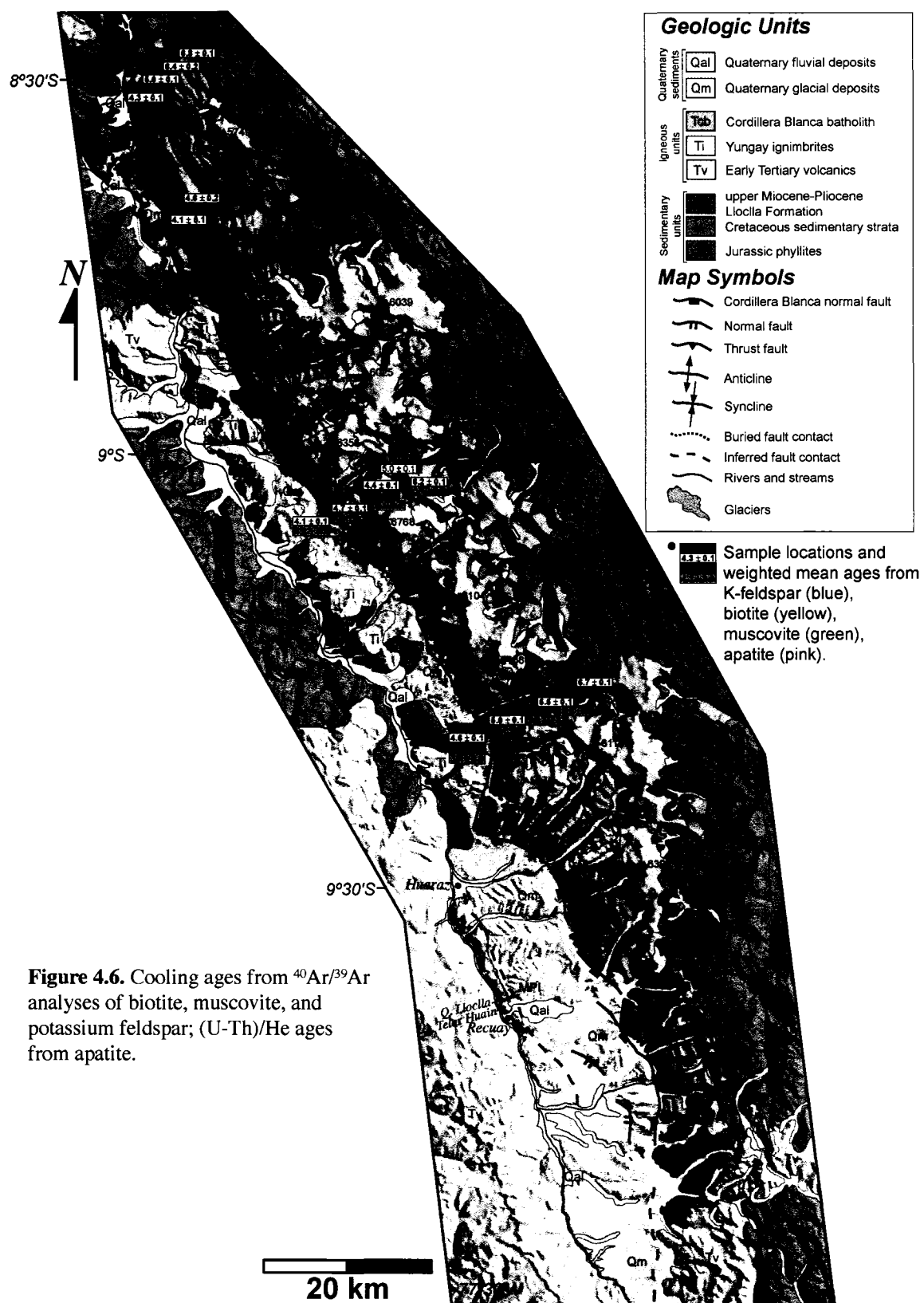


**Figure 4.6.** Cooling ages from  $^{40}\text{Ar}/^{39}\text{Ar}$  analyses of biotite, muscovite, and potassium feldspar; (U-Th)/He ages from apatite.

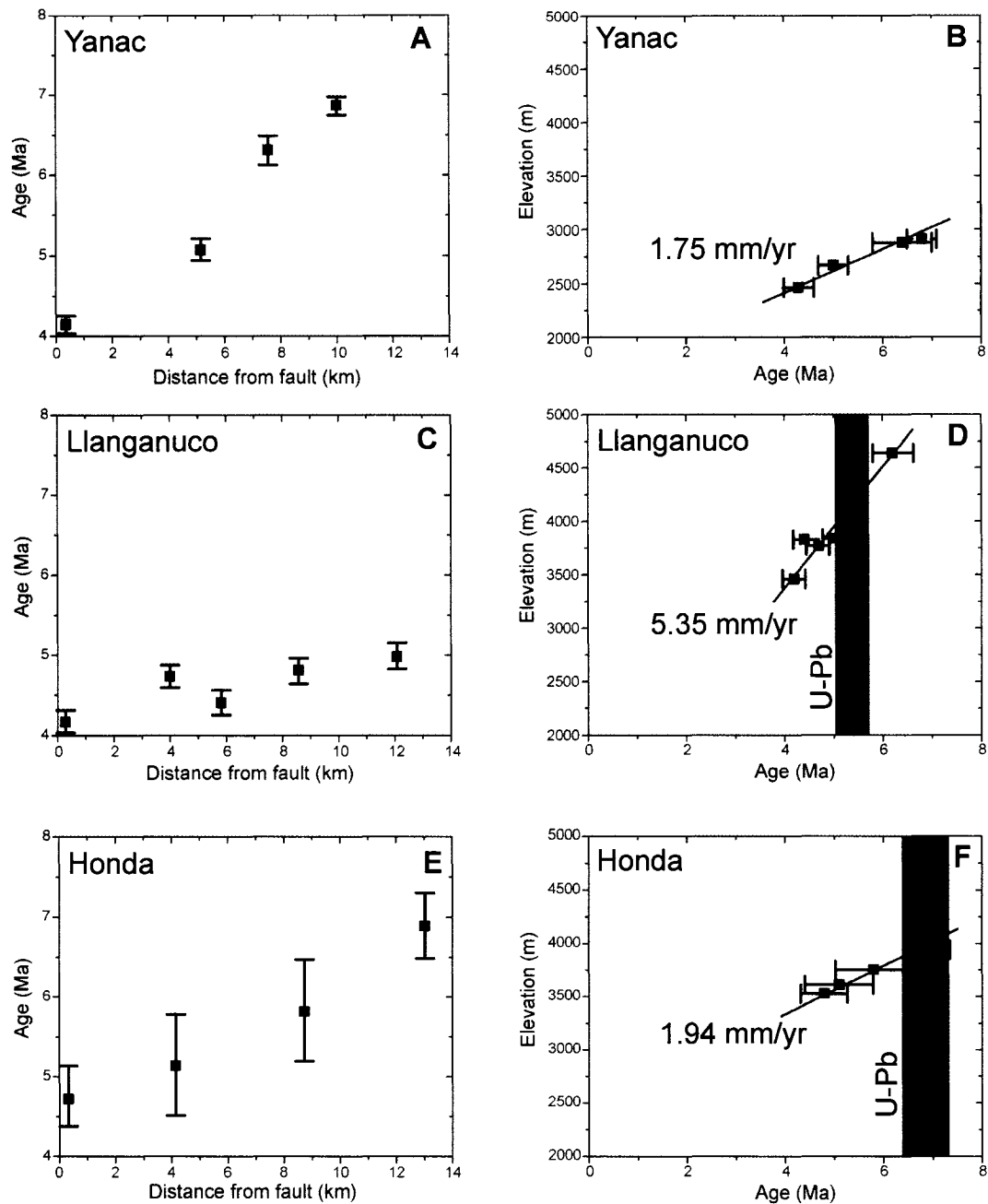


**Figure 4.7.** Age-distance plots and age-elevation plots of biotite  $^{40}\text{Ar}/^{39}\text{Ar}$  data from footwall transects Yanac (A,B), Llanganuco (C,D), and Honda (E,F). Vertical exhumation rates are calculated from slope of age-elevation plots. Youngest U-Pb zircon crystallization age  $\pm 1\sigma$  ( $5.3 \pm 0.3$  Ma) in Llanganuco transect overlaps biotite cooling ages (gray bars). Youngest U-Pb zircon crystallization age  $\pm 1\sigma$  ( $6.3 \pm 0.6$  Ma) from Honda is shown for reference. Anomalously high vertical exhumation rate in Llanganuco may be result of cooling due to batholith intrusion.

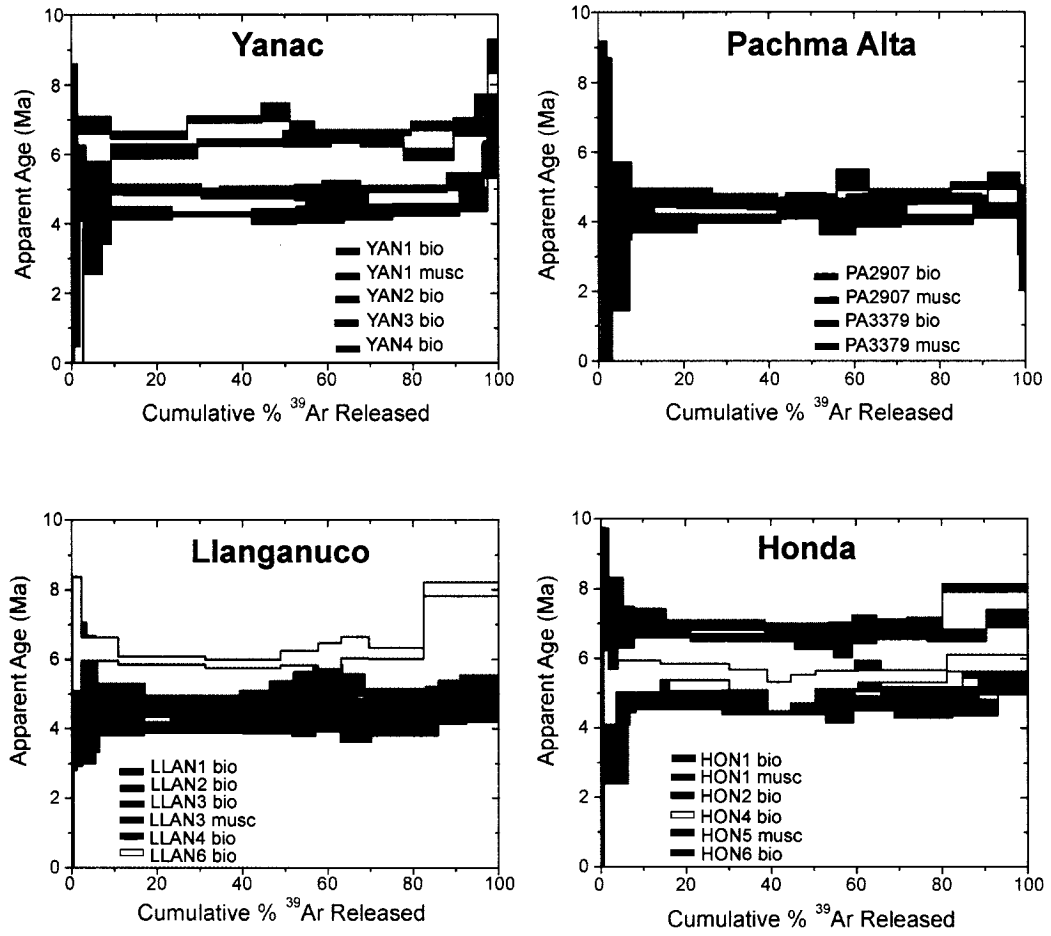


**Figure 4.8.** Mica  $^{40}\text{Ar}/^{39}\text{Ar}$  age spectra from footwall transects through Cordillera Blanca batholith (see Fig. 4.5). Analytical data is listed in Appendix 4.2.

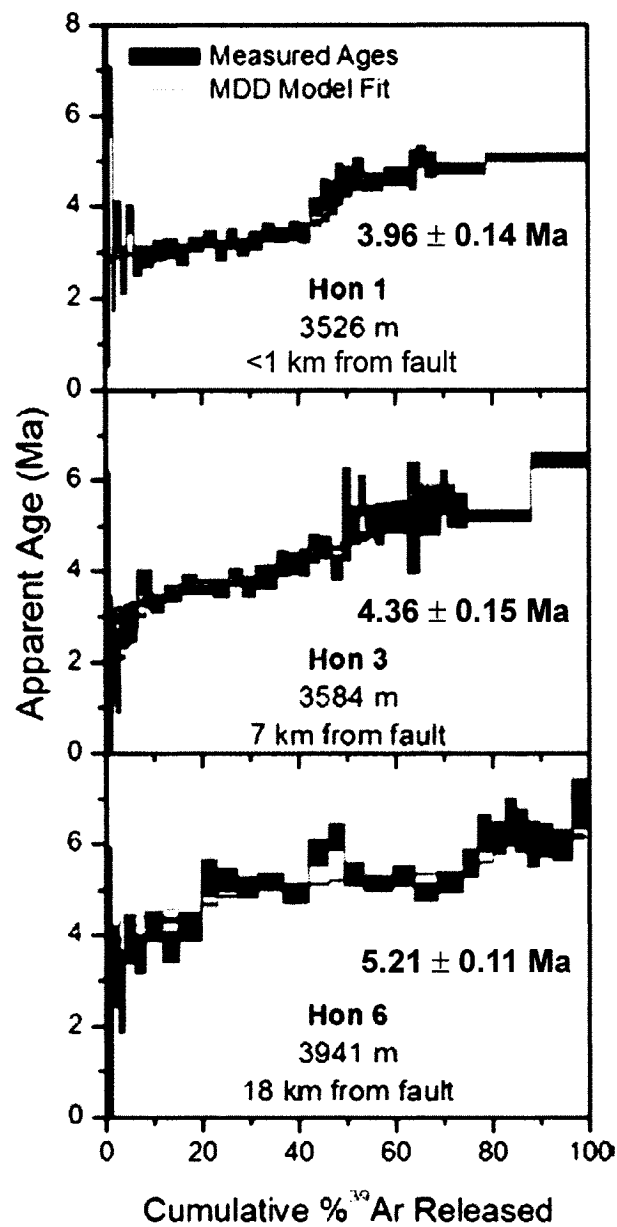


**Figure 4.9.** Results from  $^{40}\text{Ar}/^{39}\text{Ar}$  step-heating K-feldspar from Honda footwall transect, samples HON1, HON3, HON6. Errors are  $\pm 1\sigma$ . Diagrams show age spectra (green) and modeled fits from multidiffusion domain thermal modeling (red).



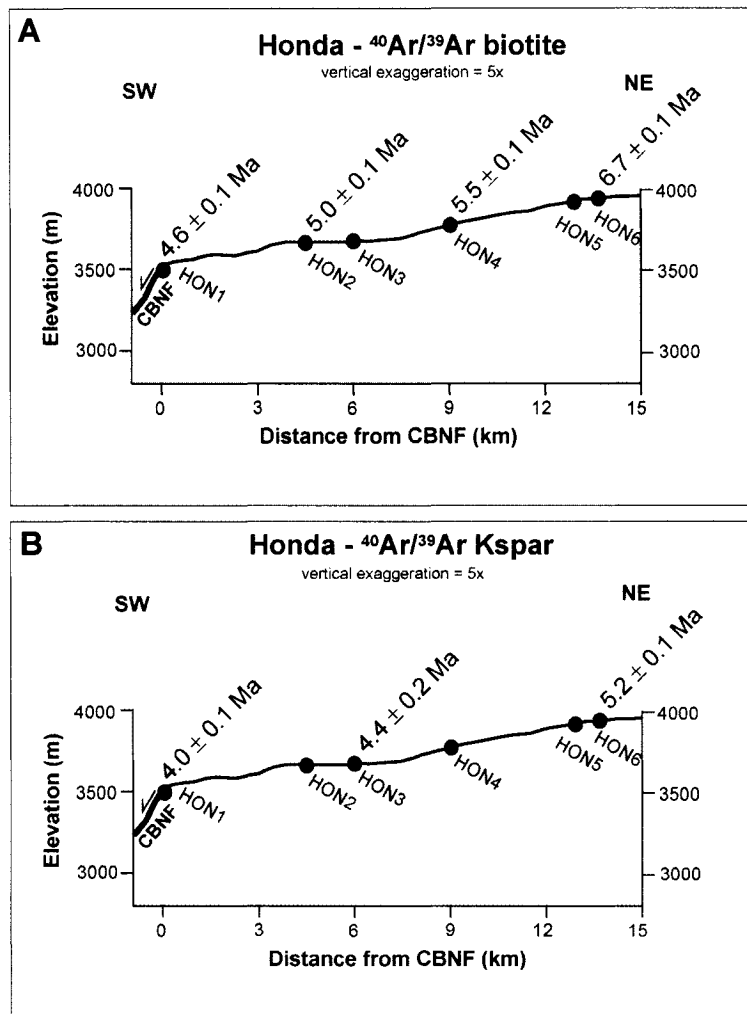


**Figure 4.10** Schematic cross sections of Honda transect.  $^{40}\text{Ar}/^{39}\text{Ar}$  cooling ages from (A) biotite and (B) potassium feldspar are plotted in relation to the Cordillera Blanca normal fault (CBNF). All errors are  $1\sigma$ . For both minerals, footwall cooling ages increase with increasing distance from the fault.

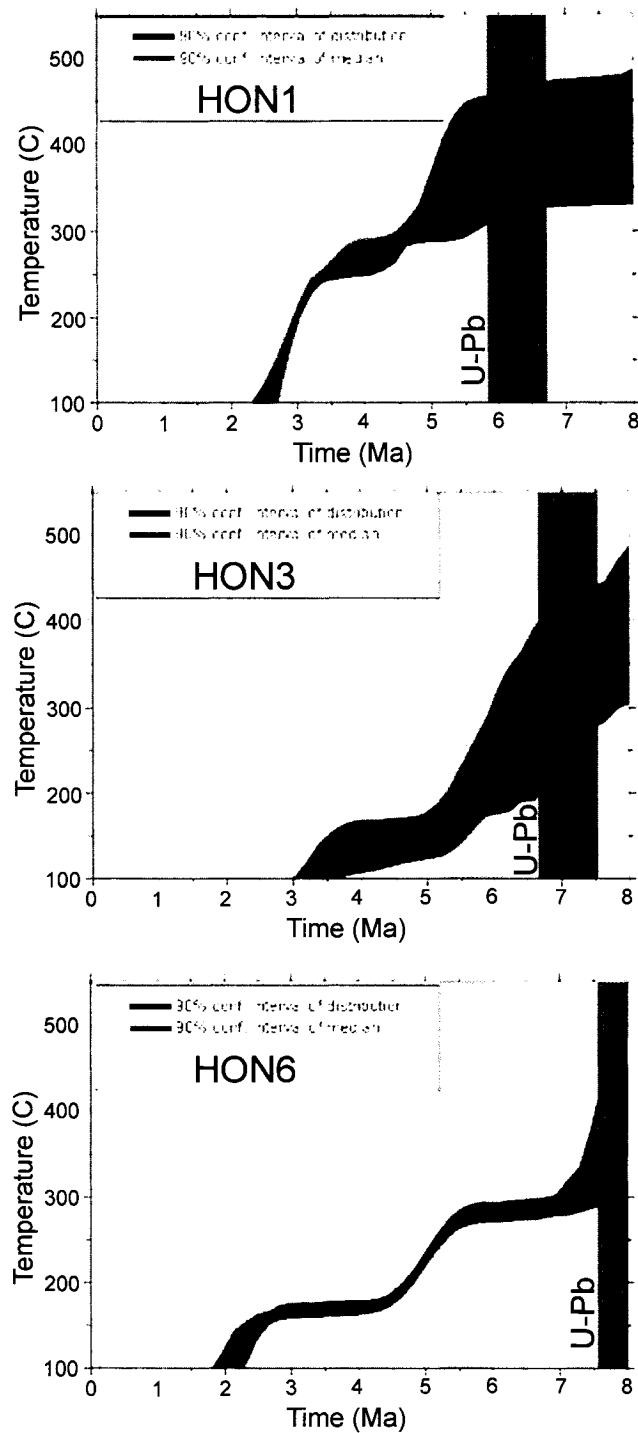


**Figure 4.11.** Multi-diffusion domain thermal model histories for HON1, HON3, HON6 kspars samples. Results indicate rapid footwall cooling between 5-6 Ma for samples further from Cordillera Blanca detachment fault. Rapid cooling began ~3 Ma for HON1, sample closest to fault. U-Pb zircon crystallization ages  $\pm 1\sigma$  (gray bars) are plotted for reference. U-Pb ages are shown in Figure 4.5.

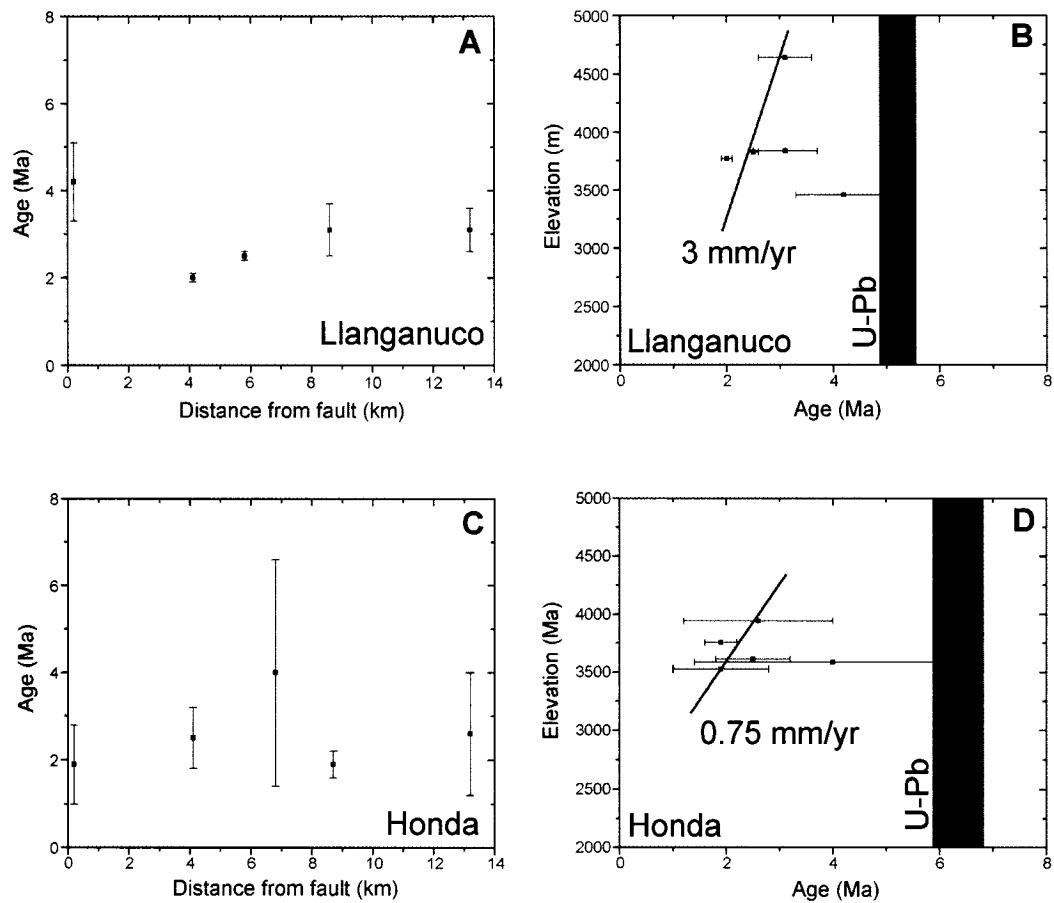


**Figure 4.12.** Age-distance plots and age-elevation plots of apatite (U-Th)/He data from footwall transects Llanganuco (A,B) and Honda (C,D). Vertical exhumation rates are calculated from slopes of age-elevation plots. U-Pb zircon crystallization ages  $\pm 1\sigma$  are shown for reference (gray bars). Anomalously high vertical exhumation rate in Llanganuco may be result of cooling due to batholith intrusion. Llanganuco U-Pb age ( $5.3 \pm 0.3$  Ma). Honda U-Pb age ( $6.3 \pm 0.6$  Ma).

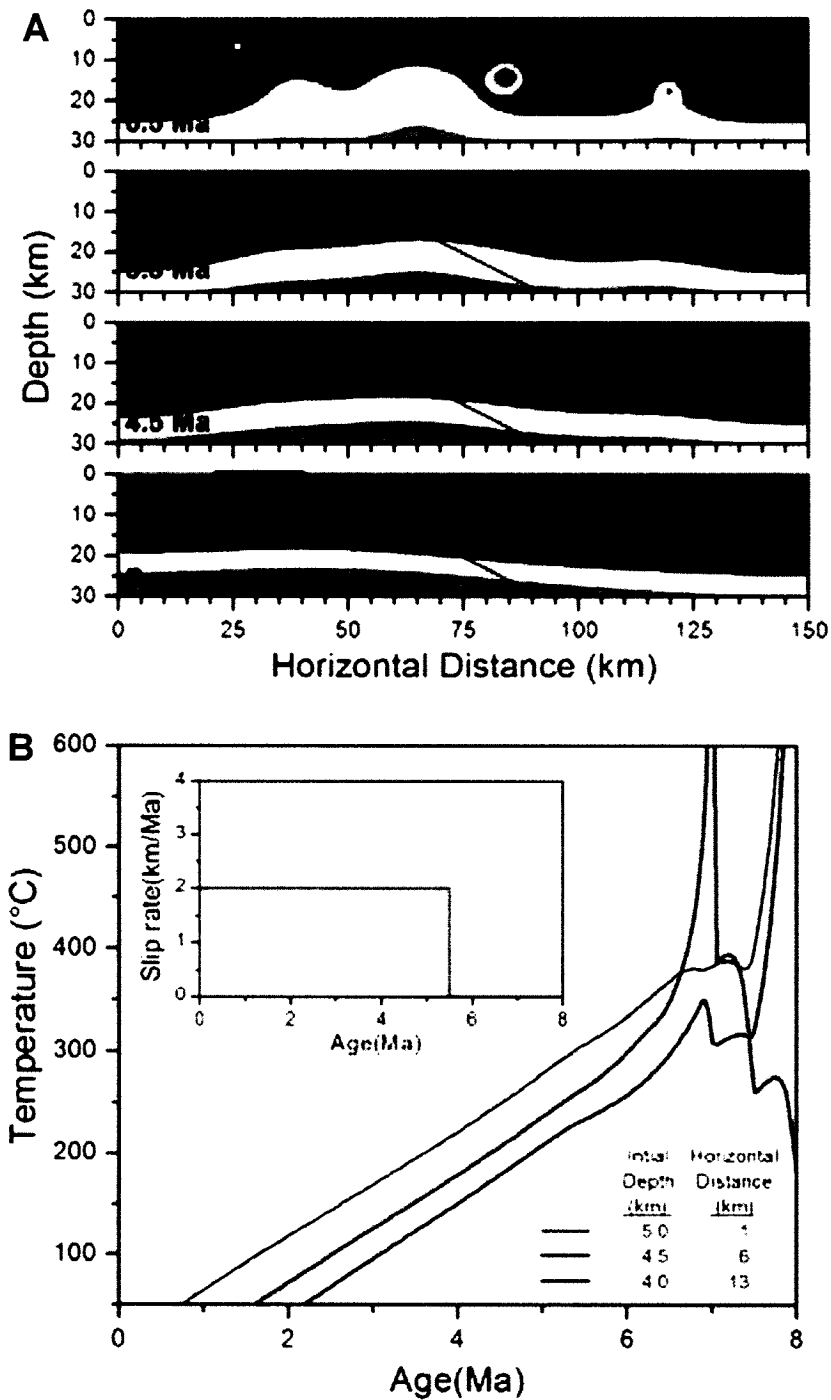


**Figure 4.13.** Thermokinetic models illustrating intrusion and normal faulting. (A) Isothermal snapshots of upper 30 km of crust (see text for details). Spherical intrusions randomly intruded between 8 - 6.5 Ma to simulate batholith intrusion. Slip on normal fault initiated at 5.5 Ma. Bold red line shows position of Honda transect at each time step. (B) Cooling histories of rocks exhumed from positions equivalent to Honda K-feldspars (see Fig. 4.10).

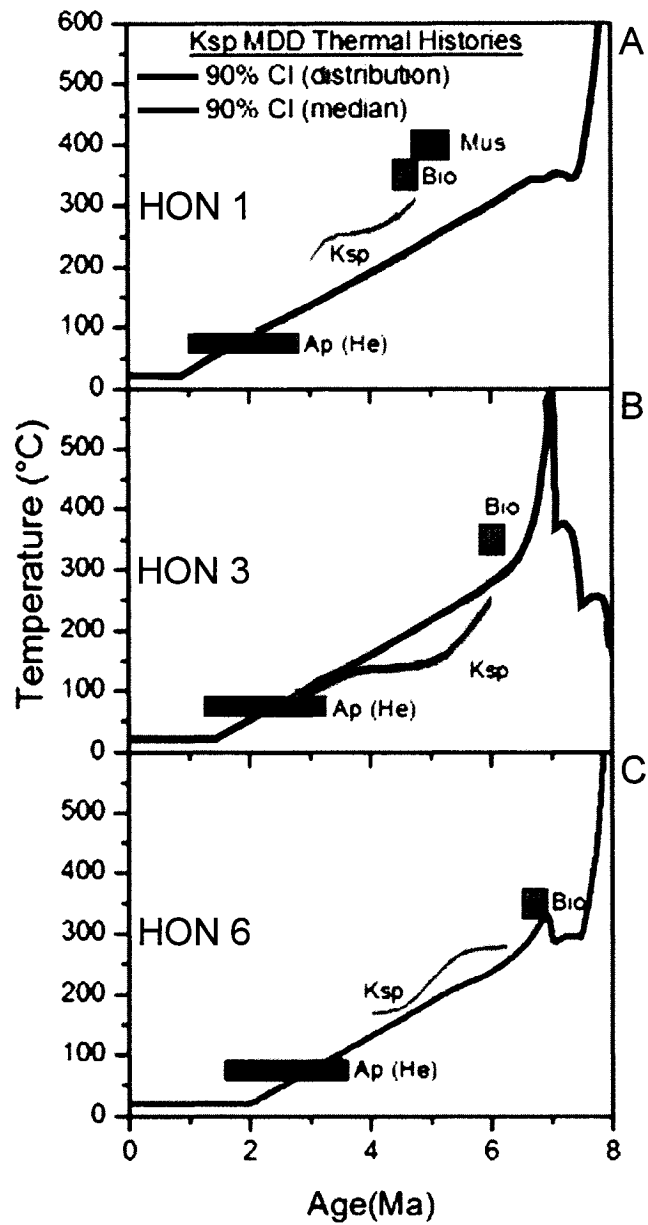


**Figure 4.14.** Thermal histories for Honda transect samples, combining  $^{40}\text{Ar}/^{39}\text{Ar}$  biotite and muscovite analyses, MDD models for  $^{40}\text{Ar}/^{39}\text{Ar}$  K-feldspar results, apatite (U-Th)/He analyses, and results from intrusion numerical models.

**Figure 4.15.** 3D image from DEM of Cordillera Blanca looking southeast along strike. Cordillera Blanca normal fault (bold white line). Thin dashed white lines delineate exposed fault surface. Thin dotted white lines mark shallowing of dips in the updip direction.



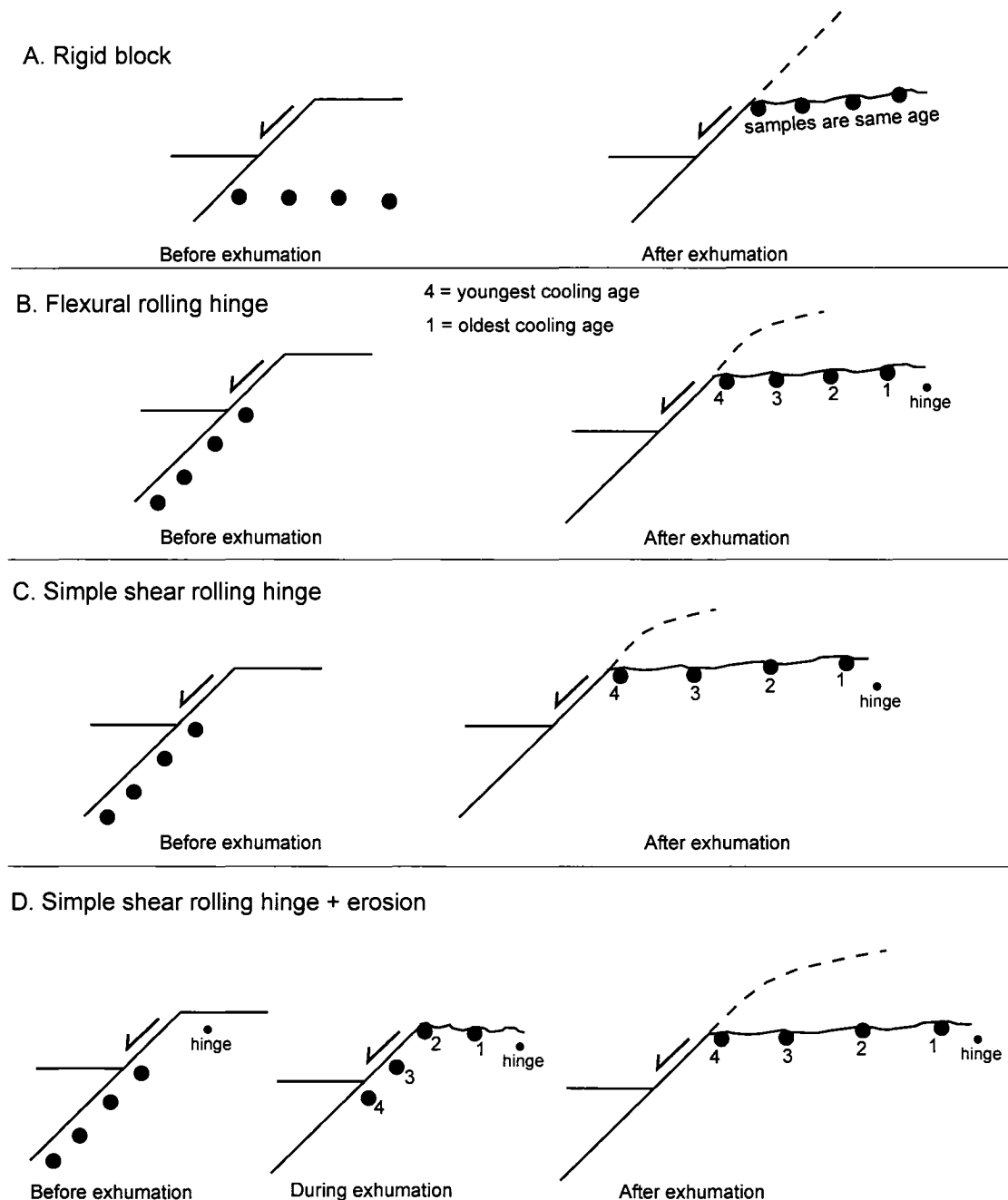
Figure 4.15

**Figure 4.16.** 3D image from DEM of Cordillera Blanca looking northwest along strike. Cordillera Blanca normal fault (bold white line). Thin dashed white lines delineate exposed fault surface. Thin dotted white lines mark shallowing of dips in the updip direction. Convex-up shape of fault surface marked by thick dashed white line.

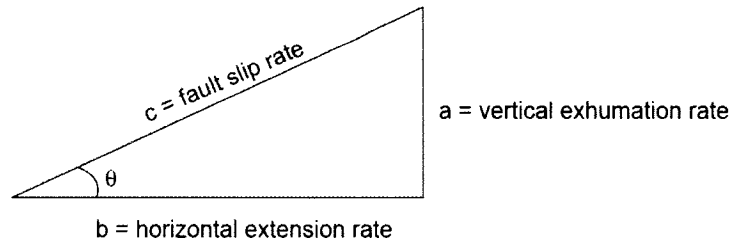




Figure 4.16



**Figure 4.17.** Schematic cross-sections of different rolling-hinge models for exhumation along a normal fault. Dashed lines represent shape of eroded fault surface. (A) A rigid-block fault model results in the same ages along a transect. (B) A flexural rolling hinge exhumes samples beneath the fault surface, such that the structurally lowest sample has the youngest age and is closest to the fault at the surface. (C) A simple shear rolling hinge has the same cooling age pattern as the flexural rolling hinge. The difference is at the surface, where the samples are found further apart than they were at depth. (D) When erosion is taken into account, the hinge migrates away from the fault as exhumation progresses.



$a = \text{closure depth (km)} / \text{cooling age (Ma)}$

$b = a / \tan \theta$

$c = \sqrt{a^2 + b^2}$

assume: geothermal gradient  $25^\circ\text{C/km}$

fault dip  $\theta = 35^\circ$

closure temperatures/depths

Biotite:  $300^\circ\text{C} / 12 \text{ km}$

K-feldspar:  $150^\circ\text{C} / 6 \text{ km}$

Apatite fission-track:  $80^\circ\text{C} / 3.2 \text{ km}$  [Montario, 2001]

Apatite (U-Th)/He:  $65^\circ\text{C} / 2.6 \text{ km}$

**Figure 4.18.** Definitions and calculations of vertical exhumation rate, horizontal extension rate and fault slip rate, with assumed geothermal gradient, fault dip angle, closure temperatures and depths.

Table 4.1 Summary of ages from Cordillera Blanca transects

Sample <sup>a</sup>	Latitude	Longitude	Elevation (m)	Biotite* <sup>40</sup> Ar/ <sup>39</sup> Ar ± 1σ (Ma)	Muscovite* <sup>40</sup> Ar/ <sup>39</sup> Ar ± 1σ (Ma)	K-feldspar* <sup>40</sup> Ar/ <sup>39</sup> Ar ± 1σ (Ma)	Apatite (U-Th)/He* ± 1σ (Ma)	Apatite FT ± 1σ (Ma) [Montario, 2001]
YAN1	8°40.142'	77°53.230'	2462	4.30 ± 0.05	5.07 ± 0.09			
YAN2	8°38.375'	77°52.893'	2668	4.98 ± 0.04				
YAN3	8°36.789'	77°51.862'	2878	6.37 ± 0.13				
YAN4	8°36.447'	77°50.875'	2911	6.77 ± 0.06				
PA2907	8°45.835'	77°50.786'	2907	4.11 ± 0.07	4.53 ± 0.52			
PA3379	8°45.489'	77°50.443'	3379	4.63 ± 0.18	4.84 ± 0.11			
LLAN1	9°06.132'	77°40.743'	3457	4.14 ± 0.09			4.18 ± 0.92	2.3 ± 1.2
LLAN2	9°04.703'	77°39.271'	3769	4.67 ± 0.12			1.97 ± 0.13	
LLAN3	9°04.115'	77°38.646'	3827	4.42 ± 0.07	4.82 ± 0.06		2.51 ± 0.15	2.9 ± 0.6
LLAN4	9°03.076'	77°37.725'	3838	4.97 ± 0.06			3.08 ± 0.58	3.0 ± 0.7
LLAN6	9°02.858'	77°35.293'	4639	6.22 ± 0.21			3.13 ± 0.46	
HON1	9°19.953'	77°30.199'	3526	4.62 ± 0.07	4.92 ± 0.12	3.96 ± 0.14	1.87 ± 0.85	
HON2	9°19.196'	77°28.015'	3610	4.99 ± 0.09			2.51 ± 0.72	
HON3	9°18.658'	77°26.776'	3584			4.36 ± 0.15	4.01 ± 2.59	
HON4	9°18.170'	77°25.798'	3753	5.49 ± 0.10			1.95 ± 0.28	
HON5	9°17.507'	77°24.037'	3886		7.25 ± 0.16			
HON6	9°17.486'	77°23.818'	3941	6.68 ± 0.07		5.21 ± 0.11	2.59 ± 1.36	

\* Weighted mean ages

<sup>a</sup> Map location on Figure 4.2

**Table 4.2 Calculated average rates for Cordillera Blanca transects ( $\pm 1\sigma$ )**

<b>Transect</b>	<b>Mineral/ Thermochronometer</b>	<b>Vertical exhumation rate (mm/yr)</b>	<b>Horizontal extension rate (mm/yr)</b>	<b>Fault slip rate (mm/yr)</b>
Yanac (YAN) <sup>‡</sup>	Biotite <sup>40</sup> Ar/ <sup>39</sup> Ar (n = 4)	2.21 ± 0.47	3.16 ± 0.68	3.86 ± 0.83
Llanganuco (LLAN) <sup>‡</sup>	Biotite <sup>40</sup> Ar/ <sup>39</sup> Ar (n = 5)	2.51 ± 0.37	3.57 ± 0.53	4.36 ± 0.64
	Apatite Fission-track <sup>†</sup> (n = 3)	1.19 ± 0.18	1.70 ± 0.25	2.07 ± 0.31
	Apatite (U-Th)/He (n = 5)	0.93 ± 0.26	1.33 ± 0.37	1.62 ± 0.45
Honda (HON) <sup>‡</sup>	Biotite <sup>40</sup> Ar/ <sup>39</sup> Ar (n = 4)	2.25 ± 0.34	3.21 ± 0.49	3.92 ± 0.60
	K-feldspar <sup>40</sup> Ar/ <sup>39</sup> Ar (n = 3)	1.35 ± 0.18	1.93 ± 0.27	2.35 ± 0.33
	Apatite (U-Th)/He (n = 5)	1.08 ± 0.30	1.55 ± 0.42	1.89 ± 0.52

<sup>‡</sup> Vertical exhumation rates calculated for each sample, which is then used to calculate other rates for each sample.

Average values for each transect are listed here. Raw data listed in Appendix 4.3.

Assumptions made in calculations listed in Figure 4.17.

<sup>†</sup> Ages from *Montario* [2001].

**Table 4.3 Raw calculations of exhumation, extension, and slip rates**

<b>Sample – mineral*</b>	<b>Closure depth (km)</b>	<b>Age (Ma)</b>	<b>a – vertical exhumation rate (mm/yr)</b>	<b>b – horizontal extension rate (mm/yr)</b>	<b>c – fault slip rate (mm/yr)</b>
YAN1 - bio	12	4.30	2.79	3.98	4.86
YAN2 - bio	12	4.98	2.41	3.44	4.20
YAN3 - bio	12	6.37	1.88	2.68	3.27
YAN4 - bio	12	6.77	1.77	2.53	3.09
LLAN1 - bio	12	4.14	2.90	4.14	5.05
LLAN2 - bio	12	4.67	2.57	3.67	4.48
LLAN3 - bio	12	4.42	2.71	3.87	4.72
LLAN4 - bio	12	4.97	2.41	3.44	4.20
LLAN6 - bio	12	6.22	1.93	2.75	3.36
LLAN1 - AHe	2.6	4.18	0.62	0.89	1.08
LLAN2 - AHe	2.6	1.97	1.32	1.86	2.27
LLAN3 - AHe	2.6	2.51	1.04	1.49	1.82
LLAN4 - AHe	2.6	3.08	0.84	1.20	1.46
LLAN5 - AHe	2.6	3.13	0.83	1.19	1.45
LLAN1 - AFT	3.2	2.30	1.39	1.99	2.43
LLAN3 - AFT	3.2	2.90	1.10	1.57	1.92
LLAN4 - AFT	3.2	3.00	1.07	1.53	1.87
HON1 - bio	12	4.62	2.60	3.71	4.53
HON2 - bio	12	4.99	2.40	3.43	4.19
HON4 - bio	12	5.49	2.19	3.13	3.82
HON6 - bio	12	6.68	1.80	2.57	3.14
HON1 - kspar	6	3.96	1.52	2.17	2.65
HON3 - kspar	6	4.36	1.38	1.97	2.41
HON6 - kspar	6	5.21	1.15	1.64	2.00
HON1 - AHe	2.6	1.87	1.39	1.99	2.43
HON2 - AHe	2.6	2.51	1.04	1.49	1.82
HON3 - AHe	2.6	4.01	0.65	0.93	1.13
HON4 - AHe	2.6	1.95	1.33	1.90	2.32
HON6 - AHe	2.6	2.59	1.00	1.43	1.74

\* bio =  $^{40}\text{Ar}/^{39}\text{Ar}$  cooling age of biotite

AHe = apatite (U-Th)/He age

AFT = apatite fission-track age

kspar =  $^{40}\text{Ar}/^{39}\text{Ar}$  cooling age of potassium feldspar

# APPENDIX 4.1 U-Pb ZIRCON ISOTOPIC DATA

HON 1								
U (ppm)	Th (ppm)	Th/U	<sup>206</sup> Pb/ <sup>238</sup> U Age (Ma)	<sup>206</sup> Pb/ <sup>238</sup> U 1	% Radiogenic <sup>206</sup> Pb	<sup>206</sup> Pb/ <sup>238</sup> U Age (Ma)	<sup>206</sup> Pb/ <sup>238</sup> U 1	% Radiogenic <sup>207</sup> Pb
56	24	0.42	5.7	0.9	52.4	7.6	17.1	7.3
175	98	0.56	5.9	0.4	78.7	5.8	6.3	16.5
464	167	0.36	5.9	0.3	92.3	5.1	2.3	36.2
3072	104	0.03	5.9	0.1	98.0	6.0	0.5	73.9
219	33	0.15	6.1	0.3	83.4	4.8	5.7	17.7
2197	351	0.16	6.1	0.1	98.4	5.5	0.5	75.0
3553	223	0.06	6.3	0.1	98.3	5.8	0.6	74.4
2786	377	0.14	6.3	0.2	98.5	6.9	0.6	80.3
5375	159	0.03	6.3	0.1	99.0	6.7	0.5	85.3
3609	193	0.05	6.4	0.1	98.7	6.7	0.4	82.1
1819	321	0.18	6.5	0.2	97.0	6.3	1.1	63.4
3807	447	0.12	6.5	0.2	98.8	6.4	0.5	81.5
1159	175	0.15	6.5	0.2	94.3	6.2	1.7	46.6
954	221	0.23	8.1	0.3	96.5	9.1	1.5	63.4
3122	558	0.18	8.6	0.2	97.1	7.5	0.8	62.1
2197	341	0.16	8.8	0.2	96.2	5.3	1.0	45.7
1895	85	0.05	9.2	0.2	97.2	8.1	0.9	63.2
994	109	0.11	9.8	0.3	96.6	10.2	2.2	62.2
1881	765	0.41	10.7	0.3	98.0	10.9	1.1	73.9
1174	598	0.51	13.6	0.3	98.4	15.0	1.6	79.5
858	69	0.08	13.8	0.3	97.2	15.2	2.1	68.1
1605	598	0.37	14.0	0.3	98.5	12.5	1.1	76.1
567	193	0.34	19.8	0.6	96.9	19.2	3.2	63.2
550	20	0.04	45.1	1.2	98.5	43.9	3.9	77.7
HON 2								
U (ppm)	Th (ppm)	Th/U	<sup>206</sup> Pb/ <sup>238</sup> U Age (Ma)	<sup>206</sup> Pb/ <sup>238</sup> U 1	% Radiogenic <sup>206</sup> Pb	<sup>206</sup> Pb/ <sup>238</sup> U Age (Ma)	<sup>206</sup> Pb/ <sup>238</sup> U 1	% Radiogenic <sup>207</sup> Pb
120	105	0.88	5.2	0.5	64.2	-3.0	9.4	-5.9
254	240	0.94	6.0	0.3	84.0	3.3	4.1	13.7
1027	77	0.07	6.1	0.2	97.2	5.7	1.4	64.1
1053	447	0.42	6.2	0.2	95.7	6.8	1.4	57.6
535	115	0.22	6.3	0.2	92.5	7.1	2.4	43.3
2400	190	0.08	6.3	0.2	98.0	6.7	0.7	74.4
929	192	0.21	6.6	0.2	96.7	6.2	1.6	61.1
4573	245	0.05	6.6	0.2	99.1	7.2	0.4	86.8
5489	409	0.07	6.8	0.1	98.8	7.3	0.4	83.4
2617	1445	0.55	7.2	0.2	98.1	7.4	0.9	74.4
6604	703	0.11	8.5	0.2	99.5	8.8	0.4	92.5
1416	87	0.06	9.1	0.2	98.1	8.5	1.0	73.1
1590	575	0.36	11.4	0.3	98.3	12.2	1.0	77.2
869	392	0.45	12.6	0.4	96.5	10.1	2.2	55.2
356	103	0.29	14.9	0.5	94.7	13.4	4.0	46.9
6114	330	0.05	25.2	0.6	99.9	25.6	0.8	97.4

<b>HON 3</b>								
U (ppm)	Th (ppm)	Th/U	$^{206}\text{Pb}/^{238}\text{U}$ Age (Ma)	$^{206}\text{Pb}/^{238}\text{U}$ 1	% Radiogenic $^{206}\text{Pb}$	$^{206}\text{Pb}/^{238}\text{U}$ Age (Ma)	$^{206}\text{Pb}/^{238}\text{U}$ 1	% Radiogenic $^{207}\text{Pb}$
180	174	0.97	6.7	0.6	74.7	4.6	8.3	9.8
4193	129	0.03	7.0	0.2	98.8	7.7	0.4	83.4
3628	124	0.03	7.0	0.2	99.1	7.5	0.4	86.1
1264	138	0.11	7.1	0.2	97.0	7.7	1.3	66.5
247	37	0.15	7.1	0.4	89.5	7.3	4.1	32.5
2521	224	0.09	7.1	0.2	98.5	7.6	0.8	79.1
4223	132	0.03	7.2	0.2	99.2	7.3	0.4	87.4
5196	210	0.04	7.2	0.2	99.2	7.7	0.4	87.6
926	161	0.17	7.5	0.2	96.7	7.1	1.3	60.9
4962	918	0.19	9.8	0.2	99.5	10.2	0.5	91.4
1103	363	0.33	13.2	0.3	100.3	17.6	1.5	104.9
3327	154	0.05	14.2	0.3	99.3	14.7	0.7	88.7
2579	291	0.11	14.8	0.3	98.9	14.1	0.6	82.8
893	770	0.86	22.8	0.6	99.3	23.7	2.4	88.8
825	509	0.62	31.6	0.8	98.4	29.6	2.7	76.7
441	85	0.19	145	4	98.4	165.9	5.6	80.9
3521	417	0.12	216	5	99.9	210.9	4.7	97.6
9702	789	0.08	275	222	99.6	253.2	186.1	92.7
360	113	0.31	796	17	100.6	904.1	14.4	106.9
<b>HON 4</b>								
U (ppm)	Th (ppm)	Th/U	$^{206}\text{Pb}/^{238}\text{U}$ Age (Ma)	$^{206}\text{Pb}/^{238}\text{U}$ 1	% Radiogenic $^{206}\text{Pb}$	$^{206}\text{Pb}/^{238}\text{U}$ Age (Ma)	$^{206}\text{Pb}/^{238}\text{U}$ 1	% Radiogenic $^{207}\text{Pb}$
815	135	0.17	22.5	0.5	98.1	21.2	2.7	72.9
657	260	0.40	22.6	0.5	98.0	23.5	3.6	73.6
748	139	0.19	22.9	0.5	98.2	24.4	2.1	76.2
748	134	0.18	22.9	0.5	98.3	22.9	2.1	76.3
806	149	0.18	23.1	0.5	97.9	23.9	3.1	73.1
1016	169	0.17	23.2	0.5	98.2	24.9	3.3	76.5
2425	372	0.15	23.4	0.5	99.7	24.3	1.0	95.3
538	237	0.44	23.6	0.6	97.2	22.7	5.3	64.8
1006	316	0.31	23.7	0.5	98.8	23.3	2.5	81.9
1098	294	0.27	23.8	0.5	98.9	24.3	2.5	84.2
476	72	0.15	25.3	0.6	98.2	28.5	3.4	77.5
<b>HON 6</b>								
U (ppm)	Th (ppm)	Th/U	$^{206}\text{Pb}/^{238}\text{U}$ Age (Ma)	$^{206}\text{Pb}/^{238}\text{U}$ 1	% Radiogenic $^{206}\text{Pb}$	$^{206}\text{Pb}/^{238}\text{U}$ Age (Ma)	$^{206}\text{Pb}/^{238}\text{U}$ 1	% Radiogenic $^{207}\text{Pb}$
1013	269	0.27	7.6	0.2	96.1	6.4	1.7	53.3
2883	804	0.28	7.8	0.2	98.6	8.6	0.9	80.9
1298	340	0.26	7.9	0.2	97.0	8.8	1.6	66.4
1585	209	0.13	8.0	0.2	97.6	8.2	1.2	69.9
836	263	0.31	8.1	0.2	96.3	8.3	1.5	59.5
248	58	0.23	8.2	0.4	87.1	7.1	4.9	23.9
2835	476	0.17	8.3	0.2	99.0	9.0	0.7	85.0
1012	452	0.45	8.3	0.2	95.2	8.0	2.3	51.6
586	220	0.38	8.4	0.3	94.0	11.6	3.9	54.5
351	42	0.12	9.8	0.4	89.7	8.4	4.7	29.2
351	162	0.46	10.0	0.4	92.2	11.5	5.9	42.5



<b>HON 6</b>								
U (ppm)	Th (ppm)	Th/U	<sup>206</sup> Pb/ <sup>238</sup> U Age (Ma)	<sup>206</sup> Pb/ <sup>238</sup> U 1	% Radiogenic <sup>206</sup> Pb	<sup>206</sup> Pb/ <sup>238</sup> U Age (Ma)	<sup>206</sup> Pb/ <sup>238</sup> U 1	% Radiogenic <sup>207</sup> Pb
209	41	0.19	10.3	0.5	88.9	12.2	6.7	34.3
465	503	1.08	11.9	0.4	92.1	8.9	5.6	32.6
1046	448	0.43	23.4	0.5	99.2	26.0	2.4	89.0
420	180	0.43	25.1	0.7	93.2	11.9	7.2	26.4
771	314	0.41	146.9	3.2	100.0	154.0	5.1	100.2

<b>LLAN 1</b>								
U (ppm)	Th (ppm)	Th/U	<sup>206</sup> Pb/ <sup>238</sup> U Age (Ma)	<sup>206</sup> Pb/ <sup>238</sup> U 1	% Radiogenic <sup>206</sup> Pb	<sup>206</sup> Pb/ <sup>238</sup> U Age (Ma)	<sup>206</sup> Pb/ <sup>238</sup> U 1	% Radiogenic <sup>207</sup> Pb
444	160	0.36	7.0	0.3	90.2	5.8	3.8	29.2
198	75	0.38	7.1	0.5	84.8	8.9	6.3	27.1
278	91	0.33	7.2	0.3	86.9	10.9	6.5	35.6
209	130	0.62	7.2	0.5	82.9	9.6	6.3	25.7
2254	835	0.37	7.2	0.2	97.8	7.0	1.0	70.6
2104	619	0.29	7.3	0.2	97.9	7.7	1.0	73.7
1635	512	0.31	7.3	0.2	97.7	8.7	1.5	74.0
368	151	0.41	7.9	0.3	88.1	9.3	4.7	32.2
573	200	0.35	8.0	0.2	94.0	7.6	2.5	45.2
1879	378	0.20	8.0	0.2	98.1	10.0	1.0	78.2
859	307	0.36	9.4	0.2	97.2	10.7	1.8	68.3
315	175	0.56	9.4	0.4	92.6	12.5	5.9	47.6
994	138	0.14	10.4	0.3	96.0	9.3	2.3	54.6
545	109	0.20	12.2	0.3	96.0	13.8	3.8	59.9
650	852	1.31	13.3	0.3	105.5	31.7	3.0	163.0
1383	602	0.44	13.4	0.3	97.9	13.3	1.5	72.4
208	178	0.85	13.8	0.6	90.3	20.5	9.9	43.0
470	174	0.37	14.8	0.5	95.3	14.1	4.0	51.8
370	145	0.39	25.3	0.7	96.6	24.4	4.9	60.6
523	149	0.29	27.0	0.8	96.5	27.3	6.6	60.9
50	23	0.45	551.7	19.4	98.7	555.2	32.6	84.7

<b>LLAN 2</b>								
U (ppm)	Th (ppm)	Th/U	<sup>206</sup> Pb/ <sup>238</sup> U Age (Ma)	<sup>206</sup> Pb/ <sup>238</sup> U 1	% Radiogenic <sup>206</sup> Pb	<sup>206</sup> Pb/ <sup>238</sup> U Age (Ma)	<sup>206</sup> Pb/ <sup>238</sup> U 1	% Radiogenic <sup>207</sup> Pb
199	131	0.66	4.7	0.6	62.6	2.6	12.2	5
281	277	0.98	5.0	0.4	70.4	2.4	9.6	6
594	382	0.64	5.2	0.3	84.8	1.5	5.2	8
3833	313	0.08	5.3	0.1	97.2	5.4	0.8	66
713	218	0.31	5.3	0.6	73.2	3.4	9.9	8.4
1879	227	0.12	5.3	0.2	94.9	5.3	1.1	51
422	278	0.66	5.4	0.4	76.8	1.9	7.4	6
1455	211	0.14	5.4	0.3	85.3	9.3	6.2	34.4
230	160	0.70	5.5	0.4	78.7	3.9	6.1	12.2
577	510	0.88	5.5	0.2	98.0	6.7	1.7	77
171	68	0.40	5.6	0.6	40.4	-0.7	13.2	-1
189	153	0.81	6.2	0.5	76.4	3.2	7.4	8.2
146	110	0.75	7.2	0.7	75.7	10.9	9.5	19.9
749	554	0.74	7.8	0.6	83.7	13.2	11.4	32.2
448	6	0.01	7.8	0.3	89.9	9.1	3.6	36.3
1553	369	0.24	8.9	4.2	90.6	26.8	42.1	41.1

1550	240	0.15	9.1	0.2	97.3	10.1	1.7	69
584	151	0.26	9.8	0.5	89.4	11.3	5.2	35
791	149	0.19	11.4	0.4	93.2	13.5	5.0	47
489	109	0.22	12.0	0.3	93.4	12.5	5.1	44.7
357	96	0.27	14.9	1.2	82.2	19.6	19.8	24.5
295	82	0.28	62.8	2.4	95.0	91.5	23.5	61.4

LLAN 3								
U (ppm)	Th (ppm)	Th/U	$^{206}\text{Pb}/^{238}\text{U}$ Age (Ma)	$^{206}\text{Pb}/^{238}\text{U}$ 1	% Radiogenic $^{206}\text{Pb}$	$^{206}\text{Pb}/^{238}\text{U}$ Age (Ma)	$^{206}\text{Pb}/^{238}\text{U}$ 1	% Radiogenic $^{207}\text{Pb}$
187	46	0.25	5.3	0.4	82.6	3.4	4.9	14.2
338	84	0.25	5.3	0.2	90.0	6.0	3.7	36.2
2368	140	0.06	5.6	0.1	98.1	6.4	0.7	76.7
1477	137	0.09	5.7	0.1	97.4	5.9	0.9	68.5
3506	187	0.05	5.7	0.1	99.0	6.0	0.5	85.6
364	190	0.52	5.7	0.3	83.6	1.8	4.4	8.2
88	59	0.67	5.9	0.7	65.6	10.9	10.6	15.9
145	97	0.67	6.0	0.6	80.1	9.1	7.8	24.9
243	86	0.36	6.1	0.4	84.0	5.0	6.4	18.8
930	382	0.41	6.2	0.2	96.2	7.2	1.5	62.3
249	104	0.42	8.4	0.3	91.2	14.5	5.5	49.9
292	22	0.08	9.5	0.4	90.6	10.5	4.5	36.8
367	68	0.19	70.6	1.6	96.2	41.6	5.2	45.4

LLAN 4								
U (ppm)	Th (ppm)	Th/U	$^{206}\text{Pb}/^{238}\text{U}$ Age (Ma)	$^{206}\text{Pb}/^{238}\text{U}$ 1	% Radiogenic $^{206}\text{Pb}$	$^{206}\text{Pb}/^{238}\text{U}$ Age (Ma)	$^{206}\text{Pb}/^{238}\text{U}$ 1	% Radiogenic $^{207}\text{Pb}$
186	106	0.57	5.6	0.3	97.8	9.122	2.35	80.5
576	306	0.53	6.4	0.2	94.1	8.108	1.69	53
311	178	0.57	6.4	0.3	88.8	7.841	4	34.6
1028	381	0.37	6.4	0.2	95.2	6.427	1.95	52.4
77	35	0.45	6.5	0.5	77	11.44	8.41	24.6
502	321	0.64	6.5	0.2	93.3	5.114	2.88	37.5
1990	297	0.15	6.5	0.1	98.5	6.437	0.49	77.7
1395	581	0.42	6.6	0.2	97.7	7.484	1.19	72.8
301	134	0.45	6.6	0.3	87.5	4.731	3.16	21.6
474	676	1.43	6.6	0.3	96.6	8.51	3.75	66.8
221	60	0.27	6.8	0.4	84.4	9.83	5.61	30.1
2486	593	0.24	6.9	0.1	98.5	7.906	0.492	81.3
238	159	0.67	7.2	0.4	87.3	9.506	4.17	33.4
608	239	0.39	7.5	0.2	95.4	9.548	2.27	59.9
95	55	0.58	7.5	0.5	81	18.25	9.17	36.1
537	188	0.35	8.3	0.2	94.8	8.657	2.83	51.3
590	46	0.08	11.1	0.2	94.5	11.23	2.97	49.2

**LLAN 5**

U (ppm)	Th (ppm)	Th/U	$^{206}\text{Pb}/^{238}\text{U}$ Age (Ma)	$^{206}\text{Pb}/^{238}\text{U}$ 1	% Radiogenic $^{206}\text{Pb}$	$^{206}\text{Pb}/^{238}\text{U}$ Age (Ma)	$^{206}\text{Pb}/^{238}\text{U}$ 1	% Radiogenic $^{207}\text{Pb}$
236	111	0.47	6.7	0.7	74.4	16.1	9.6	28
575	231	0.40	6.7	0.2	88.8	7.4	3.5	33
198	99	0.50	6.8	0.9	76.1	13.5	13.7	26
1340	293	0.22	7.0	0.2	94.0	7.9	2.9	49
822	421	0.51	7.1	0.2	91.1	6.3	3.0	34
162	79	0.49	7.2	0.9	68.8	11.6	17.7	16
170	78	0.46	7.2	0.8	71.5	10.6	14.0	17
1533	501	0.33	7.3	0.2	95.0	9.4	2.4	57
263	123	0.47	7.5	0.7	80.8	14.5	11.9	31
4172	461	0.11	7.5	0.2	98.1	8.3	1.2	76
4301	1078	0.25	8.2	0.1	96.5	8.0	1.6	60
432	27	0.06	8.9	0.7	81.7	11.9	9.5	24
314	46	0.15	11.4	0.6	83.5	8.4	10.2	17
823	118	0.14	12.5	0.4	95.2	12.6	3.3	52
293	112	0.38	13.1	0.8	87.1	8.4	6.4	19
1825	655	0.36	14.7	0.3	96.8	13.8	1.7	62
437	22	0.05	15.7	0.7	91.0	15.1	7.5	35
2526	158	0.06	17.1	0.3	98.5	17.6	1.8	79

# APPENDIX 4.2. <sup>40</sup>Ar/<sup>39</sup>Ar ISOTOPIC DATA FROM MUSCOVITE AND BIOTITE STEP-HEATING ANALYSES

YANI	Muscovite	6.4 mg	J=0.003524											
T (°C)	t (min)	<sup>40</sup> Ar/ <sup>39</sup> Ar	<sup>39</sup> Ar/ <sup>39</sup> Ar	<sup>37</sup> Ar/ <sup>39</sup> Ar	<sup>36</sup> Ar/ <sup>39</sup> Ar	<sup>35</sup> Ar/ <sup>39</sup> Ar	<sup>34</sup> Ar/ <sup>39</sup> Ar	<sup>33</sup> Ar (mol)	Σ <sup>39</sup> Ar	% <sup>40</sup> Ar*	<sup>40</sup> Ar*/ <sup>39</sup> Ar <sub>K</sub>	±σ <sub>mass</sub>	Age (Ma)	±σ <sub>Age</sub>
500	13	288.4203	0.2310428	8.74E-02	0.9743425	3.24E-15	0.4841133	0.1651023	0.4765029	17.18085	3.03	109.07		
600	13	10.76264	2.23E-02	4.23E-02	3.38E-02	4.40E-15	1.142011	6.940193	0.7556865	0.4638079	4.80	2.94		
700	13	9.743388	1.88E-02	1.47E-02	3.01E-02	1.48E-14	3.349947	8.343143	0.8160352	0.171948	5.18	1.09		
770	13	5.538505	1.60E-02	3.92E-02	1.58E-02	3.67E-14	8.838202	0.8237604	8.88E-02	5.23	0.56			
840	13	1.754575	1.32E-02	9.26E-04	3.11E-03	1.44E-13	30.43603	45.58718	0.8016055	7.91E-03	5.09	0.05		
880	13	1.463722	0.0130019	6.57E-04	2.25E-03	9.71E-14	44.94635	52.16529	0.7665251	1.97E-02	4.87	0.12		
920	13	1.742061	1.32E-02	1.15E-03	3.19E-03	4.93E-14	52.31677	43.72197	0.7665642	2.16E-02	4.87	0.14		
960	13	1.855652	1.32E-02	1.12E-03	3.55E-03	4.27E-14	58.70518	41.36418	0.7729242	0.0355822	4.91	0.23		
1000	13	1.66488	1.32E-02	1.04E-03	2.78E-03	6.00E-14	67.68243	48.39182	0.8101189	1.62E-02	5.14	0.10		
1070	13	1.065632	1.28E-02	4.97E-04	8.13E-04	1.91E-13	96.25246	74.17841	0.7926136	9.78E-03	5.03	0.06		
1150	13	1.791041	1.45E-02	1.13E-02	2.74E-03	2.04E-14	99.30661	52.26587	0.9502472	0.0430497	6.03	0.27		
500	15	7.71807	3.49E-02	0.1250524	1.54E-02	4.64E-15	99.99	40.09884	3.140406	0.2920609	19.86	1.84		
YANI	Biotite	5.8 mg	J=0.003525											
T (°C)	t (min)	<sup>40</sup> Ar/ <sup>39</sup> Ar	<sup>39</sup> Ar/ <sup>39</sup> Ar	<sup>37</sup> Ar/ <sup>39</sup> Ar	<sup>36</sup> Ar/ <sup>39</sup> Ar	<sup>35</sup> Ar/ <sup>39</sup> Ar	<sup>34</sup> Ar/ <sup>39</sup> Ar	<sup>33</sup> Ar (mol)	Σ <sup>39</sup> Ar	% <sup>40</sup> Ar*	<sup>40</sup> Ar*/ <sup>39</sup> Ar <sub>K</sub>	±σ <sub>mass</sub>	Age (Ma)	±σ <sub>Age</sub>
500	13	52.42997	7.38E-02	0.1200818	0.1777009	1.17E-14	2.636326	-0.1973936	-0.1035949	1.724448	0.00	0.00		
600	13	6.351179	2.44E-02	5.72E-02	1.97E-02	1.98E-14	7.089177	7.874982	0.5025825	0.1005796	3.19	0.64		
700	13	1.804232	2.20E-02	1.39E-02	3.70E-03	7.29E-14	23.48855	37.4067	0.6778108	0.0289334	4.31	0.18		
770	13	1.155143	0.021309	8.46E-03	1.52E-03	8.31E-14	42.17268	57.95111	0.6733657	9.12E-03	4.28	0.06		
840	13	1.457183	1.93E-02	1.87E-02	2.58E-03	4.65E-14	52.63413	45.08595	0.6624734	3.34E-02	4.21	0.21		
900	13	1.342131	1.79E-02	1.48E-02	2.17E-03	5.00E-14	63.87273	49.54068	0.6705126	3.72E-02	4.26	0.24		
960	13	1.33434	1.94E-02	1.42E-02	2.10E-03	5.03E-14	75.18388	50.781	0.6833063	3.46E-02	4.34	0.22		
1050	13	1.180016	2.08E-02	1.80E-02	1.54E-03	6.99E-14	90.9097	58.3035	0.6927135	2.72E-02	4.40	0.17		
1150	13	1.598369	2.23E-02	9.55E-02	2.82E-03	2.91E-14	97.45557	45.72286	0.7397542	5.32E-02	4.70	0.34		
1350	13	2.905806	2.25E-02	0.1437462	6.40E-03	1.10E-14	99.93601	33.55762	0.992427	0.1367083	6.30	0.87		
500	15	69.92134	0.1012118	0.282955	0.224241	2.85E-16	99.99	5.073924	3.649329	4.377476	23.06	27.49		
YAN2	Biotite	5.9 mg	J=0.003525											
T (°C)	t (min)	<sup>40</sup> Ar/ <sup>39</sup> Ar	<sup>39</sup> Ar/ <sup>39</sup> Ar	<sup>37</sup> Ar/ <sup>39</sup> Ar	<sup>36</sup> Ar/ <sup>39</sup> Ar	<sup>35</sup> Ar/ <sup>39</sup> Ar	<sup>34</sup> Ar/ <sup>39</sup> Ar	<sup>33</sup> Ar (mol)	Σ <sup>39</sup> Ar	% <sup>40</sup> Ar*	<sup>40</sup> Ar*/ <sup>39</sup> Ar <sub>K</sub>	±σ <sub>mass</sub>	Age (Ma)	±σ <sub>Age</sub>
500	13	56.82689	0.1802923	0.0981221	0.190361	3.32E-15	0.5949188	0.9654913	0.550522	2.567736	3.50	16.30		
600	13	15.10664	4.08E-02	4.77E-02	4.97E-02	7.21E-15	1.886563	2.657302	0.403753	0.3303676	2.57	2.10		
700	13	3.26978	2.30E-02	1.10E-02	8.31E-03	5.75E-14	12.18596	23.83161	0.7818444	0.0182258	4.97	0.12		
770	13	1.281766	2.06E-02	4.91E-03	1.60E-03	1.25E-13	34.67743	60.25161	0.7752936	1.56E-02	4.92	0.10		
840	13	1.139394	1.99E-02	6.52E-03	1.09E-03	1.13E-13	54.92319	68.59942	0.7854244	1.53E-02	4.99	0.10		
900	13	1.544947	1.88E-02	1.29E-02	2.56E-03	4.49E-14	62.96579	48.57999	0.7573212	3.82E-02	4.81	0.24		
960	13	1.564723	1.98E-02	1.45E-02	2.63E-03	3.66E-14	69.52032	47.85851	0.7570558	0.0429643	4.81	0.27		
1050	13	1.173801	0.0198709	7.40E-03	1.20E-03	1.02E-13	87.85776	66.79226	0.7881005	1.61E-02	5.01	0.10		
1150	13	1.401545	0.020771	6.65E-03	1.84E-03	4.88E-14	96.59831	58.74239	0.8308852	3.00E-02	5.28	0.19		
1350	13	1.887159	2.12E-02	0.2376199	3.23E-03	1.90E-14	99.99	47.95684	0.9210096	8.26E-02	5.85	0.52		

YAN3	Biotite	8.3 mg	J=0.003525	$^{40}\text{Ar}/^{39}\text{Ar}$	$^{38}\text{Ar}/^{39}\text{Ar}$	$^{37}\text{Ar}/^{39}\text{Ar}$	$^{36}\text{Ar}/^{39}\text{Ar}$	$^{39}\text{Ar}$ (mol)	$\Sigma^{39}\text{Ar}$	% $^{40}\text{Ar}^*$	$^{40}\text{Ar}^*/^{39}\text{Ar}_K$	$\pm\sigma_{\text{Ar}}$	Age (Ma)	$\pm\sigma_{\text{Age}}$
500	13	154.9979	0.1264362	7.91E-02	0.5203749	1.37E-14	2.761403	0.7743742	1.200901	1.39057	7.62	8.81		
600	13	12.15099	3.00E-02	0.2312133	0.0388255	3.20E-14	9.203485	5.457359	0.6643614	0.1278289	4.22	0.81		
700	13	3.358029	2.34E-02	0.2460666	8.07E-03	1.01E-13	29.44173	28.51226	0.959492	3.31E-02	6.09	0.21		
770	13	1.86427	2.19E-02	5.95E-02	2.84E-03	9.97E-14	49.51769	53.37187	0.9985563	1.54E-02	6.34	0.10		
840	13	2.176355	2.22E-02	2.96E-02	3.82E-03	5.58E-14	60.7453	46.49316	1.017355	0.0352894	6.46	0.22		
900	13	2.551081	2.26E-02	3.86E-02	5.07E-03	3.50E-14	67.78178	39.7787	1.022292	2.38E-02	6.49	0.15		
960	13	2.246046	2.25E-02	3.08E-02	4.06E-03	5.01E-14	77.86385	45.02534	1.017219	3.50E-02	6.46	0.22		
1050	13	1.749386	2.18E-02	4.03E-02	2.62E-03	5.81E-14	89.5696	53.66312	0.9448665	2.61E-02	6.00	0.17		
1150	13	1.81003	2.24E-02	0.3194278	2.49E-03	3.98E-14	97.58024	58.51495	1.069056	4.10E-02	6.79	0.26		
1350	13	3.358538	2.41E-02	0.9003054	6.81E-03	1.20E-14	99.99	40.6738	1.389213	7.62E-02	8.81	0.48		
YAN4	Biotite	6.5 mg	J=0.003525	$^{40}\text{Ar}/^{39}\text{Ar}$	$^{38}\text{Ar}/^{39}\text{Ar}$	$^{37}\text{Ar}/^{39}\text{Ar}$	$^{36}\text{Ar}/^{39}\text{Ar}$	$^{39}\text{Ar}$ (mol)	$\Sigma^{39}\text{Ar}$	% $^{40}\text{Ar}^*$	$^{40}\text{Ar}^*/^{39}\text{Ar}_K$	$\pm\sigma_{\text{Ar}}$	Age (Ma)	$\pm\sigma_{\text{Age}}$
500	13	112.1806	0.1100386	0.0888133	0.3845398	3.14E-15	0.5041751	-1.313618	-1.476469	5.837764	0.00	0.00		
600	13	10.75239	2.42E-02	4.00E-02	3.31E-02	5.79E-15	1.433424	8.617437	0.9363976	0.4188192	5.95	2.65		
700	13	3.163724	0.0173169	6.98E-03	6.95E-03	4.86E-14	9.23668	33.96658	1.079209	3.85E-02	6.85	0.24		
770	13	1.43988	1.59E-02	2.75E-03	1.27E-03	1.11E-13	27.07974	71.4062	1.03239	1.72E-02	6.55	0.11		
840	13	1.359037	1.56E-02	2.43E-03	7.54E-04	1.09E-13	44.54646	80.85759	1.103773	1.54E-02	7.01	0.10		
900	13	1.489866	1.57E-02	5.95E-03	1.08E-03	4.13E-14	51.17387	75.53559	1.137414	4.11E-02	7.22	0.26		
960	13	1.469284	1.62E-02	8.52E-03	1.31E-03	3.58E-14	56.9266	70.52442	1.04915	4.54E-02	6.66	0.29		
1050	13	1.279653	0.0157126	7.12E-03	6.85E-04	1.41E-13	79.58418	81.36013	1.044923	1.23E-02	6.63	0.08		
1150	13	1.427104	1.58E-02	0.1184813	1.12E-03	9.32E-14	94.55267	74.84273	1.073457	1.94E-02	6.81	0.12		
1350	13	1.768092	1.64E-02	0.2840467	1.99E-03	3.38E-14	99.9737	65.4703	1.170573	4.83E-02	7.43	0.31		
500	15	97.51327	0.115363	0.288814	0.3299727	1.64E-16	99.99	-2.71E-03	-2.75E-03	10.80383	0.00	0.00		
PA2907	Muscovite	4.7 mg	J=0.003583	$^{40}\text{Ar}/^{39}\text{Ar}$	$^{38}\text{Ar}/^{39}\text{Ar}$	$^{37}\text{Ar}/^{39}\text{Ar}$	$^{36}\text{Ar}/^{39}\text{Ar}$	$^{39}\text{Ar}$ (mol)	$\Sigma^{39}\text{Ar}$	% $^{40}\text{Ar}^*$	$^{40}\text{Ar}^*/^{39}\text{Ar}_K$	$\pm\sigma_{\text{Ar}}$	Age (Ma)	$\pm\sigma_{\text{Age}}$
500	13	104.2329	0.112204	3.87E-02	0.3479452	2.63E-15	0.5990773	1.330006	1.388695	1.744986	8.96	11.23		
600	13	6.781235	1.86E-02	6.19E-02	0.0207168	5.05E-15	1.748275	9.227397	0.6342927	0.2652172	4.10	1.71		
700	13	4.694973	1.55E-02	0.0175963	1.35E-02	1.68E-14	5.575309	14.48975	0.684323	0.1085408	4.42	0.70		
770	13	2.621848	0.0136638	2.41E-03	6.41E-03	3.28E-14	13.03739	26.58136	0.7007116	6.21E-02	4.52	0.40		
840	13	1.427645	0.0130461	8.32E-04	2.35E-03	9.64E-14	34.95356	49.28858	0.7060576	1.39E-02	4.56	0.09		
880	13	1.03462	1.26E-02	4.87E-04	1.06E-03	6.51E-14	49.75964	66.37454	0.6914914	1.73E-02	4.47	0.11		
920	13	1.217944	1.28E-02	8.61E-04	1.67E-03	3.70E-14	58.18439	56.50772	0.6953683	2.73E-02	4.49	0.18		
960	13	1.414541	0.0129852	-3.56E-05	2.34E-03	2.83E-14	64.61243	48.621	0.6958067	4.36E-02	4.49	0.28		
1000	13	1.505996	1.32E-02	1.34E-03	2.71E-03	3.33E-14	72.18677	44.53991	0.6770223	0.0410823	4.37	0.26		
1070	13	1.149198	1.27E-02	8.34E-04	1.34E-03	7.73E-14	89.76243	62.77851	0.7252477	1.92E-02	4.68	0.12		
1150	13	0.959462	1.29E-02	1.96E-03	8.63E-04	3.74E-14	98.25731	69.56409	0.6761493	2.75E-02	4.37	0.18		
500	14	2.5409	0.0152275	9.58E-03	6.38E-03	7.66E-15	99.99	24.12817	0.6277981	0.1549806	4.05	1.00		

PA3379	Biotite		5.5 mg	J=0.003525												
T (°C)	t (min)	<sup>40</sup> Ar/ <sup>39</sup> Ar	<sup>38</sup> Ar/ <sup>39</sup> Ar	<sup>37</sup> Ar/ <sup>39</sup> Ar	<sup>36</sup> Ar/ <sup>39</sup> Ar	<sup>35</sup> Ar (mol)	% <sup>40</sup> Ar*	<sup>40</sup> Ar*/ <sup>39</sup> Ar <sub>K</sub>	±σ <sub>meas</sub>	Age (Ma)	±σ <sub>sys</sub>					
500	13	117.8607	0.1020441	6.90E-02	0.3926167	2.97E-15	1.538204	1.815397	1.722395	11.51	10.88					
600	13	10.37609	2.56E-02	7.48E-02	3.23E-02	8.44E-15	7.575587	0.7901887	0.2229628	5.02	1.41					
700	13	2.042667	0.0200288	6.90E-03	4.34E-03	6.59E-14	35.45428	0.7266734	3.00E-02	4.62	0.19					
770	13	1.072139	1.94E-02	3.80E-03	1.13E-03	43.97314	65.60673	0.706174	1.46E-02	4.49	0.09					
840	13	1.146043	1.89E-02	8.28E-03	1.29E-03	3.94E-14	63.37669	0.7336614	2.57E-02	4.66	0.16					
900	13	1.200533	1.82E-02	7.60E-03	1.62E-03	61.98476	56.88387	0.6900491	2.99E-02	4.38	0.19					
960	13	1.101377	1.90E-02	2.96E-03	1.14E-03	5.31E-14	65.98091	0.732368	2.40E-02	4.65	0.15					
1050	13	1.205972	1.95E-02	6.43E-03	1.50E-03	7.00E-14	60.12827	0.7290527	1.83E-02	4.63	0.12					
1150	13	1.179578	0.0190307	0.1000435	1.14E-03	3.14E-14	68.61969	0.8194485	3.22E-02	5.20	0.20					
1350	14	4.779091	1.97E-02	6.42E-02	6.40E-03	5.46E-15	58.79443	2.859083	0.2264247	18.09	1.43					
500	13	117.8607	0.1020441	6.90E-02	0.3926167	2.97E-15	1.538204	1.815397	1.722395	11.51	10.88					
LLAN1	Biotite		4.1 mg	J=0.003605												
T (°C)	t (min)	<sup>40</sup> Ar/ <sup>39</sup> Ar	<sup>38</sup> Ar/ <sup>39</sup> Ar	<sup>37</sup> Ar/ <sup>39</sup> Ar	<sup>36</sup> Ar/ <sup>39</sup> Ar	<sup>35</sup> Ar (mol)	% <sup>40</sup> Ar*	<sup>40</sup> Ar*/ <sup>39</sup> Ar <sub>K</sub>	±σ <sub>meas</sub>	Age (Ma)	±σ <sub>sys</sub>					
500	13	304.4153	0.3176572	4.39E-02	0.9880049	9.10E-16	4.080588	12.42871	8.756832	79.07	54.51					
700	13	7.095157	2.44E-02	1.98E-02	2.10E-02	1.02E-14	3.504681	0.8615105	0.2246807	5.59	1.46					
770	13	1.675499	1.93E-02	8.03E-03	3.41E-03	4.24E-14	37.6937	0.632822	4.53E-02	4.11	0.29					
840	13	0.9808437	1.78E-02	5.77E-03	1.10E-03	7.36E-14	63.30559	0.6221515	0.0239682	4.04	0.16					
900	13	1.056487	1.71E-02	1.04E-02	1.32E-03	3.55E-14	59.60815	0.6321386	3.75E-02	4.11	0.24					
960	13	1.482724	1.66E-02	1.98E-02	2.57E-03	1.56E-14	46.22256	0.689571	8.24E-02	4.48	0.53					
1020	13	1.369634	1.58E-02	9.52E-03	2.25E-03	2.06E-14	48.71453	0.6705679	6.56E-02	4.36	0.43					
1080	13	1.342972	0.0179475	6.58E-03	2.33E-03	2.30E-14	70.18989	0.6214902	6.12E-02	4.04	0.40					
1150	13	1.041663	1.76E-02	5.59E-03	1.31E-03	4.94E-14	85.8325	0.6201203	0.0325905	4.03	0.21					
500	13	1.483845	1.81E-02	5.55E-02	2.58E-03	4.47E-14	99.99	0.6892822	4.17E-02	4.48	0.27					
LLAN2	Biotite		5.0 mg	J=0.003609												
T (°C)	t (min)	<sup>40</sup> Ar/ <sup>39</sup> Ar	<sup>38</sup> Ar/ <sup>39</sup> Ar	<sup>37</sup> Ar/ <sup>39</sup> Ar	<sup>36</sup> Ar/ <sup>39</sup> Ar	<sup>35</sup> Ar (mol)	% <sup>40</sup> Ar*	<sup>40</sup> Ar*/ <sup>39</sup> Ar <sub>K</sub>	±σ <sub>meas</sub>	Age (Ma)	±σ <sub>sys</sub>					
500	13	298.3019	0.420684	4.25E-02	0.9938478	1.21E-15	1.537631	4.588398	9.021823	29.63	57.78					
700	13	11.2534	3.01E-02	5.52E-03	3.54E-02	1.66E-14	6.607646	0.7440472	0.283388	4.84	1.84					
770	13	1.92506	2.15E-02	1.40E-03	4.00E-03	5.67E-14	36.79585	0.7090901	4.00E-02	4.61	0.26					
840	13	1.222885	2.10E-02	9.45E-04	1.77E-03	7.47E-14	54.36013	0.6655998	3.88E-02	4.33	0.25					
900	13	1.654259	2.15E-02	2.34E-03	2.93E-03	53.56024	45.41948	0.7535927	7.32E-02	4.90	0.48					
960	13	2.038007	2.13E-02	3.04E-03	4.18E-03	1.39E-14	57.85828	0.7678884	9.35E-02	4.99	0.61					
1020	13	1.716193	2.03E-02	1.64E-03	2.93E-03	1.79E-14	47.42513	0.8169505	0.0827518	5.31	0.54					
1080	13	1.129421	2.04E-02	8.31E-04	1.29E-03	4.36E-14	62.96112	0.7127567	0.0349	4.63	0.23					
1150	13	1.149269	2.03E-02	4.39E-04	1.33E-03	4.51E-14	90.97839	0.7203962	3.39E-02	4.68	0.22					
500	13	1.485951	2.07E-02	1.54E-02	2.25E-03	2.91E-14	52.93234	0.7886541	6.36E-02	5.13	0.41					

LLAN3	Biotite	4.2 mg	J=0.003611									
T (°C)	t (min)	<sup>40</sup> Ar/ <sup>39</sup> Ar	<sup>39</sup> Ar/ <sup>39</sup> Ar	<sup>37</sup> Ar/ <sup>39</sup> Ar	<sup>36</sup> Ar/ <sup>39</sup> Ar	<sup>39</sup> Ar (mol)	Σ <sup>39</sup> Ar	% <sup>40</sup> Ar*	<sup>40</sup> Ar*/ <sup>39</sup> Ar <sub>K</sub>	+σ <sub>meas</sub>	Age (Ma)	+σ <sub>Age</sub>
500	13	252.8438	0.3626047	7.25E-02	0.8289441	1.47E-15	0.3500818	3.107852	7.861623	5.616337	50.50	±35.58
700	13	6.86884	2.81E-02	8.40E-03	2.10E-02	2.56E-14	6.451517	9.295004	0.6390065	0.1268144	4.16	0.82
770	13	1.354929	1.89E-02	1.81E-03	2.12E-03	8.48E-14	26.65965	51.19808	0.6946018	2.49E-02	4.52	0.16
840	13	1.05028	1.86E-02	1.70E-03	1.09E-03	8.05E-14	45.85171	66.02897	0.6947164	2.52E-02	4.52	0.16
900	13	1.703359	1.95E-02	8.78E-03	3.33E-03	2.39E-14	51.55033	40.09064	0.6853989	7.28E-02	4.46	0.42
960	13	1.82649	1.96E-02	8.78E-03	3.84E-03	2.32E-14	57.0806	35.83658	0.6568661	7.28E-02	4.27	0.47
1020	13	1.45942	1.90E-02	5.50E-03	2.55E-03	3.43E-14	65.26248	45.99276	0.6732345	0.040303	4.38	0.26
1080	13	1.109982	1.84E-02	2.33E-03	1.37E-03	6.67E-14	81.16882	60.28328	0.670486	2.24E-02	4.36	0.15
1150	13	1.203914	0.0184403	3.82E-03	1.72E-03	4.73E-14	92.45004	54.89242	0.6625943	2.50E-02	4.31	0.16
1350	13	1.821084	1.89E-02	1.45E-02	3.69E-03	3.17E-14	99.99	38.23008	0.6980152	4.70E-02	4.54	0.31
LLAN3	Muscovite	5.1 mg	J=0.003623									
T (°C)	t (min)	<sup>40</sup> Ar/ <sup>39</sup> Ar	<sup>39</sup> Ar/ <sup>39</sup> Ar	<sup>37</sup> Ar/ <sup>39</sup> Ar	<sup>36</sup> Ar/ <sup>39</sup> Ar	<sup>39</sup> Ar (mol)	Σ <sup>39</sup> Ar	% <sup>40</sup> Ar*	<sup>40</sup> Ar*/ <sup>39</sup> Ar <sub>K</sub>	+σ <sub>meas</sub>	Age (Ma)	+σ <sub>Age</sub>
500	13	265.8887	0.4248582	3.10E-02	0.8785177	8.09E-16	0.1718877	2.350206	6.254446	6.325535	40.42	±40.43
600	13	17.84733	0.0315334	0.0110657	5.76E-02	1.17E-15	0.4209017	4.364481	0.785823	1.262749	5.13	8.23
700	13	10.76254	1.96E-02	1.21E-03	3.34E-02	3.60E-15	1.185366	7.876219	0.8517295	0.4213769	5.56	2.75
770	13	5.429716	1.54E-02	8.53E-03	1.59E-02	6.33E-15	2.529958	12.96344	0.7076629	0.2578376	4.62	1.68
840	13	5.596937	1.50E-02	6.56E-03	1.61E-02	1.63E-14	6.001531	14.17184	0.7947937	0.1255562	5.19	0.82
880	13	2.548948	0.0132071	2.05E-03	5.91E-03	5.24E-14	17.1382	30.11405	0.7686529	4.46E-02	5.02	0.29
920	13	1.216967	1.23E-02	1.22E-03	1.54E-03	8.93E-14	36.11495	59.66154	0.7272949	2.22E-02	4.75	0.14
960	13	1.036585	1.22E-02	1.45E-03	9.67E-04	7.99E-14	53.0934	68.96544	0.7164783	1.87E-02	4.68	0.12
1000	13	1.11803	1.23E-02	1.44E-03	1.22E-03	6.39E-14	66.68674	64.51479	0.7231573	0.0262029	4.72	0.17
1070	13	1.505913	1.25E-02	1.53E-03	2.62E-03	4.43E-14	76.10113	46.08749	0.6959581	3.66E-02	4.54	0.24
1150	13	1.821676	1.28E-02	1.06E-03	3.51E-03	4.58E-14	85.84162	41.0887	0.7501577	3.84E-02	4.90	0.25
500	13	1.343268	1.36E-02	4.50E-03	1.72E-03	6.66E-14	99.99	59.59884	0.8022256	2.38E-02	5.24	0.16
LLAN4	Biotite	5.0 mg	J=0.003612									
T (°C)	t (min)	<sup>40</sup> Ar/ <sup>39</sup> Ar	<sup>39</sup> Ar/ <sup>39</sup> Ar	<sup>37</sup> Ar/ <sup>39</sup> Ar	<sup>36</sup> Ar/ <sup>39</sup> Ar	<sup>39</sup> Ar (mol)	Σ <sup>39</sup> Ar	% <sup>40</sup> Ar*	<sup>40</sup> Ar*/ <sup>39</sup> Ar <sub>K</sub>	+σ <sub>meas</sub>	Age (Ma)	+σ <sub>Age</sub>
500	13	389.4788	0.513604	0.1449426	1.288491	1.56E-15	0.3460503	2.23436	8.706132	5.323826	55.86	±33.63
700	13	18.93216	5.18E-02	3.96E-02	0.0613743	1.34E-14	3.307227	4.033575	0.7642543	0.2369254	4.97	1.54
770	13	2.367702	2.78E-02	5.64E-03	1.37E-03	5.36E-14	15.20203	32.35669	0.7672858	3.78E-02	4.99	0.25
840	13	1.183597	2.65E-02	3.21E-03	2.07E-03	1.09E-13	39.31229	62.77427	0.7441182	1.64E-02	4.84	0.11
900	13	1.401195	2.65E-02	5.13E-03	2.07E-03	5.71E-14	51.97426	53.80536	0.7557521	2.78E-02	4.92	0.18
960	13	1.813875	2.49E-02	1.20E-02	3.34E-03	2.06E-14	56.53094	43.42773	0.7918395	7.58E-02	5.15	0.49
1020	13	2.244928	2.63E-02	1.38E-02	4.70E-03	2.27E-14	61.55759	36.45367	0.8214928	6.94E-02	5.35	0.45
1080	13	1.697059	2.66E-02	1.49E-02	2.89E-03	3.19E-14	68.62701	47.51449	0.8092549	0.0485234	5.27	0.32
1150	13	1.219168	2.61E-02	1.11E-02	1.42E-03	6.44E-14	82.89428	62.77839	0.7672771	2.48E-02	4.99	0.16
1350	13	1.336946	2.57E-02	3.25E-02	0.0017695	7.72E-14	99.99	58.36359	0.781781	2.06E-02	5.09	0.13

LLAN6	Biotite	4.9 mg	J=0.003614	<sup>40</sup> Ar/ <sup>39</sup> Ar	<sup>38</sup> Ar/ <sup>39</sup> Ar	<sup>37</sup> Ar/ <sup>39</sup> Ar	<sup>36</sup> Ar/ <sup>39</sup> Ar	<sup>34</sup> Ar/ <sup>39</sup> Ar	<sup>32</sup> Ar (mol)	Σ <sup>39</sup> Ar	% <sup>40</sup> Ar*	<sup>40</sup> Ar*/ <sup>39</sup> Ar <sub>K</sub>	±σ <sub>meas</sub>	Age (Ma)	±σ <sub>Age</sub>				
				441.2211	0.4395032	0.0319872	1.460772	9.95E-16	0.204933	2.159125	9.530831	9.454932	61.09	59.59					
				9.959306	5.04E-02	1.39E-02	0.0300903	9.90E-15	2.244173	10.36313	1.034074	0.2537291	6.73	1.65					
				2.885458	4.90E-02	5.15E-03	6.38E-03	4.20E-14	10.88897	33.45395	0.9668009	5.18E-02	6.29	0.34					
				1.403818	5.03E-02	2.26E-03	1.53E-03	9.89E-14	31.2523	65.18945	0.9163812	1.76E-02	5.96	0.11					
				1.22919	5.19E-02	1.73E-03	9.91E-04	8.58E-14	48.91986	73.24075	0.9018732	1.87E-02	5.87	0.12					
				1.424114	5.14E-02	3.11E-03	1.56E-03	4.26E-14	57.69767	64.95856	0.9279498	3.33E-02	6.04	0.22					
				1.775215	4.60E-02	4.81E-03	2.72E-03	2.61E-14	63.06861	52.52665	0.9362486	5.76E-02	6.09	0.37					
				1.639639	4.51E-02	5.28E-03	2.14E-03	3.18E-14	69.60873	59.14544	0.9732751	4.73E-02	6.33	0.31					
				1.42042	4.86E-02	4.35E-03	1.48E-03	6.27E-14	82.51726	66.67296	0.9490379	0.0248945	6.18	0.16					
				2.401942	0.0536534	4.38E-02	3.85E-03	8.49E-14	99.99	51.321	1.23388	3.03E-02	8.03	0.20					
				HONI	Biotite	4.9 mg	J=0.003617	<sup>40</sup> Ar/ <sup>39</sup> Ar	<sup>38</sup> Ar/ <sup>39</sup> Ar	<sup>37</sup> Ar/ <sup>39</sup> Ar	<sup>36</sup> Ar/ <sup>39</sup> Ar	<sup>34</sup> Ar/ <sup>39</sup> Ar	<sup>32</sup> Ar (mol)	Σ <sup>39</sup> Ar	% <sup>40</sup> Ar*	<sup>40</sup> Ar*/ <sup>39</sup> Ar <sub>K</sub>	±σ <sub>meas</sub>	Age (Ma)	±σ <sub>Age</sub>
								260.3603	0.4464704	0.0329385	0.859353	2.01E-15	0.4406051	2.453102	6.389341	4.048162	41.22	25.82	
5.904062	2.09E-02	5.74E-03	1.74E-02					2.87E-14	6.743529	12.24938	0.7240081	0.0969371	4.72	0.63					
1.449041	1.45E-02	2.04E-03	2.35E-03					9.86E-14	28.37181	49.7204	0.721409	2.20E-02	4.70	0.14					
1.093657	1.42E-02	2.56E-03	1.24E-03					8.42E-14	46.83679	63.25936	0.6932411	2.06E-02	4.52	0.13					
1.9015	0.0152937	8.64E-03	3.85E-03					2.66E-14	52.67556	38.23841	0.7297838	5.58E-02	4.76	0.36					
1.565734	1.49E-02	6.40E-03	2.86E-03					2.98E-14	59.20837	43.67874	0.6866276	5.14E-02	4.47	0.33					
1.382523	1.52E-02	3.23E-03	2.12E-03					4.37E-14	68.79734	52.01421	0.7213259	3.17E-02	4.70	0.21					
1.172754	1.47E-02	1.63E-03	1.53E-03					6.16E-14	82.31671	58.2649	0.6850655	2.67E-02	4.46	0.17					
1.286276	1.44E-02	4.15E-03	1.85E-03					4.89E-14	93.03742	54.6012	0.7044048	0.0351165	4.59	0.23					
2.386012	1.75E-02	1.95E-02	5.12E-03					3.17E-14	99.99	35.09108	0.8393492	6.00E-02	5.47	0.39					
HONI	Muscovite	6.2 mg	J=0.003622					<sup>40</sup> Ar/ <sup>39</sup> Ar	<sup>38</sup> Ar/ <sup>39</sup> Ar	<sup>37</sup> Ar/ <sup>39</sup> Ar	<sup>36</sup> Ar/ <sup>39</sup> Ar	<sup>34</sup> Ar/ <sup>39</sup> Ar	<sup>32</sup> Ar (mol)	Σ <sup>39</sup> Ar	% <sup>40</sup> Ar*	<sup>40</sup> Ar*/ <sup>39</sup> Ar <sub>K</sub>	±σ <sub>meas</sub>	Age (Ma)	±σ <sub>Age</sub>
								133.5296	0.3723486	2.35E-02	0.4421637	2.07E-15	0.3516292	2.123657	2.837329	2.501123	18.45	16.18	
				16.13328	4.05E-02	0.0203825	5.22E-02	1.91E-15	0.6750367	4.16906	0.6759599	0.8183874	4.41	5.33					
				6.254217	1.85E-02	1.63E-02	1.85E-02	6.77E-15	1.82458	11.77963	0.7393907	0.2332578	4.82	1.52					
				3.659747	1.45E-02	0.0131723	1.01E-02	1.26E-14	3.964176	17.28102	0.6345428	0.1357544	4.14	0.89					
				3.89153	1.43E-02	1.03E-02	1.04E-02	2.46E-14	8.147573	19.96358	0.7781324	0.0978081	5.08	0.64					
				2.974251	1.37E-02	3.93E-03	7.39E-03	4.62E-14	15.98374	25.36406	0.7552324	5.93E-02	4.93	0.39					
				1.509615	1.28E-02	1.74E-03	2.55E-03	8.61E-14	30.59328	47.83103	0.7229144	2.88E-02	4.72	0.19					
				1.158143	0.0124284	1.30E-03	1.41E-03	8.84E-14	45.60432	61.00425	0.7075711	2.06E-02	4.62	0.13					
				1.193945	1.25E-02	1.25E-03	1.56E-03	7.18E-14	57.79779	58.39433	0.6984384	2.61E-02	4.56	0.17					
				1.366317	1.27E-02	1.18E-03	2.09E-03	8.52E-14	72.26163	52.19518	0.7140878	1.96E-02	4.66	0.13					
				1.668383	1.28E-02	1.99E-03	3.05E-03	7.34E-14	84.7197	43.87267	0.7328786	0.0270862	4.78	0.18					
				1.391408	1.31E-02	1.25E-02	1.72E-03	9.00E-14	99.99	61.05803	0.8506114	1.64E-02	5.55	0.11					



HON2		Biotite	5.0 mg	J=0.003618		$^{39}\text{Ar}/^{39}\text{Ar}$	$^{37}\text{Ar}/^{39}\text{Ar}$	$^{36}\text{Ar}/^{39}\text{Ar}$	$^{38}\text{Ar}/^{39}\text{Ar}$	$\Sigma^{39}\text{Ar}$	% $^{40}\text{Ar}^*$	$^{40}\text{Ar}^*/^{39}\text{Ar}_K$	$\pm\sigma_{\text{mass}}$	Age (Ma)	$\pm\sigma_{\text{Age}}$
T (°C)	t (min)														
500	13		234.3919	0.4138336	5.93E-02	0.7677566	1.54E-15	0.4068983	3.194053	0.4068983	6.765722	7.489656	8.345088	48.24	53.03
700	13		9.091326	2.64E-02	6.14E-03	2.86E-02	2.23E-14	6.319895	6.765722	6.319895	43.16535	0.6154917	0.2487508	4.01	1.62
770	13		1.729913	1.63E-02	0.0014515	3.21E-03	8.17E-14	27.94978	0.747412	27.94978	67.42356	0.747412	2.95E-02	4.87	0.19
840	13		1.11646	1.57E-02	9.92E-04	3.11E-03	8.17E-14	53.19412	67.42356	53.19412	46.41247	0.7881097	2.54E-02	4.91	0.17
900	13		1.692588	1.70E-02	3.51E-03	0.0029449	2.38E-14	59.50729	46.41247	59.50729	65.64989	0.8438835	6.81E-02	5.14	0.40
960	13		1.816249	1.73E-02	2.97E-03	3.17E-03	2.32E-14	65.64989	46.41247	65.64989	50.78389	0.7465125	4.92E-02	4.87	0.32
1020	13		1.465553	1.71E-02	1.86E-03	2.32E-03	2.94E-14	73.44674	50.78389	73.44674	64.71124	0.7700314	0.0245512	5.02	0.16
1080	13		1.187655	1.58E-02	8.75E-04	1.30E-03	5.68E-14	88.48269	64.71124	88.48269	63.76876	0.8038495	4.18E-02	5.24	0.27
1150	13		1.257573	1.57E-02	1.70E-03	1.42E-03	4.35E-14	99.99	63.76876	99.99					
HON4		Biotite	4.9 mg	J=0.003620		$^{39}\text{Ar}/^{39}\text{Ar}$	$^{37}\text{Ar}/^{39}\text{Ar}$	$^{36}\text{Ar}/^{39}\text{Ar}$	$^{38}\text{Ar}/^{39}\text{Ar}$	$\Sigma^{39}\text{Ar}$	% $^{40}\text{Ar}^*$	$^{40}\text{Ar}^*/^{39}\text{Ar}_K$	$\pm\sigma_{\text{mass}}$	Age (Ma)	$\pm\sigma_{\text{Age}}$
T (°C)	t (min)														
500	13		222.3604	0.3202873	0.116219	0.7096856	1.25E-15	0.3388135	5.67443	0.3388135	12.6228	10.98546	80.61	68.61	
700	13		7.105201	3.50E-02	2.63E-02	2.10E-02	1.20E-14	3.592034	12.2288	3.592034	31.57998	0.8697888	0.2434401	5.67	1.58
770	13		2.638749	2.78E-02	1.06E-02	6.04E-03	3.81E-14	13.96293	12.2288	13.96293	58.72317	0.8599811	3.65E-02	5.48	0.46
840	13		1.462988	2.68E-02	7.71E-03	1.93E-03	5.92E-14	30.06486	58.72317	30.06486	63.99715	0.8256787	4.53E-02	5.61	0.24
900	13		1.287531	2.68E-02	1.10E-02	1.45E-03	3.30E-14	39.03681	63.99715	39.03681	54.74269	0.7515387	6.54E-02	5.38	0.30
960	13		1.368548	2.64E-02	1.58E-02	1.97E-03	2.03E-14	44.55196	54.74269	44.55196	51.81045	0.7839999	6.29E-02	4.90	0.43
1020	13		1.509082	2.70E-02	0.0166516	2.34E-03	2.12E-14	50.31628	51.81045	50.31628	64.43195	0.8252264	4.15E-02	5.11	0.41
1080	13		1.278398	2.70E-02	1.14E-02	1.42E-03	3.68E-14	60.33688	64.43195	60.33688	70.75626	0.841396	2.77E-02	5.38	0.27
1150	13		1.187998	2.63E-02	9.07E-03	1.06E-03	7.63E-14	81.09421	70.75626	81.09421	50.51624	0.8990745	3.76E-02	5.49	0.18
1350	13		1.778304	2.73E-02	0.1506945	2.89E-03	6.95E-14	99.99	50.51624	99.99				5.86	0.24
HON5		Muscovite	5.9 mg	J=0.003621		$^{39}\text{Ar}/^{39}\text{Ar}$	$^{37}\text{Ar}/^{39}\text{Ar}$	$^{36}\text{Ar}/^{39}\text{Ar}$	$^{38}\text{Ar}/^{39}\text{Ar}$	$\Sigma^{39}\text{Ar}$	% $^{40}\text{Ar}^*$	$^{40}\text{Ar}^*/^{39}\text{Ar}_K$	$\pm\sigma_{\text{mass}}$	Age (Ma)	$\pm\sigma_{\text{Age}}$
T (°C)	t (min)														
500	13		256.0658	0.4562795	2.21E-02	0.8441993	1.26E-15	0.2528121	2.56062	0.2528121	10.90868	6.572011	4.601253	42.43	29.36
600	13		14.86468	3.99E-02	1.79E-02	4.47E-02	1.63E-15	0.5792106	20.71571	0.5792106	26.25917	1.633594	1.002851	10.64	6.51
700	13		5.884282	1.78E-02	8.01E-03	1.57E-02	6.18E-15	1.817954	20.71571	1.817954	3.855534	1.224998	0.2689801	7.98	1.75
770	13		3.943909	1.47E-02	8.31E-03	9.71E-03	1.02E-14	3.855534	26.25917	3.855534	28.25714	1.040284	0.1675626	6.78	1.09
840	13		3.734311	1.43E-02	5.74E-03	8.94E-03	1.94E-14	7.751331	28.25714	7.751331	37.53475	1.057825	9.05E-02	6.90	0.59
880	13		2.873368	0.0136623	2.02E-03	5.95E-03	3.71E-14	15.18507	37.53475	15.18507	65.76119	1.080331	5.91E-02	7.04	0.38
920	13		1.620969	0.0124825	5.95E-04	1.76E-03	1.16E-13	38.45672	65.76119	38.45672	73.02339	1.066986	2.11E-02	6.96	0.14
960	13		1.441198	1.23E-02	6.70E-04	1.19E-03	7.52E-14	53.5749	73.02339	53.5749	1.054156	1.054156	1.90E-02	6.87	0.12
1000	13		1.600601	1.26E-02	7.15E-04	1.76E-03	4.89E-14	63.3386	65.15292	63.3386	1.04523	1.04523	3.19E-02	6.82	0.21
1070	13		1.801466	1.28E-02	9.10E-04	2.41E-03	4.21E-14	71.77707	58.38235	71.77707	1.054228	1.054228	3.82E-02	6.87	0.25
1150	13		1.915075	1.29E-02	1.73E-03	2.78E-03	4.10E-14	80.00168	55.18589	80.00168	1.059268	1.059268	4.15E-02	6.91	0.27
1350	13		1.806295	1.33E-02	2.55E-03	1.83E-03	9.98E-14	99.99	68.14428	99.99			1.72E-02	8.03	0.11

HON6	Biotite	5.1 mg	J=0.003622	$^{38}\text{Ar}/^{39}\text{Ar}$	$^{37}\text{Ar}/^{39}\text{Ar}$	$^{36}\text{Ar}/^{39}\text{Ar}$	$^{39}\text{Ar}$ (mol)	$\Sigma^{39}\text{Ar}$	% $^{40}\text{Ar}^*$	$^{40}\text{Ar}^*/^{39}\text{Ar}_K$	$\pm\sigma_{\text{Ar}}$	Age (Ma)	$\pm\sigma_{\text{Age}}$
500	13	368.0108	0.6431102	5.17E-02	1.200414	1.21E-15	0.2657594	3.599322	13.25798	6.733063	84.62	41.98	
700	13	8.015838	3.41E-02	6.91E-03	0.0231772	2.25E-14	5.195718	14.10339	1.132949	0.1449853	7.39	0.94	
770	13	2.082971	2.64E-02	2.00E-03	3.41E-03	7.23E-14	21.01054	49.85607	1.041176	3.04E-02	6.79	0.20	
840	13	1.39136	2.59E-02	1.23E-03	1.17E-03	1.12E-13	45.4091	72.52164	1.011572	0.0155844	6.60	0.10	
900	13	1.513034	2.67E-02	1.61E-03	1.63E-03	4.20E-14	54.5901	65.5174	0.9973847	3.55E-02	6.51	0.23	
960	13	2.018206	2.68E-02	3.88E-03	3.33E-03	1.98E-14	58.91439	49.04567	0.9995134	7.65E-02	6.52	0.50	
1020	13	1.984009	2.62E-02	2.87E-03	3.05E-03	2.57E-14	64.54554	52.45984	1.048751	6.16E-02	6.84	0.40	
1080	13	1.578729	2.58E-02	1.96E-03	1.74E-03	5.48E-14	76.54223	65.02614	1.031208	2.73E-02	6.73	0.18	
1150	13	1.616258	2.63E-02	3.51E-03	1.90E-03	6.27E-14	90.26328	62.9901	1.021999	2.62E-02	6.67	0.17	
500	13	2.274184	2.65E-02	8.78E-02	3.89E-03	4.45E-14	99.99	47.99656	1.095809	4.00E-02	7.15	0.26	

APPENDIX 4.3.  $^{40}\text{Ar}/^{39}\text{Ar}$  ISOTOPIC DATA FROM K-FELDSPAR STEP-HEATING ANALYSES

HONI	15.6 mg	J=0.003619										
T (°C)	t (min)	$^{40}\text{Ar}/^{39}\text{Ar}$	$^{38}\text{Ar}/^{39}\text{Ar}$	$^{37}\text{Ar}/^{39}\text{Ar}$	$^{36}\text{Ar}/^{39}\text{Ar}$	$^{39}\text{Ar}$ (mol)	$\Sigma^{39}\text{Ar}$	% $^{40}\text{Ar}^*$	$^{40}\text{Ar}/^{39}\text{Ar}_K$	$+\sigma_{\text{cons}}$	Age (Ma)	$+\sigma_{\text{Age}}$
400	15	250.2401	0.4452644	6.32E-02	0.8099136	1.44E-15	0.1203555	4.346421	10.88097	6.322075	69.68	39.71
400	22	81.96619	0.1270487	2.82E-02	0.2708618	4.74E-16	0.1598608	2.302856	1.893967	3.759649	12.32	24.38
450	15	28.95076	6.62E-02	4.15E-02	7.94E-02	1.11E-15	0.2520594	18.81448	5.469385	1.28528	35.36	8.23
450	22	15.95728	3.22E-02	3.25E-02	4.91E-02	1.21E-15	0.3532474	8.762669	1.40777	1.061604	9.17	6.90
500	15	8.640963	2.55E-02	0.024524	0.0227501	3.08E-15	0.6100881	21.71312	1.885484	0.3924886	12.27	2.55
500	22	4.203946	0.0146438	1.66E-02	1.29E-02	3.56E-15	0.9063787	8.307381	0.3523026	0.2756125	2.30	1.80
550	15	3.092141	0.0161897	2.29E-02	7.06E-03	7.50E-15	1.531246	31.24221	0.9715277	0.1179323	6.33	0.77
550	22	1.806767	1.33E-02	2.36E-02	4.77E-03	7.90E-15	2.18942	20.05086	0.3656043	0.1032777	2.39	0.67
600	15	1.613903	1.39E-02	2.71E-02	3.49E-03	1.32E-14	3.29341	33.77934	0.5485172	8.53E-02	3.58	0.56
600	22	1.211494	1.27E-02	2.90E-02	2.63E-03	1.29E-14	4.369755	32.7752	0.4004026	7.94E-02	2.61	0.52
650	15	1.232654	1.25E-02	3.26E-02	2.12E-03	1.90E-14	5.950488	46.35824	0.5746526	4.87E-02	3.75	0.32
650	22	0.940075	1.26E-02	3.33E-02	1.61E-03	1.97E-14	7.595649	45.51357	0.4308929	4.92E-02	2.81	0.32
700	15	0.8031825	1.23E-02	4.11E-02	1.63E-03	2.75E-14	9.888213	46.33731	0.4475632	3.53E-02	2.92	0.23
700	22	0.8148757	1.24E-02	4.27E-02	1.03E-03	2.67E-14	12.10995	57.71572	0.4664143	3.63E-02	3.04	0.24
750	15	0.7785743	1.25E-02	5.37E-02	1.06E-03	3.32E-14	14.8745	57.55359	0.4712834	0.0325144	3.07	0.21
750	22	0.7672693	1.24E-02	5.48E-02	1.00E-03	3.02E-14	17.38898	57.68837	0.4516714	3.57E-02	2.95	0.23
800	15	0.7746964	1.22E-02	5.95E-02	8.52E-04	3.51E-14	20.31041	62.93995	0.4852961	2.47E-02	3.17	0.16
800	22	0.7576461	1.22E-02	5.85E-02	8.10E-04	3.13E-14	22.92177	64.8381	0.5050331	2.60E-02	3.29	0.17
825	19	0.7624702	1.24E-02	5.73E-02	7.67E-04	2.78E-14	25.2413	61.30662	0.4673945	3.49E-02	3.05	0.23
850	15	0.7482427	1.23E-02	5.57E-02	8.19E-04	2.79E-14	29.65457	63.14195	0.5052736	3.45E-02	3.30	0.23
875	15	0.7544827	1.20E-02	5.02E-02	7.61E-04	3.48E-14	32.55214	65.7541	0.4754431	2.73E-02	3.10	0.18
900	19	0.8395182	1.22E-02	4.17E-02	9.48E-04	2.90E-14	34.97121	62.50466	0.4986006	3.10E-02	3.25	0.20
950	15	0.7661409	1.22E-02	3.64E-02	7.30E-04	3.57E-14	37.94943	67.33907	0.5183954	0.0316655	3.44	0.21
975	19	0.7894209	1.22E-02	3.06E-02	7.60E-04	2.75E-14	40.23791	67.05711	0.5325741	2.57E-02	3.38	0.17
1000	15	0.8119916	1.23E-02	2.72E-02	8.62E-04	2.61E-14	42.4101	64.19405	0.5244873	2.96E-02	3.47	0.19
1025	15	0.9311413	1.23E-02	2.44E-02	9.71E-04	2.74E-14	44.69572	65.32198	0.6113711	3.53E-02	3.42	0.23
1050	19	0.9320136	1.20E-02	2.02E-02	8.26E-04	1.78E-14	46.18031	69.69348	0.6548867	2.85E-02	3.99	0.19
1075	15	1.015636	1.18E-02	1.96E-02	1.14E-03	1.94E-14	47.79361	63.06625	0.6448002	5.11E-02	4.27	0.33
1100	19	1.134876	1.25E-02	1.86E-02	1.35E-03	1.84E-14	49.32561	61.52023	0.702571	5.60E-02	4.20	0.36
1100	25	1.2836	1.26E-02	1.90E-02	1.84E-03	2.36E-14	51.29524	54.71425	0.7053548	5.76E-02	4.58	0.38
1100	45	1.440035	1.29E-02	1.77E-02	2.31E-03	2.80E-14	53.62968	50.12478	0.7241681	4.08E-02	4.60	0.27
1100	90	1.726422	1.30E-02	1.78E-02	3.37E-03	4.70E-14	57.547	40.27726	0.6964878	5.26E-02	4.72	0.34
1100	180	2.133946	0.0134446	1.86E-02	4.69E-03	6.48E-14	62.94981	33.44307	0.7143435	3.11E-02	4.54	0.20
1100	420	1.700894	1.35E-02	3.33E-02	3.14E-03	1.74E-14	64.39819	43.33471	0.7403629	3.03E-02	4.66	0.20
1200	19	1.389098	1.30E-02	3.10E-02	1.95E-03	2.38E-14	66.38046	55.87967	0.7793193	6.68E-02	4.83	0.43
1240	15	1.368313	1.33E-02	0.0296857	1.97E-03	2.54E-14	68.49812	54.85241	0.7533975	3.78E-02	5.08	0.25
1280	15	1.204297	1.29E-02	2.06E-02	1.46E-03	1.24E-13	78.83224	61.32949	0.7392495	0.0437789	4.91	0.29
1350	19	1.228021	1.29E-02	1.45E-02	1.41E-03	2.54E-13	99.99	63.25095	0.7770702	1.76E-02	4.82	0.11
400	15									1.46E-02	5.07	0.10

HON3	T (°C)	t (min)	$^{40}\text{Ar}/^{39}\text{Ar}$	$^{38}\text{Ar}/^{39}\text{Ar}$	J=0.003614	$^{37}\text{Ar}/^{39}\text{Ar}$	$^{36}\text{Ar}/^{39}\text{Ar}$	$^{36}\text{Ar}/^{39}\text{Ar}$	$^{39}\text{Ar}$ (mol)	$\Sigma^{39}\text{Ar}$	% $^{40}\text{Ar}^*$	$^{40}\text{Ar}^*/^{39}\text{Ar}$	$\pm Q_{\text{app}}$	Age (Ma)	$\pm \sigma_{\text{Age}}$
			192.8998	0.2758728		5.38E-02	0.6384673	2.10E-15	0.2020021	2.177489	2.814257	27.19	18.07		
400	15		8.82E-02	4.36E-02		0.1508815	1.13E-15	0.3107147	2.252068	1.030871	1.652693	6.71	10.74		
400	22		22.47875	6.57E-02		7.10E-02	1.55E-15	0.4601326	6.482849	1.463181	0.8926023	9.51	5.79		
450	15		15.66987	4.12E-02		5.48E-02	1.71E-15	0.6247551	-3.585996	-0.5648988	0.7769288	0.00	0.00		
450	22		7.417138	2.41E-02		0.0214927	2.32E-02	3.56E-15	0.9679784	7.252405	0.5408006	0.4098632	3.52	2.67	
500	15		5.189264	1.79E-02		2.20E-02	1.66E-02	4.26E-15	1.378703	5.046308	0.2635401	0.2666327	1.72	1.74	
550	15		3.125029	1.64E-02		1.75E-02	9.25E-03	8.25E-15	2.174354	0.1316919	0.3593276	2.34	0.86		
550	22		2.458323	1.42E-02		1.42E-02	7.32E-03	9.27E-15	3.068108	10.61541	0.2625777	0.1279287	1.71	0.83	
600	15		1.886093	1.35E-02		1.49E-02	4.84E-03	1.59E-14	4.599201	22.29956	0.4225739	6.49E-02	2.75	0.42	
600	22		1.515819	0.0134549		1.42E-02	3.52E-03	1.73E-14	6.26512	29.04465	0.4426377	6.56E-02	2.88	0.43	
650	15		1.542893	1.31E-02		1.42E-02	3.16E-03	3.21E-14	9.360359	37.23326	0.5761099	4.36E-02	3.75	0.28	
650	22		1.114098	1.25E-02		1.56E-02	1.95E-03	2.90E-14	12.15642	45.1615	0.5053439	3.18E-02	3.29	0.21	
700	15		1.032442	1.27E-02		1.73E-02	1.55E-03	3.67E-14	15.69436	52.11814	0.5400984	2.80E-02	3.52	0.18	
700	22		1.003724	1.26E-02		1.85E-02	1.36E-03	3.29E-14	18.86164	56.51918	0.5697293	3.29E-02	3.71	0.21	
750	15		0.9278824	1.27E-02		2.24E-02	1.13E-03	3.67E-14	22.39479	60.30187	0.5618592	2.66E-02	3.66	0.17	
750	22		0.9601176	1.25E-02		2.08E-02	1.25E-03	3.01E-14	25.29918	57.75896	0.5572648	3.10E-02	3.63	0.20	
800	15		0.9762959	1.24E-02		2.32E-02	1.19E-03	3.06E-14	28.245	60.4292	0.5927655	2.90E-02	3.86	0.19	
800	22		0.9918939	1.24E-02		2.28E-02	1.36E-03	2.83E-14	30.9768	56.0024	0.5582794	2.91E-02	3.64	0.19	
825	19		0.9609975	1.23E-02		2.13E-02	1.13E-03	2.47E-14	33.33328	61.5484	0.5950068	4.03E-02	3.88	0.26	
850	15		0.9695289	1.27E-02		2.15E-02	1.16E-03	2.05E-14	35.33296	60.83186	0.5939667	4.35E-02	3.87	0.28	
875	15		0.9481094	1.23E-02		1.96E-02	9.27E-04	2.22E-14	37.47097	67.16158	0.6410423	4.40E-02	4.17	0.29	
900	20		0.9173178	0.0122764		1.77E-02	8.25E-04	2.75E-14	40.12539	69.3991	0.6401708	3.60E-02	4.17	0.23	
925	15		0.9642089	1.21E-02		1.53E-02	9.73E-04	2.06E-14	42.10923	66.24976	0.6433302	4.57E-02	4.19	0.30	
950	15		0.9470947	1.22E-02		1.34E-02	7.53E-04	2.08E-14	44.11856	72.45673	0.6911393	4.89E-02	4.50	0.32	
975	19		0.9719509	0.0121828		1.06E-02	8.24E-04	2.63E-14	46.65016	71.07836	0.6946664	3.63E-02	4.52	0.24	
1000	15		0.9810133	1.24E-02		1.04E-02	1.09E-03	2.35E-14	48.91406	63.31867	0.6249689	4.18E-02	4.07	0.27	
1025	15		1.078071	1.35E-02		9.25E-03	8.02E-04	1.75E-14	50.60424	74.32722	0.8072795	0.1597582	5.26	1.04	
1050	19		1.025035	1.22E-02		5.60E-03	7.41E-04	1.90E-14	52.43408	74.7745	0.7720187	5.97E-02	5.03	0.39	
1075	15		1.049869	1.17E-02		4.98E-03	4.96E-04	1.34E-14	53.7296	81.9725	0.8692019	6.82E-02	5.66	0.44	
1100	19		1.126698	1.20E-02		7.22E-03	1.00E-03	2.17E-14	55.82294	70.22029	0.7957316	4.03E-02	5.18	0.26	
1100	25		1.293833	1.27E-02		9.70E-03	1.65E-03	1.80E-14	57.55505	59.4243	0.7735171	7.11E-02	5.04	0.46	
1100	45		1.535536	1.24E-02		9.10E-03	2.39E-03	2.36E-14	59.82972	51.53659	0.7944461	5.23E-02	5.17	0.34	
1100	90		2.042273	1.26E-02		9.28E-03	4.10E-03	2.62E-14	62.35144	38.95251	0.7976208	5.46E-02	5.19	0.35	
1100	180		2.73006	1.44E-02		9.39E-03	6.43E-03	2.69E-14	64.94302	29.10365	0.7960784	0.1900401	5.18	1.24	
1100	420		3.652744	1.40E-02		1.20E-02	9.47E-03	4.42E-14	69.20258	22.43963	0.820386	8.70E-02	5.34	0.57	
1200	19		2.364228	1.43E-02		3.14E-02	4.90E-03	1.44E-14	70.59428	37.24766	0.8842776	7.43E-02	5.76	0.48	
1240	15		1.8786	1.35E-02		2.76E-02	3.42E-03	1.59E-14	72.12437	44.23926	0.8350246	7.07E-02	5.44	0.46	
1280	15		1.840489	1.36E-02		2.83E-02	3.66E-03	2.62E-14	74.65421	44.23344	0.8165053	0.0582781	5.32	0.38	
1350	19		1.603773	1.33E-02		1.98E-02	2.61E-03	1.39E-13	88.0935	49.86922	0.8003059	1.91E-02	5.21	0.12	
400	15		1.596233	1.32E-02		1.11E-02	1.93E-03	1.24E-13	99.99	62.06014	0.9913409	2.55E-02	6.45	0.17	

HON6	T (°C)	t (min)	<sup>40</sup> Ar/ <sup>39</sup> Ar	15.2 mg	J=0.003618	<sup>37</sup> Ar/ <sup>39</sup> Ar	<sup>36</sup> Ar/ <sup>39</sup> Ar	<sup>39</sup> Ar (mol)	Σ <sup>39</sup> Ar	% <sup>40</sup> Ar*	<sup>40</sup> Ar*/ <sup>39</sup> Ar <sub>K</sub>	$\pm \sigma_{\text{stat}}$	Age (Ma)	$\pm \sigma_{\text{Age}}$
400	15	15	474.8076		0.5090027	0.1065346	1.567529	1.43E-15	0.2612708	2.437594	11.57656	12.82238	72.03	78.21
400	22	22	72.41888		0.1270653	0.228037	0.2609662	4.28E-16	0.3393885	-6.490649	-4.716551	3.237008	0.00	0.00
450	15	15	26.59443		6.81E-02	9.99E-02	8.90E-02	8.05E-16	0.4865077	0.9528443	0.2546157	1.4214	1.62	9.01
450	22	22	19.61634		4.70E-02	0.1251577	7.16E-02	8.70E-16	0.6455342	-7.934106	-1.565695	1.437913	0.00	0.00
500	15	15	8.017315		2.24E-02	5.42E-02	2.57E-02	2.06E-15	1.023378	4.994237	0.4028564	0.392009	2.56	3.39
500	22	22	5.71241		1.83E-02	3.95E-02	1.85E-02	2.52E-15	1.483175	3.801182	0.2186621	0.392009	1.39	2.49
550	15	15	2.78437		1.42E-02	3.04E-02	7.54E-03	5.70E-15	2.524739	18.65144	0.5226275	0.1365415	3.31	0.87
550	22	22	2.235717		1.40E-02	3.27E-02	5.97E-03	6.45E-15	3.702854	0.439329	0.439329	0.1433806	2.79	0.91
600	15	15	1.610492		1.28E-02	2.95E-02	3.24E-03	1.21E-14	5.921438	38.25292	0.6192423	8.46E-02	3.93	0.54
600	22	22	1.450816		1.26E-02	3.20E-02	2.89E-03	1.21E-14	8.136172	38.6301	0.5636703	6.33E-02	3.57	0.40
650	15	15	1.223657		1.25E-02	3.52E-02	1.79E-03	1.86E-14	11.53872	54.00713	0.6637964	5.25E-02	4.21	0.33
650	22	22	1.248438		1.31E-02	3.71E-02	2.11E-03	1.83E-14	14.87865	47.38701	0.5942216	5.33E-02	3.77	0.34
700	15	15	1.088597		1.26E-02	4.29E-02	1.34E-03	2.68E-14	19.77291	60.44265	0.6602687	0.0485042	4.19	0.31
700	22	22	1.054192		1.21E-02	3.97E-02	6.46E-04	1.63E-14	22.74869	78.42268	0.8315932	6.35E-02	5.27	0.40
750	15	15	0.9855891		1.17E-02	4.39E-02	4.35E-04	2.42E-14	27.17112	83.4201	0.8256735	3.71E-02	5.23	0.24
750	22	22	0.9693286		1.19E-02	4.12E-02	4.72E-04	2.30E-14	31.38065	81.96526	0.798116	3.63E-02	5.06	0.23
800	15	15	0.9493927		1.20E-02	4.77E-02	3.29E-04	2.81E-14	36.51526	86.13264	0.8208501	2.77E-02	5.20	0.18
800	22	22	0.968833		1.21E-02	4.04E-02	5.43E-04	2.87E-14	41.75822	79.88197	0.776747	3.33E-02	4.92	0.21
825	19	19	1.037625		1.21E-02	3.94E-02	3.04E-04	2.27E-14	45.90279	87.88583	0.9158492	4.63E-02	5.80	0.29
850	15	15	0.9918077		1.19E-02	3.69E-02	-4.55E-05	1.88E-14	49.32922	97.60245	0.9732896	4.76E-02	6.17	0.30
875	15	15	0.9144042		1.18E-02	3.65E-02	1.35E-04	2.18E-14	53.31848	91.68835	0.8426487	3.98E-02	5.34	0.25
900	19	19	0.9324395		1.23E-02	3.27E-02	3.00E-04	3.21E-14	59.18167	86.75211	0.8116503	0.0259788	5.14	0.16
925	15	15	0.9578588		1.20E-02	2.82E-02	2.93E-04	2.48E-14	63.71298	87.18683	0.83868	3.38E-02	5.32	0.21
950	15	15	0.9721987		1.22E-02	2.79E-02	5.34E-04	2.68E-14	68.61185	80.11756	0.7819235	2.88E-02	4.96	0.18
975	19	19	0.9947556		1.20E-02	2.36E-02	5.12E-04	2.76E-14	73.65737	81.19785	0.8106917	3.34E-02	5.14	0.21
1000	15	15	1.025073		1.18E-02	2.13E-02	3.75E-04	1.74E-14	76.84451	85.4742	0.8811142	5.05E-02	5.58	0.32
1025	15	15	1.014548		1.19E-02	1.92E-02	-9.29E-06	1.42E-14	79.44236	96.327	0.9841092	6.31E-02	6.24	0.40
1050	19	19	1.133785		1.21E-02	1.65E-02	4.18E-04	1.65E-14	82.45916	85.69216	0.9767952	4.86E-02	6.19	0.31
1075	15	15	1.163134		1.18E-02	1.52E-02	3.45E-04	1.17E-14	84.58978	87.71423	1.027808	8.18E-02	6.51	0.52
1100	19	19	1.226108		1.20E-02	1.75E-02	6.70E-04	1.38E-14	87.11413	80.66087	0.9948728	7.36E-02	6.30	0.47
1100	25	25	1.363728		1.24E-02	1.41E-02	1.29E-03	1.29E-14	89.46851	69.13887	0.9482709	7.89E-02	6.01	0.50
1100	45	45	1.551574		1.28E-02	1.59E-02	1.88E-03	1.54E-14	92.27641	61.7362	0.9619333	5.87E-02	6.10	0.37
1100	90	90	1.783218		1.27E-02	1.63E-02	2.72E-03	2.22E-14	96.33427	52.83912	0.9446408	0.0520873	5.99	0.33
1100	180	180	2.137344		1.30E-02	1.55E-02	3.45E-03	2.01E-14	99.99	50.64351	1.084977	8.55E-02	6.87	0.54

**APPENDIX 4.4. (U-Th)/He APATITE ISOTOPIC DATA**

<b>HON 1</b>								
U (ppm)	Th (ppm)	He (nmol/mg)	Mass ( $\mu$ m)	Ft	Raw age (Ma)	Corrected age (Ma)	Average age (Ma)	1 $\sigma$
6.85	11.70	0.04	3.01	0.74	0.84	1.13		
14.93	5.94	0.21	3.31	0.75	2.33	3.09		
9.42	4.45	0.08	4.54	0.78	1.34	1.72		
24.40	24.42	0.19	3.69	0.73	1.14	1.55	<b>1.87</b>	<b>0.85</b>
<b>HON 2</b>								
U (ppm)	Th (ppm)	He (nmol/mg)	Mass ( $\mu$ m)	Ft	Raw age (Ma)	Corrected age (Ma)	Average age (Ma)	1 $\sigma$
8.25	17.48	0.09	8.22	0.81	1.39	1.72		
9.33	11.04	0.16	6.81	0.80	2.41	3.02		
11.68	12.13	0.20	8.35	0.80	2.57	3.23		
36.59	6.08	0.34	5.09	0.78	1.63	2.08	<b>2.51</b>	<b>0.72</b>
<b>HON 3</b>								
U (ppm)	Th (ppm)	He (nmol/mg)	Mass ( $\mu$ m)	Ft	Raw age (Ma)	Corrected age (Ma)	Average age (Ma)	1 $\sigma$
23.40	19.97	0.26	4.00	0.77	1.67	2.18		
16.33	11.09	0.45	3.25	0.74	4.35	5.85	<b>4.01</b>	<b>2.59</b>
<b>HON 4</b>								
U (ppm)	Th (ppm)	He (nmol/mg)	Mass ( $\mu$ m)	Ft	Raw age (Ma)	Corrected age (Ma)	Average age (Ma)	1 $\sigma$
16.82	16.07	0.18	5.11	0.77	1.63	2.13		
36.77	32.35	0.34	3.85	0.72	1.40	1.94		
18.01	16.00	0.14	3.69	0.73	1.18	1.61		
21.51	22.82	0.17	3.80	0.75	1.14	1.52		
17.43	15.44	0.17	8.22	0.80	1.46	1.81		
38.26	41.77	0.41	5.11	0.77	1.56	2.04		
34.07	35.72	0.39	4.38	0.75	1.71	2.29		
32.60	31.92	0.37	3.90	0.74	1.68	2.26	<b>1.95</b>	<b>0.28</b>
<b>HON 6</b>								
U (ppm)	Th (ppm)	He (nmol/mg)	Mass ( $\mu$ m)	Ft	Raw age (Ma)	Corrected age (Ma)	Average age (Ma)	1 $\sigma$
3.13	4.06	0.03	5.09	0.77	1.26	1.63		
6.16	8.49	0.12	5.63	0.79	2.80	3.55	<b>2.59</b>	<b>1.36</b>
<b>LLAN 1</b>								
U (ppm)	Th (ppm)	He (nmol/mg)	Mass ( $\mu$ m)	Ft	Raw age (Ma)	Corrected age (Ma)	Average age (Ma)	1 $\sigma$
5.22	11.85	0.11	4.64	0.76	2.56	3.35		
8.20	8.68	0.17	3.46	0.75	3.01	4.00		
9.46	9.93	0.25	3.01	0.74	3.84	5.17		
6.57	4.45	0.38	3.64	0.76	9.16	12.08	<b>4.18</b>	<b>0.92</b>

<b>LLAN 2</b>								
U (ppm)	Th (ppm)	He (nmol/mg)	Mass (μm)	Ft	Raw age (Ma)	Corrected age (Ma)	Average age (Ma)	1σ
28.20	42.48	0.27	1.73	0.69	1.28	1.86		
3.62	13.86	0.05	1.52	0.64	1.25	1.93		
16.75	8.29	0.15	2.36	0.69	1.46	2.12		
13.24	11.27	0.13	3.41	0.74	1.54	2.09		
18.91	16.80	0.16	2.50	0.71	1.28	1.81		
9.58	12.55	0.11	6.18	0.78	1.59	2.04	<b>1.97</b>	<b>0.13</b>

<b>LLAN 3</b>								
U (ppm)	Th (ppm)	He (nmol/mg)	Mass (μm)	Ft	Raw age (Ma)	Corrected age (Ma)	Average age (Ma)	1σ
9.02	10.25	1.22	4.06	0.76	19.58	25.85		
12.69	16.48	0.18	4.88	0.76	1.98	2.62		
9.34	13.19	0.12	4.00	0.76	1.79	2.34		
13.71	8.73	0.16	3.85	0.73	1.86	2.57	<b>2.51</b>	<b>0.15</b>

<b>LLAN 4</b>								
U (ppm)	Th (ppm)	He (nmol/mg)	Mass (μm)	Ft	Raw age (Ma)	Corrected age (Ma)	Average age (Ma)	1σ
17.13	6.28	0.56	7.11	0.80	5.54	6.88		
17.22	29.29	0.37	7.67	0.81	2.84	3.53		
9.27	45.73	0.28	5.11	0.76	2.58	3.42		
15.41	15.28	0.26	7.15	0.79	2.48	3.13		
9.92	10.14	0.11	2.44	0.73	1.63	2.24		
9.15	9.29	0.39	3.01	0.74	6.27	8.44	<b>3.08</b>	<b>0.58</b>

<b>LLAN 6</b>								
U (ppm)	Th (ppm)	He (nmol/mg)	Mass (μm)	Ft	Raw age (Ma)	Corrected age (Ma)	Average age (Ma)	1σ
6.77	12.56	0.13	3.47	0.73	2.51	3.46		
4.45	7.91	0.07	4.63	0.74	2.09	2.80	<b>3.13</b>	<b>0.46</b>

#### 4.11 REFERENCES

- Armstrong, P. A., Ehlers, T.A., Chapman, D.S., Farley, K.A., and Kamp, P.J.J., 2003, Exhumation of the Wasatch Mountains, Utah: 1. Patterns and timing of exhumation deduced from low-temperature thermochronology data: *Journal of Geophysical Research*, v. 108, doi:10.1029/2001JB001708.
- Axen, G. J., and Bartley, J.M., 1997, Field tests of rolling hinges: Existence, mechanical types, and implications for extensional tectonics: *Journal of Geophysical Research*, v. 102, p. 20,515-20,537.
- Brady, R. J., 2002, Very high slip rates on continental extensional faults: new evidence from (U-Th)/He thermochronometry of the Buckskin Mountains, Arizona: *Earth and Planetary Science Letters*, v. 197, p. 95-104.
- Braun, J., 2002, Quantifying the effect of recent relief changes on age-elevation relationships: *Earth and Planetary Science Letters*, v. 200, p. 331-343.
- Brunel, M., Arnaud, N., Tapponnier, P., Pan, Y., and Wang, Y., 1994, Kongur Shan normal fault: Type example of mountain building assisted by extension (Karakoram fault, eastern Pamir): *Geology*, v. 22, p. 707-710.
- Buck, W. R., 1988, Flexural rotation of normal faults: *Tectonics*, v. 7, p. 959-973.
- Buck, W. R., 1991, Modes of continental lithospheric extension: *Journal of Geophysical Research*, v. 96, p. 20,161-20,178.
- Burchfiel, B. C., Chen, Z., Hodges, K.V., Liu, Y., Royden, L.H., Deng, C., and Xu, J., 1992, The South Tibetan detachment system, Himalayan orogen: Extension contemporaneous with and parallel to shortening in a collisional mountain belt, *Geological Society of America Special Paper* 269, 41 p.
- Carter, T. J., Kohn, B.P., Foster, D.A., and Gleadow, A.J.W., 2004, How the Harcuvar Mountains metamorphic core complex became cool: Evidence from apatite (U-Th)/He thermochronometry: *Geology*, v. 32, p. 985-988.
- Cebula, G. T., Kunk, M.J., Mehnert, H.H., Naeser, C.W., Obradovich, J.D., and Sutter, J.F., 1986, The Fish Canyon Tuff, a potential standard for the  $^{40}\text{Ar}/^{39}\text{Ar}$  and fission-track dating methods: *Terra Cognita*, v. 6, p. 139-140.
- Cemen, I., Tekeli, O., Seyitoglu, G., and Isik, V., 2005, Are turtleback fault surfaces common structural elements of highly extended terranes?: *Earth-Science Reviews*, v. 73, p. 139-148.



- Chery, J., 2001, Core complex mechanics: From the Gulf of Corinth to the Snake Range: *Geology*, v. 29, p. 439-442.
- Cobbing, E. J., and Sanchez, A.W., 1996, Mapa geologico del cuadrangulo de Recuay, 1:100 000, digitized 1996: Instituto Geologico Minero y Metalurgico.
- Cobbing, E. J., Pitcher, W.S., Wilson, J.J., Baldock, J.W., Taylor, W.P., McCourt, W., and Snelling, N.J., 1981, The geology of the Western Cordillera of northern Peru, *Overseas Memoir*, Institute of Geological Sciences, 143 p.
- Coney, P. J., and Harms, T.A., 1984, Cordilleran metamorphic core complexes: Cenozoic extensional relics of Mesozoic compression: *Geology*, v. 12, p. 550-554.
- Cossio, A., and Blanco, E., 1964, Mapa geologico del cuadrangulo de Santa Rosa, 1:100 000: Instituto Geologico, Minero y Metalurgico.
- Dalmayrac, B., and Molnar, P., 1981, Parallel thrust and normal faulting in Peru and constraints on the state of stress: *Earth and Planetary Science Letters*, v. 55, p. 473-481.
- Davis, G. A., and Lister, G.S., 1988, Detachment faulting in continental extension; Perspectives from the Southwestern U.S. Cordillera, *Geological Society of America Special Paper* 218, p. 133-159.
- DeSmedt, M., Farber, D.L., Hancock, G., Finkel, R., McNulty, B., and Torres, V., 1999, Uplift and extension rates of the central Peruvian Andes: Slip rates along the Cordillera Blanca detachment fault deduced from in-situ produced  $^{10}\text{Be}$  and  $^{26}\text{Al}$  cosmogenic radionuclide model ages: *Eos, Transactions, AGU*, v. 80, p. F1037.
- Deverchere, J., Dorbath, C., and Dorbath, L., 1989, Extension related to a high topography: results from a microearthquake survey in the Andes of Peru and tectonic implications: *Geophysical Journal International*, v. 98, p. 281-292.
- Doser, D. I., 1987, The Ancash, Peru, earthquake of 1946 November 10: evidence for low-angle normal faulting in the high Andes of northern Peru: *Geophysical Journal of the Royal Astronomical Society*, v. 91, p. 57-71.
- Ehlers, T. A., Willett, S.D., Armstrong, P.A., and Chapman, D.S., 2003, Exhumation of the central Wasatch Mountains, Utah: 2. Thermokinematic model of exhumation, erosion, and thermochronometer interpretation: *Journal of Geophysical Research*, v. 108, doi: 10.1029/2001JB001723.
- Farley, K. A., 2000, Helium diffusion from apatite: general behavior as illustrated by Durango fluorapatite: *Journal of Geophysical Research*, v. 105, p. 2903-2914.

- Farley, K. A., Wolf, R.A. and Silver, L.T., 1996, The effects of long alpha-stopping distances on (U-Th)/He ages: *Geochimica et Cosmochimica Acta*, v. 60, p. 4223-4229.
- Garver, J. I., Schiffman, C.R., and Perry, S.E., 2003, Rapid tectonic exhumation of the Cordillera Blanca, Northern Peru: *Geological Society of America Abstracts with Programs*, v. 35, no. 169-9, p. 429.
- Giovanni, M. K., Horton, B.K., Lovera, O.M., Grove, M., Farley, K.A., Kimbrough, D.L., and McNulty, B., 2006, Emplacement and exhumation of the Cordillera Blanca batholith, Peru, *in* *Geological Society of America Abstracts with Programs, Specialty Meeting No. 2, Backbone of the Americas - Patagonia to Alaska, Mendoza, Argentina*, p. 40, Paper 3-17.
- Gutscher, M.-A., 2002, Andean subduction styles and their effect on thermal structure and interplate coupling: *Journal of South American Earth Sciences*, v. 15, p. 3-10.
- Gutscher, M.-A., Olivet, J.-L., Aslanian, D., Eissen, J.-P., and Maury, R., 1999, The "lost Inca Plateau": cause of flat subduction beneath Peru?: *Earth and Planetary Science Letters*, v. 171, p. 335-341.
- Hampel, A., 2002, The migration history of the Nazca Ridge along the Peruvian active margin: a re-evaluation: *Earth and Planetary Science Letters*, v. 203, p. 665-679.
- Harrison, T. M., Copeland, P., Kidd, W.S.F., and Lovera, O., 1995, Activation of the Nyainqentanghla Shear Zone: Implications for uplift of the southern Tibetan Plateau: *Tectonics*, v. 14, p. 658-676.
- Henry, S. G., and Pollack, H.N., 1988, Terrestrial heat flow above the Andean subduction zone in Bolivia and Peru: *Journal of Geophysical Research*, v. 93, p. 15,153-15,162.
- House, M. A., and Hodges, K.V., 1994, Limits on the tectonic significance of rapid cooling events in extensional settings: Insights from the Bitterroot metamorphic core complex, Idaho-Montana: *Geology*, v. 22, p. 1007-1010.
- House, M. A., Wernicke, B.P., Farley, K.A., and Dumitru, T.A., 1997, Cenozoic thermal evolution of the central Sierra Nevada, California, from (U-Th)/He thermochronometry: *Earth and Planetary Science Letters*, v. 151, p. 167-179.
- House, M. A., Wernicke, B.P. and Farley, K.A., 1998, Dating topography of the Sierra Nevada, California, using apatite (U-Th)/He ages: *Nature*, v. 396, p. 66-69.

- Jacobson, C. E., Barth, A.P., and Grove, M., 2000, Late Cretaceous protolith age and provenance of the Pelona and Orocopia schists, southern California: Implications for evolution of the Cordilleran margin: *Geology*, v. 28, p. 219-222.
- Ketcham, R. A., 1996, Thermal models of core-complex evolution in Arizona and New Guinea: Implications for ancient cooling paths and present-day heat flow: *Tectonics*, v. 15, p. 933-951.
- Lister, G. S., and Baldwin, S.L., 1993, Plutonism and the origin of metamorphic core complexes: *Geology*, v. 21, p. 607-610.
- Lister, G. S., and Davis, G.A., 1989, The origin of metamorphic core complexes and detachment faults formed during Tertiary continental extension in the northern Colorado River region, U.S.A.: *Journal of Structural Geology*, v. 11, p. 65-94.
- Lovera, O. M., Richter, F.M., and Harrison, T.M., 1989, The  $^{40}\text{Ar}/^{39}\text{Ar}$  thermochronometry for slowly cooled samples having a distribution of diffusion domain sizes: *Journal of Geophysical Research*, v. 94, p. 17,917-17,935.
- Lovera, O. M., Grove, M., Harrison, T.M., and Mahon, K.I., 1997, Systematic analysis of K-feldspar  $^{40}\text{Ar}/^{39}\text{Ar}$  step heating results: I. Significance of activation energy determinations: *Geochimica et Cosmochimica Acta*, v. 61, p. 3171-3192.
- Lovera, O. M., Grove, M., and Harrison, T.M., 2002, Systematic analysis of K-feldspar  $^{40}\text{Ar}/^{39}\text{Ar}$  step heating results II: Relevance of laboratory argon diffusion properties to nature: *Geochimica et Cosmochimica Acta*, v. 66, p. 1237-1255.
- Malavieille, J., 1993, Late orogenic extension in mountain belts: Insights from the Basin and Range and the late Paleozoic Variscan belt: *Tectonics*, v. 12, p. 1115-1130.
- McDougall, I., and Harrison, T.M., 1999, *Geochronology and thermochronology by the  $^{40}\text{Ar}/^{39}\text{Ar}$  method*: New York, Oxford University Press, 269 p.
- McNulty, B. A., and Farber, D.L., 2002, Active detachment faulting above the Peruvian flat slab: *Geology*, v. 30, p. 567-570.
- McNulty, B. A., Farber, D.L., Wallace, G.S., Lopez, R., and Palacios, O., 1998, Role of plate kinematics and plate-slip-vector partitioning in continental magmatic arcs: Evidence from the Cordillera Blanca, Peru: *Geology*, v. 26, p. 827-830.
- Miller, J. M. G., and John, B.E., 1988, Detached strata in a Tertiary low-angle normal fault terrane, southeastern California: A sedimentary record of unroofing, breaching, and continued slip: *Geology*, v. 16, p. 645-648.

- Miller, M. G., 1991, High angle origin of the currently low-angle Badwater Turtleback fault, Death Valley, California: *Geology*, v. 9, p. 372-375.
- Miller, M. G., 1992, Brittle faulting induced by ductile deformation of a rheologically stratified rock sequence, Badwater Turtleback, Death Valley, California: *Geological Society of America Bulletin*, v. 104, p. 1376-1385.
- Montario, M. J., 2001, Exhumation of the Cordillera Blanca, Northern Peru, based on apatite fission track analysis, [B.S. Thesis]: Union College, Schenectady, 55 p.
- Mukasa, B. S., 1984, Comparative Pb isotope systematics and zircon U-Pb geochronology for the Coastal, San Nicholas and Cordillera Blanca batholiths, Peru, [Ph.D. Thesis]: University of California, Santa Barbara, 362 p.
- Petford, N., 1990, The relation between deformation, granite source type and crustal growth, Peru [Ph.D. Thesis]: University of Liverpool, Liverpool, 247 p.
- Petford, N., and Atherton, M.P., 1992, Granitoid emplacement and deformation along a major crustal lineament: the Cordillera Blanca, Peru: *Tectonophysics*, v. 205, p. 171-185.
- Robinson, A. C., 2005, Tectonic evolution of the Kongur Shan extensional system, northeastern Pamir: Implications for the evolution of the western Himalayan-Tibetan orogen, [Ph.D. Thesis]: University of California, Los Angeles, 333 p.
- Rosenbaum, G., Giles, D., Saxon, M., Betts, P.G., Weinberg, R.F., and Duboz, C., 2005, Subduction of the Nazca Ridge and the Inca Plateau: Insights into the formation of ore deposits in Peru: *Earth and Planetary Science Letters*, v. 239, p. 18-32.
- Rousse, S., Gilder, S., Farber, D., McNulty, B., and Torres, V., 2002, Paleomagnetic evidence for rapid vertical-axis rotation in the Peruvian Cordillera ca. 8 Ma: *Geology*, v. 30, p. 75-78.
- Rousse, S., Gilder, S., Farber, D., McNulty, B., Patriat, P., Torres, V., and Sempere, T., 2003, Paleomagnetic tracking of mountain building in the Peruvian Andes since 10 Ma: *Tectonics*, v. 22, doi: 10.1029/2003TC001508.
- Ruppel, C., 1995, Extensional processes in continental lithosphere: *Journal of Geophysical Research*, v. 100, p. 24,187-24,215.
- Schwartz, D. P., 1988, Paleoseismicity and neotectonics of the Cordillera Blanca fault zone, northern Peruvian Andes: *Journal of Geophysical Research*, v. 93, p. 4712-4730.

- Smith, J. A., Finkel, R.C., Farber, D.L., Rodbell, D.T., and Seltzer, G.O., 2005, Moraine preservation and boulder erosion in the tropical Andes: interpreting old surface exposure ages in glaciated valleys: *Journal of Quaternary Science*, v. 20, p. 735-758.
- Smith, W. H. F., and Sandwell, D.T., 1997, Global seafloor topography from satellite altimetry and ship depth soundings: *Science*, v. 277, p. 1957-1962.
- Spencer, J. E., 1984, Role of tectonic denudation in warping and uplift of low-angle normal faults: *Geology*, v. 12, p. 95-98.
- Spencer, J. E., 1994, A numerical assessment of slab strength during high- and low-angle subduction and implications for Laramide orogenesis: *Journal of Geophysical Research*, v. 99, p. 9227-9236.
- Stewart, J. W., Evernden, J.F., and Snelling, N.J., 1974, Age determinations from Andean Peru: a reconnaissance survey: *Geological Society of America Bulletin*, v. 85, p. 1107-1116.
- Suarez, G., Molnar, P., and Burchfiel, B.C., 1983, Seismicity, fault plane solutions, depth of faulting, and active tectonics of the Andes of Peru, Ecuador, and southern Colombia: *Journal of Geophysical Research*, v. 88, p. 10,403-10,428.
- Wells, M. L., Snee, L.W., and Blythe, A.E., 2000, Dating of major normal fault systems using thermochronology: An example from the Raft River detachment, Basin and Range, western United States: *Journal of Geophysical Research*, v. 105, p. 16,303-16,327.
- Wernicke, B., and Axen, G.J., 1988, On the role of isostasy in the evolution of normal fault systems: *Geology*, v. 16, p. 848-851.
- Wilson, J. J., 1967a, Mapa geológico del cuadrángulo de Huari, 1:100 000: Instituto Geológico Minero y Metalúrgico.
- Wilson, J. J., 1967b, Mapa geológico del cuadrángulo de Carhuaz, 1:100 000: Instituto Geológico Minero y Metalúrgico.
- Wilson, J. J., 1967c, Mapa geológico del cuadrángulo de Corongo, 1:100 000: Instituto Geológico Minero y Metalúrgico.
- Yin, A., 1989, Origin of regional, rooted low-angle normal faults: A mechanical model and its tectonic implications: *Tectonics*, v. 8, p. 469-482.

- Yin, A., 2006, Cenozoic tectonic evolution of the Himalayan orogen as constrained by along-strike variation of structural geometry, exhumation history, and foreland sedimentation: *Earth-Science Reviews*, v. 76, p. 1-131.
- Yin, A., and Harrison, T.M., 2000, Geologic evolution of the Himalayan-Tibetan orogen: *Annual Review of Earth and Planetary Sciences*, v. 28, p. 211-280.
- Yin, A., and Kelty, T.K., 1991, Structural evolution of the Lewis plate in Glacier National Park, Montana - Implications for regional tectonic development: *Geological Society of America Bulletin*, v. 103, p. 1073-1089.

**- Chapter 5 -**  
**Conclusions**

## 5.1 SUMMARY OF CORDILLERA BLANCA EVOLUTION

(1) The buoyant, aseismic Nazca Ridge entered the Peru trench, south of the Cordillera Blanca, at  $\sim 11^{\circ}\text{S}$  latitude between 10 and 12 Ma [e.g., *Rosenbaum et al.*, 2005]. The slab beneath Peru began to flatten in all directions, shutting off arc volcanism in the overriding plate. The oblique orientation of the Nazca Ridge relative to the convergence direction resulted in southward propagation of the ridge as it continued to subduct beneath Peru [e.g., *Gutscher et al.*, 1999; *Hampel*, 2002; *Rosenbaum et al.*, 2005; *Chapter 1*].

(2) The final magmatic events included the eruption of the Yungay ignimbrites at  $\sim 7\text{--}8$  Ma and emplacement of the Cordillera Blanca batholith at  $\sim 7$  Ma at approximately 10 km depth [e.g., *Petford and Atherton*, 1992; *McNulty and Farber*, 2002; *Chapter 4*]. The batholith was emplaced into overthickened crust in the hinterland of an early Tertiary fold-thrust belt. The surface elevation at this time was at or near the modern elevation of 3000–3500 meters above sea level [e.g., *Garzione et al.*, 2000, 2004; *Chapter 3*].

(3) Intrusive heating weakened the crust and faulting initiated at 5.4 Ma along the listric Cordillera Blanca normal fault [e.g., *Coney and Harms*, 1984; *Coney*, 1987; *Sonder et al.*, 1987; *Chapter 3, 4*]. Exhumation of the footwall coincided with continued batholith crystallization [*Chapter 4*].



(4) As a result of either a plunging intrusion (i.e., the batholith was emplaced with the northern end closer to the surface) [e.g., *Cobbing et al.*, 1981] or enhanced erosion in the north, displacement on the Cordillera Blanca normal fault was greatest along the northern segment [*Chapter 2*]. This resulted in deeply incised drainages, greater fault surface exposure, and steeper stream profiles in the northern region of the footwall [*Chapter 2*].

(5) Displacement along the fault propagated southward along strike, unroofing the batholith at the same time. Lower relief, less exposed fault relief, less footwall incision and less steep stream profiles characterize the southern fault region [*Chapter 2*]. As a result of continued footwall exhumation in the north, erosion outpaced deposition and sediment only accumulated in the supradetachment basin along the southern half of the fault [*Chapter 3*]. Southward fault propagation was linked to the continued southward propagation of the Nazca Ridge. Viscous coupling between the flat slab and overriding plate transferred oblique shear stress, resulting in extension in the Cordillera Blanca region [e.g., *Coney and Reynolds*, 1977; *Dickinson and Snyder*, 1978; *Coney and Harms*, 1984; *Miller et al.*, 1992; *Chapter 1*].

(6) A massive episode of glaciation removed a large amount of footwall material at ~1-2 Ma [e.g., *Smith et al.*, 2005]. This may have affected low-temperature thermochronometers and might be observable along strike where glacial erosion was most active [e.g., *Armstrong et al.*, 2003; *Ehlers et al.*, 2003; *Chapter 4*].

(7) Since at ~3 Ma, fault slip and vertical exhumation rates have slowed along the Cordillera Blanca normal fault [*Chapter 4*]. The lack of intrusive heating and the continued refrigeration of the upper plate from the flat slab has strengthened the crust, removing the main driving force behind extension.

## 5.2 REFERENCES

- Armstrong, P. A., Ehlers, T.A., Chapman, D.S., Farley, K.A., and Kamp, P.J.J., 2003, Exhumation of the Wasatch Mountains, Utah: 1. Patterns and timing of exhumation deduced from low-temperature thermochronology data: *Journal of Geophysical Research*, v. 108, doi:10.1029/2001JB001708.
- Cobbing, E. J., Pitcher, W.S., Wilson, J.J., Baldock, J.W., Taylor, W.P., McCourt, W., and Snelling, N.J., 1981, *The geology of the Western Cordillera of northern Peru*, Overseas Memoir, Institute of Geological Sciences, 143 p.
- Coney, P. J., 1987, The regional tectonic setting and possible causes of Cenozoic extension in the North American Cordillera, *in* Coward, M. P., Dewey, J.F., and Hancock, P.L., ed., *Continental Extensional Tectonics*, Geological Society Special Publication No. 28, p. 177-186.
- Coney, P. J., and Harms, T.A., 1984, Cordilleran metamorphic core complexes: Cenozoic extensional relics of Mesozoic compression: *Geology*, v. 12, p. 550-554.
- Coney, P. J., and Reynolds, S.J., 1977, Cordilleran Benioff zones: *Nature*, v. 270, p. 403-406.
- Dickinson, W. R., and Snyder, W.S., 1978, Plate tectonics of the Laramide orogeny: *Geological Society of America Memoir* 151, p. 335-366.
- Ehlers, T. A., Willett, S.D., Armstrong, P.A., and Chapman, D.S., 2003, Exhumation of the central Wasatch Mountains, Utah: 2. Thermokinematic model of exhumation, erosion, and thermochronometer interpretation: *Journal of Geophysical Research*, v. 108, doi: 10.1029/2001JB001723.
- Garzione, C. N., Quade, J., DeCelles, P.G., and English, N.B., 2000, Predicting paleoelevation of Tibet and the Himalaya from  $\delta^{18}\text{O}$  vs. altitude gradients in

meteoric water across the Nepal Himalaya: *Earth and Planetary Science Letters*, v. 183, p. 215-229.

Garzione, C. N., Dettman, D.L., and Horton, B.K., 2004, Carbonate oxygen isotope paleoaltimetry: evaluating the effect of diagenesis on paleoelevation estimates for the Tibetan plateau: *Palaeogeography Palaeoclimatology Palaeoecology*, v. 212, p. 119-140.

Gutscher, M.-A., Olivet, J.-L., Aslanian, D., Eissen, J.-P., and Maury, R., 1999, The "lost Inca Plateau": cause of flat subduction beneath Peru?: *Earth and Planetary Science Letters*, v. 171, p. 335-341.

Hampel, A., 2002, The migration history of the Nazca Ridge along the Peruvian active margin: a re-evaluation: *Earth and Planetary Science Letters*, v. 203, p. 665-679.

McNulty, B. A., and Farber, D.L., 2002, Active detachment faulting above the Peruvian flat slab: *Geology*, v. 30, p. 567-570.

Miller, D. M., Nilsen, T.H., and Bilodeau, W.L., 1992, Late Cretaceous to early Eocene geologic evolution of the U.S. Cordillera, *in* Burchfiel, B. C., Lipman, P.W., and Zoback, M.L., ed., *Geology of North America, Cordilleran orogen: Conterminous U.S.*: v. G-3, p. 205-260.

Petford, N., and Atherton, M.P., 1992, Granitoid emplacement and deformation along a major crustal lineament: the Cordillera Blanca, Peru: *Tectonophysics*, v. 205, p. 171-185.

Rosenbaum, G., Giles, D., Saxon, M., Betts, P.G., Weinberg, R.F., and Duboz, C., 2005, Subduction of the Nazca Ridge and the Inca Plateau: Insights into the formation of ore deposits in Peru: *Earth and Planetary Science Letters*, v. 239, p. 18-32.

Smith, J. A., Finkel, R.C., Farber, D.L., Rodbell, D.T., and Seltzer, G.O., 2005, Moraine preservation and boulder erosion in the tropical Andes: interpreting old surface exposure ages in glaciated valleys: *Journal of Quaternary Science*, v. 20, p. 735-758.

Sonder, L. J., England, P.C., Wernicke, B.P., and Christiansen, R.L., 1987, A physical model for Cenozoic extension of western North America, *in* Coward, M., Dewey, J.F., and Hancock, P.L., ed., *Continental Extensional Tectonics*, Special Publication 28: London, Geological Society of London, p. 187-201.